DEPARTAMENT D'ASTRONOMIA I ASTROFISICA

NEW INSIGHTS INTO GALAXY CLUSTERS: FROM SIMULATIONS TO OBSERVATIONS.

SUSANA PLANELLES MIRA

UNIVERSITAT DE VALÈNCIA
Servei de Publicacions
2011

Aquesta Tesi Doctoral va ser presentada a València el dia 31 de maig de 2011 davant un tribunal format per:

- Dra. Rosa Domínguez Tenreiro
- Dr. Stefano Borgani
- Dr. Frazer Pearce
- Dr. Enrique Gaztañaga Balbás
- Dr. José María Ibáñez Cabanell

Va ser dirigida per:
Dr. Vicent Quilis Quilis

Dipòsit legal: V-479-2012
I.S.B.N.: 978-84-370-8204-2
Edita: Universitat de València
Servei de Publicacions
C/ Arts Gràfiques, 13 baix
46010 València
Spain
Telèfon:(0034)963864115

VNIVERSITAT DE VALÈNCIA
Departament d'Astronomia i Astrofísica

New Insights into Galaxy Clusters: from Simulations to Observations

TESIS DOCTORAL PRESENTADA POR
SUSANA PLANELLES MIRA

Burjassot (Valencia), abril de 2011

Dr. Vicent Quilis Quilis, Profesor Titular de la Universitat de València,

CERTIFICA:

Que la presente memoria, "New Insights into Galaxy Clusters: from Simulations to Observations", ha sido realizada bajo su dirección, por Susana Planelles Mira, y que constituye su tesis doctoral para optar al grado de Doctora en Física.

Y para que quede constancia y tenga los efectos que corresponda, firma el presente certificado en Burjassot, a 1 de abril de 2011.

Firmado: Vicent Quilis Quilis

A mi tía Filo

Portada. Imagen de un cúmulo de galaxias obtenido en una simulación cosmológica.
En el centro de la imagen se puede apreciar un cúmulo de galaxias de unas $\sim 10^{14}\, M_{\odot}$. La imagen de fondo (en azul) representa la distribución de su componente gaseosa, mientras que la imagen superpuesta (en rojo) constituye su componente de materia oscura.
El puzle ilustra el gran reto que estos objetos suponen para la Cosmología actual.

Cover. Image of a galaxy cluster obtained in a cosmological simulation.
In the centre of the image, a cluster of galaxies of $\sim 10^{14}\, M_{\odot}$ is clearly visible. The background image (in blue) represents the distribution of its gaseous component, whereas the superposed image (in red) stands for its dark matter component.
The puzzle illustrates the great challenge that these objects represent for present-day Cosmology.

Agradecimientos

Cuando empecé esta aventura llamada *Doctorado* sabía que me aportaría grandes conocimientos, pero no me imaginaba, en absoluto, que sería una experiencia tan gratificante, divertida y enriquecedora. Ya han pasado cuatro años desde entonces y la verdad es que el tiempo se me ha pasado literalmente volando. De hecho, no era consciente de lo rápido que estaba pasando hasta que me senté por primera vez a escribir estos agradecimientos. Tras estos años de seminarios, congresos, *papers*, viajes y algún que otro "susto" numérico, ha llegado el momento de dar las gracias.

Esta Tesis, aunque fruto de la constancia, la tenacidad y el trabajo llevado a cabo durante estos últimos años, también lo es de la colaboración, tanto científica como personal, con un numeroso grupo de personas que, sin duda, de una forma u otra y cada uno a su manera, me han ayudado a madurar tanto a nivel personal como científico permitiéndome llegar a encontrarme en situación de escribirla. Son tantas las personas a las que me siento profundamente agradecida que sería casi imposible recordarlas a todas. Sin embargo, no quisiera por ello dejar de agradecer su aportación a algunas de ellas que, de manera especialmente relevante, son responsables de que este trabajo haya tomado forma.

En primer lugar quisiera mostrar mi más profundo agradecimiento a mi director de Tesis. Gracias Vicent por la confianza que has depositado en mí desde el primer día, por valorar tanto mi trabajo (a veces, creo, incluso en exceso) y por estar siempre dispuesto a discutir conmigo mis numerosas dudas. Gracias también por enseñarme a "respirar" antes de que cunda el pánico ("como dicen los ingleses...*do not panic!* "), y por demostrarme que el esfuerzo y la constancia terminan dando, casi siempre, grandes resultados.

No me puedo olvidar de mi "otro" director, José María. Gracias por el apoyo, la ilusión, la energía y el cariño casi paternal que nos has mostrado siempre, especialmente en los momentos más delicados. En definitiva, muchas gracias a los dos. No os imagináis todo lo que he disfrutado y aprendido de vosotros durante estos años.

Por supuesto también me gustaría agradecer al resto de compañeros del DAA el haberme hecho sentir desde el primer momento como parte de una gran familia. Estoy especialmente agradecida a aquéllos que de una forma u otra se han interesado por mi trabajo o han contribuido a que mi día a día en el departamento fuera aún más agradable: Feli, Manel, Enric, Morales, Diego, Manolo, Toni y Nicolás.

Considero que para alcanzar cualquier meta, tanto en el trabajo como en la vida en general, es fundamental la gente que nos rodea y comparte con nosotros nuestro día a día. Esos compañeros en los que confías y te apoyas en los buenos y, no tan buenos, momentos; los que se enteran a la hora del café de qué estás haciendo y de qué harás después. En ese sentido, para mí ha sido fundamental tener cerca a Javi, un grandísimo amigo desde que llegué por primera vez a Valencia hace ya unos

cuantos años, y con el que he compartido clases y exámenes, y ahora también el trabajo. Siempre recordaré las horas de estudio el día antes del examen, las fiestas, las visitas a la máquina, las largas charlas sobre física o sobre la vida en general, las excursiones, las observaciones, los momentos de sueño de verdad y un largo etcétera. Gracias por estar ahí siempre. Y no te agobies mucho pero...¡el próximo eres tú!

También me he visto influida de forma muy positiva por una malagueña muy "salá" a la que he tenido la fortuna de tener como compañera de despacho durante más de tres años y con la he compartido muchísimos buenos momentos, tanto fuera como dentro del mismo. Gracias Isica por la alegría y el entusiasmo que contagias. Por si no lo sabías, el 4.02 es demasiado silencioso sin ti.

Estoy muy agradecida también a todos esos "amigos de congresos" que he hecho durante estos años. Esos que en un momento dado encuentras en un ámbito puramente laboral y con los que empiezas a entrelazar lazos mucho más personales casi sin darte cuenta. Gracias también a los "raveros" por los grandes momentos que compartimos allá donde nos manden; a los prestonianos, por acogerme como una más desde el primer día; y a esos triestinos con los que he compartido los últimos momentos de esta Tesis y con los que he aprendido "tantísimo" italiano...

Al margen de la vida en el departamento, para mí también ha sido fundamental durante todos estos años la gran familia "valenciana" de la que he formado parte. Aquí me refiero sobre todo a mis compañeras de piso, las antiguas y las nuevas, a los físicos, a los futboleros jueveros para los que *"el fútbol es nuestra vida"* y, por supuesto, a esa gran familia astronómica que ha ido creciendo a lo largo de todos estos años, la AAUV. Siempre recordaré con mucho cariño las fiestas en el piso, las partidas de Catán hasta las tantas, las cenas "frikis", los partidazos de los jueves y las cenas post-partido, las excursiones, las observaciones, las *cookies*, el frío del Penyagolosa,... Gracias especialmente a Kevin, Vicky, Isa, Natalia, Eva, Marteta, Arnau y Gess. No me imagino mi vida en Valencia sin todos vosotros.

Quisiera agradecer también su apoyo a todas esas personas que, sin pertenecer al ámbito científico, han estado ahí completando mi vida en otros aspectos. En este sentido, una mención muy especial merecen mis amigos de siempre, los del pueblo, esos con los que he crecido a nivel personal y con los que he compartido casi todos los momentos importantes de mi vida; esos que en ocasiones me conocen mejor que yo misma pero que ponen caras raras si les hablo de mi trabajo; esos para los que nos soy Susana, sino *la Ploych*. Ellos también son responsables de este trabajo hasta un punto que dudo mucho que sean capaces de imaginar.

Gracias especialmente a Adolfo y a Natalia. *Pichandal*, ¿qúe quieres que te diga? Gracias por ser tal y como eres. Ya sabes que para mí ha sido fundamental tenerte cerca. Por si no lo sabías, estoy muy orgullosa de ti y he aprendido muchísimo contigo. Además, es muy reconfortante saber que siempre estarás ahí. Natalieta, gracias por tu impulsividad, por enseñarme a ver la vida de la forma más práctica posible y por aportar ese puntito de locura que a veces es tan necesario y que sólo tú eres capaz de transmitir. Por supuesto no me puedo olvidar de Carmen, Jose, Raulet, y Dani. Gracias a todos por ser como sois y por estar ahí siempre.

Gracias también a toda mi familia, a la que me siento muy unida y con la que he compartido tantísimos buenos momentos a lo largo de toda mi vida. Gracias a

mi hermano, Luisito, a mis primos Clara, Paquito, Sergio y Nieves, a mi yaya y a mis tíos Rafelito, Paco, Julia y Emilio. No me puedo olvidar del nexo de unión de todos nosotros y la persona a la que dedico esta memoria: mi tía, que estaría orgullosísima de su *gitaneta* al leer estas líneas.

Gracias también a mi "otra" familia, especialmente a Yoli, Agustín y Diana. Gracias por vuestro cariño, por vuestra sencillez y por esa gastronomía con la me obsequiáis desde el primer día que entré en vuestra casa.

Para acabar, me gustaría mostrar mi más profunda gratitud y todo mi cariño a las personas que más me han apoyado durante todos estos años. Este trabajo también está dedicado a ellos.

Gracias Jorge por estar ahí siempre, de forma incondicional, en los buenos y en los malos momentos, por tu apoyo, tu cariño, tu confianza ciega en mí y por tu ayuda, no sólo en esta Tesis, sino en muchos aspectos de mi vida. Pero sobre todo, mil gracias por todos los buenos momentos y por saber siempre cómo hacerme sonreír. YEETSyTEELM.

Y por supuesto no puedo terminar sin dar unas gracias enormes a mis padres. Sin ellos no estaría escribiendo estas líneas. A ellos les debo todo lo que soy. Ellos me han inculcado que con honradez, humildad y mucho esfuerzo se puede alcanzar cualquier meta. Gracias por apoyarme siempre y mostrar interés en todo lo que hago, por los numerosos viajes Valencia-Alicante, por las visitas en todas mis estancias,... Muchísimas gracias. Aunque no os lo diga a menudo, soy muy consciente de que sin vosotros no lo habría conseguido.

En fin, pues esto no ha hecho más que empezar. Haga lo que haga a partir de ahora y vaya donde vaya, estoy segura de que seguiré contando con todos vosotros y, al fin y al cabo, es lo único que importa.

MUCHAS GRACIAS A TODOS.

Susana Planelles Mira

Contents

[1] This Chapter, a summary written in Spanish of the Thesis, is included to fulfil the Ph.D. regulations of the University of Valencia

[2] This Chapter is based on Planelles & Quilis (2010)
[3] This Chapter is based on Planelles & Quilis (2009)

[4] This Appendix corresponds to a paper submitted to MNRAS by Knebe et al. (2010).

List of Figures

Chapter 1

Resumen *

El trabajo llevado a cabo durante la presente Tesis se enmarca dentro del campo de la Cosmología Numérica y se centra en el estudio de la formación y la evolución de los cúmulos de galaxias. Para identificar las distintas estructuras cosmológicas y analizar sus historias evolutivas, ha sido necesario desarrollar varias herramientas numéricas. Por lo tanto, el presente estudio se dirige a entender y caracterizar los cúmulos de galaxias y sus procesos evolutivos asociados desde un punto de vista numérico. Sin embargo, puesto que el objetivo final de las simulaciones cosmológicas es obtener universos simulados tan similares como sea posible al verdadero, las comparaciones con datos observacionales serán una constante a lo largo del manuscrito. En este sentido, mi trabajo se ha centrado en varias líneas de investigación íntimamente relacionadas que tratan con el estudio teórico y numérico de los cúmulos de galaxias: (i) el problema de encontrar los halos de materia oscura, (ii) nuevas mejoras en simulaciones cosmológicas y, (iii) la formación y evolución de los cúmulos de galaxias. Respecto a las herramientas empleadas y los resultados presentados en este trabajo, tanto las propiedades de los distintos códigos numéricos como los modelos físicos considerados, juegan un papel fundamental complementándose mutuamente.

1.1 Introducción

Los cúmulos de galaxias son los objetos gravitacionalmente ligados más grandes del Universo. La primera referencia escrita a un cúmulo de galaxias probablemente es la del astrónomo francés Charles Messier en 1784 (Messier, 1784). En su *Catalogue des nébuleuses et des amas d'étoiles que l'on découvre parmi les étoiles fixes, sur l'horizon de Paris*, Messier catalogó 103 nebulosas, 30 de las cuales en la actualidad son identificadas como galaxias. En 1785 F. Wilhelm Herschel publicó *On the Construction of the Heavens* (Herschel, 1785), en el que sugería que el *"sidereal system we inhabit"* era una nebulosa, común en aspecto a muchas otras y que por lo tanto éstas debían ser externas a la nuestra. Lo más relevante en esta obra es la

*This Chapter, a summary written in Spanish of the Thesis, is included to fulfil the Ph.D. regulations of the University of Valencia

descripción que W. Herschel hace del cúmulo de galaxias Coma: *"that remarkable collection of many hundreds if nebulae which are to be seen in what I have called the nebulous stratum of Coma Berenices"*. Estos dos pioneros trabajos lideraron el nacimiento de la investigación científica con cúmulos de galaxias.

Muchos astrónomos del siglo XIX y principios del XX investigaron la distribución de las nebulosas con tal de entender su relación con el *"sidereal system"* local, la Vía Láctea. La pregunta a la que buscaban respuesta era si realmente las nebulosas eran externas a nuestra propia galaxia. La respuesta se obtuvo a principios del siglo XX, principalmente por los trabajos de V.M. Slipher y E. Hubble. Una vez establecida la naturaleza extragaláctica de las nebulosas, los astrónomos empezaron a considerar los cúmulos de galaxias como sistemas físicos. En 1933, F. Zwicky estimó la masa de un cúmulo de galaxias (Zwicky, 1933) estableciendo así, por primera vez, la necesidad de materia oscura.

El papel que juegan los cúmulos como laboratorios para estudiar la evolución de las galaxias pronto se hizo notar. En los años 50 la investigación con cúmulos de galaxias comenzó a cubrir un amplio abanico de aspectos: desde la distribución y las propiedades de las galaxias en cúmulos, hasta la existencia de agrupamientos a pequeña y gran escala; desde el origen y la evolución de los cúmulos, hasta su estado dinámico y la naturaleza de la materia oscura. La publicación en 1958 por Abell de *The distribution of rich clusters of galaxies* se convirtió en un libro de consulta básico en el estudio de los cúmulos de galaxias. Desde entonces, los cúmulos de galaxias se han convertido en uno de los temas de investigación fundamentales en el marco de la astrofísica extragaláctica y muchos autores han contribuido a su estudio, tanto con aspectos teóricos y/o numéricos como observacionales.

En los últimos años, la Cosmología ha experimentado un avance espectacular. Junto con los avances observacionales producidos por la nueva generación de telescopios y satélites, el desarrollo tecnológico ha estimulado la aparición de la Cosmología Computacional, que ha contribuido crucialmente a la comprensión que tenemos hoy sobre la formación y evolución de las estructuras cósmicas. A diferencia de otras ramas de la física, en Cosmología los fenómenos físicos objeto de estudio no pueden ser recreados en un laboratorio. Así, los actuales superordenadores hacen de laboratorios virtuales donde los astrofísicos analizan y ponen a prueba los diferentes modelos teóricos sobre la formación del universo que observamos.

Las nuevas observaciones, como las producidas por los satélites de rayos X CHANDRA y XMM-Newton, han despertado un nuevo entusiasmo en el estudio de los cúmulos de galaxias. Además, han puesto en evidencia un gran número de cuestiones abiertas en el marco actual de la formación y evolución de los cúmulos de galaxias, como por ejemplo, el problema de los flujos de gas frío o la ruptura de las relaciones de escala autosemejantes.

Para profundizar en el conocimiento de los escenarios cosmológicos más relevantes, tanto desde un punto de vista numérico como físico, son necesarios nuevos estudios complementarios usando las diferentes estrategias numéricas disponibles. En este sentido, el trabajo recogido en el pesente manuscrito contribuye a un excitante campo de investigación tratando de aportar algo de luz sobre algunos de los problemas abiertos anteriormente mencionados.

1.2 Propiedades físicas de los cúmulos de galaxias

En la actualidad, está ampliamente aceptado que la formación de estructuras cósmicas procede vía un paradigma fundamentalmente jerárquico. El modelo sobre el que este paradigma descansa se enmarca dentro del modelo de materia oscura fría con constante cosmológica, Λ-*Cold Dark Matter* (ΛCDM; Blumenthal et al., 1984), también conocido como el modelo concordante. Gracias a la combinación de diversas pruebas observacionales, los parámetros en los que se basa este modelo cosmológico se han podido acotar con gran precisión.

En este contexto, la formación de estructuras en el Universo procede de la evolución de pequeñas perturbaciones iniciales en el campo de densidad primordial que se expanden hasta escalas cosmológicas de acuerdo a modelos inflacionarios. La componente de materia oscura, que es no colisional, sufre colapso gravitacional dando lugar al crecimiento de las perturbaciones. De esta forma se va creando una red de estructuras cósmicas interconectadas entre sí a través de paredes y filamentos que constituyen lo que se conoce como la red cósmica.

Dentro de esta jerarquía de estructuras cósmicas los cúmulos de galaxias ocupan una posición muy especial: son los objetos más grandes que han tenido tiempo de sufrir colapso gravitacional. Como consecuencia, son una parte fundamental de la estructura a gran escala del Universo (LSS).

Los cúmulos de galaxias, cuyas masas totales varían entre 10^{13} y $10^{15} M_{\odot}$, están formados típicamente por cientos o miles de galaxias esparcidas en una región de unos pocos megaparsecs (Mpc). A pesar del gran número de galaxias, éstas no son la componente dominante en los cúmulos. El espacio intergaláctico está ocupado por un plasma muy caliente y difuso, el medio intracúmulo (ICM), que radía intensamente en rayos X. Este ICM, formado principalmente por hidrógeno y helio ionizados, se calienta hasta temperaturas de aproximadamente $10^7 - 10^8$ K. El ICM contiene la mayor parte del material bariónico en un cúmulo, aportando alrededor del 15% de la masa total del mismo. Sin embargo, esta masa total está dominada por una componente no bariónica, aún sin detectar y bastante evasiva, la materia oscura, cuya presencia se puede inferir a partir de sus efectos gravitacionales sobre la materia visible. Cuantitativamente, la masa total de un cúmulo de galaxias se subdivide, aproximadamente, como sigue: 80% materia oscura, 15% materia bariónica caliente en el ICM, y 5% materia bariónica fría en estrellas y galaxias.

Los cúmulos de galaxias constituyen una importante fuente de información sobre el modelo cosmológico subyacente haciendo posible un gran número pruebas críticas.

En este sentido, puesto que los cúmulos son los objetos más grandes cuyas masas pueden ser medidas con cierta exactitud, se pueden emplear para trazar la LSS del Universo. Además, mediante comparaciones de la distribución actual de masa de los cúmulos con la distribución de masa en tiempos más tempranos se puede medir el ritmo de formación de estructuras cósmicas, aportando importantes restricciones sobre los diferentes modelos cosmológicos.

Por otro lado, en escalas más pequeñas ($\leq$ 1 Mpc) la física de los bariones se hace más importante complicando considerablemente los procesos asociados. Durante el proceso jerárquico de formación de los cúmulos de galaxias, mediante compresión adiabática y ondas de choque, el gas intergaláctico se calienta hasta

temperaturas emisoras de rayos X, alcanza el equilibrio hidroestático dentro del potencial del cúmulo y se hace más denso. Una vez que el gas es suficientemente denso, se enfría, abandonando así la fase caliente y formando la componente estelar, y puede acretar hacia los agujeros negros supermasivos (SMBHs) albergados en los cúmulos de galaxias masivos. Estos procesos de enfriamiento y formación de estrellas y SMBHs pueden causar realimentación enérgetica debido a supernovas (SNe) o núcleos galácticos activos (AGN) que, a su vez, pueden calentar considerablemente el ICM y esparcir elementos pesados a lo largo del volumen del cúmulo. A pesar de esta enorme inyección de energía, dado que los pozos de potencial gravitacional de los cúmulos son suficientemente profundos como para conservar todos los bariones difusos, los cúmulos son esencialmente como "cajas cerradas" y se espera que contengan una fracción universal de bariones dentro de un radio relativamente grande. Por tanto, la componente bariónica de los cúmulos conserva información importante sobre los procesos asociados con la formación de galaxias, incluyendo tanto aspectos relacionados con la eficacia de la formación estelar como con los procesos de calientamiento y retroalimentación energética resultantes.

Debido a la diferente naturaleza de los distintos componentes de los cúmulos de galaxias, éstos pueden ser observados en distintas longitudes de onda:

- **Cúmulos en el óptico.** Las galaxias que forman los cúmulos son las responsables de esta emisión. Aunque la identificación de cúmulos en el óptico ha alcanzado un alto grado de sofisticación en los últimos años, el procedimiento habitual se basa en la técnica de inspección visual iniciada por Abell y colaboradores en los años 50 (Abell, 1958). Una vez identificados los candidatos a cúmulo, su verdadero estatus se puede confirmar midiendo la masa subyacente. Para ello exiten varios métodos complementarios basados en, por ejemplo, la riqueza óptica de los cúmulos, las velocidades orbitales de las galaxias miembro, o el grado de deformación que sufren las galaxias situadas detrás de un cúmulo como consecuencia del efecto lente provocado por el potencial gravitatorio del mismo.

- **Cúmulos en rayos X.** El gas caliente y difuso que forma el ICM es el responsable de la emisión en rayos X de los cúmulos. Para temperaturas típicas de cúmulo ($kT \gtrsim 2keV$), la emisividad del ICM, que se comporta como un plasma totalmente ionizado, está dominada por un continuo de bremsstrahlung térmico. Si se consideran sistemas más fríos hay que tener en cuenta una contribución adicional de líneas de emisión de metales. Las luminosidades en rayos X típicas de los cúmulos están en el rango de $\sim 10^{43}$–$10^{45} erg/s$.

- **Cúmulos en microondas.** Si se observa en la dirección de los cúmulos de galaxias, el gas caliente del ICM también se puede detectar por sus efectos sobre el fondo cósmico de microondas (CMB). El CMB tiene un espectro de cuerpo negro casi perfecto con una temperatura de aproximadamente 2.7 K. La dispersión de Compton inverso de los electrones térmicos en cúmulos induce distorsiones pequeñas pero detectables en el espectro del CMB, desviando así ligeramente algunos de los fotones de microondas hacia energías más altas a medida que pasan a través del gas caliente intergaláctico. Este

efecto se conoce como el efecto Sunyaev-Zel'dovich (Sunyaev & Zel'dovich, 1970, 1972; Carlstrom et al., 2002).

El modelo más sencillo que trata de explicar las propiedades del ICM se basa en la idea de que la gravedad es la única fuerza responsable de la evolución del mismo. En este escenario, el gas colapsa en los pozos de potencial de la materia oscura formando ondas de choques de acreción que se mueven hacia el exterior, calentando así el gas del ICM hasta la temperatura virial del cúmulo. Puesto que la gravedad actúa indistintamente sobre todas las escalas, este modelo se conoce con el nombre de modelo autosemejante (Kaiser, 1986). Este modelo adiabático proporciona predicciones muy precisas sobre la forma y la evolución de diferentes relaciones de escala entre algunas de las propiedades fundamentales de los cúmulos como son la luminosidad, la masa, la temperatura o la entropía de los mismos. Estas relaciones de escala son esenciales para entender la evolución de los cúmulos de galaxias.

A pesar de la simplicidad y las importantes predicciones proporcionadas por el modelo autosemejante, siguen exitiendo algunos problemas abiertos a los que éste no puede dar explicación y que suponen grandes retos para la cosmolgía actual. Entre algunos de estos problemas, destacamos los siguientes:

- **Relaciones de escala no autosemejantes.** Recientes obervaciones en rayos X han demostrado que las relaciones de escala predichas por el modelo autosemejante no concuerdan con los resultados observacionales completamente. En concreto: (i) la relación luminosidad-temperatura es más pronunciada de lo predicho (Markevitch, 1998; Arnaud & Evrard, 1999; Osmond & Ponman, 2004), (ii) la entropía del gas en cúmulos pequeños y grupos es mayor de lo esperado (Ponman et al., 2003; Sun et al., 2009), y (iii) se ha observado una tendencia decreciente de la fracción de gas en sistemas pequeños (Balogh et al., 2001; Lin et al., 2003; Sanderson et al., 2003; Vikhlinin et al., 2006b; Croston et al., 2008).

- **El problema de los flujos de gas frío.** El modelo clásico de los flujos de gas frío predice que, en ausencia de un mecanismo que aporte calor, a medida que el gas de alta densidad en el centro de los cúmulos se enfría, la falta de presión que soporte al gas externo hace que éste fluya hacia el centro del cúmulo, creando así una superposición de gas en diferentes fases con distintas temperaturas. El famoso problema de los flujos de gas frío proviene de la observación de que en algunos de estos cúmulos, los llamados cúmulos de núcleo frío o *cool core* (CC), los ritmos de enfriamiento y de conversión de gas frío en estrellas son menores de lo esperado. Además, la temperatura central es mayor de lo predicho por el modelo (por ejemplo, Peterson et al., 2003; Bauer et al., 2005).

Estas discrepancias entre el modelo autosemejante y las observaciones han puesto en evidencia la necesidad de incluir algún proceso físico adicional relacionado, básicamente, con la componente bariónica. La solución más plausible para explicar estas desviaciones es la existencia de alguna fuente de calentamiento o retroalimentación energética en el centro de los cúmulos. En la actualidad, el candidato más aceptado es el AGN (Fabian et al., 1984). Sin embargo, el reto es

entender con exactitud el método de funcionamiento de alguna de estas fuentes en el escenario global de los cúmulos de galaxias.

1.3 Cosmología Numérica

Las simulaciones numéricas de formación de estructuras son herramientas esenciales en cosmología teórica. En los últimos treinta años, gracias al progreso experimentado tanto numérica como computacionalmente, estas simulaciones se han podido aplicar sistemáticamente como instrumentos científicos dando lugar a importantes avances en nuestro conocimiento del Universo.

Históricamente, el uso de simulaciones cosmológicas empieza en los años 60 (Aarseth, 1963) y 70 (por ejemplo, Peebles, 1970; White, 1976). Estas primeras simulaciones modelaban la componente de materia oscura mediante la técnica de N-cuerpos sobre un número reducido de partículas. Sin embargo, cualquier simulación realista que trate de explicar el crecimiento de estructuras en el Universo debe contener, además, un tratamiento hidrodinámico para describir la evolución de la componente bariónica. La física bariónica es mucho más compleja de modelar que la de la componente de materia oscura. Los códigos hidrodinámicos acoplados a técnicas de N-cuerpos son las herramientas más avanzadas para describir y analizar los complejos procesos asociados a la formación y evolución de galaxias y cúmulos de galaxias, así como el papel que éstos juegan durante la evolución jerárquica de las estructuras cósmicas. Las primeras simulaciones hidrodinámicas son de la década de los 70 (Gingold & Monaghan, 1977), mientras que las primeras simulaciones cosmológicas hidrodinámicas/N-cuerpos son de los años 80 (Evrard, 1988; Hernquist & Katz, 1989).

Una vez especificado el modelo cosmológico subyacente, estas simulaciones parten de un conjunto de condiciones iniciales obtenidas a alto *redshift* y avanzan los campos de densidad y velocidad integrando numéricamente las ecuaciones que gobiernan la dinámica de la materia oscura y de la materia bariónica. Debido a su diferente naturaleza, la evolución de estas componentes se resuleve mediante diferentes técnicas numéricas.

- **Dinámica de la materia oscura**

  Para la componente de materia oscura sólo se resuelve un subconjunto representativo de ecuaciones. Para ello, se discretiza y se muestrea el espacio de fase inicial mediante N partículas y luego se integran sus ecuaciones de movimiento en el campo gravitatorio global. Las partículas se evolucionan temporalmente usando las leyes de Newton escritas en coordenadas comóviles (Peebles, 1980).

  El núcleo de las simulaciones de N-cuerpos descansa en el algoritmo computacional empleado para obtener la fuerza gravitatoria, es decir, para resolver la ecuación de Poisson. El método más directo y preciso se basa en calcular la fuerza entre cada par de partículas. Sin embargo, este método de integración requiere un número de operaciones que escala como N^2, siendo computacionalmente prohibitivo para grandes simulaciones cosmológicas. Por esta razón, para obtener un buen compromiso entre el coste computacional y la

resolución numérica, se han desarrollado diferentes técnicas de integración entre las que destacan métodos basados en una malla como el *particle-mesh* (PM) y el *particle-particle/particle-mesh* (P^3M) (Hockney & Eastwood, 1988; Couchman, 1991), métodos sin malla que se basan en la ordenación de partículas vecinas (Barnes & Hut, 1986; Bouchet & Hernquist, 1988), y métodos que combinan ambos enfoques (Bagla, 2002; Bode & Ostriker, 2003; Springel, 2005).

- **Dinámica del gas**

  Las ecuaciones que gobiernan la evolución de las inhomogeneidades cosmológicas son más complejas que las de la materia oscura (Peebles, 1980). En este caso, tanto la gravedad como los gradientes de presión son los responsables de la evolución. La componente gaseosa está ligada a la de materia oscura mediante el campo gravitatorio global a través de la ecuación de Poisson.

  La integración de las ecuaciones de la hidrodinámica que gobiernan la evolución del gas se puede llevar a cabo usando diferentes técnicas. La adopción de una técnica particular, con sus ventajas y desventajas asociadas, tiene consecuencias directas sobre el resultado de la simulación. Las técnicas numéricas que se usan para resolver la evolución de la componente bariónica se pueden dividir en dos grandes grupos:

  Técnicas Lagrangianas. El método más popular es el *Smooth Particle Hydrodynamics* (SPH; Lucy, 1977; Gingold & Monaghan, 1977). Relativamente fácil de implementar y con un coste computacional bajo, proporciona un gran rango dinámico ya que, dado su carácter lagrangiano, no existe una malla que lo restrinja. Esta propiedad ha hecho que los métodos lagrangianos sean particularmente exitosos en simulaciones cosmológicas de formación de estructuras. Sin embargo, a pesar de sus ventajas, la técnica SPH también presenta algunos puntos débiles entre los que destacan: (i) tratamiento y descripción aproximadas de las ondas de choque y de los fuertes gradientes, (ii) descripción pobre de regiones de baja densidad, (iii) necesidad de usar artefactos numéricos como la viscosidad artificial, y (iv) posible violación de propiedades de conservación. No obstante, en la actualidad existen diversos códigos SPH que incluyen numerosas mejoras que resuelven favorablemente algunas de estas limitaciones (por ejemplo, Springel et al., 2001b; Serna et al., 2003; Wadsley et al., 2004; Springel, 2005; Wetzstein et al., 2009).

  Técnicas Eulerianas. Estas técnicas, también conocidas como métodos de malla de captura de choques, representan una alternativa a los métodos lagrangianos. Entre las técnicas eulerianas, las basadas en resolvedores de Riemann han resultado ser particularmente satisfactorias (por ejemplo, Ryu et al., 1993; Quilis et al., 1994; Bryan et al., 1995; Gheller et al., 1998). Estos métodos numéricos están escritos de forma conservativa, asegurando así una excelente conservación de las cantidades físicas. Las ondas de choque, las discontinuidades y los gradientes pronunciados son resueltos, típicamente, en una o dos celdas en 1-D. El uso de resolvedores

de Riemann evita la necesidad de viscosidad artificial para integrar las ecuaciones con discontinuidades. Aunque estas propiedades son fundamentales para construir un método hidrodinámico robusto, debido precisamente a su carácter euleriano – se necesitan mallas numéricas fijas para integrar las ecuaciones hidrodinámicas –, estas técnicas están limitadas por una baja resolución espacial. Para alcanzar una resolución adecuada son necesarias mallas numéricas más densas que rápidamente elevan el coste computacional. Afortunadamente, esta limitación se ha superado en los últimos años con la adopción de la técnica conocida como *Adaptive Mesh Refinement* (AMR; Berger & Oliger, 1984; Berger & Colella, 1989). La idea fundamental de esta técnica es mejorar la resolución numérica de las simulaciones basadas en esquemas de malla fija. Para ello, se emplea un esquema euleriano como los ya descritos pero ganando resolución, tanto espacial como temporal, refinando de forma selectiva la malla computacional original. El resultado es una jerarquía de mallas anidadas que se comporta, de manera natural, de forma lagrangiana (las mallas sólo se refinan en regiones de interés como, por ejemplo, regiones de alta densidad). Además, cada una de estas mallas, con condiciones de contorno adecuadas, es tratada por el esquema euleriano como un dominio computacional independiente. Esta técnica ha demostrado ser muy útil en aplicaciones cosmológicas.

Aunque ambos enfoques numéricos – lagrangiano y euleriano – tratan de solucionar el mismo problema físico, debido a sus diferencias intrínsecas, existen importantes discrepancias en la solución numérica de algunas aplicaciones físicas (véanse, por ejemplo, Agertz et al., 2007; Tasker et al., 2008). Sin embargo, puesto que ambas técnicas son extremadamente útiles y complementarias, es importante comparar sus resultados e identificar posibles errores sistemáticos asociados a un método en particular.

- **Física adicional**

  Además de la gravedad y de la dinámica del gas adiabático, las simulaciones cosmológicas que traten de describir consistentemente la formación de galaxias y la evolución del medio intergaláctico necesitan incluir modelos de procesos átomicos y radiativos. Los procesos más habituales considerados en las simulaciones cosmológicas de última generación incluyen, para un gas ópticamente delgado, procesos de enfriamiento y calentamiento para un gas primordial, múltiples especies químicas y un tratamiento fenomenológico de la formación estelar y de sus procesos de retroalimentación energética asociados. Todos estos procesos se modelan parametrizando fenomenológicamente la física relevante e incluyéndolos como términos fuente a la derecha de la igualdad en las ecuaciones de la hidrodinámica (Cen, 1992; Cen & Ostriker, 1992; Katz, 1992; Yepes et al., 1997).

Como se ha explicado en la Sección anterior, la aproximación más simple es considerar el gas no radiativo y realizar simulaciones adiabáticas (Evrard, 1990). Este modelo es capaz de reproducir la tendencia general de las leyes de escala autosemejantes pero muestra algunas discrepancias con las observaciones. Mientras

las regiones más externas de los cúmulos, más allá de aproximadamente el 10% del radio virial, son bastante regulares, casi autosemejantes, y están bien descritas por las simulaciones, las regiones centrales más internas exhiben una gran dispersión y efectos de formación galáctica e inyección de energía por un AGN central. Estudios de estos efectos han dado lugar, en los últimos años, a una línea de investigación muy activa y vibrante en el campo de las simulaciones cosmológicas.

Para tratar de solucionar estas discrepancias, las simulaciones cosmológicas han incluido algunos procesos no gravitacionales como enfriamiento radiativo (Pearce et al., 2000; Muanwong et al., 2001; Davé et al., 2002; Motl et al., 2004; Kravtsov et al., 2005) y precalentamiento (Navarro et al., 1995a; Bialek et al., 2001; Borgani et al., 2002). Las simulaciones más sofisticadas acoplan procesos de retroalimentación energética con procesos de enfriamiento y formación estelar (por ejemplo, Kay et al., 2003; Tornatore et al., 2003; Valdarnini, 2003; Borgani et al., 2004; Ettori et al., 2004a; Kay et al., 2004, 2007). Otros estudios también han incluido generación de metales y enriquecimiento químico (Valdarnini, 2003; Schindler & Diaferio, 2008; Borgani et al., 2008), así como campos magnéticos y sus procesos no térmicos asociados (Dolag et al., 1999, 2008).

Dentro de este contexto, debido tanto a su posición central como a su capacidad para proporcionar cantidades suficientes de energía, la retroalimentación energética producida por un AGN central se considera la fuente de calentamiento más probable. Se cree también que el calentamiento de AGN juega un papel fundamental en detener la formación estelar en los cúmulos de galaxias más brillantes (BCGs), reduciendo así la fracción de masa estelar en los mismos. Las tendencias observadas de las fracciones de gas caliente y de la entropía en las regiones más centrales en función de la masa del cúmulo también sugieren calentamiento de AGN. Todos estos motivos ponen en evidencia la importancia de incluir este mecanismo de forma consistente en las simulaciones cosmológicas. Sin embargo, los detalles del proceso de calentamiento por los chorros galácticos de los AGN todavía son algo inciertos (Voit, 2005).

La principal dificultad a la hora de tratar con la mayor parte de estos procesos disipativos reside en el hecho de que ocurren a escalas mucho más pequeñas que la resolución espacial de la simulación y, por tanto, deben ser aproximados mediante recetas fenomenológicas. Como consecuencia, en la actualidad, una tarea bastante compleja para las simulaciones consiste en concordar simultáneamente con las observaciones las propiedades termodinámicas del ICM, la fracción de masa estelar y la función de luminosidad de las galaxias.

La gran cantidad de procesos físicos a tener en cuenta, así como la necesidad de grandes recursos computacionales a la hora de correr simulaciones N-cuerpos/hidrodinámicas que proporcionen una descripción lo más realista posible de la formación de galaxias y cúmulos de galaxias, supone un gran reto en el campo de la Cosmología Numérica, tanto desde el punto de vista computacional como físico.

1.4 Simulaciones cosmológicas con MASCLET

Las simulaciones cosmológicas analizadas en esta Tesis se han llevado a acabo con el código cosmológico MASCLET (Quilis, 2004). MASCLET (*Mesh Adaptive Scheme for CosmologicaL structurE evoluTion*) es un código euleriano diseñado para aplicaciones cosmológicas que combina un tratamiento hidrodinámico del gas con un esquema de N-cuerpos para las componentes sin colisiones, es decir, la materia oscura y las estrellas. Además, está basado en un esquema AMR.

En MASCLET el resolvedor de la hidrodinámica se basa en el método *Piecewise Parabolic Method* (PPM; Colella & Woodward, 1984), mientras que el esquema de N-cuerpos que se emplea es el clásico PM según Hockney & Eastwood (1988). Gas, materia oscura y estrellas están acoplados a través del resolvedor de la gravedad y se benefician de la técnica AMR.

MASCLET está escrito en FORTRAN 90 y existe una versión paralelizada en OpenMP.

Debido a su diferente naturaleza, las diversas componentes de materia se tratan numéricamente de forma distinta.

- **Dinámica del gas**

  En MASCLET, el tratamiento de la hidrodinámica se basa en reescribir las ecuaciones que gobiernan la evolución de las inhomogeneidades cosmológicas como un sistema hiperbólico de leyes de conservación. Las propiedades matemáticas de este tipo de sistemas y los algoritmos numéricos diseñados específicamente para resolverlos han sido ampliamente estudiados en la literatura (LeVeque, 1992; Toro, 1997). Este sistema de ecuaciones se completa con una ecuación de estado de gas ideal.

  Desde un punto de vista numérico, las propiedades matemáticas de este tipo de sistemas son cruciales para desarrollar la mayor parte de los algoritmos numéricos empleados en simulaciones hidrodinámicas. De hecho, las propiedades matemáticas resultantes del carácter hiperbólico de este sistema de ecuaciones nos permiten diseñar un conjunto de técnicas numéricas conocidas como de *captura de choque de alta resolución* (HRSC). Estas técnicas son la implementación moderna del método original de Godunov (Godunov, 1959).

  Las técnicas HRSC tienen varios ingredientes fundamentales como el procedimiento de reconstrucción, el resolvedor de Riemann, y los esquemas de avance temporal que pueden variar en diferentes implementaciones. Sin embargo, todas estas implementaciones comparten las mismas propiedades básicas: la capacidad de tratar adecuadamente con choques, discontinuidades y fuertes gradientes en las cantidades integradas, y unas excelentes propiedades de conservación.

  El resolvedor de la hidrodinámica usado en MASCLET está basado en una implementación particular de los métodos HRSC. Los principales ingredientes de este resolvedor son los siguientes:

  1. Está escrito en forma conservativa.

2. Procedimiento de reconstrucción. Permite ganar resolución reconstruyendo, mediante interpolaciones, la distribución de las cantidades dentro de las celdas numéricas. Para aumentar la precisión espacial se ha implementado una subrutina de reconstrucción parabólica (PPM) según el procedimiento ideado por Colella & Woodward (1984). Con esta reconstrucción parabólica, el algoritmo tiene una precisión espacial de tercer orden. Los flujos numéricos se pueden calcular a través de la resolución de problemas de Riemann locales entre las iterfaces de celdas vecinas.
3. Flujos numéricos en las interfaces. Se emplea un resolvedor de Riemann linealizado similar al descrito en Roe (1981).
4. Avance temporal. Una vez conocidos los flujos numéricos, la evolución de las cantidades conservadas se rige por un sistema de ecuaciones diferenciales ordinarias. Para resolver este sistema se emplea un resolvedor de Runge-Kutta de tercer orden (Shu & Osher, 1988).

- **Dinámica de la materia oscura**

  La materia oscura se trata como un sistema de partículas sin colisiones. Cada una de estas partículas se evoluciona según las leyes de Newton en coordenadas comóviles.

  En MASCLET estas ecuaciones se resuelven mediante un esquema de Lax-Wendroff que es de segundo orden. Para obtener el campo de densidad continua de materia oscura se usa el método *triangular shaped cloud* (TSC; Hockney & Eastwood, 1988) en cada paso temporal.

- **Formación estelar**

  En MASCLET se ha incluido una formación estelar fenomenológica siguiendo las ideas de Yepes et al. (1997) y Springel & Hernquist (2003). Al igual que la materia oscura, las estrellas se tratan como un sistema de partículas sin colisiones que evolucionan según las mismas ecuaciones. En nuestro método, el gas frío en una celda se transforma en partículas estelares según un cierto tiempo característico y una densidad umbral de formación estelar. Además, se permite que una fracción de la masa de estrellas masivas sea devuelta a la componente gaseosa tras explotar como supernovas. Se asume una función de masa inicial (IMF) compatible con la de Salpeter.

  Al igual que con la materia oscura, se emplea la técnica TSC para obtener la densidad estelar continua sobre la malla a partir de la distribución de partículas.

- **Enfriamiento del gas y metalicidad**

  El enfriamiento del gas se trata de forma similar que en Springel & Hernquist (2003). Nuestras simulaciones incluyen procesos de enfriamiento y calentamiento que tienen en cuenta enfriamiento Compton y libre-libre, calentamiento UV, y enfriamiento atómico y molecular para un gas primordial. Para calcular las abundancias de cada especie se asume que el gas es

ópticamente delgado y está en equilibrio de ionización pero no en equilibrio térmico.

Los ritmos de enfriamiento dependen fuertemente de la temperatura del gas y de su metalicidad. En MASCLET, estas dependencias se modelan mediante las curvas de enfriamiento por ionización colisional de Sutherland & Dopita (1993).

En nuestra particular implementación, para considerar la contribución de los metales asumimos una serie de premisas: (i) los metales son las especies más pesadas que el hidrógeno y el helio; (ii) son instantáneamente mezclados en el ICM; y (iii) evolucionan según la componente gaseosa. Para tener en cuenta esta contribución de la metalicidad hemos completado el sistema de ecuaciones de la hidrodinámica con una nueva ecuación de continuidad para la densidad de metales.

- **Criterios de evolución temporal**

  Para resolver numéricamente las ecuaciones de la hidrodinámica y de evolución de la materia oscura es importante escoger adecuadamente un paso temporal. La estabilidad numérica de los métodos usados para integrar estas ecuaciones impone varios criterios sobre el paso de tiempo. En cada iteración numérica calculamos diversos pasos temporales dados por las diferentes condiciones de estabilidad. El más restrictivo de todos ellos es seleccionado para avanzar todas las componentes.

- **Resolvedor de la gravedad**

  El potencial gravitatorio se calcula resolviendo la ecuación de Poisson. Según el nivel de la malla computacional sobre el que se requiera resolver esta ecuación se usan diferentes métodos: métodos de transformada de Fourier rápida (FFT; Press et al., 1996) para el nivel base, y métodos de sobrerrelajación sucesiva (SOR) para niveles superiores.

Como se ha explicado con anterioridad, la idea fundamental en la que se basa la técnica AMR es superar la falta de resolución asociada a una descripción euleriana de malla fija. La idea básica es sencilla. Regiones del dominio computacional original en las que es necesario aumentar la resolución se seleccionan de acuerdo con ciertos criterios. Estos nuevos dominios computacionales, llamados mallas hijo o parches, se vuelven a muestrear con un mayor número de celdas y, por tanto, con una mejor resolución. Los valores de las diferentes cantidades definidas sobre las mallas hijo se obtienen por interpolación desde las mallas padre. Una vez se han construido las mallas hijo, éstas se evolucionan como un dominio computacional independiente utilizando los mismos métodos que se han descrito anteriormente. Aunque conceptualmente el método es simple, existen grandes complicaciones técnicas relacionadas con la comunicación entre los diferentes parches y los problemas de contorno entre diferentes niveles.

Nuestra implementación particular de la técnica AMR sigue la descrita en Berger & Colella (1989).

1.5 El buscador de halos ASOHF

Las simulaciones cosmológicas han proporcionado importantes avances en nuestra comprensión del Universo. Sin embargo, los principales resultados de estas complejas simulaciones "tan sólo" consisten en grandes cantidades de datos en bruto que requieren ser tratados de una forma u otra dependiendo de la aplicación particular. En el caso de las simulaciones de N-cuerpos, los agregados de millones de partículas no colisionales de materia oscura requieren ser interpretados y, de alguna forma, comparados con el universo observable. Para ello es necesario identificar los grupos de partículas de materia oscura gravitacionalmente ligadas, que representan la contraparte oscura de las componentes observables de las estructuras cosmológicas (galaxias, cúmulos de galaxias, ...). Estos cúmulos de materia oscura son los llamados halos de materia oscura y la tarea de identificarlos en simulaciones se realiza, generalmente, con la ayuda de herramientas numéricas conocidas como buscadores de halos.

A lo largo de los años se han propuesto y se han perfeccionado diferentes algoritmos para identificar estructuras y subestructuras en simulaciones cosmológicas. Como consecuencia, en la actualidad existen varios tipos de buscadores de halos ampliamente utilizados aunque, en el fondo, la idea básica de todos ellos es la identificación de objetos gravitacionalmente ligados en simulaciones de N-cuerpos. Todos estos buscadores de halos parecen funcionar extraordinariamente bien cuando se trata de identificar halos sin subestructura. Sin embargo, el notable desarrollo experimentado por las simulaciones de N-cuerpos y las aplicaciones estudiadas con estos nuevos códigos necesitan nuevos algoritmos capaces de tratar con el escenario de halos dentro de halos (por ejemplo, Klypin et al., 1999a,b; Moore et al., 1999).

La mayor parte de los buscadores de halos existentes están basados en alguna de las dos técnicas clásicas de identificación: el algoritmo *friends-of-friends* (FoF; Davis et al., 1985) o el método *spherical overdensity* (SO; Lacey & Cole, 1994). El método FoF básicamente consiste en identificar vecinos de partículas de materia oscura y vecinos de éstos vecinos de acuerdo con una longitud característica de ligadura. La colección de partículas ligadas forma un grupo que es considerado como un halo virializado. Entre las ventajas de esta técnica cabe destacar que sus resultados son relativamente fáciles de de interpretar y que no hace ninguna suposición previa sobre la forma de los halos. Por el contrario, una de sus principales desventajas es precisamente la elección "artifical" de la longitud característica de ligadura. Además, para identificar halos dentro de halos se necesitan definir diferentes longitudes de ligadura. Existen diversas variantes del método FoF original que tratan se superar estas limitaciones. Entre ellas destacan el FoF adaptativo (AFoF; van Kampen, 1995) o el FoF jerárquico (HFoF; Klypin et al., 1999a).

El otro método más popular, el SO, utiliza el criterio de sobredensidad media para la detección de halos virializados. La idea básica de esta técnica es identificar regiones esféricas con una densidad media correspondiente a la densidad de una región virializada según el modelo de colapso *top hat*. El principal inconveniente de esta definición de masa es que es algo artificial puesto que asume simetría esférica para todos los objetos. Además, definir de esta forma una masa puede resultar algo ambiguo debido a que dos esferas definidas de este modo podrían superponerse para dos picos de densidad cercanos. Debido a estas características,

el método SO implica algunas simplificaciones que pueden conducir a resultados poco realistas y que, por lo tanto, requieren un tratamiento cuidadoso. A pesar de estas, aparentemente, importantes desventajas, una de las propiedades más relevantes de esta técnica es que no se necesita una longitud característica de ligadura para definir las estructuras.

Para una descripción más detallada de los buscadores de halos más populares y las técnicas en las que se basan, véanse la Sección 6.2 y el Apéndice A.

El buscador de halos desarrollado para MASCLET, ASOHF (*Adaptive Spherical Overdensity Halo Finder*; Planelles & Quilis, 2010), comparte algunas características con el buscador de halos AHF (Knollmann & Knebe, 2009). Aunque hemos utilizado una técnica de identificación basada en la idea original del método SO, la aplicación práctica de nuestro buscador tiene varios pasos destinados a mejorar los resultados de este método, deshacerse de los posibles inconvenientes del mismo, y aprovechar las ventajas de la estructura de malla con AMR proporcionada por MASCLET.

Los principales pasos en los que se basa ASOHF son los siguientes:

1. En un primer paso, el algoritmo lee el campo de densidad calculado sobre la jerarquía de mallas proporcionada por las simulaciones. A continuación, se aplica el método SO sobre cada máximo de densidad: se crecen capas radiales alrededor de cada pico de densidad hasta que la sobredensidad media cae por debajo de un determinado umbral o hay un aumento significativo en la pendiente del perfil de densidad. La sobredensidad media depende del modelo cosmológico adoptado (se puede aproximar por la expresión dada en Bryan & Norman, 1998). Este primer paso, que sólo define la escala de los objetos que buscamos, proporciona una estimación aproximada de la posición, el radio y la masa de cada halo identificado.

2. El segundo paso corrige los posibles solapamientos que puedan existir entre los halos preliminares que se encuentran en el primer paso. En nuestro método, si dos halos se superponen y la masa común es mayor del 80% de la masa mínima de los halos implicados, el menos masivo de ellos se elimina de la lista. Por el contrario, si la masa compartida está entre el 40% y el 80% de la masa mínima de los halos, el algoritmo une estos halos en uno único y calcula el nuevo centro de masas. En consecuencia, se elimina el halo menos masivo de la lista y se aplica otra vez el primer paso para el nuevo centro de masas con tal de obtener las propiedades físicas del nuevo halo. Al final, este paso proporciona un número final de halos.

3. Una vez tenemos una selección provisional de halos, un tercer paso proporciona una muestra más precisa trabajando sólo con las partículas de materia oscura dentro de cada uno de ellos. Estas partículas se distribuyen a lo largo de todo el volumen simulado y no están limitadas por las fronteras de la malla. ASOHF puede tratar con varias especies de partículas (partículas con masas diferentes) proporcionando, por lo tanto, una mejor resolución en masa. Este paso es crucial para obtener una estimación precisa de las principales propiedades físicas de los halos, sobre todo, de la masa y de la posición del centro de masas de los mismos.

4. En este punto ya disponemos de un conjunto de posibles halos definidos mediante el espacio de posiciones de sus partículas. Sin embargo, estos candidatos a halo pueden incluir partículas que no están físicamente ligadas. Con el fin de eliminar las partículas no ligadas gravitacionalmente tenemos que obtener la velocidad de escape (local) en la posición de cada partícula. Si la velocidad de una partícula es mayor que la velocidad de escape, la partícula se supone no ligada y, por lo tanto, es eliminada del halo considerado. Este proceso de "limpieza" termina cuando un halo alcanza menos partículas que un mínimo fijado previamente o cuando no hay más partículas que eliminar. Las listas finales de partículas (ligadas) se utilizan para calcular propiedades canónicas de los halos como el perfil de densidad, la curva de rotación, la masa, la forma, etc.

5. El proceso termina cuando se comprueba que el perfil de densidad radial de los halos es coherente con la forma funcional propuesta por Navarro, Frenk & White (NFW; Navarro et al., 1997) entre dos veces la resolución de la fuerza y el radio virial.

Tras este proceso, el resultado final para cada halo incluye una estimación precisa de sus propiedades físicas fundamentales, la lista de sus partículas ligadas, la ubicación y la velocidad de su centro de masas, y los perfiles radiales de densidad y velocidad. Nótese que este método es completamente general y fácilmente aplicable a cualquier simulación de N-cuerpos suponiendo que el campo de densidad esté evaluado previamente sobre una malla o jerarquía de mallas anidadas.

Generalmente, las subestructuras se definen como grupos de partículas ligadas que representan máximos locales de densidad identificados dentro de halos mayores. En nuestro análisis, el proceso de identificación de halos descrito anteriormente se puede aplicar de forma independiente sobre cada nivel de refinamiento de la simulación. De esta forma, ASOHF puede identificar de manera natural halos dentro de halos obteniendo así una jerarquía de halos anidados. Además, es capaz de encontrar varios niveles de subestructura dentro de subestructura. Esta propiedad nos permite aprovechar la alta resolución espacial proporcionada por la técnica AMR, identificando así una amplia variedad de objetos de masas y escalas muy diferentes. Aunque conceptualmente el método es sencillo, debido al procedimiento seguido y a la naturaleza de la malla AMR, esta técnica puede mezclar subestructuras reales con halos superpuestos y con halos identificados más de una vez en diferentes niveles de refinamiento. Con el fin de hacer frente a estas posibles complicaciones, tenemos que aplicar una serie de condiciones adicionales.

Mediante este procedimiento las subestructuras sólo se pueden definir en los diferentes niveles de refinamiento de la malla. Estos niveles se han definido previamente por los criterios de refinamiento asumidos, los cuales pueden venir fijados por la evolución, cuando los *outputs* a analizar son directamente importados de un código como MASCLET, o por cualquier otro criterio, como el número de partículas por celda, cuando ASOHF funciona como un código independiente. Por lo tanto, ASOHF es capaz de encontrar subestructuras y asignarles masa con una gran precisión en la mayor parte de los halos anfitriones, estando limitado sólo por la existencia de refinamientos en la malla computacional.

Una vez que el código ha actuado sobre los distintos niveles de resolución de

la malla considerada, se obtiene una única muestra de halos clasificándolos en tres categorías según su naturaleza: halos individuales (con o sin grandes subestructuras), subhalos (pertenecientes a halos individuales) y halos pobres (halos con menos de un número fijo de partículas de materia oscura, o halos que en realidad son duplicados de otros halos). Por lo tanto, es posible obtener una muestra completa de objetos con masas y escalas muy diferentes, abarcando desde los halos más grandes hasta las escalas mínimas impuestas por la resolución de las simulaciones analizadas.

Una de las principales ventajas de nuestro método es que la jerarquía de mallas anidadas utilizada por las simulaciones cosmológicas con AMR se construye siguiendo los picos de densidad y, por lo tanto, estas mallas ya están convenientemente ajustadas para realizar el seguimiento de los halos de materia oscura. Por último, pero no por ello menos importante, el uso de AMR implica que no necesitamos definir una longitud de ligado.

Los halos de materia oscura y sus historias evolutivas son esenciales en cualquier teoría de formación de estructuras basada en el modelo ΛCDM. Sin embargo, la construcción de estos árboles evolutivos a partir de los resultados de una simulación de N-cuerpos no es una tarea trivial. ASOHF incluye una rutina que es capaz de obtener la historia evolutiva de cada uno de los halos encontrados. El método de identificación de progenitores se basa en la comparación de las listas de partículas que pertenecen a los halos en diferentes momentos, tanto anteriores como posteriores, de la evolución. Es decir, se trata de rastrear la historia de todas las partículas de materia oscura que pertenecen a un halo dado en una época determinada. Este procedimiento se repite hacia atrás en el tiempo hasta que se localiza el primer progenitor del halo considerado. Este mecanismo nos permite, no sólo conocer todos los progenitores de cada halo considerado, sino también la cantidad de masa que recibe de cada uno de sus antepasados.

En ASOHF, la forma de los halos se evalúa aproximando sus distribuciones de masa por la de un elipsoide triaxial. Los ejes de inercia de los diferentes halos se evalúan a partir del tensor de inercia (por ejemplo, Cole & Lacey, 1996; Shaw et al., 2006), cuyos autovalores determinan los ejes del elipsoide.

Con el objetivo de comprobar el comportamiento y los resultados obtenidos con ASOHF, hemos llevado a cabo diversas comparaciones y ejercicios de análisis. Por un lado, desarrollamos un conjunto de tests idealizados (artificiales pero emulando resultados reales de simulaciones cosmológicas) para poner a prueba el comportamiento del buscador en diferentes situaciones. Por otro lado, aplicamos ASOHF a una simulación cosmológica realizada con MASCLET y comparamos los resultados obtenidos por éste con los obtenidos por otros dos buscadores de diferente naturaleza: AHF (Knollmann & Knebe, 2009) y AFoF (van Kampen, 1995). Para detalles sobre los resultados obtenidos en cada uno de los casos, léanse las Secciones 6.5 y 6.6, respectivamente.

Durante el mes de mayo de 2010 fuimos invitados a participar en la reunión *Haloes going MAD* destinada a llevar a cabo el primer gran proyecto de comparación entre los buscadores de halos más populares y usados del momento. El principal objetivo de esta reunión era definir y utilizar un único conjunto de escenarios de prueba para verificar la credibilidad y la fiabilidad de los diferentes

buscadores de halos. Una vez discutidas las diferentes simulaciones y escenarios a tener en cuenta, la idea era aplicar todos y cada uno de los códigos participantes al nuevo conjunto de tests y hacer una comparación exhaustiva de los resultados. Un total de 17 buscadores de halos diferentes participaron en este proyecto, el cual supone la primera gran comparación de buscadores de halos existente hasta la fecha. Para más detalles sobre los códigos utilizados en la comparación y los resultados obtenidos, véase el Apéndice A.

Motivados por este proyecto, durante el último periodo de esta Tesis hemos implementado diversas mejoras en ASOHF con el fin de utilizarlo como un buscador de halos totalmente independiente de la simulación cosmológica a analizar. Aunque ASOHF fue creado originalmente para ser acoplado a un código cosmológico euleriano, en su versión actual es un buscador de halos independiente capaz de analizar los resultados de simulaciones cosmológicas con diferentes componentes, es decir, materia oscura, gas y estrellas.

Cuando se emplea ASOHF como un buscador de halos independiente se puede aplicar a una densidad continua sobre una malla o a un conjunto discreto de partículas. El primer paso consiste por lo tanto en traducir esta información a un campo de densidad continua sobre una nueva malla o conjunto de mallas anidadas. Cuando se trabaja con partículas, para obtener la densidad continua sobre la malla se emplea la técnica TSC. ASOHF incluye una subrutina AMR capaz de crear una jerarquía de mallas anidadas situadas en diferentes niveles de refinamiento (este método de generación de la jerarquía de mallas sigue el procedimiento general descrito para MASCLET en la Sección 5.3). Todas las mallas en un cierto nivel, llamadas parches, tienen la misma resolución numérica. Cuanto mayor sea el nivel de refinamiento mejor será la resolución espacial puesto que las celdas numéricas se hacen más pequeñas. Los criterios de refinamiento están abiertos y se pueden elegir en función de la aplicación: número de partículas por celda, umbral de densidad, etc. Para un uso general ASOHF refina cuando el número de partículas (de cualquier tipo) por celda excede un parámetro definido por el usuario. Este método de refinamiento soporta de manera natural diferentes especies de partículas (partículas de diferentes masas). Además, es capaz de construir la jerarquía de mallas a partir de sólo una de las especies de partículas existentes.

Una vez construida la jerarquía de mallas anidadas, ASOHF funciona tal y como se ha explicado en esta Sección.

1.6 Fusiones de cúmulos de galaxias

Como se ha explicado en la Sección 1.4, las simulaciones cosmológicas incluyen algunos procesos no gravitacionales para tratar de resolver así la ruptura de autosemejanza observada en las relaciones de escala. En el caso de los cúmulos de galaxias, los procesos de formación jerárquica y de acreción son particularmente energéticos debido a las grandes masas de los sistemas involucrados y a las estructuras filamentosas que los rodean. Por lo tanto, en este caso, los eventos de fusión también pueden ser una fuente importante de retroalimentación energética. Durante estas fusiones o colisiones se pueden producir ondas de choques y de compresión en los halos que, eventualmente, pueden liberar parte de la energía asociada

con la colisión como energía térmica en el sistema final (McCarthy, 2007).

De hecho, las fusiones mayores de cúmulos de galaxias son los eventos más energéticos del Universo desde el *Big Bang* (Sarazin, 2002). En estas fusiones los subcúmulos chocan a velocidades de unos $\simeq 2000 km/s$ liberando energías de enlace gravitacional de hasta $\geq 10^{64} ergs$. Durante estos eventos se generan ondas de choque en el ICM que disipan energías de $\simeq 3 \times 10^{63} ergs$. Estos choques son la fuente de calor más importante del ICM emisor de rayos X. También es probable que, tras la fusión, los procesos de turbulencia y de mezclado desempeñen un papel fundamental en cómo esta energía se mezcla y se libera en el ICM del halo final.

Por otro lado, es bien sabido que los resultados obtenidos en algunas aplicaciones físicas dependen de la capacidad de las diferentes técnicas numéricas para describir las ondas de choque, los fuertes gradientes, la turbulencia, y el proceso de mezclado, los cuales pueden ser muy diferentes dependiendo de la implementación numérica empleada. Aunque sigue siendo un tema de debate, se ha demostrado, al menos para algunas pruebas idealizadas, que la comparación entre los códigos de malla y los códigos SPH – cuando la resolución numérica es similar – puede dar diferencias sustanciales en los resultados (Frenk et al., 1999; Agertz et al., 2007). Parece razonable pensar que estas diferencias numéricas inherentes a la técnica empleada podrían traducirse en diferencias importantes cuando se aplican a escenarios más complejos y realistas como son los cúmulos de galaxias. Esta situación hace interesante, necesario y complementario, fomentar el número de estudios utilizando las diferentes estrategias numéricas disponibles.

Por estos motivos, nuestro objetivo en esta Sección es investigar el papel que juegan las fusiones de cúmulos de galaxias como fuente de retroalimentación energética y de recalentamiento en un marco general totalmente cosmológico. En nuestro estudio (Planelles & Quilis, 2009), los cúmulos de galaxias se forman y se desarrollan debido a la propia evolución no lineal de las perturbaciones primordiales y, por lo tanto, no consideramos simetrías especiales o cúmulos idealizados. En este escenario los eventos de fusión suceden, de forma natural, de acuerdo con la evolución jerárquica. Estudios previos han analizado las fusiones de cúmulos de galaxias usando colisiones controladas (véanse, por ejemplo, Ricker & Sarazin, 2001; Poole et al., 2006, 2007; McCarthy, 2007; Poole et al., 2008). El enfoque adoptado en el presente estudio es totalmente complementario a estos trabajos. Es evidente que, al comparar con las fusiones controladas, nuestro enfoque tiene algunas debilidades importantes como, por ejemplo, una peor resolución o la imposibilidad de controlar los diferentes parámetros involucrados en el problema. Sin embargo, proporciona una descripción del problema en un contexto cosmológico, sin simetrías, incluyendo la presencia de subestructuras y teniendo en cuenta los efectos de los diferentes entornos.

Con el fin de estudiar el papel de las fusiones de cúmulos de galaxias cumpliendo todos los requisitos anteriores, hemos analizado una simulación realizada con MASCLET de un volumen cosmológico relativamente grande ($100\, h^{-1}\, Mpc$ comóviles de lado). La simulación incluye los procesos habituales de enfriamiento y calentamiento para un gas primordial, y una formación estelar fenomenológica (aunque de muy baja eficiencia debido a las condiciones particulares de esta simulación – véase la Sección 7.2 para más detalles). Con la ayuda del buscador de halos ASOHF, hemos extraído y seguido la evolución de los cúmulos de galaxias de

nuestra simulación y los hemos clasificados según el tipo de fusiones que sufrían a lo largo de su evolución. Estos halos han sido estudiados directamente de la simulación sin emplear ninguna técnica de resimulación. Este enfoque implica una limitación debido a las restricciones numéricas. Dado que el esquema numérico tiende a resolver mejor los halos más masivos, la muestra de halos está sesgada hacia estos sistemas. Sin embargo, es en los sistemas más grandes donde los efectos de las fusiones son más relevantes. Por otra parte, este inconveniente relacionado con la falta de resolución en los halos pequeños se compensa con la ventaja de que las fusiones pueden ser seguidas de una manera consistente, ya que ocurren de forma natural a lo largo de la evolución del volumen de universo simulado.

Hemos asumido una definición de fusión de cúmulos de galaxias en función de la relación de masas de los halos que participan en la misma. Como condición adicional, hemos introducido un límite de tiempo de tal manera que sólo las fusiones que se producen en el pasado más reciente de los halos se tienen en cuenta. Por lo tanto, si las masas de los halos involucrados en una fusión son similares – entre el 1 y 1 / 3 – definimos estos eventos como fusiones mayores. Sucesos con relaciones de masa mayores son clasificados como fusiones menores. Por último, los cúmulos que evolucionan sin eventos relevantes de fusión se clasifican como relajados.

Una vez asumido este criterio para agrupar los cúmulos de nuestra simulación, hemos estudiado los perfiles radiales de cada cúmulo para las densidades de gas y de materia oscura, la temperatura, y la entropía. Con el fin de comparar las principales diferencias entre las tres clases de cúmlos, hemos calculado los perfiles promedio para cada grupo. Las formas de los diferentes perfiles son básicamente las mismas para las tres categorías, indicando que no hay cambios sustanciales en la física de los cúmulos. Sin embargo, existe una cierta tendencia en la normalización: los cúmulos con fusiones menores y los relajados tienen valores similares de todas las cantidades, mientras que los cúmulos con fusiones mayores están ligeramente más calientes y tienen mayor entropía.

Estas tendencias, en la entropía y la temperatura de los cúmulos en función de su historia evolutiva, se pueden cuantificar analizando un cúmulo representativo de cada clase y comparando la evolución temporal de sus perfiles de temperatura y entropía. De la misma manera, los efectos asociados a las fusiones de cúmulos se pueden detectar en la evolución temporal de cantidades globales como la entropía por debajo del 10% del radio virial, la proporción de energía interna sobre cinética, o la luminosidad en rayos X. Tras realizar estos análisis hemos obtenido que, en todos los casos, las fusiones de cúmulos liberan energía que acaba, parcialmente, en el objeto final. Sin embargo, la cantidad de energía almacenada en el cúmulo final es significativamente mayor para las fusiones de cúmulos con masas similares (fusiones mayores).

También hemos analizado la muestra completa de los cúmulos de la simulación sin diferenciar entre sus eventos de fusión. Estos resultados los hemos comparado con resultados de simulaciones anteriores (Voit et al., 2005; Burns et al., 2008; Kay et al., 2007) y con datos observacionales (Ponman et al., 2003; Vikhlinin et al., 2005; Pratt et al., 2007) prestando especial atención a los perfiles de entropía y temperatura. Nuestros resultados parecen ser consistentes, en sentido promedio, tanto con las simulaciones como con las observaciones. Sin embargo, todavía existen diferencias importantes como la falta de gradientes centrales en los perfiles

de temperatura de los cúmulos más masivos.

Hemos calculado para varios *redshifts* la fracción de cúmulos en nuestra muestra que tienen núcleo frío. A $z = 0$ nuestros resultados son totalmente compatibles con anteriores simulaciones con AMR realizadas por Burns et al. (2008) aunque parecen diferir con los resultados de una simulación SPH llevada a cabo por Kay et al. (2007). Además, hemos comparado la fracción de núcleos fríos en nuestra simulación con los datos observacionales de Chen et al. (2007) obteniendo una tendencia similar, es decir, el número de cúmulos con núcleo frío disminuye con la masa del cúmulo.

Dado que en nuestra simulación la retroalimentación energética gravitacional es el mecanismo de retroalimentación más relevante, hemos intentado correlacionar los eventos de fusión entre cúmulos con la existencia de núcleos fríos en los mismos. Así, hemos calculado la fracción de cúmulos relajados (sin fusiones) en función de la masa del cúmulo. Curiosamente, tanto la fracción de cúmulos con núcleo frío como la fracción de cúmulos relajados muestran una tendencia muy similar en función de la masa del cúmulo. Por desgracia, las fracciones de núcleos fríos obtenidas en nuestra simulación son muy diferentes de las observacionales. Para explicar estas discrepancias sugerimos dos posibilidades. La primera estaría relacionada con el hecho de que en la simulación analizada no se ha considerado enfriamiento dependiente de la metalicidad. Esta simplificación podría hacer que el enfriamiento fuera menos eficiente, especialmente en las regiones centrales de los cúmulos. La segunda razón estaría vinculada con una posible falta de resolución, lo cual parece ser muy poco probable dadas las características de la simulación considerada. En cualquier caso, parece evidente que existe cierta relación entre los eventos de fusión y la existencia de núcleos fríos.

Por otro lado, la evolución temporal de la fracción de núcleos fríos muestra que esta cantidad no ha cambiado sustancialmente desde $z \sim 0$ hasta $z \sim 1$. Este resultado es compatible con anteriores simulaciones (Burns et al., 2008) pero está en desacuerdo con ciertos datos observacionales (Vikhlinin et al., 2006a).

La muestra de cúmulos analizada en esta aplicación está limitada debido a que no se han realizado resimulaciones y, por lo tanto, a pesar del uso de un código con AMR, todavía existen algunas limitaciones de resolución. A pesar de ello, hemos analizado las relaciones de escala derivadas de nuestra muestra. Nuestros resultados para $L \propto T^{2.5}$, $M \propto T^{1.5}$ y $S \propto T^{0.9}$ son consistentes con resultados anteriores que no introducen ningún tipo de recalentamiento adicional. Además, hemos encontrado un cierto grado de segregación en las relaciones de escala dependiendo de si los cúmulos se han visto envueltos, o no, en una fusión reciente. Los sistemas que han sufrido eventos de fusión se sitúan, normalmente, en las regiones de altas temperaturas, luminosidades, masas, y entropías, en las diferentes relaciones de escala. Estos resultados podrían ser comparables con estudios recientes sobre la existencia de núcleos fríos en cúmulos (Burns et al., 2008; Poole et al., 2008). A partir del análisis de la evolución temporal de la relación L-T para los cúmulos con fusiones mayores, hemos obtenido que estos cúmulos tienen cierta tendencia a avanzar hacia las regiones de esta relación con mayor temperatura y luminosidad. Este comportamiento es similar al encontrado en Hartley et al. (2008), donde los autores investigan la relación L-T en una simulación con un fuerte precalentamiento.

Una clara mejora para futuros trabajos consistiría en aumentar el número de cúmulos en la muestra simulando volúmenes más grandes y con mayor resolución. De esta forma, sería factible estudiar de manera más fiable las relaciones de escala para cada una de las tres familias de cúmulos que hemos considerado. En cualquier caso, aun cuando la muestra puede ser algo limitada, las propiedades individuales de cada uno de los cúmulos más masivos están bien definidas.

El papel de las fusiones de cúmulos de galaxias como fuente de retroalimentación energética, transfiriendo parte de la energía gravitatoria a energía térmica, es todavía un tema de debate y estudio. Las fusiones son cruciales para entender la formación de los cúmulos de galaxias y los escenarios de formación galáctica puesto que influyen directamente sobre las propiedades del ICM. Se requieren simulaciones con mayor resolución e incluyendo más procesos físicos para cuantificar el papel de las fusiones de cúmulos de galaxias en el escenario jerárquico de formación de estructuras.

1.7 Ondas de choque cosmológicas

Tras analizar el papel que juegan las fusiones de cúmulos de galaxias en las propiedades termodinámicas del ICM, iniciamos una nueva línea de investigación, continuación natural de la anterior, destinada a analizar el papel que tienen las ondas de choque en el modelo jerárquico de formación de estructuras. En particular, nos centramos en la descripción cualitativa de las ondas de choque formadas en simulaciones cosmológicas.

Según las simulaciones N-cuerpos/hidrodinámicas, las ondas de choque cosmológicas se desarrollan como consecuencia de la formación jerárquica de estructuras en el Universo. Los choques provocan retroalimentación energética en el medio circundante y, por tanto, retienen información sobre la formación de estructuras y sus efectos térmicos sobre el gas.

Clasificamos las ondas de choque en dos grandes categorías: externas e internas. Las ondas de choque externas envuelven a filamentos y halos a gran escala, mientras que las internas se localizan en las regiones acotadas por las ondas de choque externas y son originadas por movimientos de flujo correlacionados con la formación jerárquica de las diferentes estructuras cósmicas.

La existencia y caracterización de las ondas de choque cosmológicas es crucial por diversos motivos (véanse, por ejemplo, Quilis et al., 1998; Ryu et al., 2003; Miniati et al., 2001; Pfrommer et al., 2006). Como prueba de ello, existen numerosos trabajos que tratan el problema desde puntos de vista observacionales, analíticos y numéricos. Debido a las dificultades que presenta abordar el problema tanto observacional como analíticamente, las técnicas numéricas basadas en simulaciones hidrodinámicas son esenciales para profundizar en la comprensión del mismo.

Desde un enfoque puramente numérico, existen estudios de las ondas de choque usando tanto códigos eulerianos – de malla fija y con AMR – (por ejemplo, Quilis et al., 1998; Miniati et al., 2000; Ryu et al., 2003; Kang et al., 2007; Skillman et al., 2008; Vazza et al., 2009), como SPH (por ejemplo, Pfrommer et al., 2006, 2008). Una de las principales ventajas de los códigos de malla respecto de los

lagrangianos son, precisamente, sus excelentes propiedades de captura de choques. A pesar de los estudios existentes y del grado de sofisticación alcanzado en alguno de ellos (véase, por ejemplo, Skillman et al., 2008), la identificación y caracterización de las ondas de choque continúa siendo una tarea difícil debido, tanto a la compleja dinámica que caracteriza la formación de estructuras cosmológicas, como a las limitaciones físicas y de resolución numérica que afectan a las simulaciones actuales.

Nuestro objetivo en la presente Sección es analizar las principales propiedades cualitativas y estadísticas de las ondas de choque desarrolladas durante la evolución de una simulación cosmológica realizada con el código MASCLET (para más detalles de la simulación véase la Sección 6.5.1). Para ello hemos desarrollado un algoritmo numérico capaz de detectar y caracterizar los choques en simulaciones 3-D con AMR. El uso de AMR nos permite obtener un gran rango dinámico con un código hidrodinámico capaz de capturar los choques con gran precisión.

Las ondas de choque producen cambios irreversibles en el ICM. Como consecuencia, el movimiento de una onda de choque a lo largo de un volumen simulado se traduce en un salto en todas las variables termodinámicas. Toda la información necesaria para evaluar la fuerza de una onda de choque, caracterizada por su número de Mach, está contenida en las condiciones de salto de Rankine-Hugoniot. Por tanto, el objetivo de cualquier "buscador de ondas de choque" consiste en identificar las ondas de choque y obtener sus números de Mach asociados. Nuestra particular implementación (véanse más detalles en la Sección 8.2.2), basada en un enfoque direccional, nos permite acotar y caracterizar las ondas de choque a lo largo de todo el volumen simulado. Para ello, tras marcar todas las celdas chocadas (regiones de compresión con $\nabla \cdot \mathbf{v} < 0$) dentro de nuestro volumen computacional, calculamos los números de Mach de los choques detectados mediante la condición de Rankine-Hugoniot relativa al salto en la temperatura. Además, puesto que este método se aplica independientemente a cada nivel de resolución de la malla AMR, nos permite localizar de forma natural ondas de choque asociadas a las diferentes escalas cosmológicas proporcionadas por la propia simulación.

Haciendo uso de esta nueva herramienta numérica, hemos podido analizar diversos aspectos de interés relacionados con las ondas de choque cosmológicas. Nuestras principales conclusiones son las siguientes:

- De acuerdo con estudios previos, la morfología de los diferentes patrones de ondas de choque detectados en nuestra simulación es bastante compleja. Estos patrones se distribuyen según la red cósmica: mientras halos y filamentos están rodeados por ondas de choque externas y fuertes, la región virial de los cúmulos de galaxias está ocupada por choques internos mucho más débiles. Además, las ondas de choque externas que rodean a los cúmulos presentan formas cuasi esféricas alrededor de éstos.

- A $z = 0$ encontramos que aproximadamente el 20% del volumen simulado está chocado, obteniendo un número de Mach medio de $\simeq 4$.

- Hemos analizado, a $z = 0$, la distribución diferencial del número de celdas chocadas en función de su número de Mach. Encontramos que la mayor parte de los choques cosmológicos son essencialemente débiles ($\mathcal{M} \leq 2$).

Además, hemos ajustado esta distribución a dos leyes de potencias diferentes de la forma $dN(\mathcal{M})/d\mathcal{M} \propto \mathcal{M}^{\alpha}$. Para números de Mach relativamente bajos (hasta $\simeq 20$) obtenemos una pendiente de $\alpha \simeq -1.7$, mientras que encontramos una relación algo más pronunciada ($\alpha \simeq -4.1$) para ondas de choque más fuertes. Este cambio de pendiente muestra la transición entre dos escalas bien diferentes: las asociadas a las ondas de choque internas y externas, respectivamente.

- Hemos tratado de correlacionar las ondas de choque con la población de cúmulos de galaxias de la simulación. En este sentido, hemos encontrado que el número de Mach medio dentro del radio virial de los halos a $z = 0$ es $\mathcal{M} \approx 5$. Atendiendo a la evolución del volumen simulado, el número de Mach medio de la población de halos en un instante particular siempre tiene un valor por debajo de ≈ 20. Este valor está en perfecto acuerdo con el cambio de pendiente observado en la distribución del número de Mach de las celdas chocadas e indica, efectivamente, la transición entre dos escalas bien distintas.

  Hemos analizado la distribución del número de Mach medio dentro del radio virial de los halos en función de sus respectivas masas viriales obteniendo dos tendencias claramente diferenciadas. Por un lado, existe una franja casi constante de números de Mach bajos (hasta 5), que parece ser independiente de la masa de los halos. Estos choques de bajo número de Mach pueden provenir de la formación primordial de los cúmulos y son más visibles en las estructuras que han alcanzado un cierto estado de equilibrio. Por otro lado, una tendencia más pronunciada a lo largo de todo el rango de números de Mach parece estar correlacionada con la masa de los halos y podría representar los choques que tienen lugar durante la evolución jerárquica de las diferentes estructuras cosmológicas como consecuencia de las fusiones y procesos de acreción. Nuestra hipótesis para explicar este comportamiento bimodal es que, como consecuencia de su evolución, el movimiento de los halos a lo largo del plano $\mathcal{M} - M_{vir}$ está intímamente relacionado con sus diferentes historias evolutivas.

A la luz de estos primeros resultados, en un futuro no muy lejano trataremos de abordar algunas cuestiones relacionadas que aún están por aclarar. Lo que parece obvio es que las ondas de choque juegan un papel fundamental en los cúmulos de galaxias así como en la termalización del ICM. A pesar de ello, sólo un número muy reducido de ondas de choque han sido detectadas en cúmulos de galaxias. Como consecuencia, se requieren más observaciones y predicciones teóricas y numéricas para profundizar en el rol que las ondas de choque juegan en el modelo jerárquico de formación de estructuras.

1.8 Conclusiones

Durante el periodo de tiempo transcurrido a lo largo de mi Tesis he estado involucrada en la investigación teórica y numérica, como dos aspectos importantes y complementarios, centrándome en la caracterización, la formación y la evolución

de los cúmulos de galaxias, y las propiedades físicas del ICM. Todo mi trabajo se ha enmarcado dentro del campo de la Cosmología Numérica y se ha orientado a comparar resultados numéricos con datos observacionales.

En cuanto a la parte numérica de esta Tesis, he realizado progresos en varias líneas de investigación. Por un lado, me he convertido en usuaria y programadora del código cosmológico MASCLET. He llevado a cabo personalmente varias simulaciones que se han utilizado para el estudio de diferentes escenarios físicos. Además, he participado directamente en los nuevos módulos incluidos en MASCLET, es decir, el de formación estelar y el de enfriamiento dependiente de la metalicidad. Por otra parte, he desarrollado y puesto a prueba un nuevo buscador de halos capaz de analizar los resultados de complejas simulaciones cosmológicas. Este buscador de halos, ASOHF, ha sido exhaustivamente probado y comparado con otros buscadores de halos en el que, hasta la fecha, constituye el primer gran proyecto de comparación de buscadores de halos.

Además de esta parte numérica, he analizado importantes procesos físicos que afectan a la física del ICM y, por lo tanto, a las propiedades de los cúmulos de galaxias. En particular, he estudiado el papel que las fusiones de cúmulos de galaxias juegan como fuente de retroalimentación energética y de recalentamiento del ICM, prestando especial atención a la existencia de núcleos fríos. También se ha llevado a cabo un análisis cualitativo de las ondas de choque generadas durante la evolución jerárquica de un volumen de universo simulado.

Por lo tanto, preveo un conjunto de posibles ampliaciones o aplicaciones de mi trabajo en diferentes subcampos íntimamente relacionados.

Desde el punto de vista puramente numérico aún quedan varios proyectos por realizar. Considero fundamental, y bastante urgente, completar la paralelización en OpenMP del buscador halos ASOHF. Los grandes rangos dinámicos y las resoluciones alcanzadas por las simulaciones cosmológicas actuales requieren buscadores de halos muy sofisticados y capaces de afrontar con eficiencia la enorme cantidad de datos que generan. Otro proyecto muy interesante desde el punto de vista numérico, pero más a largo plazo, sería la inclusión de campos magnéticos y de enriquecimiento químico en el código MASCLET.

Desde el punto de vista físico, puesto que la comprensión del ICM aún no está completa, una descripción precisa de los distintos procesos hidrodinámicos desde un punto de vista totalmente cosmológico resulta crucial. Siguiendo esta línea, estoy analizando un nuevo conjunto de simulaciones cosmológicas de alta resolución especialmente destinadas a cuantificar el papel que juegan las ondas de choque generadas durante la formación de las distintas estructuras cosmológicas.

Vinculando la escala de cúmulos con la de galaxias, estoy involucrada en un proyecto destinado a estudiar los procesos de retroalimentación energética asociados a los AGN en un contexto puramente cosmológico. Para ello, trataremos de incluir en MASCLET un nuevo módulo especialmente diseñado para modelar la formación de chorros galácticos. Nuestra idea para la introducción de este nuevo módulo es describir los chorros fenomenológicamente, utilizando para ello sus propiedades generales tal y como se observan en diferentes galaxias.

Como consecuencia de los análisis realizados sobre las fusiones de cúmulos de galaxias en un contexto puramente cosmológico, sería muy interesante comple-

mentar este trabajo mediante el estudio de eventos de fusión controlados. Con un estudio de este tipo podríamos analizar en detalle cómo los diferentes parámetros orbitales afectan a las propiedades del ICM final, así como a la condición de equilibrio hidrostático de los cúmulos.

Además de estos proyectos, estoy particularmente interesada en el estudio de los diferentes procesos de retroalimentación energética así como en la conexión que existe, precisamente a través de estos procesos, entre las escalas galáctica y cosmológica. Una posible lista de temas a abordar en un futuro no muy lejano podría ser la siguiente: (i) descripción del recalentamiento en cúmulos debido a la actividad de los AGN y todas sus implicaciones, especialmente, en las relaciones de escala; (ii) transformaciones morfológicas experimentadas por las galaxias en los cúmulos debido a las propiedades del medio en el que residen; (iii) consecuencias del entorno de los cúmulos en las propiedades de las galaxias, especialmente, en sus poblaciones estelares.

Además, considero extremadamente interesantes los retos numéricos que los futuros avances podrían abrir en el campo de la Cosmología Computacional. En este sentido, los códigos cosmológicos no sólo tienen que cumplir los requisitos de los nuevos supercomputadores, sino que deben mejorar sus algoritmos y su descripción de los procesos físicos relevantes. Por lo tanto, considero esencial la comparación de los resultados numéricos, tanto con los diferentes códigos disponibles como con las observaciones, con tal de abordar los nuevos retos científicos desde una descripción completa, tanto teórica como observacional.

Chapter 2

Introduction

The work carried out during this Thesis is framed within the field of Computational Cosmology and focused on the study of the formation and the evolution of galaxy clusters. To identify the different cosmological structures and follow their evolutionary histories, it has been necessary to develop several numerical tools. Therefore, the present work is address to understand and characterize clusters of galaxies and their associated evolutionary processes from a numerical point of view. However, since the final goal of cosmological simulations is to obtain simulated universes as similar as possible to the real one, comparisons with observational data will be a constant throughout the manuscript. In this sense, my research efforts have focused on several broad lines intimately related which deal with the theoretical and numerical study of galaxy clusters: (i) the halo-finding problem, (ii) new improvements in cosmological simulations, and (iii) the formation and evolution of galaxy clusters. Concerning the tools used and the results presented in this work both, the properties of the numerical schemes and the physical models considered, play a fundamental role complementing each other.

2.1 Motivation

Galaxy clusters are the largest gravitationally bound, relaxed structures in the Universe. The first written reference to a cluster of galaxies is probably that of the French astronomer Charles Messier in 1784 (Messier, 1784). In the following years (see Biviano, 2000, for a historical overview), in his *Catalogue des nébuleuses et des amas d'étoiles que l'on découvre parmi les étoiles fixes, sur l'horizon de Paris*, he listed 103 nebulae, 30 of which are now identified as galaxies. In 1785 F. Wilhelm Herschel published *On the Construction of the Heavens* (Herschel, 1785). In this work he suggested that the *"sidereal system we inhabit"* is a nebula, common in appearance to many others, which therefore must be external to our own. However, the most relevant was the description that W. Herschel did of the Coma cluster of galaxies: *"that remarkable collection of many hundreds if nebulae which are to be seen in what I have called the nebulous stratum of Coma Berenices"*. These two early works led up to the birth of the scientific investigation of galaxy clusters.

During the XIX and early XX century, many astronomers investigated the distribution of nebulae in order to understand if they were external to the local *"sidereal system"*, the Milky Way. However, it was not until the beginning of the XX century, mainly through the works of V.M. Slipher and E. Hubble, when the extragalactic nature of nebulae was confirmed. After this finding, many clusters of galaxies were discovered and astronomers started to consider them as physical systems. In 1933, F. Zwicky (Zwicky, 1933) estimated for the first time the mass of a galaxy cluster, thus establishing the need for dark matter.

The role of clusters as laboratories for studying the evolution of galaxies was also soon realized. In the 50's, the number of known galaxy clusters grew, from about 20 in Hubble's time, up to thousands. In addition, the investigation of galaxy clusters started to cover all aspects, from the distribution and properties of galaxies in clusters, to the existence of sub- and super-clustering, from the origin and evolution of clusters, to their dynamical status, and the nature of dark matter. The publication in 1958 by Abell of *The distribution of rich clusters of galaxies* became a crucial work of reference in the study of clusters of galaxies. Since then, galaxy clusters have become one of the main research topics in extragalactic astrophysics and many authors have contributed to their study with both theoretical and observational aspects.

In the last years, Cosmology has undergone a spectacular step forward. Coupled with observational advances produced by the new generation of telescopes and satellites, computer development has spurred the emergence of Computational Cosmology, which has contributed crucially to the understanding that we have today on the formation and evolution of galaxy clusters. Unlike other branches of physics, in Cosmology the physical phenomena in study can not be recreated in a laboratory. Therefore, modern supercomputers have become virtual laboratories where astrophysicists analyse and test theoretical models on the formation of the universe we observe.

Together with these technical advances, great progress has also been made in the development of different numerical schemes able to faithfully resolve the dynamics of the main components of the Universe, namely, the dark matter and the gaseous component. In this regard, hydrodynamical numerical codes coupled to N-body techniques are the most advanced instruments to describe the complex processes involved in the formation and evolution of galaxy clusters as well as to explore the physics of the intracluster medium (ICM). Direct simulation is the only available technique to capture the dynamics of clusters in a full cosmological context, and hence to make detailed theoretical predictions about cluster properties in different cosmological models. For these reasons, cosmological simulations have been used to investigate a large number of topics related with galaxy clusters such as basic cluster properties, the X-ray emission of clusters, or their radiative cooling properties.

Despite the strong predictions provided by "simple" adiabatic simulations, recent observations, like the ones produced by the X-ray satellites CHANDRA and XMM-Newton, have awaken a new enthusiasm in the study of galaxy clusters. They have highlighted an important number of open questions in the actual picture of the formation and evolution of galaxy clusters, such as the breaking up of the self-similar scaling relations or the cooling flow problem. These shortcomings

represent some of the main challenges that numerical simulations have to face in the coming years in order to completely understand the relevant physical processes that establish the observational properties of clusters.

These discrepancies with the observations have motivated the idea that, besides gravity and adiabatic gas dynamics, some important non-gravitational processes related with the baryonic component are missing in the model. In fact, observations support the existence of a feedback mechanism which prevents the gas from cooling and, currently, the most popular candidate is heating by active galactic nuclei (AGN).

Studies of different non-gravitational processes have given rise in the last years to an exciting field of research in Numerical Cosmology. Among the considered processes, we can cite, for instance, AGN heating by jets and radio bubbles, cold fronts in the ICM, dissipative heating of the ICM by sound waves, metal enrichment, thermal conduction, or magnetic field amplification during cluster formation.

In order to deepen in the knowledge of the relevant cosmological scenarios from a numerical and a physical point of view, new and complementary studies using the different numerical strategies available are needed. In addition, as the simulations increase in resolution and complexity, the main numerical challenge consists in reliably describing as many physical processes as possible but in a full, self-consistent, cosmological context. Thus, besides the different feedback sources in study, processes inherent to the hierarchical formation of structures also need to be properly described in order to understand the role they play within this scenario.

In this line, galaxy cluster mergers are crucial to understand galaxy cluster formation scenarios. In addition, they produce phenomena of turbulence, mixing, and shock generation, which influence directly the ICM properties and deserve a careful treatment. In spite of the importance of these processes, their role within this picture is still a matter of debate and study.

In this sense, our aim is to describe, in a self-consistent way, some of the heating processes associated with the hierarchical evolution of galaxy clusters in a full cosmological context. To do so, our tools are an Eulerian cosmological code and a halo finder able to identify the cluster haloes within the simulations. Following this approach, the work presented in this Thesis contributes to an exciting field trying to shed some light over some of the previous mentioned open problems.

2.2 Organization of the manuscript

In this Section, the outline of the Thesis is briefly described.

Chapter 1, written in Spanish, includes the introduction, an overview which summarizes the main ideas of this work, and the conclusions of the Thesis. This is done in order to fulfil the Ph.D. regulations of the University of Valencia.

Chapter 2 presents the introduction and the organization of the manuscript.

In Chapter 3, a brief analysis of galaxy clusters from an observational point of view is made. The role that galaxy clusters play in Cosmology as well as some detection methods and theoretical models are reviewed.

Chapter 4 briefly describes the main issues concerning Numerical Cosmology.

The main numerical techniques used to simulate the different components of the Universe are explained. Advantages and disadvantages associated to each technique as well as future improvements are discussed.

Chapters 5 and 6 contain the core of the numerical work carried out during this Thesis. In Chapter 5 the main properties of the Eulerian adaptive mesh refinement (AMR) hydrodynamical and N-body cosmological code MASCLET are described. Special attention is paid on the process of grid generation as well as in two new features included during the period of this Thesis, namely, the analysis of the star formation, and the metal-dependent cooling. In Chapter 6 the Adaptive Spherical Overdensity Halo Finder (ASOHF) is presented and tested. This finding algorithm, developed during the period of this Thesis, was originally designed to be coupled to the outputs of the MASCLET code and has turned out to be an essential tool to analyse the results of such large cosmological simulations.

Chapters 7 and 8 contain some physical applications of the numerical tools developed so far. In Chapter 7 we discuss the role of galaxy cluster mergers as a source of feedback and reheating of the intracluster medium in a full cosmological context. The effects of mergers on the existence of cool cores in galaxy clusters as well as in the scaling relations are also discussed. These mergers can produce shocks and compression waves in the clusters which eventually can release part of the energy associated with the collision as thermal energy in the final system. In Chapter 8 we pay special attention to discuss the generation and characterization of these cosmological shock waves as well as to correlate them with the evolution of galaxy clusters.

Chapter 9 summarizes the main conclusions of our research and outlines the future work to be done.

In Appendix A, the complete text of a paper (*Haloes gone MAD: The Halo-Finder comparison project*) submitted for publication is presented.

This Thesis fulfils the **European Ph.D.** conditions.

Chapter 3

Physical properties of Galaxy Clusters

In this Chapter, the main observational properties of galaxy clusters as well as the role they play in Cosmology are reviewed. The aim of this introduction is to motivate the numerical treatment of galaxy clusters.

3.1 Galaxy clusters in a hierarchical Universe

Nowadays, it is widely accepted that the formation of cosmic structures proceeds via a fundamentally hierarchical paradigm. The model on which this paradigm relies is set within the spatially flat Λ-*Cold Dark Matter* (ΛCDM) model (Blumenthal et al., 1984) with cosmological constant, also known as the *concordance* model.

A combination of different observational probes, such as studies of the Cosmic Microwave Background (CMB; Dunkley et al., 2009), the large scale structure of the Universe (Tegmark et al., 2004; Cole et al., 2005; Tegmark et al., 2006; Percival et al., 2007a,b), the Type Ia supernovae magnitude-redshift relation (Kowalski et al., 2008), and galaxy clusters (Mantz et al., 2010; Vikhlinin et al., 2009; Rozo et al., 2010), have now placed strong constraints on the parameters of the underlying cosmological model. As shown in Fig. 3.1, the picture that emerges (Komatsu et al., 2010) is one in which the energy density of the Universe is shared between dark energy ($\Omega_\Lambda = 0.728^{+0.015}_{-0.016}$) and matter – dark ($\Omega_{\rm DM} = 0.227 \pm 0.014$) and baryonic ($\Omega_{\rm b} = 0.0456 \pm 0.0016$) matter –, with a Hubble constant of $H = 70.4^{+1.3}_{-1.4}$ km/s/Mpc. Perturbations on the uniform model seem to be well described by a scale-free primordial power spectrum with power-law index $n_{\rm s} = 0.963 \pm 0.012$ and amplitude $\sigma_8 = 0.809 \pm 0.024$. Given such a cosmological model, the Universe is 13.75 ± 0.11 Gyr old.

Within this paradigm, the formation of structures in the Universe is seeded by minute perturbations in matter density expanded to cosmological scales according to inflationary models. The dark matter component, since it is collisionless, must undergo gravitational collapse leading to the growth of the perturbations.

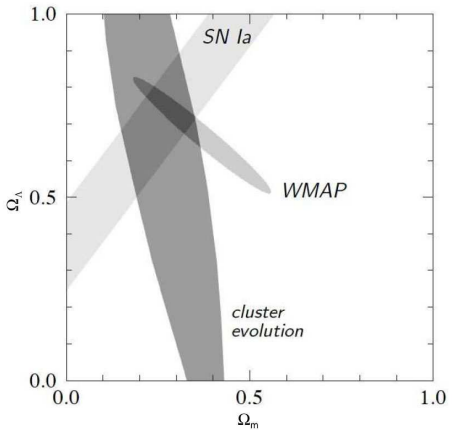

Figure 3.1: Best fit confidence regions in the Ω_Λ versus $\Omega_m = \Omega_{DM} + \Omega_b$ plane. It combines data from cluster evolution (Vikhlinin et al., 2003), supernovae (Riess et al., 1998; Perlmutter et al., 1999), and WMAP observations of the CMB (Spergel et al., 2003). The common region overlaps near $\Omega_m = 0.3$ and $\Omega_\Lambda = 0.7$ giving an evidence of consistency in the overall picture.

The linear theory of cosmological perturbations is well understood and provides an accurate description of the early evolution of these perturbations. Once the perturbations become nonlinear, their evolution is significantly more complicated, but simple arguments, such as those from the spherical top-hat collapse (Gunn, 1977), provide insight into the basic behaviour. There are also empirical methods to determine the statistical distribution of matter in the nonlinear regime (Hamilton et al., 1991; Peacock & Dodds, 1996; Smith et al., 2003; Heitmann et al., 2009). These, together with N-body simulations (e.g., Klypin & Shandarin, 1983; Springel et al., 2005; Heitmann et al., 2008), show how a network of cosmic structures interconnected along walls and filaments forms, giving rise to a cosmic web which involves a wide range of scales.

Within this hierarchy of cosmic structures galaxy clusters occupy a special position: they are the largest objects that have had time to undergo gravitational collapse. As a consequence, they are a crucial part of the large scale structure (LSS) of the Universe. The connection between clusters and the LSS has become evident with extended galaxy redshift surveys, like the CfA (de Lapparent et al., 1986), the SDSS (York et al., 2000), and the 2dF (Colless et al., 2001).

Clusters of galaxies, whose total masses vary from 10^{13} up to $10^{15} M_\odot$, typically contain hundreds to thousands of galaxies, spread over a region of a few megaparsecs (Mpc). Despite their large number of galaxies they are not the dominant component in a cluster of galaxies. The space between galaxies is filled with a very hot and diffuse plasma, the intracluster medium (ICM), which strongly emits X-ray radiation. This ICM, formed mainly by ionized hydrogen and helium with a typical particle number density of $10^{-1} - 10^{-4}\ cm^{-3}$, is heated up to temperatures of roughly $10^7 - 10^8$ K. The ICM contains most of the baryonic material in

the cluster providing about the 15% of the total cluster mass. However, the total cluster mass is dominated by an unseen and elusive non-baryonic component, the dark matter, whose presence can be inferred from gravitational effects on visible matter. Quantitatively, the mass composition of a cluster is roughly subdivided as follows: 80% dark matter, 15% hot baryons in the ICM, and 5% cold baryons in stars and galaxies.

3.1.1 Tracing the cosmic evolution

Galaxy clusters make possible a number of critical tests about the underlying cosmological model.

Given their large masses, they stem from the collapse of density fluctuations involving comoving scales of ~ 10 Mpc (Borgani & Kravtsov, 2009). Since clusters are the largest objects that have undergone gravitational relaxation (Lynden-Bell, 1969) and entered into virial equilibrium, they are the biggest objects whose masses can be reliably measured. Thus, mass measurements of nearby clusters can be used to trace the LSS in the Universe.

On the other hand, at scales below 1 Mpc, and in addition to gravity, the physics of baryons becomes more important, thus complicating the associated processes. During the process of cluster formation, by means of adiabatic compression and shock waves, the intergalactic gas is heated up to high X-ray emitting temperatures, settling in hydrostatic equilibrium within the cluster potential well and becoming denser. Once the gas is dense enough, it cools, leaving, therefore, the hot phase and forming the stellar component, and can accrete onto supermassive black holes (SMBHs) hosted by the massive galaxy clusters. These processes of cooling and formation of stars and SMBHs can then result in energetic feedback due to supernovae (SNe) or active galactic nuclei (AGN), which can significantly heat the ICM and spread heavy elements throughout the cluster volume. In spite of this enormous energy input, given that the gravitational potential wells of clusters are deep enough to retain all the diffuse baryons, clusters are essentially like "closed boxes" and are expected to contain a universal fraction of baryons within a large radius. Consequently, the baryonic component of clusters retains important information about the processes associated with galaxy formation, including both, those related with the star formation efficiency as well as the effects of the resulting feedback processes.

Within this global picture, galaxy clusters are essential tools to understand the different processes involved in galaxy formation and evolution as well as their effects on the surrounding intergalactic medium.

3.2 Observable properties of galaxy clusters

Galaxy cluster surveys are a potentially powerful means of placing tight constraints on key cosmological parameters. This is primarily because the mass function of galaxy clusters is highly sensitive to different choices of these parameters. Therefore, by means of comparisons of the present-day cluster mass distribution with the mass distribution at earlier times, it is possible to measure the rate of structure formation, imposing constraints on cosmological models. This is a non-trivial task

since the total masses of galaxy clusters must first be inferred from their observable properties.

This Section outlines how clusters are observed in different wavebands and how those observations reveal the partition of the overall cluster mass. See Voit (2005) for an interesting review on our theoretical and observational understanding of galaxy clusters.

3.2.1 Clusters in optical light

Optical identification of galaxy clusters has been going on for quite a long time. By the end of the eighteenth century Charles Messier (Messier, 1784) and William Herschel (Herschel, 1785) had already recognized concentrations of galaxies in the present-day Virgo and Coma clusters, respectively. Over the next two centuries, thanks to the development in observing facilities, optical discoveries of clusters culminated with the definitive cluster catalogs of George Abell and collaborators (Abell, 1958; Abell et al., 1989). These catalogs provided the first extensive and statistically complete sample of nearby galaxy clusters.

Abell estimated the distance of each cluster candidate from the apparent brightness of its tenth brightest member galaxies. Then, he counted all the galaxies within a fixed projected radius ($\sim 2\ Mpc$) and brighter than a magnitude limit two magnitudes fainter than the third brightest member. To compensate for projection effects, he subtracted from his galaxy counts a background level equivalent to the mean number of galaxies brighter than the magnitude limit for the cluster in similarly-sized, cluster-free regions of the plate, and retained all cluster candidates with a net excess of 50 galaxies brighter than the limiting magnitude.

Nowadays most of the optical cluster identification techniques refine Abell's basic approach (Lumsden et al., 1992; Dalton et al., 1997; Postman et al., 1996), often extending it with information about galaxy colours (Gladders & Yee, 2000; Bahcall et al., 2003; Nichol, 2004). These improvements are necessary because the contrast of clusters against the background galaxy counts decreases with cluster distance. Galaxy colours can help identify distant clusters because many cluster galaxies are significantly redder than other galaxies, at a similar redshift, owing to their lack of ongoing star formation. These colours can therefore help in placing galaxies on the "red sequence" relation in a plot of galaxy colour versus magnitude (Gladders & Yee, 2000). The dispersion, the colour and the slope of this relation are used to study the evolution of high redshift clusters as well as their photometric redshifts. Following this technique, the Red-sequence Cluster Survey (RCS; Gladders & Yee, 2000) compiles a fairly large number of optically selected clusters out to $z \sim 1.4$.

The efficiency of cluster selection as well as the accuracy of their estimated redshifts have augmented thanks to the increase in the number of observed passbands together with the improvements in the spectro-photometric techniques. In this respect, a significant step forward in mapping distant clusters has been made by wide field deep multicolour surveys in the optical and near-infrared such as the SDSS (Sloan Digital Sky Survey; York et al., 2000) or the 2dF Galaxy Redshift Survey (Colless et al., 2001).

Once suitable cluster candidates are found, their status as true mass concen-

trations can be checked by measuring the underlying mass. To perform such measurements, optical observations offer three complementary ways: through the optical richness of clusters, through the orbital velocities of member galaxies, and through the degree to which galaxies lying behind the cluster are lensed by the cluster gravitational potential.

- **Optical richness**

  Since light traces mass in the Universe, the total optical luminosity of a cluster is itself an indicator of its mass. Measuring the luminosity of every galaxy in a cluster is impractical, especially for distant clusters in which only the brightest galaxies can be observed. However, because the luminosity distribution function of cluster galaxies is nearly the same from cluster to cluster, observing the high-luminosity trend of that distribution allows one to normalize the overall galaxy luminosity function for the cluster, providing estimates for both the total optical luminosity of the cluster and its mass. Making assumptions about the shape of the luminosity distribution function helps to link richness (net excess of galaxies brighter than the magnitude limit used to define each cluster) more directly to the total luminosity of a cluster.

- **Galaxy velocities**

  The velocity distribution of the galaxies of a relaxed cluster is expected to be gaussian in velocity space. Thus, galaxies with radial velocities v_r falling well outside the best-fitting gaussian envelope are unlikely to be cluster members and are generally discarded. Fitting the velocity distribution $\exp[-(v_r - \langle v_r \rangle)^2/2\sigma_v^2]$ to the remaining galaxies then provides a 1-D velocity dispersion σ_v for the cluster. If the velocity distribution of a cluster candidate is far from gaussian, then it is probably a superposition of smaller structures but not a real cluster. The number of galaxies with measured velocities and the method for identifying and eliminating non-members affect the accuracy of σ_v. Quantitatively, the velocity dispersion of cluster galaxies is of the order of $\sim 10^3 \mathrm{km\,s^{-1}}$.

  Zwicky was the first to measure the velocity dispersion of a cluster (Zwicky, 1933, 1937), obtaining $\sigma_v \sim 700\,\mathrm{km\,s^{-1}}$ for the Coma cluster. From this fact and his estimate of the radius of the cluster, he concluded that the mass of this cluster must be much greater than the observed mass in stars. This was the first evidence for dark matter in the Universe.

- **Gravitational lensing**

  Zwicky also proposed (Zwicky, 1937) that cluster masses could be measured through gravitational lensing of background galaxies. Since the mass within a given projected radius deflects photons along our line of sight through the cluster centre, lensing is sensitive to the cluster mass within this radius. The deflection angle itself depends on the gradient of the gravitational potential in the lensing system.

  The effects of gravitational lensing, which is stronger in the inner regions of clusters, can be observed in the distorted images of background galaxies

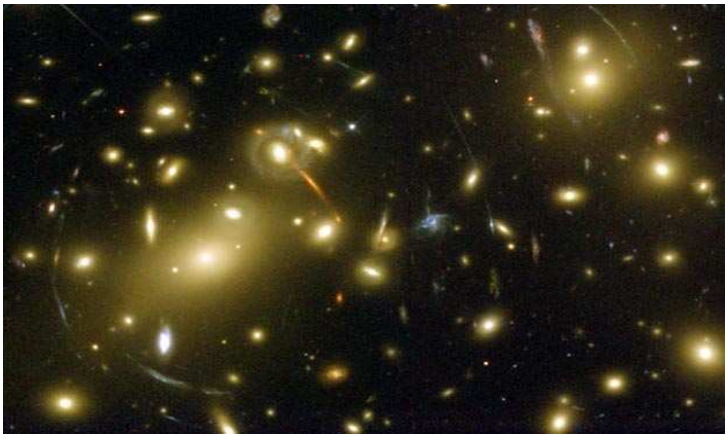

Figure 3.2: Optical image of the galaxy cluster Abell 2218. While yellow spots are the galaxies in the optical band, long arcs and arclets are the images of background galaxies distorted by the gravitational field of the cluster. ©*Hubble Space Telescope*.

appearing as long thin arcs curved around the cluster centre.

The gravitational lensing is a direct probe of the overall mass distribution in clusters, becoming a powerful tool to check other methods for measuring cluster masses (see a review about lensing in Bartelmann & Schneider, 2001).

In Fig. 3.2 an optical image of the galaxy cluster Abell 2218 is shown. In this image, in addition to galaxies and stars, the presence of the unseen dark matter component can be inferred through the gravitational lensing of background galaxies.

3.2.2 Clusters in X-rays

In 1966, M87, in the centre of the Virgo cluster, was the first object outside of our galaxy to be identified as a source of astronomical X-ray emission (Byram et al., 1966; Bradt et al., 1967). Five years later, X-ray sources were also detected in the directions of the Coma and Perseus clusters (Fritz et al., 1971; Gursky et al., 1971; Meekins et al., 1971). Since these are three of the nearest rich clusters, it was suggested that clusters of galaxies might generally be X-ray sources (Cavaliere et al., 1971).

With the advent of astrophysics from space in 1960's, it was revealed that clusters are among the most luminous extended X-ray sources on the sky with luminosities typically in the range of $10^{43} - 10^{45} erg/s$. The sizes of the X-ray sources associated with clusters were comparable to the size of the galaxy distribution in the clusters. In addition, unlike other bright X-ray sources but consistent with their spatial extents, cluster X-ray sources did not vary temporally in their brightness (Elvis, 1976). Although several emission mechanisms were proposed, the X-ray spectra of clusters were most consistent with thermal bremsstrahlung from hot gas.

Most baryons in the Universe, which are distributed throughout the intergalactic space, are extremely difficult to observe. Nevertheless, the deep potential wells of galaxy clusters compress the associated baryonic gas and heat it to X-ray emitting temperatures. Therefore, the gas temperature inferred from the X-ray spectrum of a cluster indicates the depth of the cluster potential well, and the emission-line strengths in that spectrum indicate the abundances of elements like iron, oxygen, and silicon in the ICM. Then, altogether, the X-ray spectrum of a galaxy cluster is a continuum thermal bremsstrahlung with metal emission lines. In the following, the main characteristics of that X-ray emission are outlined (see Sarazin, 1988; Rosati et al., 2002, for further details).

- **Thermal Bremsstrahlung**

  Mass estimates can be derived from X-ray observations of the hot ICM by assuming that the gas is in hydrostatic equilibrium within the cluster gravitational potential well (e.g., Sarazin, 1988). Ideally, galaxy clusters are relaxed structures in which both gas and galaxies feel the same dynamics. Then, in this case, the ICM is expected to have a typical temperature such that the typical atomic velocity is similar to the velocity of the galaxies in the cluster:

$$k_B T \simeq \mu m_p \sigma_v^2 \simeq 6 \left(\frac{\sigma_v}{10^3 km/s} \right)^2 keV, \tag{3.1}$$

  where m_p is the proton mass, k_B is the Boltzman constant, μ is the mean molecular weight ($\mu = 0.6$ for a primordial gas with a 76% fraction of hydrogen), and σ_v is the line-of-sight velocity dispersion of galaxies in the cluster. At such temperatures, the emissivity of a gas composed mainly of hydrogen is dominated by thermal bremsstrahlung.

  As shown in Fig. 3.3, observational data for nearby (e.g., Wu et al., 1999) and distant clusters follow this correlation, although with some scatter. There are however some exceptions demonstrating the presence of a more complex dynamics.

  Assuming that collisional ionization equilibrium determines the relative abundance of each ion, we can compute a cooling function $\Lambda(T)$ which characterize the rate at which the ICM radiates energy. Given that these cooling processes involve electrons colliding with ions, the resulting cooling function is usually defined so that either $n_e n_{\rm H} \Lambda(T)$ or $n_e n_{\rm ion} \Lambda(T)$ is the luminosity per unit volume being n_e, n_H and n_{ion} the number density of electrons, hydrogen atoms and ions, respectively.

  If ρ_{gas} is the gas density, assuming that $n_e \sim n_{\rm ion}$, the total X-ray luminosity is given by

$$L_X = \int_V \left(\frac{\rho_{gas}}{\mu m_p} \right)^2 \Lambda(T) dV, \tag{3.2}$$

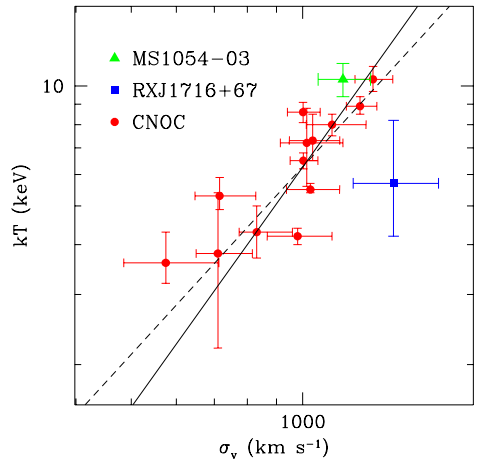

Figure 3.3: Relation between galaxy velocity dispersion, σ_v, and ICM temperature, T, for distant ($z > 0.15$) galaxy clusters. The solid line shows the relation $k_B T = \mu m_p \sigma_v^2$, and the dashed line is the best-fit to the low-z T-σ_v relation from Wu et al. (1999). Figure taken from Rosati et al. (2002).

where $\Lambda(T) \propto T^{1/2}$ for pure thermal Bremsstrahlung emission. These powerful luminosities, within the range of $\sim 10^{43}$–$10^{45} erg/s$, allow clusters to be identified as extended sources out to large cosmological distances.

- **Metal emission lines**

  In 1976, X-ray line emission from iron was detected from the Perseus cluster of galaxies (Mitchell et al., 1976), and shortly thereafter from Coma and Virgo as well (Serlemitsos et al., 1977). The emission mechanism for this line is thermal and its detection confirmed the thermal interpretation of cluster X-ray sources. Whereas the pure bremsstrahlung emissivity is a good approximation for typical cluster temperatures ($kT \gtrsim 2keV$) at which most of the atoms are completely ionized, a further contribution from metal emission lines should be taken into account when considering cooler systems (e.g., Raymond & Smith, 1977).

  The presence of emission lines in an X-ray spectrum of a cluster is an important aspect since it allows to study the metal production in clusters and their diffusion in the ICM (Rasmussen & Ponman, 2007).

  A powerful mechanism to analyse the metal content of the ICM is the X-ray spectroscopy. Early measurements of over a hundred of nearby clusters gave a mean metallicity of about one third of the solar value, largely independent of the cluster temperature (e.g., Renzini, 1997). In the last years, thanks to the new generation of X-ray satellites it has been possible to map the

distribution of different metals in the ICM, such as Fe, S, Si, O, in a very good detail. Actually, a number of observations have established that significant radial gradients of the iron abundance are present in the central regions of relaxed clusters and groups (e.g., de Grandi et al., 2004; Vikhlinin et al., 2005; Rasmussen & Ponman, 2007), with increase of the metallicity associated to the brightest cluster galaxies (BCGs). However, these gradients have not been found at larger distances from the centre of clusters (e.g., Snowden et al., 2008).

The X-ray emission is an efficient and robust way to identify cluster candidates. Imaging X-ray cluster surveys have high and well understood completeness, low rates of contamination, and the selection function is well understood (see Rosati et al., 2002, for a review). The cluster surveys derived from the ROSAT satellite, launched in 1990, are still the best all-sky X-ray sample available compiling a large number of clusters out to high redshifts. With the launch in 1999 of the new space telescopes CHANDRA and XMM-Newton, spectacular detailed images and spectra have been obtained. Progress is still being made in the use of these surveys for characterizing the growth and evolution of clusters through cosmic time.

3.2.3 Clusters in microwaves

When observed in the direction of galaxy clusters, hot gas in clusters can also be detected through its effects on the CMB. The background itself has a nearly perfect black-body spectrum with a temperature of about 2.7 K (Mather et al., 1990). The inverse Compton scattering in the population of thermal electrons in clusters produces small but measurables distortions in the CMB spectrum, equivalent to temperature variations of about 10^{-4}–10^{-5} K, slightly shifting some of the microwave photons to higher energies as they passed through hot intergalactic gas. This phenomenon is known as the thermal Sunyaev-Zel'dovich (S-Z) effect (Sunyaev & Zel'dovich, 1970, 1972; Carlstrom et al., 2002). The motion of a cluster with respect to the microwave background produces additional distortion known as the kinetic S-Z effect.

Unlike optical and X-ray surface brightness, one of the main advantages of the thermal S-Z effect in clusters is that it is nearly independent of distance.

In the next few years, cluster surveys based on the S-Z effect, such as those being conducted with the South Pole Telescope (Vanderlinde et al., 2010) and the Atacama Cosmology Telescope (Hincks et al., 2010), will allow wide-field cosmological studies of clusters to be extended through much of the observable universe (Carlstrom et al., 2002).

Figure 3.4 shows a comparison of the optical, microwave, and X-ray images of the Coma cluster. It illustrates all of the main components of the clusters: the luminous stars, the hot ICM observed via its X-ray emission, and the S-Z effect.

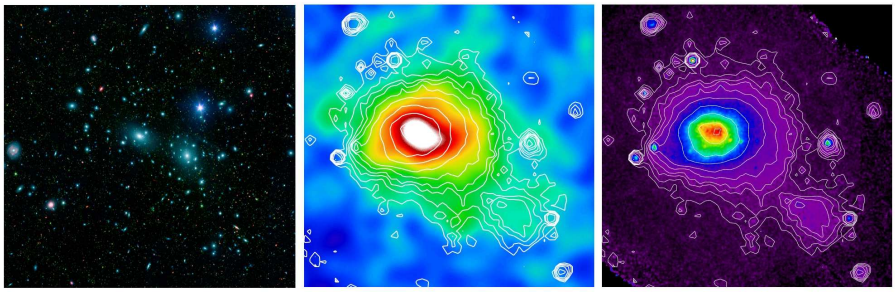

Figure 3.4: The Coma cluster, also known as Abell 1656, as it appears in the optical band (left panel), through the S-Z effect (middle panel), and in X-rays (right panel). ©*NASA/ESA/DSS2* (visible image); *ESA/LFI* and *HFI Consortia* (Planck image); *MPI* (ROSAT image).

3.3 A theoretical model of galaxy clusters

The simplest model to explain the properties of the ICM assumes that gravitational processes, such as adiabatic compression during the collapse and shocks due to supersonic accretion of the surrounding gas, are the only responsible mechanisms determining the evolution of the thermodynamical properties of the hot diffuse gas. In this scenario, the gas collapses into the dark matter potential wells and then, accretion shocks form moving outwards and heating up the gas until the virial temperature of the cluster (e.g., Quilis et al., 1998). Such a model assumes that cluster properties and correlations between them are determined only by gravity and that clusters are in virial equilibrium. Since gravity acts indifferently on all scales, this model is known as the self-similar model (Kaiser, 1986). See Borgani & Kravtsov (2009) for a good review of this model.

If, at redshift z, M_{Δ_c} represents the mass contained within the radius r_{Δ_c}, enclosing a mean overdensity Δ_c times the critical cosmic density, $\rho_c(z)$, then the mass scales as

$$M_{\Delta_c} \propto \rho_c(z)\Delta_c r^3_{\Delta_c}. \tag{3.3}$$

The critical density of the Universe scales with redshift as

$$\rho_c(z) = \rho_{c0}E^2(z), \tag{3.4}$$

where

$$E(z) = H(z)/H_0 = \left[(1+z)^3\Omega_m + (1+z)^2\Omega_k + \Omega_\Lambda\right]^{1/2} \tag{3.5}$$

gives the evolution of the Hubble parameter $H(z)$. In the above expressions $\Omega_k = 1 - \Omega_m - \Omega_\Lambda$ is the contribution from curvature (any contribution from relativistic species is neglected here, e.g., Peebles, 1993), whereas H_0 and ρ_{c0} are the values of the Hubble constant and the critical density at $z = 0$, respectively. The overdensity, Δ_c, depends on the adopted cosmological model and can be approximated by this expression (Bryan & Norman, 1998)

$$\Delta_c = \begin{cases} 18\pi^2 + 82x - 39x^2 & \text{if } \Omega_k = 0 \\ 18\pi^2 + 60x - 32x^2 & \text{if } \Omega_\Lambda = 0 \end{cases} \tag{3.6}$$

where $x = \Omega(z) - 1$ and $\Omega(z) = [\Omega_m(1+z)^3]/E(z)^2$. Typical values of this overdensity are between 100 and 500, depending on the adopted cosmology.

On the other hand, the cluster size r_{Δ_c} scales with z and M_{Δ_c} as

$$r_{\Delta_c} \propto M_{\Delta_c}^{1/3} E^{-2/3}(z). \tag{3.7}$$

Therefore, assuming hydrostatic equilibrium, from the above relation we obtain

$$M_{\Delta_c} \propto T^{3/2} E^{-1}(z)\,. \tag{3.8}$$

This relation between mass and temperature can be turned into scaling relations among other observable quantities.

Assuming that the gas distribution traces the dark matter distribution and that the thermal bremsstrahlung process dominates the emission from the ICM plasma, the X-ray luminosity scales as

$$L_X \propto M_{\Delta_c} \rho_c T^{1/2} \propto T^2 E(z). \tag{3.9}$$

The entropy is another useful quantity to characterize the thermodynamical properties of the ICM (Voit, 2005). In X-ray studies of the ICM, it is usually defined as

$$K = \frac{k_B T}{\mu m_p \rho_{gas}^{2/3}}\,. \tag{3.10}$$

With this definition, the quantity K is the constant of proportionality in the equation of state of an adiabatic mono-atomic gas, $P = K\rho_{gas}^{5/3}$.

Another quantity, often called "entropy", that we will also use in the following chapters, is

$$S = k_B T n_e^{-2/3}\,. \tag{3.11}$$

Within the self-similar model, this quantity, computed at a fixed overdensity Δ_c, scales with temperature and redshift according to

$$S_{\Delta_c} \propto T E^{-4/3}(z)\,. \tag{3.12}$$

In cases where the hydrostatic equilibrium condition is not possible, cluster masses at different redshifts can be inferred from these self-similar scaling relations since they connect X-ray observables, like luminosity or temperature, with cluster mass. Understanding the evolution of these scaling relations is also crucial for constraining cosmological parameters with galaxy cluster surveys. However, as it will be discussed in Section 3.3.1, the observed scaling relations differ from the self-similar model predictions.

3.3.1 Some problems of the adiabatic model

The latest generation of X-ray telescopes have revolutionized our understanding of the ICM of galaxy clusters. They have confirmed that, despite the simplicity and the important predictions provided by the adiabatic model just described, there are still some important questions to be studied in detail.

- **The cooling flow problem**

  To characterize the role of cooling in the ICM, it is useful to define the cooling time-scale. This parameter, which gives the time scale for the gas to cool to low temperatures due to its own radiation, is defined as $t_{cool} = k_B T/(n\Lambda(T))$, n being the number density of gas particles, and $\Lambda(T)$ the cooling function characterizing the emission process.

  For a pure bremsstrahlung emission: $t_{cool} \simeq 8.5 \times 10^{10}\mathrm{yr}\,(n/10^{-3}\mathrm{cm}^{-3})^{-1}$ $(T/10^8 K)^{1/2}$ (e.g., Sarazin, 1988). Therefore, the high densities existing in central cluster regions allow the cooling time to be shorter than the age of the Universe. Since a substantial fraction of gas undergoes cooling in these regions, it drops out of the hot diffuse, X-ray emitting phase. As a consequence, we expect to observe a surface brightness peak in these regions (with a typical radius of the order of 70 kpc - see for instance Vikhlinin et al., 2005) along with some other features such as an increasable iron abundance. These kind of clusters are the so-called cool core clusters (CC).

  According to observations (e.g., Fabian et al., 1994; Chen et al., 2007), relaxed galaxy clusters are most often found to exhibit at their centres a significant drop in the ICM gas temperature due to radiative cooling.

  The classical model of cooling flows predicted that, in the absence of any heating mechanism, as the high-density gas in the cluster core cools down, the lack of pressure support causes external gas to flow in, thus creating a superpositions of many gas phases, each one characterized by a different temperature. However, the well-known cooling flow problem stems from the observation that the few detected emission lines are not as strong as expected to justify the predicted cooling rate. Further observational evidence is found in the ratio of the central temperature with respect to the global cluster temperature ($T_{central}/T$), which remains at a factor $\sim$1/3 (e.g., Peterson et al., 2003; Bauer et al., 2005), and the mass deposition rates ($\dot{\mathrm{M}}$) are much smaller than expected (e.g., Edge & Freyer, 2003).

- **Breaking up the self-semilarity**

  Since the late 1980s, using X-ray observations for statistically representative samples of clusters, it has been demonstrated that the scaling relations predicted by the self-similar model do not match the observational results completely.

  For instance, the relation between X-ray luminosity and mass is steeper than expected from gravitational heating alone (e.g., Reiprich & Böhringer, 2002; Chen et al., 2007). The first calibration of this relation was done in Reiprich & Böhringer (2002) with a sample of bright clusters extracted

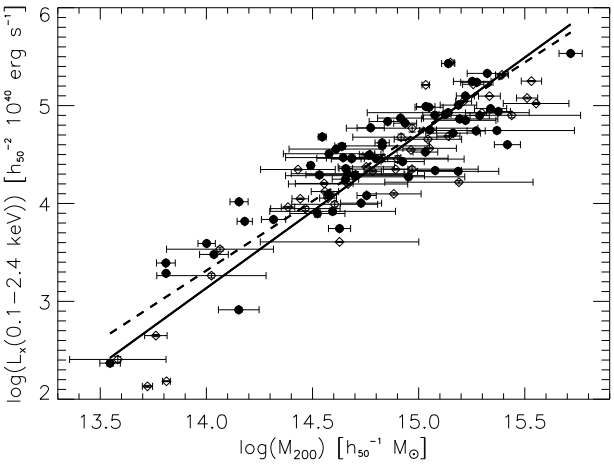

Figure 3.5: The L_X-M relation for nearby clusters from Reiprich & Böhringer (2002). The two lines are the best log-log linear fit to two different data sets indicated with filled and open circles.

from the ROSAT All-Sky Survey (RASS). The obtained $L_X - M$ relation is shown in Fig. 3.5 (see Reiprich & Böhringer, 2002, for further details on the data), showing clearly the existence of a tight correlation although with some scatter.

Consistently with the L_X-M relation, the observed X-ray luminosity-temperature scaling is also steeper than predicted (e.g., Markevitch, 1998; Arnaud & Evrard, 1999; Osmond & Ponman, 2004), $L_X \propto T^\alpha$ with $\alpha \simeq 2.5 - 3$ for clusters ($T \geq 2$ keV) and possibly even steeper for groups ($T \leq 1$ keV).

Furthermore, the measured gas entropy in central regions is higher than expected (e.g., Ponman et al., 2003; Sun et al., 2009), especially for poor clusters and groups, with respect to the $S \propto T$ predicted scaling.

Correspondingly, it has been observed a decreasing trend of the gas mass fraction in poorer systems (e.g., Balogh et al., 2001; Lin et al., 2003; Sanderson et al., 2003; Vikhlinin et al., 2006b; Croston et al., 2008).

In addition, there is also an important scatter in these relations (Fabian et al., 1994) partly, but not totally, connected with the effect of the different environments where clusters live and their evolutionary histories. The main source of scatter is the highly X-ray luminous central regions of CC clusters (e.g., O'Hara et al., 2006; Chen et al., 2007). A commonly used artifact to reduce this scatter consists in excluding the core region from the measurements (e.g., Markevitch, 1998). However, besides these corrections, it is also crucial to properly understand how different processes inherent to the hierarchical formation of cosmic structures can affect the scaling relations. In this sense, and as we will discuss in Chapter 7, galaxy cluster mergers can

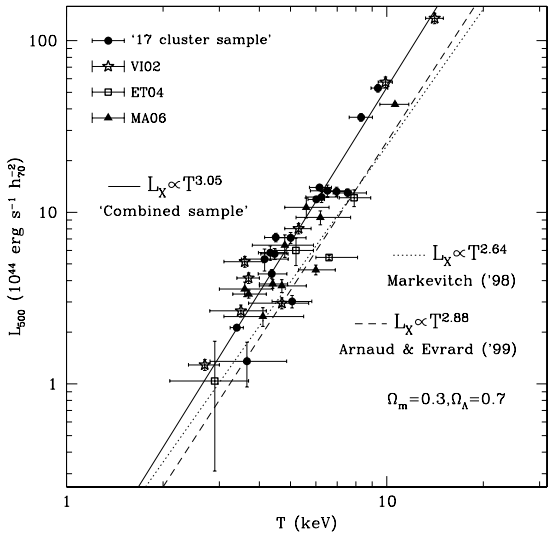

Figure 3.6: L_{500}-T relation for a sample of 39 high redshift ($0.25 < z < 1.3$) clusters observed either by CHANDRA or XMM-Newton. The solid line indicates the best fit to the 'combined sample' of 39 clusters which includes the '17 cluster sample' from Branchesi et al. (2007) together with data from Maughan et al. (2006) (MA06), Vikhlinin et al. (2002) (VI02), and Ettori et al. (2004b) (ET04). Dotted and dashed lines refer to the nearby cluster samples from Markevitch (1998) and Arnaud & Evrard (1999), respectively. Figure from Branchesi et al. (2007).

also be an important source of scatter because they can boost clusters along the L_X-T relation.

In spite of the scatter, the scaling relations at low redshift are reasonably well calibrated, at least for relaxed clusters. Measuring the evolution of these relations at high redshift is much more challenging. In this regard, despite the number of studies performed using CHANDRA and XMM-Newton data (e.g., Vikhlinin et al., 2002; Ettori et al., 2004b; Maughan et al., 2006; Branchesi et al., 2007), there is a significant lack of concordance. These discrepancies are however more likely due to an inconsistent cluster selection. In general, regarding the L_X-T relation, clusters at high redshift are relatively brighter, at fixed temperature. As for the resulting evolution of the X-ray scaling relations, the emerging picture is that the self-similar evolution cannot persist to arbitrarily high redshift because of the increasing importance of radiative cooling and feedback from galaxy formation (Voit, 2005). An example of an observational result supporting this argument is that of Branchesi et al. (2007). Using a sample of 39 distant clusters ($0.25 < z < 1.3$, see Fig. 3.6), they found that the evolution of the L_X-T relation is comparable with the self-similar prediction for $z \lesssim 0.3$, followed by a much weaker, if any, evolution at higher redshifts.

These discrepancies between the self-similar model and the observations have motivated the idea that, besides gravity, some important physics related with the baryonic component is missing in the model. The main physical processes thought to be responsible for boosting the entropy of the ICM are heating from astrophysical sources, such as SNe and AGN, and the removal of low-entropy gas via radiative cooling. In addition to these feedback sources, other processes associated to the hierarchical formation of structures and happening in a full cosmological context, like galaxy cluster mergers, also need to be considered in order to understand their role within this picture.

Nowadays, as required by X-ray spectral observations, the existence of a feedback mechanism which prevents the gas from cooling is widely accepted and, currently, the most popular candidate is heating by AGN (Fabian et al., 1984). In spite of several existing models which may explain how this mechanism works, and the evidence for enough output energy to suppress cooling, it remains unclear how this energy is distributed in a homogenous way such that CCs appear in the observed form. Nevertheless, many observations (e.g., Burns, 1990; Eilek, 2003; Sanderson et al., 2006) support that nearly every CC cluster hosts a radio emitting AGN, creating cavities in the X-ray gas. Although these findings demonstrate unambiguously the CC-AGN connection, many fundamental questions remain to be answered.

Within this scenario, and as it will be discussed in the next Chapter, it is only with hydrodynamical/N-body simulations that one can capture the full complexity of the problem and their impact on the formation history of cosmic structures.

Chapter 4

Numerical Cosmology

Hydrodynamical codes coupled to N-body techniques are the most advanced instruments to describe and analyse the complex processes involved in the formation and evolution of galaxies and galaxy clusters, as well as the role they play during the hierarchical assembly of cosmic structures.

Two types of approaches can be used in order to study structure formation in Cosmology: analytical and numerical methods. Among the numerical methods, several Eulerian and Lagrangian hydrodynamical approaches have been proposed. In this Chapter, the main properties of these numerical techniques are discussed.

4.1 Introduction

Over the last three decades, numerical simulations of structure formation have become a powerful theoretical mechanism to accompany, interpret, and sometimes to lead cosmological observations because they bridge the gap that often exists between basic theory and observation. Their main role, in addition to many other uses, has been to test the viability of the different structure formation models, such as variants of the CDM model.

In the case of galaxy clusters, numerical simulations have been used for the following goals, among others (see Bertschinger, 1998, for a classical review about simulations of structure formation in the Universe): (i) understanding the general processes of formation and evolution of isolated clusters (galaxy evolution and dynamics, ICM); (ii) testing observational methods of mass estimation (for both dark matter and baryons); (iii) using the scaling relations (of temperature, luminosity and/or mass) and their evolution to constrain cosmological parameters; and (iv) using substructure, morphology, shape, or radial profile to constrain cosmological parameters.

Besides the numerical progress, computers and computational resources have experienced such an advance that simulations can be applied systematically as scientific tools and their use has led to important results in our knowledge of the Universe.

Historically, the use of cosmological simulations started in the 1960s (Aarseth,

1963) and 1970s (e.g., Peebles, 1970; White, 1976). These calculations were N-body collisionless simulations with few particles. Since then, great progress has been made in the development of these N-body codes that model the distribution of dissipationless dark matter particles. However, the physics of the gaseous, baryonic, component of the Universe is far more complicated to model than the formation of structures in the dark matter due to gravitational instability. Understanding the behaviour of baryons is crucial for a complete theory of the formation of cosmic structures, particularly on galactic and cluster scales. Any realistic simulation which sets out to explain the growth of structures in the Universe must therefore contain a hydrodynamical treatment of the evolution of the baryonic fluid. Pioneering simulations using Smoothed Particle Hydrodynamics (SPH) techniques were first carried out by Gingold & Monaghan (1977). Early cosmological simulations that followed baryons and dark matter include those by Evrard (1988) and Hernquist & Katz (1989).

4.2 Initial conditions

The procedure of initial condition generation for simulations of structure formation consists in specifying the background cosmological model and the kind of perturbations imposed on this background. The background model is generally taken to be a spatially flat spacetime with specified composition of dark matter, baryons, the cosmological constant, etc.

At very high redshift, after the recombination ($z \simeq 1100$), the initial conditions are represented by small-amplitude ("linear") density fluctuations. Inflationary models of early universe expect these fluctuations to be Gaussian. The main advantage of Gaussian fluctuations is that all their statistical properties are completely defined by their two-point correlation function or, equivalently, by their power spectra, $P(k)$:

$$P(k) \propto \mid \delta(\mathbf{k}) \mid^2, \tag{4.1}$$

where $\delta(\mathbf{k})$ is the Fourier transform of the initial three-dimensional Gaussian overdensity field $\delta(\mathbf{x})$. Then, the difficulty of generating initial conditions resides in obtaining a field that has the correct power spectrum.

Under the assumption of a Gaussian model, and once it has been fully specified, there are several main steps to generate the initial conditions:

1. The post-recombination density field is the linear convolution of the primordial fluctuation field with a transfer function T(k). Therefore, the power spectrum used to initialize simulations generally takes the form

$$P(k) = Ak \mid T(k) \mid^2, \tag{4.2}$$

where A is the normalization, related with the parameter σ_8. The details of the transfer function depend upon the cosmological parameters (see Holtzman, 1989, for an early compendium). This step specifies the linear density fluctuation field at some initial time (at $z \simeq 1000$ for typical high-resolution simulations).

2. Now, particle positions and velocities can be obtained. The standard approach is to displace equal-mass particles from a uniform Cartesian grid using the Zel'dovich approximation (Zel'dovich, 1970; Klypin & Shandarin, 1983; Efstathiou et al., 1985). Higher-order perturbation theory (Crocce et al., 2006) can be also used. This step is necessary in order to evolve from the above initial conditions up to the starting redshift of cosmological simulations (usually $z \simeq 50 - 100$).

3. At this point, the density and the velocity profiles of the initial perturbation are known. Then, the composition of this perturbation, namely, the ratio between the dark matter and baryonic densities, is defined. The baryon temperature is generally initialized to the maximum between the (redshift-dependent) microwave background temperature or 10^4 K.

For some purposes, however, constrained simulations are required, for instance, if we are interested in looking for the seeds of some sort of cosmological structures in a limited volume. In these cases, constraints may be imposed on the initial fluctuation field. A relatively simple algorithm for sampling Gaussian random fields with arbitrary linear constraints is that of Hoffman & Ribak (1991).

Thanks to a number of observational constraints (see Section 3.1), initial conditions for cosmological simulations can now be inferred with a low degree of ambiguity. Thus, the main challenge for the simulations is to faithfully follow the dynamics of the dark matter and baryonic components.

4.3 Numerical techniques

Owing to their different nature, dark matter and baryonic components are evolved using different numerical techniques.

4.3.1 Dark matter dynamics

For the dark matter component, only a representative subset of equations is solved by discretizing and sampling the initial phase space by N particles and then integrating their equations of motion in the global gravity field. Particles are evolved forwards in time using Newton's laws written in comoving coordinates (Peebles, 1980):

$$\frac{d\mathbf{x}}{dt} = \frac{\mathbf{v}}{a} \tag{4.3}$$

$$\frac{d\mathbf{v}}{dt} = -\frac{\nabla\phi}{a} - H\mathbf{v} \tag{4.4}$$

where $\mathbf{x}$ and $\mathbf{v} = a(t)\frac{d\mathbf{x}}{dt} = (v_x, v_y, v_z)$ are, respectively, the Lagrangian coordinates and the peculiar velocity associated to the dark matter particles. $\phi(t, \mathbf{x})$ is the peculiar Newtonian gravitational potential, whereas the background parameters are the scale factor, a, the background density, $\rho_{_B}$, and the Hubble constant, H.

Equations 4.3 and 4.4 need to be integrated for every dark matter particle by using the gravity field produced by all the matter contributing to the density, that

is, dark and baryonic matter. Thus, their solution can be found by solving the elliptic Poisson's equation which depends on the boundary conditions:

$$\nabla^2\phi = \frac{3}{2}H^2a^2\delta_T. \tag{4.5}$$

Here, the total density contrast, δ_T, is defined as $\delta_T = \delta + \delta_* + \delta_{DM} + 2$ when $\delta = \rho/\rho_{_B} - 1$, $\delta_* = \rho_*/\rho_{_B} - 1$, and $\delta_{DM} = \rho_{_{DM}}/\rho_{_B} - 1$, being ρ, ρ_*, and $\rho_{_{DM}}$ the continuous densities associated to the gas, stellar, and dark matter components, respectively.

Once $\phi(t, \mathbf{x})$ is known, the position and velocities of each one of the dark matter particles can be updated from the previous time step.

The core of N-body simulations relies on the computational algorithm used to obtain the gravitational force. The most direct and accurate scheme is based on computing the force among each pair of particles (e.g., Aarseth, 2001). However, since this integration method requires a number of operations scaling like N^2, it is computationally expensive for large cosmological simulations. For this reason, different schemes have been developed to obtain a good compromise between computational cost and numerical resolution. Such schemes include grid-based particle-mesh (PM) and particle-particle/particle-mesh (P^3M) methods (Hockney & Eastwood, 1988; Couchman, 1991), the gridless tree method where neighbouring particles are properly sorted in a recursive tree structure and forces are computed by multipole expansion (Barnes & Hut, 1986; Bouchet & Hernquist, 1988), or a combination of both methods with the fast PM scheme used to compute gravitational forces on large scales and the tree algorithm to compute forces on smaller scales (Bagla, 2002; Bode & Ostriker, 2003; Springel, 2005). See Section 5.4 for a detailed explanation of how the PM method operates.

4.3.2 Gas dynamics

For spatial scales where relativistic corrections are not required, cosmological inhomogeneities evolve according to the following equations (Peebles, 1980):

$$\frac{\partial\delta}{\partial t} + \frac{1}{a}\nabla\cdot(1+\delta)\mathbf{v} = 0 \tag{4.6}$$

$$\frac{\partial\mathbf{v}}{\partial t} + \frac{1}{a}(\mathbf{v}\cdot\nabla)\mathbf{v} + H\mathbf{v} = -\frac{1}{\rho a}\nabla p - \frac{1}{a}\nabla\phi \tag{4.7}$$

$$\frac{\partial E}{\partial t} + \frac{1}{a}\nabla\cdot[(E+p)\mathbf{v}] = -3H(E+p) - H\rho\mathbf{v}^2 - \frac{\rho\mathbf{v}}{a}\nabla\phi \tag{4.8}$$

where $\mathbf{x}$, $\mathbf{v} = a(t)\frac{d\mathbf{x}}{dt} = (v_x, v_y, v_z)$, ρ, and δ are, respectively, the Eulerian coordinates, the peculiar velocity, the continuous density, and the density contrast associated to the gaseous component.

The peculiar Newtonian gravitational potential, $\phi(t, \mathbf{x})$, as well as the background parameters have the same meaning than in Eqs.(4.3–4.5).

The total energy density, $E = \rho\epsilon + \frac{1}{2}\rho v^2$, is defined as the addition of the thermal energy, $\rho\epsilon$, where ϵ is the specific internal energy, and the kinetic energy (where $v^2 = v_x^2 + v_y^2 + v_z^2$).

In this case, pressure gradients and gravitational forces are the responsible for the evolution.

Poisson's equation 4.5 has to be solved coupled with Eqs. (4.6–4.8) to compute the source term $\nabla\phi$ which appears in Eqs. 4.7 and 4.8. An equation of state (usually an ideal gas equation of state), $p = p(\rho, \epsilon)$, closes the system.

The integration of the hydrodynamics equations governing the evolution of gas can be done using different techniques. The adoption of a particular technique, with its associated benefits and drawbacks, has a direct consequence on the outcome of the simulation. The numerical techniques used to model the evolution of the gas can be split into two general classes: Lagrangian and Eulerian.

The most popular of the Lagrangian schemes is SPH (Lucy, 1977; Gingold & Monaghan, 1977). Other schemes which could be defined as quasi-Lagrangian include those by Gnedin (1995) and Pen (1995). SPH techniques have made possible huge advances in the field of numerical cosmology in the recent past. Relatively easy to implement and with a low computational cost, SPH techniques have a huge dynamical range because of their Lagrangian nature as there is no grid constraining the dynamic range in spatial resolution or the globlal geometry of the modelled systems. This feature has made them particularly successful in simulations of cosmic structure formation. The SPH technique, however, also has weak points including (i) an approximate treatment and description of shock waves and strong gradients, (ii) a poor description of low density regions, (iii) a requirement to the use of numerical artifacts such as the artificial viscosity, and (iv) the possible violation of conservation properties (Okamoto et al., 2003). Nevertheless, nowadays several SPH codes including improvements to successfully overcome some of those limitations have been developed (e.g., Springel et al., 2001b; Serna et al., 2003; Wadsley et al., 2004; Springel, 2005; Wetzstein et al., 2009).

Eulerian schemes – or grid-based shock-capturing methods – present an alternative to Lagrangian schemes. Within this board class of techniques, the ones based on Riemann solvers have been particularly successful (e.g., Quilis et al., 1993, 1994; Ryu et al., 1993; Bryan et al., 1995; Gheller et al., 1998). These numerical schemes are written in conservative form, which ensures excellent conservation of physical quantities. Shock waves, discontinuities and strong gradients are sharply resolved in typically one or two cells in 1-D. The use of Riemann solvers removes the need to invoke artificial viscosity to integrate equations with discontinuities. Although these properties are needed in order to build a robust hydrodynamical scheme, precisely due to their Eulerian character – fix numerical grids are needed to integrate the hydrodynamical equations – these techniques are limited by poor spatial resolution. In order to achieve adequate resolution, dense numerical grids are needed which quickly shoots up the computational cost. Even with the best computers available nowadays, a simple Eulerian approach cannot compete with a Lagrangian approach in cosmological applications, which demand a good spatial resolution over a huge dynamical range.

In the last years, the situation has changed due to a wider use of a numerical technique known as Adaptive Mesh Refinement (AMR), described originally by Berger & Oliger (1984) and Berger & Colella (1989). The basic idea of this technique is to improve the numerical resolution of grid-based simulations. In order to do this, an Eulerian approach as the ones described above is used, but gaining

resolution – both spatial and temporal – by selectively refining the original computational grid. The result is a hierarchy of nested grids which naturally behaves like a Lagrangian scheme (the grids are refined only in regions of interest such as high-density regions). Each of these grids, with appropriated boundary conditions, is treated by the Eulerian scheme as an independent computational domain.

The AMR schemes have proved to be extremely powerful in many fluid dynamics applications. For cosmological applications, only few AMR implementations have been designed (e.g., Bryan & Norman, 1997; Fryxell et al., 2000; Kravtsov et al., 2002; Teyssier, 2002; Quilis, 2004). These numerical codes share the basic ingredients although there are slight differences depending on each particular implementation.

Although these numerical approaches – Lagrangian and Eulerian– aim to solve the same physical problem, due to their different nature, there are important differences in the numerical solution of some physical applications (e.g., Agertz et al., 2007; Tasker et al., 2008). However, since both approaches are extremely useful and complementary, it is important to compare their results and identify possible systematic errors associated with a particular method.

4.3.3 Additional physics

Besides gravity and adiabatic gas dynamics, cosmological simulations that aim to describe, in a consistent way, the formation of galaxies and the evolution of the intergalactic medium, need to include models of atomic and radiative processes. The most common processes taken into account in state-of-the-art cosmological simulation codes include, for an optically thin gas, cooling and heating processes for a primordial gas, multispecies chemistry, a phenomenological treatment of star formation and its associated energy feedback. These processes are included, by means of phenomenological parametrizations, in the right hand side of the energy equation (Eq. 4.8) as extra source terms (e.g., Cen, 1992; Cen & Ostriker, 1992; Katz, 1992; Yepes et al., 1997).

A natural improvement for cosmological simulations would be to include, consistently, the exact solution of the radiative transfer equations for an optically thick gas. However, the high computational cost demanded and the complexity of this process, have made that, for the moment, only very basic approximations have been considered.

In the case of the star formation, it is a process that occurs on physical scales many orders of magnitude below the resolution limit of cosmological simulations, yet the products (radiation, thermal energy, and heavy elements) have significant influence on the scales resolved by the simulations. Numerous prescriptions for feedback have been introduced with slightly varying parameterizations (e.g., Cen & Ostriker, 1992; Yepes et al., 1997; Springel & Hernquist, 2003), that are capable of broadly reproducing the observed star formation history. However, it is important to point out that stellar particles in simulations do not represent individual stars but samples of the stellar distribution (Borgani & Kravtsov, 2009). Therefore, each stellar particle is treated as a single-age population of stars and its feedback on the surrounding gas is implemented accordingly.

Figure 4.1 shows how the distributions of DM (left panels), gas (central panels)

and stars (right panels) evolve across cosmic time within a cosmological cubic box of 64 comoving Mpc side length, as predicted by a cosmological hydrodynamical simulation. This simulation, performed with the MASCLET code (Quilis, 2004), assumes a spatially flat ΛCDM model. In addition, it includes cooling and heating processes for a primordial gas as well as a phenomenological star formation. These density maps highlight the hierarchical fashion in which the formation of cosmic structures proceeds: at high redshift the smooth density field evolves into a much more pronounced, knotty and filamentary field at later times. By the present time (bottom panels) many galaxy clusters have formed at the intersection of quite large filamentary structures.

4.4 Present status of cosmological simulations

In spite of the achievements and the degree of sophistication reached by present-day cosmological simulations, additional physical processes need to be properly described and taken into account. See Borgani & Kravtsov (2009) for a recent review on the present status of cosmological simulations. In this Section, however, we will only do a brief summary.

As explained in Section 3.3, the simplest approximation is to consider the gas non-radiative and perform adiabatic simulations (Evrard, 1990). This model is able to reproduce the general trend of the self-similar scaling laws but shows some discrepancies with observations. While the outer regions of clusters, at radii larger than about 10 per cent of the virial radius, are nearly self-similar, and are well described by simulations, the inner core regions exhibit large scatter and evidence of non-gravitational effects.

Studies of these effects have given rise in the last years to an exciting field of research in cosmological simulations.

To solve these discrepancies and reproduce the observations more closely, cosmological simulations have implemented several non-gravitational processes, such as radiative cooling (e.g., Thomas & Couchman, 1992; Katz & White, 1993; Pearce et al., 2000; Muanwong et al., 2001; Davé et al., 2002; Motl et al., 2004; Kravtsov et al., 2005), preheating (e.g., Navarro et al., 1995a; Bialek et al., 2001; Borgani et al., 2002; Muanwong et al., 2002), feedback coupled with cooling and star formation (e.g., Kay et al., 2003; Tornatore et al., 2003; Valdarnini, 2003; Borgani et al., 2004; Ettori et al., 2004a; Kay et al., 2004, 2007), and black hole growth with associated feedback from AGN (e.g., Puchwein et al., 2008; McCarthy et al., 2010; Fabjan et al., 2010; Short et al., 2010). Other studies have also included metal production and chemical enrichment (Valdarnini, 2003; Schindler & Diaferio, 2008; Borgani et al., 2008; Martínez-Serrano et al., 2008), and magnetic fields and its associated non-thermal processes (Dolag et al., 1999, 2008).

Radiative cooling was soon suggested as a possible solution for the observed discrepancies (e.g., Bryan, 2000; Voit & Bryan, 2001). Cooling provides a selective removal of low-entropy gas from the hot phase and, therefore, only gas having a relatively high entropy will be observed in X-rays (Pearce et al., 2000; Muanwong et al., 2001; Davé et al., 2002; Valdarnini, 2002, 2003; Kay et al., 2004; Nagai et al., 2007; Ettori & Brighenti, 2008). However, this mechanism presents important

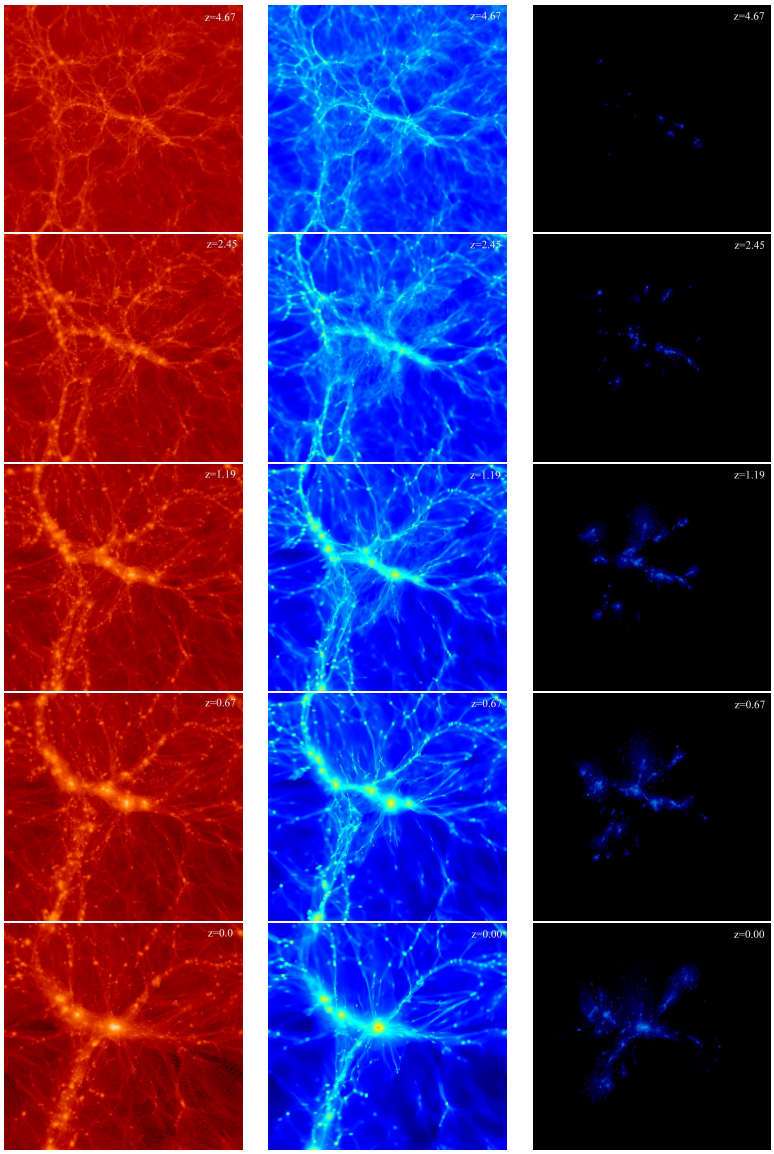

Figure 4.1: Formation and evolution of galaxy clusters in a cosmological context, as described by a hydrodynamical simulation carried out with the MASCLET code (Quilis, 2004). Left, central and right panels show the density maps of dark matter, gas and stellar distributions, respectively. From top to bottom several snapshots at $z \simeq 4, 2, 1, 0.6, 0$ are shown. At $z = 0$, the biggest cluster, formed in the centre of the box, has a virial mass of $\sim 10^{15} M_{\odot}$ and a radius of ~ 3 Mpc. Each panel is 64 comoving Mpc length per edge and 5 comoving Mpc depth.

drawbacks: (i) cooling alone is not able to explain the observed level of self-similarity breaking because the dependence of the condense gas fraction on cluster mass is very weak; (ii) the fraction of cooled condensed gas converted into stars is too high ($\sim 50\%$) compared with the observations ($\sim 10 - 15\%$) (overcooling, e.g., Balogh et al., 2001; Lin et al., 2003; Gonzalez et al., 2007); (iii) paradoxically, radiative cooling increases the ICM temperature at the centre of clusters because it causes a lack of central pressure support making the gas from more external regions to flow in while being heated by adiabatic compression.

Another non-gravitational process taken into account was the preheating of the gas at some early epoch ($z > 1$) by feedback from a non-gravitational astrophysical source, such as galactic winds and/or AGNs (e.g., Kaiser, 1991; Evrard & Henry, 1991; Tozzi & Norman, 2001; Voit, 2005). This heating would increase the entropy of the ICM, preventing it from reaching a high central density during the cluster gravitational collapse and, therefore, decreasing the X-ray luminosity. For a fixed amount of extra energy per gas particle, this effect is more prominent in small clusters. Therefore, smaller systems would have a relatively lower gas fraction and X-ray luminosity, thus leading to a steepening of the L_X-T relation. This solution, which appears to describe considerably better the observed scaling relations, presents, however, several undesirable features: (i) the amount of energy required to heat the ICM to the desired levels is too large to be provided by SNe for a typical initial stellar mass function (Kravtsov & Yepes, 2000); (ii) fairly large isentropic cores are generated in contrast to the low entropy level observed at the centre of relaxed clusters (e.g., Donahue et al., 2006); and (iii) the void statistics of the $Ly\alpha$ forest impose that any preheating should take place only in high density regions of the high-redshift intergalactic medium (e.g., Borgani & Viel, 2009).

The solution to these problems should be provided by a suitable mechanism combining the action of heating and cooling processes in a self-regulated way.

In this sense, different forms of energy feedback from SN explosions have been originally proposed to generate a self-regulated star formation (Springel & Hernquist, 2003). However, the main reason against this stellar feedback is that, besides the complexity of the sub-resolution description required, given the low star formation rates observed in the BCGs they can not provide any significant source of feedback from SN explosions.

Within this scenario, as suggested in Section 3.3.1., it is becoming increasingly clear that AGN feedback is the most plausible source of heating. The main reasons for this mechanism are its central location, its ability to provide enough amounts of energy, and the observed trends of hot gas fractions and entropy in the inner regions with cluster mass (e.g., Sun et al., 2009). In addition, the AGN heating is thought to play an important role in quenching star formation in the BCGs, thereby reducing the cluster stellar mass fractions.

In this regard, the first theoretical studies only were able to analyse the effect of AGN feedback out the cosmological context of cluster formation (e.g., Churazov et al., 2001; Quilis et al., 2001). Only very recently it has been possible to include AGN feedback self-consistently in cosmological simulations (e.g., Puchwein et al., 2008; Fabjan et al., 2010; McCarthy et al., 2010; Short et al., 2010). In general, this approach significantly improves the ability of cosmological hydrodynamical simulations to yield more realistic population of galaxy clusters and groups. An

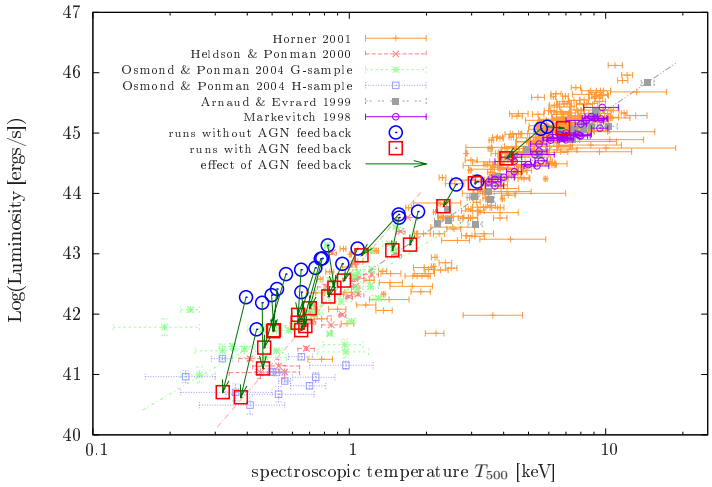

Figure 4.2: L_X-T relation for clusters and groups simulated without AGN feedback (circles) and with the feedback model (squares). For each halo, the arrow illustrates the effect of the AGN heating. Data from several observational X-ray studies is shown for comparison. For a subset also the best-fit power-law L_X-T relation is plotted. Figure taken from Puchwein et al. (2008). See this reference for a detailed description of the feedback model.

example of these results is shown in Fig. 4.2 in which the effect of a model of AGN feedback on a population of galaxy clusters and groups significantly improves the simulated L_X-T relation (see Puchwein et al., 2008, for further details). Although this solution seems to go in the right direction, a number of discrepancies between observations and simulations, such as those concerning the level of central entropy in groups, still exist, especially, within the core regions of massive clusters (e.g., Fabjan et al., 2010). Therefore, although it is crucial to include self-consistent AGN heating in cluster simulations, the details of the heating mechanism by AGN jets remain uncertain (e.g., Voit, 2005).

Within this complex scenario, processes of turbulence, mixing and energy conservation play a crucial role. As for the simulations, it is well known that some results could depend on the ability of different numerical techniques to properly describe these processes. In this sense, since most of the work in this field has been done using SPH cosmological simulations, it is desirable and, at the same time, complementary to increase the number of studies using also Eulerian simulation codes.

Moreover, there are observational evidences that a number of complex physical processes (e.g., thermal conduction, injection of relativistic particles and turbulence associated to jets, magnetic fields,...) should all cooperate to make AGN feedback a self-regulated process. In this sense, additional insights from observations would be very helpful for discriminating between contending models and to further constrain the parameters of the different non-gravitational processes.

The main difficulty when treating most of the dissipative processes, such as

gas cooling, star formation or stellar evolution, resides in the fact that they occur on scales much smaller ($\ll 1$ pc) than the spatial resolution of the simulation and must be approximated by phenomenological recipes. In addition, they have effects on galactic and extragalactic scales ($\gg 1$ Mpc) and, therefore, the simulations should model a spatial range of at least six orders of magnitude. These large dynamic ranges can be covered by neither a single numerical simulation nor simulations which rely on the resimulation technique (e.g., Navarro et al., 1995b). As a consequence, a difficult task for present-day cosmological simulations is to simultaneously match the observations for the thermodynamical properties of the ICM, the stellar mass fraction, and the galaxy luminosity function.

The large number of physical processes to be included, as well as the large computational resources required to run N-body/hydrodynamical simulations for a realistic modelling of cluster and galaxy formation, is a challenging task in the field of Numerical Cosmology for the near future, both from a computational and from a physical point of view.

Chapter 5

Cosmological simulations with MASCLET

The simulations analysed throughout this Thesis were carried out with the cosmological code MASCLET (Quilis, 2004). In this Chapter the main numerical properties of this code are summarized. In addition, an update of the new features that have been included during the last years, namely, the star formation and the metal enrichment, is presented.

5.1 Introduction

The MASCLET code – *Mesh Adaptive Scheme for CosmologicaL structurE evoluTion* – is an Eulerian coupled hydrodynamical and N-body code for cosmological applications based on an AMR scheme.

The central tenet of the AMR scheme, the refinement of the computational grid wherever better resolution is needed, can be exploited to incorporate an N-body scheme to follow the evolution of dark matter. The PM method is ideally suited for grating onto an hydro-AMR code. In practise, a PM scheme is used for each nested grid, with progressively higher spatial resolution when the cell size gets smaller. This implementation of the AMR-PM has the advantage of avoiding the problem of setting a softening parameter in the gravitational force law, as this parameter is naturally determined by the cell size. Several implementations of this approach for dark matter only have been presented in the literature with different degrees of success (Villumsen, 1989; Jessop et al., 1994; Splinter, 1996; Kravtsov et al., 1997).

In MASCLET, the basic hydrodynamical solver is based on the Piecewise Parabolic Method (PPM; Colella & Woodward, 1984) whereas the N-body method used is a classic PM according to Hockney & Eastwood (1988). Within this scheme, gas and dark matter are coupled by the gravity solver and both components benefit by using the AMR strategy.

The MASCLET code is written in FORTRAN 90 and there is a parallel version using OpenMP standard directives.

5.2 Numerical procedure

5.2.1 Gas dynamics

The basic equations governing the evolution of cosmological inhomogeneities (Eqs. 4.6–4.8) can be rewritten in a slightly different form as a *hyperbolic system of conservation laws*:

$$\frac{\partial \mathbf{u}}{\partial t} + \frac{\partial \mathbf{f}(\mathbf{u})}{\partial x} + \frac{\partial \mathbf{g}(\mathbf{u})}{\partial y} + \frac{\partial \mathbf{h}(\mathbf{u})}{\partial z} = \mathbf{s}(\mathbf{u}). \tag{5.1}$$

Here, $\mathbf{u}$ is the vector of *unknowns* (conserved variables):

$$\mathbf{u} = [\delta, m_x, m_y, m_z, E], \tag{5.2}$$

where $m_x = (\delta + 1)v_x$, $m_y = (\delta + 1)v_y$, and $m_z = (\delta + 1)v_z$, E is the total energy density, and δ is the density contrast.

The mathematical properties of this kind of systems and the numerical algorithms specifically designed for solving it have been well studied in the literature (LeVeque, 1992; Toro, 1997). In this kind of systems, the three *flux* functions, $\mathbf{F}^\alpha \equiv \{\mathbf{f}, \mathbf{g}, \mathbf{h}\}$, and the *sources*, $\mathbf{s}(\mathbf{u})$, are three-dimensional arrays formed by combinations, more or less complex, of the conserved variables that appear in Eq. 5.2 (see Quilis, 2004, for further details).

In addition, the sources do not contain any term with differential operators acting on the hydrodynamical variables $\mathbf{u}$.

In all the simulations analysed during this Thesis an ideal gas equation of state, $p = (\gamma - 1)\rho\epsilon$ with $\gamma = 5/3$, completes the system.

From the numerical point of view, the mathematical properties of this kind of systems are crucial to develop the most part of the numerical algorithms used in hydrodynamical simulations.

5.2.1.1 The hydro code

The mathematical properties resulting from the hyperbolic character of the system of equations 5.1 allow us to design a set of numerical techniques known as *high-resolution shock-capturing* (HRSC). These techniques are the modern implementation of Godunov's original method (Godunov, 1959).

The HRSC techniques have several key ingredients such as the reconstruction procedure, the Riemann solver, and time advancing schemes which can vary in different implementations. Nevertheless, all of these implementations share the same basic properties: the ability to handle shocks, discontinuities and strong gradients in the integrated quantities, and excellent conservation properties.

Our basic hydro solver is based on a particular implementation of the HRSC methods (see Quilis et al., 1996, for more details). The main ingredients of this solver are the following:

1. It is written in *conservation form*. This is a very important property for a numerical algorithm designed to solve a hyperbolic system of conservation laws. That is, in the absence of sources, those quantities that ought to be

conserved – according to the differential equations – are exactly conserved in the difference form.

2. *Reconstruction procedure*. This procedure allows the method to gain resolution by reconstructing, through interpolations, the distribution of the quantities within the numerical cells. In order to increase the spatial accuracy, we have implemented a parabolic reconstruction (PPM) subroutine according to the procedure derived by Colella & Woodward (1984). With this parabolic reconstruction, the algorithm is third order accurate in space. Hence, from the cell-averaged quantities $\mathbf{u}_{i,j,k}$ we construct, in each direction, a piecewise parabolic function which preserves monotonicity. Thus, the values of $\mathbf{u}_{i,j,k}$ at both sides of a given interface between neighbour cells can be computed. These values at each side of a given interface allow us to define the local Riemann problems. The numerical fluxes can be computed through the solution of these local Riemann problems.

3. *Numerical fluxes* at interfaces. We have used a linearized Riemann solver following an approach similar to the one described in Roe (1981).

4. *Advancing in time*. Once the numerical fluxes are known, the evolution of conserved quantities is governed by an ordinary differential equation system (ODE). A third order Runge-Kutta solver (Shu & Osher, 1988) is used to solve these equations.

Gravity is included in the gas evolution through the source term, $\mathbf{s}_{i,j,k}$. This term includes the gradient of the gravitational potential which is produced by the total mass distribution, gas plus dark matter plus stars. The procedure used to solve Poisson's equation 4.5 is described in Section 5.2.5.

The criteria to select the time step is very important and it must be considered globally with other time constraints that are unrelated to the gas part. This aspect will be discussed in Section 5.2.6.

5.2.2 Dark matter dynamics

The dark matter is treated as a collisionless system of particles. Each of these particles evolves obeying the equations 4.3 and 4.4.

In MASCLET these equations are solved using a Lax-Wendroff scheme which is second order. With this method, the procedure to go from time step n, where all the variables are known, to the step $n+1$, using an intermediate step $t^{n+\frac{1}{2}} = t^n + \frac{\Delta t}{2}$, is the following:

1. Compute the intermediate step:

$$\mathbf{x}^{n+\frac{1}{2}} = \mathbf{x}^n + \frac{1}{2}\frac{\mathbf{v}^n}{a^n}\Delta t \tag{5.3}$$

$$\mathbf{v}^{n+\frac{1}{2}} = \mathbf{v}^n - \frac{1}{2}\left[\frac{\nabla\phi^n}{a^n} + H^n\mathbf{v}^n\right]\Delta t \tag{5.4}$$

2. Step $n+1$:

$$\mathbf{x}^{n+1} = \mathbf{x}^n + \frac{\mathbf{v}^{n+\frac{1}{2}}}{a^{n+\frac{1}{2}}}\Delta t \tag{5.5}$$

$$\mathbf{v}^{n+1} = \mathbf{v}^n - \left[\frac{\nabla\phi^{n+\frac{1}{2}}}{a^{n+\frac{1}{2}}} + H^{n+\frac{1}{2}}\mathbf{v}^{n+\frac{1}{2}}\right]\Delta t \tag{5.6}$$

where the potential at intermediate step, $\phi^{n+\frac{1}{2}}$, is computed using a linear extrapolation from ϕ^{n-1} and ϕ^n.

In order to recover the continuous density field for the dark matter component, ρ_{DM}, we use a triangular shaped cloud scheme (TSC; Hockney & Eastwood, 1988) at each time step.

5.2.3 Star formation

A phenomenological star formation following the ideas of Yepes et al. (1997) and Springel & Hernquist (2003) has been introduced in the MASCLET code. Like the dark matter, stars are treated like a collisionless system of particles that evolves according to equations 4.3 and 4.4.

In our particular implementation, we assume that cold gas in a cell is transformed into star particles on a characteristic time scale t_* according to the following expression:

$$\frac{d\rho_*}{dt} = -\frac{d\rho}{dt} = \frac{\rho}{t_*(\rho)} - \beta\frac{\rho}{t_*(\rho)} = (1-\beta)\frac{\rho}{t_*(\rho)}, \tag{5.7}$$

where ρ and ρ_* are the gas and star densities, respectively. The parameter β stands for the mass fraction of massive stars ($> 8\,M_\odot$) that explode as supernovae, and therefore return to the gas component in the cells. We have adopted $\beta = 0.1$, a value compatible with a Salpeter initial mass function (IMF). For the characteristic star formation time, we make the common assumption $t_*(\rho) = t_o^*(\rho/\rho_{th})^{-1/2}$, equivalent to $\dot{\rho}_* = \rho^{1.5}/t_o^*$ (Kennicutt, 1998). In this way, we have introduced a dependence on the local dynamical time of the gas and two parameters , the density threshold for star formation (ρ_{th}) and the corresponding characteristic time scale (t_0^*). In our simulations we have taken $t_0^* = 2\,Gyr$ and $\rho_{th} = 2\times10^{-25}\,g\,cm^{-3}$. From the energetic point of view, we consider that each supernova dumps in the original cell $10^{51}\,erg$ of thermal energy.

In the practical implementation, we usually assume that star formation occurs once every global time step, $\Delta t_{l=0}$, and only in the cells at the highest levels (l) of refinement. The cells at those levels of refinement, where the gas temperature drops below $T < 2\times10^4\,K$, and the gas density is $\rho > \rho_{th} = 2\times10^{-25}\,g\,cm^{-3}$, are suitable to form stars. In these cells, collisionless star particles with mass $m_* = \dot{\rho}_*\Delta t_{l=0}\Delta x_l^3$ are formed. In order to avoid sudden changes in the gas density, an extra condition restricts the mass of the star particles to be $m_* = \min(m_*, \frac{2}{3}m_{gas})$, where m_{gas} is the total gas mass in the considered cell.

Like for the dark matter, in order to recover the continuous density field for the stellar component, ρ_*, we use the TSC scheme (Hockney & Eastwood, 1988) at each time step.

5.2.4 Gas cooling and metal enrichment

Gas cooling is treated in a similar way as in Springel & Hernquist (2003). Our simulations include cooling and heating processes which take into account Compton and free-free cooling, UV heating (Haardt & Madau, 1996), and atomic and molecular cooling for a primordial gas. In order to compute the abundances of each specie, we assume that the gas is optically thin and in ionization equilibrium, but not in thermal equilibrium (Katz et al., 1996; Theuns et al., 1998). The cooling and heating are included in the energy equation (Eq. 4.8) as extra source terms.

The cooling rates are strongly dependent on the temperature of the gas and on its metallicity. We model these dependences using the collisional ionisation cooling curves of Sutherland & Dopita (1993). At high temperatures ($\geq 10^8 K$), the cooling is dominated by the bremsstrahlung continuum. At lower temperatures line cooling from heavy elements dominates. Using metal-dependent cooling makes cooling more efficient. As a consequence, it produces an overall increase of the brightness of the considered systems. In the particular case of galaxy clusters, as it will be discussed in the next chapters, this effect is stronger in low mass clusters.

In our particular implementation, to take into account the contribution of metals, we make the following assumptions:

1. Species heavier than hydrogen and helium are considered metals.

2. Instantaneous mixing. Metals are instantaneously mixed over the ICM.

3. Metals are advected following the gas component.

Under these assumptions, metals are described by the following equation:

$$\frac{\partial \rho_z}{\partial t} + \frac{1}{a}\nabla \cdot (\rho_z \mathbf{v}) = -3H\rho_z, \tag{5.8}$$

where $\mathbf{v}$ is the peculiar velocity, and ρ_z is the metal density. Equation 5.8 is the continuity equation for the metal content. Due to the ongoing star formation, the fraction of gas in a given cell can vary locally and, hence, the metal content is not conserved.

5.2.5 The time step criteria

To solve numerically the hydro equations and Eqs. 4.3–4.4, we need to choose a time step. The numerical stability of the methods used to integrate these equations imposes several criteria on the time step. At each numerical iteration, we compute several time steps given by the different stability conditions. The most restrictive of all of them is selected to advance all components.

The time step criteria we consider are the following:

1. Courant time. It is based on the Courant condition for stability of an algorithm to solve partial differential equations. We compute Δt_C as:

$$\Delta t_C = CFL_1 \times \frac{\Delta x}{c_s + max(|v_x|, |v_y|, |v_z|)}, \tag{5.9}$$

where CFL_1 is a dimensionless factor between 0 and 1, and c_s is the sound speed. This quantity is computed for all cells and the final Courant time step is $\Delta t_C = min(\Delta t_C)_{i,j,k}$, $\forall i,j,k$. Typically, we use $CFL_1 = 0.5$.

2. Dark matter particle cell-crossing time. We compute the cell-crossing time for the fastest dark matter particle, and define the new time step as a fraction of this crossing time:

$$\Delta t_{DM} = CFL_2 \times \frac{\Delta x}{max(|\mathbf{v}|)}, \tag{5.10}$$

where we choose $CFL_2 = 0.2$.

3. Expansion time. The equations we are considering have source terms which include factors due to the cosmological expansion. At early times in particular, these factors can be important and their time variations introduce another time step constraint. We compute this new time step by imposing a maximum change of 2% in the expansion of the Universe. In the case of flat Universe with cosmological constant, we approach the time step by:

$$\Delta t_e = [(1.0 + CFL_3)^{3/2} - 1.0] \cdot t \ , \tag{5.11}$$

where $CFL_3 = 0.02$ represents the allowed variation (per one) for the scale factor.

4. Dynamical time. The free-fall collapse time that would take a cloud of dust (pressureless) to collapse under its own gravity is given by:

$$\Delta t_{dyn} = CLF_4 \sqrt{\frac{3\pi^2}{4G\rho_{max}}}, \tag{5.12}$$

where G is the gravitational constant, ρ_{max} is the maximum baryonic density in all cells, and $CFL_4 = 1$.

This timescale, however, only is considered in applications with extremely low pressure values.

5. As an extra criteria to avoid unexpected numerical instabilities, we also introduce another time step, Δt_{in}, which prevents the new time step to increase more than 25% of the global time step for the previous iteration:

$$\Delta t_{in} = \Delta t^{n-1} + 0.25\Delta t^{n-1}. \tag{5.13}$$

The global time step is defined as the most stringent of all the previous time steps:

$$\Delta t = min(\Delta t_C, \Delta t_{DM}, \Delta t_e, \Delta t_{dyn}, \Delta t_{in}). \tag{5.14}$$

At the beginning of the cosmological simulations, Δt_e is the dominant time criterium but Δt_C and Δt_{DM} quickly take over.

5.3 The Adaptive Mesh Refinement strategy

The fundamental idea behind the AMR technique is to overcome the lack of resolution associated with the fix grid Eulerian description. The basic idea is simple. Regions in the original computational domain in which improved resolution is required are selected according to some criteria (see Section 5.3.1). These new computational domains, which we call *child grids* or *patches*, are remapped with a higher number of cells and therefore with better resolution. The values of the different quantities defined on the child grids are obtained by interpolating from the *parent grid*. Once the child grids are built, they can be evolved as an independent computational domain by using the same methods we have described in Section 5.2. Although conceptually simple, there are severe technical complications concerning with the communication among the different patches and the boundary problems at different levels.

Our implementation of the AMR technique follows the one described in Berger & Colella (1989).

5.3.1 Creating the grid hierarchy

The first step in the construction of the hierarchy of patches is the coarse basic grid on which all the relevant quantities are known. From this starting point, some criteria must be applied to decide which cells are *refinable*. These criteria are application dependent and may need to be modified in certain cases. Generally speaking, our code uses two conditions: (i) if quantities (like density or pressure) are larger than a given threshold, and (ii) if gradients of quantities are steeper than a given limit. Depending on the applications, we may ask for only one of these conditions to be satisfied, whereas in other cases both conditions must apply. The routine controlling this process can easily incorporate new conditions. All the numerical cells from the coarse grid which satisfy the refinement criteria are labelled as *refinable*.

In order to illustrate the process of patch generation, let us describe in detail the mechanism for creating new patches at level, $l+1$, once all the relevant information is known at a lower level, l.

Let us begin with the level, l, where according to a set of refinement criteria, we have identified all the cells which fulfil these conditions. Then, we select among the *refinable* cells the one which maximizes the refinement criteria (i.e. if the criteria are based on local density, we choose the cell with the highest density). Around this maximum, the minimal patch is created by adding two cells along each coordinate direction. Once a patch containing $5 \times 5 \times 5$ cells is created, the patch is extended one cell along x-axis direction at the high-x end of the patch, such that the new dimension of the patch becomes $6 \times 5 \times 5$ cells. If the number of *refinable* cells after the extension increases, then the extension is accepted, otherwise this edge remains fixed to the value before the extension. The same procedure is repeated for the low-x end of the patch. In this way, the extension of the patch along x-axis direction is controlled. Exactly same mechanism is repeated for y- and z-axes. The patch extension procedure goes on until no new *refinable* cells are included in the patch, and therefore its dimensions remain unchanged. At this point, the

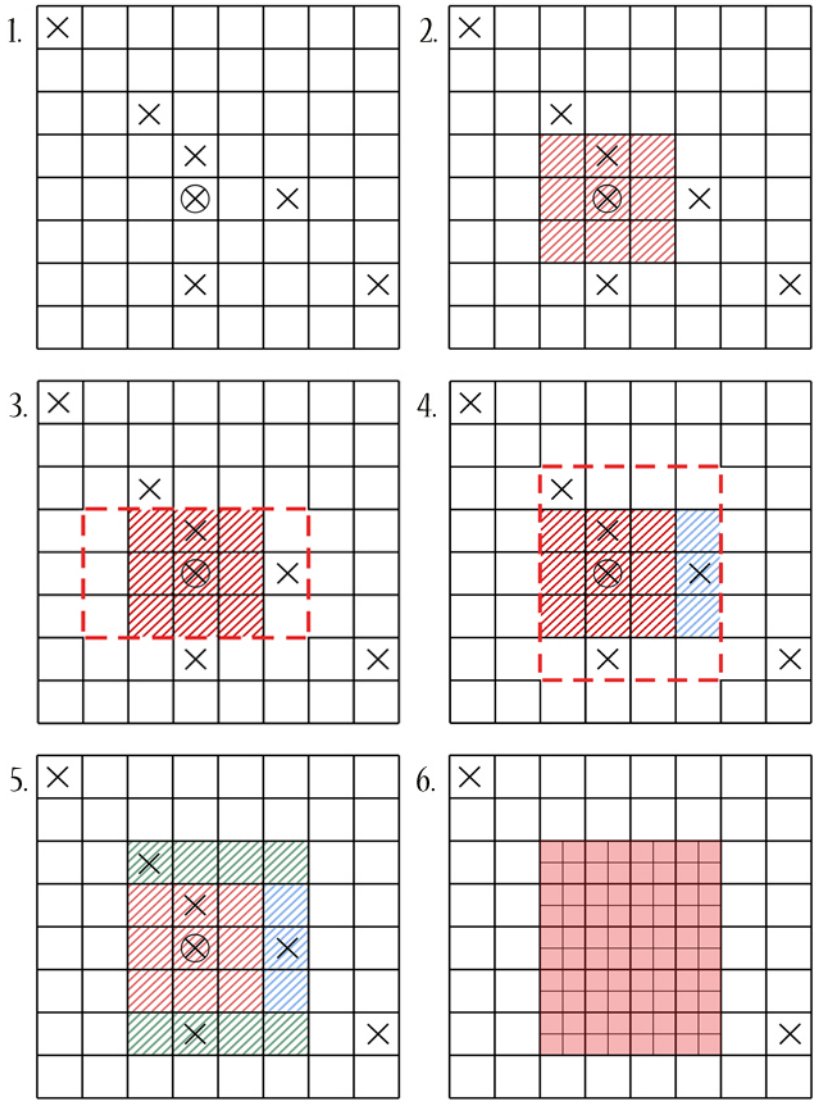

Figure 5.1: Schematic 2-D AMR grid generation in the MASCLET code. *Refinable* cells are marked with $\times$, whereas the cell that maximizes the refinement criteria is represented by $\otimes$. A complete explanation of the different panels can be found in the text.

patch is perfectly defined. All the cells contained in the recently formed patch are removed from the list of *refinable* cells at level l. Then, we look again for the remaining *refinable* cell which maximizes the refinement criteria, and the process is repeated. The procedure goes on until all *refinable* cells have been allocated in patches, and therefore, all patches at levels $l+1$ have been defined.

According to this mechanism, the lower level, l, is divided into patches which contain the *refinable* cells. As an additional precaution, every patch is extended in every direction by adding one extra cell.

When regions on the parent grids are already identified and defined, they are remapped with higher resolution by splitting the coarse cells into new, smaller cells. The ratio, r, between the coarse cell size Δx and the finer cell size $\Delta x\prime$ is a free integer parameter depending on the particular AMR implementation. In our code we have chosen, $r = \Delta x/\Delta x\prime = 2$. This choice is a compromise between gaining resolution and avoiding possible numerical instabilities that can result from using a too high value of r. The method previously described produces patches with a boxy geometry and cubic cells ($\Delta x = \Delta y = \Delta z$) at any level.

At this point, the geometry of the patches, their positions in the parent grid, and their new number of cells, are known. The next step must be to define the values of the quantities in the equations onto the new, finer grids. In order to do this, we have implemented a *trilinear* conservative interpolation.

The procedure described above can be applied recursively. The patches formed from the lower-level grid, now become parent grids. The above process can be applied to them, thus producing a new set of patches in a higher level of refinement. This method allows us to create a whole set of patches at different levels which map our computational domain with adaptable resolution.

For simplicity, we illustrate in Fig. 5.1 the procedure of generation of a reduced patch in 2-D. Here, *refinable* cells are marked with $\times$, whereas the cell that maximizes the refinement criteria is represented by $\otimes$. Around this maximum, the minimal patch (red region with an extension of 3×3 cells) is created by adding one cell (for simplicity) along each coordinate direction (panel 2). Panels 3, 4 and 5 represent the provisional extensions of the first patch along the x and y axis, respectively. Only when the number of *refinable* cells increases in one direction, the extension is accepted (blue and green regions in the x and y directions, respectively). When there are no more cells to add to the patch, this is perfectly defined and can be remapped with smaller cells (panel 6).

The grid hierarchy is reconstructed after each time step, once the system has been evolved in time. At the new time step, the hierarchy is rebuilt with the procedure described above. Only a fraction of cells would be brand new refined cells, in the sense that they would map a region of the computational domain not previously covered at the previous time step and with the same resolution. In this situation, it would be a great waste of computational resources to completely rebuild the grid hierarchy by interpolating from the parent levels. In order to improve performance, the cells at a certain level of refinement – at the advanced time – which were in refined patches at the same level at the previous time step, are simply updated with their time evolution within their patch. Only those cells covering regions of the computational domain, which were not refined at the previous time step with the same resolution, are assigned with interpolated values

from the respective parent patch at a lower level.

It should be noted that the process of grid creation described above, produces a certain degree of overlapping between patches at the same level. This situation must be kept under control by the code as we do not wish to have a scenario in which cells – located at the same coordinates but belonging to different patches – could be assigned with slightly different values of the physical quantities.

The process of building the whole set of nested grids and the multidimensional interpolations needed to assign values to the new created cells is very CPU demanding. In our implementation, the hierarchy may not be rebuilt every time step. A free parameter, which depends on the application, controls how frequently the hierarchy can be modified, in the meantime, it remains unchanged.

5.4 Gravity solver

The gravitational potential is computed by solving Poisson's equation 4.5. As three components are considered (gas, dark matter and stars), the source in Poisson's equation is the total density contrast:

$$\nabla^2\phi = \frac{3}{2}H^2a^2\delta_T = \frac{a^2}{2}(\rho_{_T} - \rho_{_B}), \tag{5.15}$$

where $\delta_T = \delta + \delta_{DM} + \delta_* + 2$ and $\rho_{_T} = \rho + \rho_{_{DM}} + \rho_*$.

In order to solve Poisson's equation, the continuous dark matter density is required at each cell of the computational box. The dark matter density is obtained using the TSC mesh assignment method within the considered grid level. At levels $l > 0$, all particles within a patch contribute to the density of that patch. Therefore, particles can contribute to the density of different patches at different levels, but are "spread" with different cloud sizes. This approach naturally offers the advantage of not having to specify a softening length parameter.

The procedure to solve Poisson's equation differs depending on the considered level.

- **Coarse level ($l = 0$)**

  In the coarse level Poisson's equation is solved using Fast Fourier Transform (FFT) methods (Press et al., 1996). The FFT is used as follows:

  1. The density contrast in physical space – with suitable boundary conditions – is the starting point.
  2. A FFT gives $\delta_T(\mathbf{k})$ (the Fourier component of δ_T).
  3. Poisson's equation in Fourier space, $\phi(\mathbf{k}) = G(\mathbf{k})\delta_T(\mathbf{k})$, – being $G(\mathbf{k})$ the Green's function – is used to get $\phi(\mathbf{k})$.
  4. The inverse FFT leads to the required gravitational potential in physical space.

- **AMR levels ($l > 0$)**

In order to solve Poisson's equation at higher levels we use a successive overrelaxation method (SOR). These kind of methods solve Eq. 4.5 by discretizing the equation and treating it as a linear system of equations (see Press et al., 1996):

$$\phi_{i+1,j,k} + \phi_{i-1,j,k} + \phi_{i,j+1,k} + \phi_{i,j-1,k} + \phi_{i,j,k+1} + \phi_{i,j,k-1} - 6\phi_{i,j,k} = \eta\delta_{T_{i,j,k}} \ , \tag{5.16}$$

where $\eta = \frac{3}{2}H^2a^2\Delta x_l^2$, being Δx_l the resolution of the considered level.

The new potential ϕ^{new} is defined by an iterative process as follows:

$$\phi^{new}_{i,j,k} = \omega\phi^{*}_{i,j,k} + (1-\omega)\phi^{old}_{i,j,k} \ , \tag{5.17}$$

where

$$\phi^{*}_{i,j,k} = (\eta\delta_{T_{i,j,k}} - \phi_{i+1,j,k} - \phi_{i-1,j,k} - \phi_{i,j+1,k} - \phi_{i,j-1,k} - \phi_{i,j,k+1} - \phi_{i,j,k-1})/6. \tag{5.18}$$

The overrelaxation parameter, ω, is defined in the interval $1 < \omega < 2$. In order to find the optimum value for this parameter, we have used the asymptotic Chebyshev acceleration procedure (see Press et al., 1996). Following this method, the number of iterations (typically ~ 10) is minimized.

Once the potential is known at each level, the positions and velocities of all particles can be updated using the Eqs. (5.3–5.6).

Chapter 6

The ASOHF halo finder *

The halo identification is a crucial step in the analysis of any cosmological simulation. With the final idea of analysing in a consistent way the outputs generated by the MASCLET code, we have developed a halo finder especially suited to deal with the results of the AMR Eulerian cosmological codes, although it can be easily applied to the outcomes of a general N-body simulation. In this Chapter, the main properties of this *Adaptive Spherical Overdensity Halo Finder* (ASOHF) are extensively described. The behaviour of ASOHF in several real and non so real situations is also presented and tested.

6.1 Introduction

In Chapter 4 we have seen how the use and development of cosmological simulations have led to important advances in our knowledge of the Universe. However, the primary results of these complex simulations "only" consist in huge amounts of raw data which need to be somehow analysed depending on the application. In the particular case of N-body simulations, the aggregates of millions of dissipationless dark matter particles produced in the simulations require to be interpreted and somehow compared with the observable Universe. To do so, it is necessary to identify the groups of gravitationally bound dark matter particles which are the dark counterparts of the observable components of the cosmological structures (galaxies, galaxy clusters, ...). These dark matter clumps are the so-called dark matter haloes, and the task to identify them in simulations is usually carried out with the help of numerical tools known as halo finders.

Different algorithms to identify structures and substructures in cosmological simulations have been proposed and have seen many improvements over the years. As a consequence, there are several kinds of halo finders currently widely used although, at heart, the basic idea of all of them is to identify gravitationally bound objects in an N-body simulation. All these halo-finding algorithms seem to perform exceedingly well when they deal with the identification of haloes without substructure. However, the remarkable development of N-body simulations and

*This Chapter is based on Planelles & Quilis (2010)

the applications studied with these new codes necessitated new algorithms able to deal with the scenario of haloes-within-haloes (e.g., Klypin et al., 1999a,b; Moore et al., 1999).

6.2 Background

Let us briefly outline some of the most popular halo finders.

The classical method to identify dark matter haloes is the purely geometrical friends-of-friends algorithm (FoF; Davis et al., 1985). This technique consists in finding neighbours of dark matter particles and neighbours of these neighbours according to a given linking length parameter. The characteristic linking length, l_{FoF}, is usually set to ~ 0.2 of the mean particle separation. The collection of linked particles forms a group that is considered as a virialized halo. The mass of the halo is defined as the sum of the mass of all dark matter particles within the halo. Among the main advantages of this algorithm we can point out that its results are relatively easy to interpret and that it does not make any assumption concerning the halo shape. The greatest disadvantage is its rudimentary choice of linking length, which can lead to a connection of two separate objects via the so-called "linking bridges". Moreover, because structure formation is hierarchical, each halo contains substructure and thus, different linking lengths are needed to identify "haloes-within-haloes". There are several modified implementations of the original FoF, such as the adaptive FoF (AFoF; van Kampen, 1995) or the hierarchical FoF (HFoF; Klypin et al., 1999a), among others, which try to overcome these limitations.

The other most general method is the spherical overdensity (SO; Lacey & Cole, 1994) that uses the mean overdensity criterion for the detection of virialized haloes. The basic idea of this technique is to identify spherical regions with an average density corresponding to the density of a virialized region according the top-hat collapse model. The main drawback of the SO mass definition is that it is somehow artificial, enforcing spherical symmetry on all objects while, in reality, haloes often have an irregular structure (White, 2002), for example, haloes that were formed in a recent merger event or haloes at high redshifts. Furthermore, defining an SO mass can be ambiguous because the corresponding SO spheres might overlap for two close density peaks. Owing to these characteristics, the SO method implies oversimplifications that could lead to unrealistic results and which therefore deserve a careful treatment. Despite these apparently significant disadvantages, one of the most relevant features of this technique is that no linking length is needed to define the structures.

Almost all existing halo finders are based on either the FoF algorithm, the SO, or a combination of both methods.

The DENMAX (Bertschinger & Gelb, 1991; Gelb & Bertschinger, 1994) and SKID (Weinberg et al., 1997) algorithms are similar methods. Both of them calculate a density field from the particle distribution, then gradually move the particles in the direction of the local density gradient ending with small groups of particles around each local density maximum. The FOF method is then used to associate these small groups with individual haloes. The difference between the two meth-

ods is in the calculation of the density field. DENMAX uses a grid, while SKID applies an adaptive smoothing kernel similar to that employed in SPH techniques (Gingold & Monaghan, 1977; Lucy, 1977). The effectiveness of these methods is limited by the technique used to determine the density field (Götz et al., 1998).

The HOP method (Eisenstein & Hu, 1998) is based on a density field similar to the SKID. However, it uses a different type of particle sliding. The HOP algorithm searches for the maximum density among the n nearest neighbours of a particle and attaches the particle to the densest neighbour. Finally, it groups particles in a local density maximum, defining a virialized halo.

The BDM method (Klypin et al., 1999a) uses randomly placed spheres with predefined radius, which are iteratively moved to the centre of mass of the particles contained in them until the density centre is found.

Completely different is the VOBOZ technique (Neyrinck et al., 2005), which uses a Voronoi tessellation to calculate the local density.

The halo finder MHF (Gill et al., 2004) took advantage of the grid hierarchy generated by the AMR code MLAPM (Knebe et al., 2001) to find the haloes in a given simulation. In most of the cosmological AMR codes, the grid hierarchy is built in such a way that the grid is refined in high-density regions and hence naturally traces the densest regions. This can be used not only to select haloes, but also to identify the substructure. The AHF (Amiga Halo Finder), which is the direct successor of the original MHF, has been recently presented and tested (Knollmann & Knebe, 2009).

Similarly to SKID, in SUBFIND (Springel et al., 2001a) the density of each particle is estimated with a cubic spline interpolation. In a first step, the FOF method is used and then any locally overdense region enclosed by an isodensity contour that traverses a saddle point is considered as a substructure candidate. SUBFIND runs on individual simulation snapshots, but can afterwards reconstruct the full merger tree of each subclump by using the subhalo information from previous snapshots. All subhalo candidates are then examined and unbound particles are removed.

A quite different method is provided by the code SURV (Tormen et al., 2004; Giocoli et al., 2008, 2009), which identifies subhaloes within the virial radius of the final host by following all branches of the merger tree of each halo (rather than just the main branch), in order to reconstruct the full hierarchy of substructure down to the mass resolution of the simulation.

The parallel group finder 6DFOF (Diemand et al., 2006, 2007) finds peaks in phase-space density, i.e., it links the most bound particles inside the cores of haloes and subhaloes together. The same objects identified by 6DFOF at different times therefore always have quite a large fraction of particles in common (in most cases over 90%). This makes finding progenitors or descendants rather easy.

An updated list of currently working halo finders and a complete analysis of their drawbacks and strong points can be found in Knebe et al. (2010).

6.3 The numerical procedure

The halo finder developed for MASCLET, ASOHF, shares some features with AHF (Knollmann & Knebe, 2009), which is the evolution of the original MHF halo finder (Gill et al., 2004). Although we used an identification technique based on the original idea of the SO method, the practical implementation of our finder has several steps designed to improve the performance of this method and to get rid of the possible drawbacks as well as to take advantage of an AMR grid structure.

The particular implementation of our halo finder follows several main steps.

1. In a first step, the algorithm reads the density field computed on a hierarchy of grids provided by the simulations. Then the SO method is applied to each density maximum: radial shells are stepped out around each density peak until the mean overdensity falls below a given threshold or there is a significant rising in the slope of the density profile. The overdensity, Δ_c, depends on the adopted cosmological model and can be approximated (see Eq. 3.6) by the expression (Bryan & Norman, 1998)

$$\Delta_c = 18\pi^2 + 82x - 39x^2, \tag{6.1}$$

where $x = \Omega(z) - 1$ and $\Omega(z) = [\Omega_m(1+z)^3]/[\Omega_m(1+z)^3 + \Omega_\Lambda]$.

Therefore, the virial mass of a halo, M_{vir}, is defined as the mass enclosed in a spherical region of radius, r_{vir}, with an average density Δ_c times the critical density of the Universe ($\rho_c(z) = 3H(z)^2/8\pi G$):

$$M_{vir}(\leq r_{vir}) = \frac{4}{3}\pi\Delta_c\rho_c r_{vir}^3. \tag{6.2}$$

This first step, which only defines the scale of the objects we are looking for, provides a crude estimation of the position, radius and mass for each detected halo.

2. The second step takes care of possible overlaps among the preliminary haloes found in the first step. In our method, if two haloes overlap and the shared mass is larger than the 80% of the minimum mass of the implicated haloes, the less massive of them is removed from the list. On the other hand, if the shared mass is between the 40% and the 80% of the minimum mass of the haloes, the algorithm joins these haloes and computes the centre of mass of the new halo. Consequently, it removes the less massive halo from the list, and applies again the first step to the new centre of mass to obtain the physical properties of the new halo. In the end, this step provides a final number of haloes.

3. Once we have a tentative halo selection, a third step provides a more accurate sample by working only with the dark matter particles within each halo. These particles are distributed through the complete simulated volume and are not limited by cell boundaries. ASOHF can deal with several particles species (particles with different masses), providing therefore a best-mass resolution. This step is crucial to obtain a precise estimation of the main

physical properties of the haloes, particularly, a new prediction for the mass and position of the centre of mass.

4. We now have a set of prospective haloes defined using the spatial positions of the particles. However these prospectives haloes may include particles which are not physically bound. In order to remove gravitationally unbound particles we have to obtain the (local) escape velocity $v_{\rm esc}(r)$ at the position of each particle. As $v_{\rm esc}$ is directly related to the (local) value of the potential ($v_{\rm esc} = \sqrt{2\,|\phi|}$), we integrate Poisson's equation (assuming spherical symmetry):

$$\Delta\phi(r) = \frac{1}{r}\frac{d}{dr}\left(r^2\frac{d\phi}{dr}\right) = 4\pi G\rho(r). \tag{6.3}$$

After the first integral we have the following:

$$r^2\frac{d\phi}{dr} - \left[r^2\frac{d\phi}{dr}\right]_{r=0} = 4\pi G\int_0^r \rho(r')r'^2dr' = GM(<r), \tag{6.4}$$

where we can see that $r^2 d\phi/dr \to 0$ when $r \to 0$. Then, we have to solve the following first-order differential equation for $\phi(r)$:

$$\frac{d\phi}{dr} = G\frac{M(<r)}{r^2}. \tag{6.5}$$

Integrating once more we obtain

$$\phi(r) = G\int_0^r \frac{M(<r')}{r'^2}dr' + \phi_0. \tag{6.6}$$

To calculate ϕ_0 we assume that $\phi(\infty) = 0$:

$$\begin{aligned}
\phi(\infty) &= G\int_0^\infty \frac{M(<r')}{r'^2}dr' + \phi_0 && (6.7)\\
&= G\int_0^{r_{\rm vir}} \frac{M(<r')}{r'^2}dr' + G\int_{r_{\rm vir}}^\infty \frac{M(<r')}{r'^2}dr' + \phi_0 && (6.8)\\
&= G\int_0^{r_{\rm vir}} \frac{M(<r')}{r'^2}dr' + GM_{\rm vir}\int_{r_{\rm vir}}^\infty \frac{1}{r'^2}dr' + \phi_0 && (6.9)\\
&= G\int_0^{r_{\rm vir}} \frac{M(<r')}{r'^2}dr' + G\frac{M_{\rm vir}}{r_{\rm vir}} + \phi_0 && (6.10)
\end{aligned}$$

and, therefore,

$$\phi_0 = -\left(G\int_0^{r_{\rm vir}} \frac{M(<r')}{r'^2}dr' + G\frac{M_{\rm vir}}{r_{\rm vir}}\right). \tag{6.11}$$

Note that, when evaluating the integral $\int_{r_{\rm vir}}^\infty \frac{M(<r')}{r'^2}dr'$, we assume that the halo is truncated at $r_{\rm vir}$. Following this integration scheme, unbound particles are removed iteratively where we integrate Eq. 6.6 along a list of radially ordered particles. In the same way, ϕ_0 has to be re-evaluated for every new iteration. If the velocity of a particle is higher than the escape velocity, the

particle is assumed to be unbound and is therefore removed from the halo being considered. This pruning is halted when a given halo holds fewer than a fixed minimum number of particles or when no more particles need to be removed. The (bound) particle lists will be then used to calculate canonical properties of haloes like the density profile, rotational curve, mass, shape, etc.

5. The process finishes when it verifies that the radial density profile of the haloes is consistent with the functional form proposed by Navarro, Frenk & White (NFW; Navarro et al., 1997) in the range from twice the force resolution to r_{vir}:

$$\rho(r) = \frac{\rho_0}{(r/r_s)^\alpha [1 + (r/r_s)]^\beta} \ , \tag{6.12}$$

where ρ_0 is the normalization, α and β are the inner and outer slopes respectively, and r_s is the scale radius. The virial and the scale radius are related through the concentration parameter $C = r_{vir}/r_s$.

After this process, the final output for each halo includes a precise estimation of its main physical properties, the list of its bound particles, the location and velocity of its centre of mass, and the density and velocity radial profiles. Note that this method is completely general and easily applicable to any N-body code, assuming the density field is previously evaluated on a grid or set of nested grids.

6.3.1 Substructure

Substructures within haloes are usually defined as locally overdense self-bound particle groups identified within a larger parent halo.

In our analysis, the process of halo-finding outlined above can be performed independently at each level of refinement of the simulation. Then our halo finder can trace haloes-in-haloes in a natural way obtaining a hierarchy of nested haloes. Moreover, it is able to find several levels of substructure within substructure. This property allows us to take advantage of the high spatial resolution provided by the AMR scheme, identifying a wide variety of objects with very different masses and scales.

Still, due to this procedure and to the nature of the AMR grid, this technique could mix real substructures and overlapping haloes. In order to deal with possible misidentifications of subhaloes, we need to implement an extra mechanism.

Let us consider two haloes from two different but consecutive refinement levels, h_1 (lower level and, hence, lower resolution) and h_2 (upper level and, therefore, higher spatial resolution), with masses m_1 and m_2, radii r_1 and r_2, and the velocity of the centre of mass equal to v_{cm1} and v_{cm2}, respectively. In our method, these haloes are considered as host halo (lower level) and subhalo (upper level), respectively, if they satisfy the conditions

1. $\kappa = min(m_1, m_2)/max(m_1, m_2) \leq 0.2$
2. $distance(h_1, h_2) < 1.2\, r_1$

3. h_2 gravitationally bound to h_1.

Whilst the first condition ensures that the halo in the lower level (the biggest one) has a reasonable mass to host the halo in the upper level, the second condition checks if the smaller halo is placed within the radius of the biggest one or at least in its surroundings. The last condition is essential to guarantee that the subhalo is gravitationally bound to its host and therefore define the system halo-subhalo.

On the other hand, given the structure of nested grids generated by the AMR scheme, it is possible that sometimes the same halo would be identified more than once in different levels with centres slightly shifted in position. To capture these duplicates, a similar criterion to that used for the substructures is used, but now with these conditions:

1. $\kappa = min(m_1, m_2)/max(m_1, m_2)$>0.3

2. $distance(h_1, h_2) < min(r_1, r_2)$

3. $\mid v_{cm1} - v_{cm2} \mid /min(\mid v_{cm1} \mid, \mid v_{cm2} \mid) \leq 1.$

The set of these three conditions checks if two considered haloes have similar masses, positions and velocities of their centres of mass. If two haloes satisfy these conditions, they are a duplicate identification of the same halo, and then the halo from the upper level is considered as a misidentification of the other halo and is dropped out of the list.

At this point, substructures are defined only on the different levels of the grid. These levels have been defined and established by the assumed refining criteria which can be fixed by the evolution, when the outputs are directly imported from a code like MASCLET, or by any other criteria, like the number of particles per cell, when ASOHF works as a stand-alone code. Thus, ASOHF is able to find substructures and assign masses to them with a good accuracy throughout most of the host halo and is only limited by the existence of refinements in the computational grid.

Once the code has acted on the different levels of resolution of the considered grid, it obtains a single halo sample classifying all the haloes in three categories according to their nature: single haloes (with or without significant substructures), subhaloes (belonging to single haloes) and poor haloes (in our method these are haloes with less than a fixed number of dark matter particles, e.g. 50, or haloes that are a misidentification of other haloes). Thus, it is possible to obtain a complete sample of objects with very different masses and scales, ranging from the biggest haloes down to the minimum scales imposed by the resolution of the analysed simulations.

One of the main advantages of our method is that the hierarchy of nested grids used by the AMR cosmological simulations is built following the density peaks, and therefore these grids are already suitably adjusted to track the dark matter haloes. Last but not least, the use of AMR grids implies that we need no longer to define a linking length.

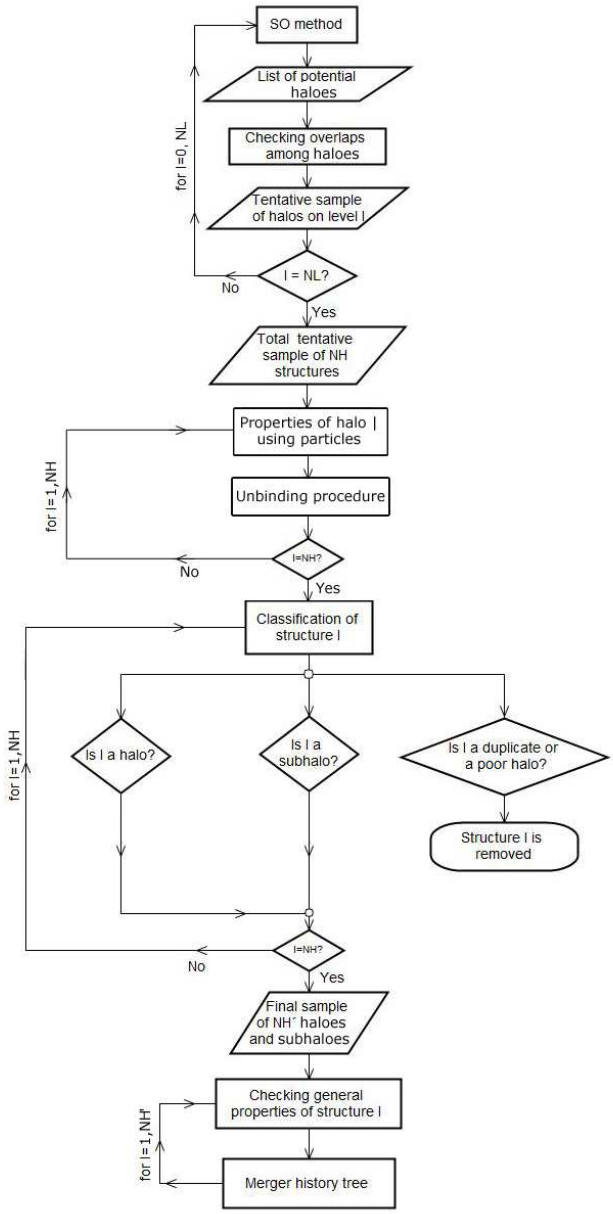

Figure 6.1: Flowchart for ASOHF. In this diagram, NL stands for the total number of analysed AMR grid levels. NH and NH' represent the total number of tentative and final found haloes, respectively.

6.3.2 Merger tree

Dark matter haloes and their mass assembly histories are essential pieces of any non-linear structure formation theory based on the ΛCDM model. Yet the construction of a merger tree from the outputs of an N-body simulation is not a trivial matter. We included in the halo finder programme a routine that is able to obtain the evolution history of each one of the found haloes. The method of progenitor identification is based on the comparison of lists of particles belonging to the haloes at different moments both backwards and forwards in time, i.e., it tracks the history of all dark matter particles belonging to a given halo at a given epoch. This procedure is repeated backwards in time until the first progenitor of the considered halo is reached. This mechanism allows us not only to know all progenitors of each halo, but also the amount of mass received from each one of its ancestors.

This mechanism can be applied to build the merging history tree of either the haloes or the subhaloes of the simulation. This procedure is very useful when we are interested in an exhaustive analysis of all the linking relations among the haloes, for example, when we want to analyse mergers or collisions between two or more haloes, or when we are interested in following the history of individual haloes as well as different processes of halo disruption. However, sometimes we are only interested in the main branch of the merger tree of each halo or, in other words, in a "simplified" merger tree. In order to have a quick estimate of the history of the main branch we included a reduced merger tree routine in the halo finder which, instead of following all particles of the haloes, looks only for the closest particle to the centre of each halo. This particle, which is supposed to be the most bound particle in the halo, is followed backwards in time until the first progenitor of the considered halo is found. With this method, each parent halo is allowed to have only one descendant.

The ASOHF method is summarized in Fig. 6.1, where a flowchart of the main process is shown.

6.3.3 Halo shapes

In the ASOHF code the shape of haloes is evaluated by approximating their mass distribution by a triaxial ellipsoid. The axes of inertia of the different haloes and subhaloes are evaluated from the tensor of inertia (e.g., Cole & Lacey, 1996; Shaw et al., 2006):

$$I_{\alpha\beta} = \frac{1}{N_p} \sum_{i=1}^{N_p} r_{i,\alpha} r_{i,\beta}, \tag{6.13}$$

where the positions r_i are given with respect to the centre of mass and the summation is over all particles in the halo (N_p). The axes of the ellipsoid can be determined from the eigenvalues λ_i of the inertia tensor as $a = \sqrt{\lambda_1}$, $b = \sqrt{\lambda_2}$, $c = \sqrt{\lambda_3}$, where $a \geq b \geq c$. Haloes can be classified in terms of their axis ratios by defining their degree of sphericity s, prolateness q, and oblateness p as

$$s = \frac{c}{a};\;\; p = \frac{c}{b};\;\; q = \frac{b}{a}. \tag{6.14}$$

An additional measure for the shape of the ellipsoid is the triaxiality parameter (Franx et al., 1991):

$$T = \frac{a^2 - b^2}{a^2 - c^2}. \tag{6.15}$$

An ellipsoid is considered oblate if $0 < T < 1/3$, triaxial with $1/3 < T < 2/3$, and prolate if $2/3 < T < 1$.

6.4 Testing the halo finder

Before using the ASOHF finder in real cosmological applications, we have to be sure that it provides accurate and credible results. In order to validate and assess the robustness of our method, we developed a set of tests that will allow us to quantify the uncertainty of the halo finder algorithm and to check the properties of the haloes found with it.

In these tests we build mock distributions of dark matter particles, made by hand, resembling real outputs of cosmological simulations. Therefore, we have perfectly known distributions of dark matter particles forming a given number of cosmological structures with physical parameters completely known. Once these distributions are built, we apply the halo finder and compare the results obtained with the ones originally adopted to create the mock distributions by hand.

The different numerical implementations presented in this Section were performed assuming the following cosmological parameters: matter density parameter, $\Omega_m = 0.25$; cosmological constant, $\Omega_\Lambda = \Lambda/3H_o^2 = 0.75$; baryon density parameter, $\Omega_b = 0.045$; reduced Hubble constant, $h = H_o/100km\,s^{-1}\,Mpc^{-1} = 0.73$; power spectrum index, $n_s = 1$; and power spectrum normalization, $\sigma_8 = 0.8$.

The set of tests was designed to help us check different aspects of interest in cosmological simulations: (i) test 1 and test 2 are focussed in looking for and characterizing single haloes and subhaloes, respectively, (ii) test 3 builds the merger trees of haloes, and (iii) test 4 analyses big samples of haloes.

All cases considered in this Section were placed in a comoving volume of $100\,h^{-1}$ Mpc on a side. The computational box has been discretised with 256^3 cubical cells. All our modelled haloes will be spherical, with a given dark matter density profile, mass, and radius. From now on, these artificial or modelled haloes will be called template haloes.

Depending on the test we are analysing, we need to define the number of template haloes we want to study, the number of time outputs (different redshifts we look at), as well as the total number of dark matter particles to be used. The total number of particles must be conserved during the whole evolution to guarantee mass conservation, and it must be chosen as a compromise between having a good resolution in mass for each halo and the computational cost. In the particular implementation of all tests presented in this Section we assumed, for the sake of simplicity, equal mass dark matter particles with masses $m_p \simeq 5.0{\times}10^9\,M_\odot$.

Halo	x (Mpc)	y (Mpc)	z (Mpc)	M_{vir} ($10^{14}\,M_\odot$)	r_{vir} (Mpc)	C	α	β	N_{DM}	$level$
H1	0.0	0.0	0.0	20.8	2.07	6.12 (6.25)	0.98	2.06	400000	0
H2	-10.0	-10.0	-10.0	5.19	1.30	6.92 (7.01)	0.97	2.04	100000	0
H3	25.0	25.0	25.0	1.29	0.82	7.88 (7.87)	1.006	1.99	25000	1
H4	10.0	10.0	10.0	0.78	0.69	8.36 (8.22)	0.992	1.97	15000	2

Table 6.1: Mean features of the generated haloes at $z = 0$ in test 1. Column 1 contains the halo name; Cols. 2, 3, and 4 stand for the x, y, and z coordinates respectively of the centre of mass of each halo in units of Mpc; Col. 5 shows the total mass within the virial radius in units of $10^{14}\,M_\odot$; Col. 6 the virial radius in units of Mpc; Col. 7 the concentration given by the fitting and between parenthesis the concentration of the input density profile; Col. 8 the density profile inner slope (α) given by the fitting; Col. 9 the density profile outer slope (β) of the fitting; Col. 10 the number of dark matter particles within each halo; Col. 11 the AMR level on which the halo is located.

6.4.1 Test 1: Looking for single haloes

The first test presented is designed to check the ability of the halo finder to look for single haloes and compute their main physical properties at a given redshift: position, mass, and radius. To achieve this we generate an artificial sample of haloes with different numbers of dark matter particles, and with positions, virial radii, and virial masses fixed by hand. Then the halo finder is applied to this mock universe to verify whether the detected haloes agree with those previously made by hand.

Let us describe the method to generate these artificial haloes. Assuming some general features (cosmological parameters, number of time steps, number of desired haloes and total number of particles), the properties of the haloes that populate each time step are made by hand: the number of dark matter particles within each halo (and hence, their masses) and the coordinates of their centres. With this information and the cosmological parameters, the average density corresponding to a given epoch as well as the virial radius of the haloes are computed from Eq. 6.2. Once the main physical properties of the haloes have been defined, each halo is created by a random distribution of dark matter particles – using the rejection sampling method (von Neumann, 1951) –, in a way that its density profile is consistent with a NFW profile (Navarro et al., 1997).

In this subsection we present a case characterized by the usual cosmological parameters and with $\sim 10^5$ dark matter particles in a unique time step corresponding to $z = 0$. For this test we generated four dark matter haloes with density profiles compatible with NFW, in the way explained before. The main properties of these mock haloes are summarized in Table 6.1.

The ASOHF halo finder was applied to this mock simulation. The mean relative errors found in the computation of the positions and radii are of the order of 0.1%. The masses are perfectly recovered because all particles forming the halo are identified. Note that although the results seem excellent, they correspond to an extremely idealised test.

In Fig. 6.2 we plot the radial density profiles used as input to generate – using the rejection method – the haloes (continuous line) and the obtained profiles

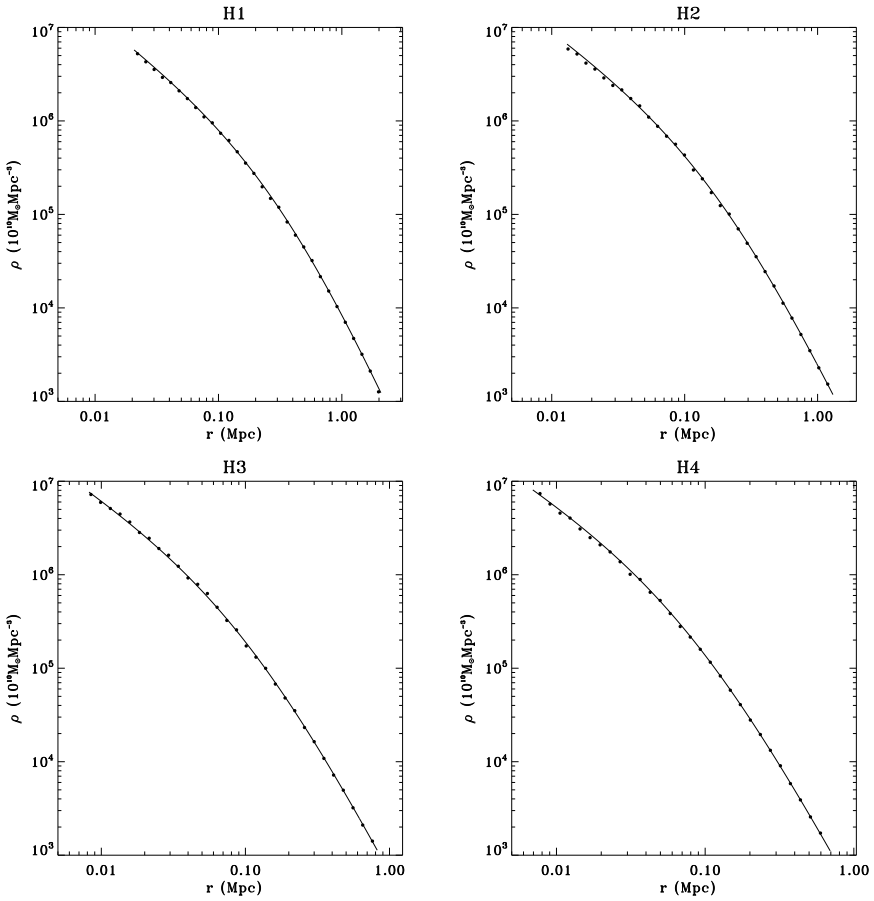

Figure 6.2: Radial dark matter density profiles for the four generated haloes compiled in Table 6.1 as a function of the radius at $z = 0$ (test 1). Continuous lines stand for the input profiles of the mock haloes, whilst points represent the profiles obtained by the halo finder.

(dots). These last profiles were computed by averaging the dark matter density in spherical shells of a fixed logarithmic width.

We fitted a NFW density profile to each one of the obtained profiles. The concentration, inner and outer slopes are shown in Table 6.1, respectively. In Col. 7 of this Table, we present the concentration obtained from the fitting together with the concentration of the density profile used as input (between parenthesis). For the inner (outer) slope of the density profile that we denoted by α (β), the fitted value must be compared with 1.0 (2.0), which corresponds to the value adopted in the input profile.

We checked that the errors encountered for the fitted profiles are mostly caused by the rejection sampling method. In this line we tested that the sampling of an input density profile with the rejection method produces particle distributions that trace the underlying density profile with a precision of a few per cent. Therefore, when the halo finder finds a halo and obtains its density profile, there is also a small error when compared with the input density profile. But it must be kept in mind that this error does not arise from the halo finder algorithm itself but from the way in which this particular test has been set up.

Although this test is very simple, because it only considers four haloes in a single time step, it provides us with a powerful tool to verify the behaviour of our finder in a very basic situation. We checked many other configurations (some of them really unrealistic) with similar results. Due to its clarity and simplicity we have chosen this one to demonstrate our objective.

6.4.2 Test 2: Looking for subhaloes

In this Section we present a simple test that was designed to check the ability of ASOHF to deal with substructures.

Following the idea of test 1, we generated by hand a simple distribution of haloes placed in different levels of resolution of a very basic AMR grid similar to that of the MASCLET code. For the sake of simplicity, only three levels of refinement (the ground grid and two upper levels) were considered. The hierarchy of structures and substructures generated for this test are distributed according to these levels.

Among all configurations that we tried for this test, we chose because of its clarity a simple one in which four structures are considered: a big dark matter halo in the coarse level hosting two subhaloes where at the same time one of these subhaloes hosts a smaller subhalo, which is a sub-subhalo of the big one.

Figure 6.3 shows the configuration analysed in this test. A visual inspection of this plot shows that the halo finder also works properly when dealing with substructures located in different levels of an AMR grid.

Additionally, the mean relative errors given by ASOHF in the estimation of the main properties of the generated structures are of the order of 3%, 0.1% and 1% for the mass, position, and radius, respectively. This value together with a visual inspection of Fig. 6.3 is an excellent indicator of the good performance of ASOHF when working with structures that contain different substructures, at least in a simple configuration like the one considered here.

Because this configuration is very basic, we check this situation in Section 6.5

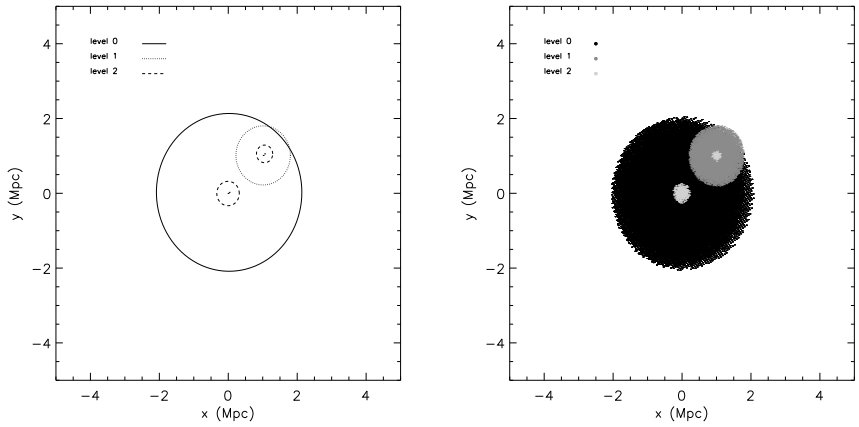

Figure 6.3: Mock distribution of a halo with three substructures: two subhaloes and one sub-subhalo (test 2). The left panel shows the 2-D projection of the structures found by ASOHF. Circles represent the radii of the different structures, while the different line types stand for the different refinement levels in which the haloes have been found. The right panel shows the known distribution of dark matter particles in this test. Different colours stand for the level to which the particles belong.

for a proper cosmological simulation and compare the results obtained by ASOHF with those obtained by other well-known halo finders.

6.4.3 Test 3: Testing the merger tree

Once we checked that the ASOHF finder works properly when it looks for single haloes and subhaloes, we checked how well it computes the merger tree for each.

In this Section we consider several configurations characterized by the same parameters as in the previous ones, but with more than one time step. Now the idea is to generate a given number of haloes, in the simple way explained before, but forcing different time evolutions of these haloes.

We are interested in studying the most common events in the evolution of dark matter haloes: (i) relaxed or isolated evolution, i.e., without important interactions or mergers with other haloes (case I), (ii) ruptures or disruptions of a single halo into two or more smaller haloes owing mainly to interactions with the environment or with other haloes (case II), and (iii) mergers between two or more haloes (case III). To do this we chose four haloes at a given redshift which are those compiled in Table 6.1, and studied their evolution in the three different cases that have into account in a simple way the most common events explained before. Then, ASOHF is applied to these artificial evolutions to compare the obtained merger trees with the generated ones.

Again, for the sake of simplicity and brevity, a reduced number of haloes will be considered, but note that more complicated configurations were studied and can be easily implemented.

Figure 6.4 shows the merger trees obtained by ASOHF in the different cases considered in this Section. The top panel of Fig. 6.4 shows the complete merger tree obtained for the four haloes studied in each of the three cases presented here. In the bottom panel of the same figure, the same cases are represented but following only the closest particle to the centre of each halo (reduced merger tree).

The line segments joining the circles in Fig. 6.4 are a relevant feature of the plot because they indicate that the halo at the earlier time is considered to merge into (or to be identical to) the halo at the later time. Moreover, in the upper panel the different line types represent the percentage of mass that goes from one halo to another. Thus, a halo at later time connected with a halo at earlier time by a dash-dotted line means that up to 25% of its total mass comes from that halo at earlier time. The same idea applies to the other line types.

The horizontal axis is designed to separate the haloes according to their future merging activity. It does not directly indicate space positions, although there should be some correlation between how close two haloes are in the plot and how close they are in space (because haloes need to be close to merge later on). The vertical axis shows the redshift of each time step in the simulation. The size of each circle indicates the virial mass of each halo normalized to its final mass at the last iteration. Because the iterations go in descending order, the last iteration corresponds to the lowest redshift.

The different cases analysed in this Section and their representation in Fig. 6.4 are discussed in detail in the subsections below.

6.4.3.1 Case I

In this first case, we study the most trivial situation. Only two time steps corresponding to $z \sim 0.5$ and $z \sim 0.3$ are considered. The objective is that the four haloes generated at $z \sim 0.5$ would be exactly the same as those at $z \sim 0.3$. The selection of the redshifts is made in order to obtain a fast evolution of the haloes, but it is possible to make it for time steps much more realistic and separated in time. In any case, this selection is not relevant to achieve our objective, which is to check the performance of the halo finder computing the merger tree of a given halo, i.e., following the particles that belong to a halo at a given epoch through the evolution.

The haloes at different epochs are generated in the way explained above. In this particular case, we force that the four considered haloes at both epochs would be identical, i.e., with the same particles in each one and with the same radius and position of the centre.

In order to be as clear as possible when talking about haloes at different epochs, we will use the notation h_{ij}, where i stands for the iteration number (iterations in descendant order and then corresponding the iteration or time step 1 to the lowest redshift) and j for the halo number in the iteration i, respectively.

According to this notation, the generated relations between the haloes in this case are

- $h_{21} \Longrightarrow h_{11}[100\%]$
- $h_{22} \Longrightarrow h_{12}[100\%]$

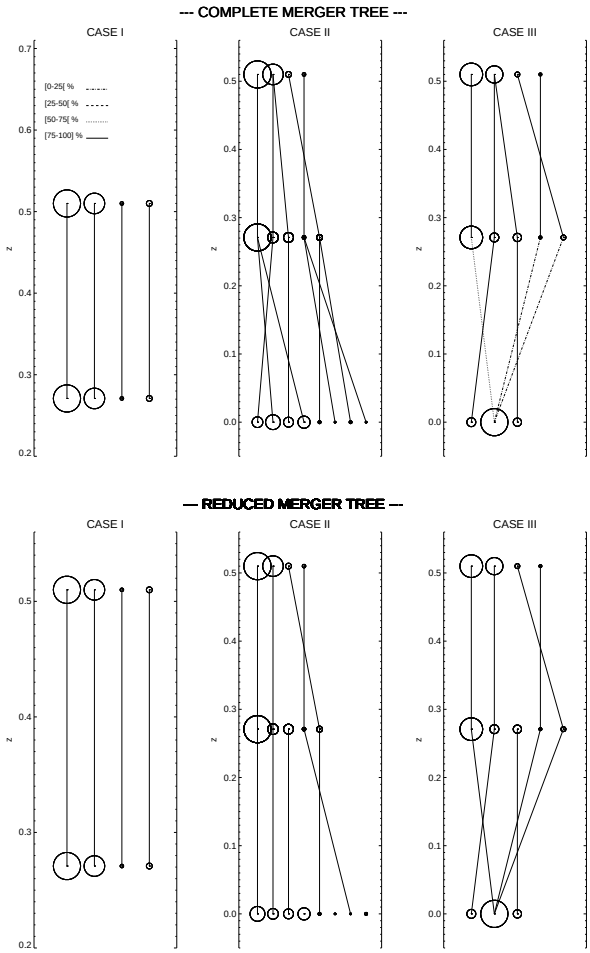

Figure 6.4: Merger trees for several haloes in the three different cases analysed in Section 6.4.3 (test 3). Left, central, and right panels stand for case I, II, and III, respectively. The top panels represent the results obtained following all dark matter particles within each halo (complete merger tree), whereas the bottom panels stand for the results obtained following only the closest particle to the centre of each halo (reduced merger tree). Haloes are represented by circles whose sizes are normalized to the final mass at $z = 0$. The different line types connecting haloes at different times in the upper plots indicate the amount of mass transferred from the progenitors to their descendants.

- $h_{23} \Longrightarrow h_{13}[100\%]$
- $h_{24} \Longrightarrow h_{14}[100\%]$.

These connections tell us we are working only with two time steps (2 corresponding to $z \sim 0.5$ and 1 to $z \sim 0.3$, respectively) and each one of these epochs has four haloes (j runs from 1 to 4 in both time steps). In addition, the number between square brackets informs us about the percentage of the mass of each halo that it obtains from its progenitor. For instance, the first relation tells us that the 100% of the mass of the halo number one in the last iteration (h_{11}) comes totally (100%) from the halo number one in the previous time step (h_{21}).

We applied the halo finder to this artificial evolution and constructed the merger tree of the selected haloes tracking all dark matter particles for a given halo backwards in time. For each halo in this case, two merger trees, the complete and the reduced one, have been built. The left panels of Fig. 6.4 show the obtained results. The upper-left plot of this figure shows the complete merger tree for the considered haloes, whereas the lower-left plot represents the reduced merger tree for the same haloes.

According to these plots it is evident that for case I the halo finder tracks the correct history for all considered haloes.

Additionally, the connection lines linking the haloes at different redshifts in the complete merger tree inform us about the percentage of mass that each younger halo receives from its progenitors. In this particular case, this percentage is in all cases greater than 75%, in perfect agreement with the expected results (100%). More precisely, the obtained results are

- $h_{21} \Longrightarrow h_{11}[99.97\%]$
- $h_{22} \Longrightarrow h_{12}[99.98\%]$
- $h_{23} \Longrightarrow h_{13}[99.99\%]$
- $h_{24} \Longrightarrow h_{14}[99.99\%]$.

Although in this example the obtained percentages are very accurate with regard to the expected ones, we should point out that they are not always exact. This is because although the particles are forced to be the same and belong to a given halo, they are distributed randomly. Thus, the haloes are not exactly found within the same boundaries by the finder for different redshifts in this test and then some particles are not taken into account.

6.4.3.2 Case II

In this case we are interested in checking the capabilities of the halo finder when some haloes suffer one or several disruptions during their evolution, when they lose mass and reduce their size. This process operates at two regimes for different reasons. This is quite common in very small size haloes. The reason is that these haloes are not really gravitationally well bound and can easily be disrupted by interactions with environment or with other haloes. For larger haloes, those mass losses are smaller and they are usually associated with tidal interactions.

To study this case we started at $z \sim 0.5$ with the four haloes summarized in Table 6.1. Now, three time steps of the haloes evolution corresponding to $z \sim 0.5$, $z \sim 0.3$ and $z = 0$ are considered. The results of this situation are shown in the middle panels (top and bottom) of Fig. 6.4.

Here the generated evolutions can be summarized in the following relations. In a first step, the connections between the haloes of the third ($z \sim 0.5$) and the second ($z \sim 0.3$) iterations are

- $h_{31} \Longrightarrow h_{21}[100\%]$
- $h_{32} \Longrightarrow h_{22}[100\%], h_{23}[100\%]$
- $h_{33} \Longrightarrow h_{24}[100\%]$
- $h_{34} \Longrightarrow h_{25}[100\%]$.

On the other hand, the links between the haloes generated in the second iteration ($z \sim 0.3$) with those in the first one ($z = 0$) are

- $h_{21} \Longrightarrow h_{12}[100\%], h_{14}[100\%]$
- $h_{22} \Longrightarrow h_{11}[100\%]$
- $h_{23} \Longrightarrow h_{13}[100\%]$
- $h_{24} \Longrightarrow h_{16}[100\%], h_{18}[100\%]$
- $h_{25} \Longrightarrow h_{15}[100\%], h_{17}[100\%]$.

As a result of the whole evolution there are eight haloes instead of the first four, which were generated in the same manner as in the previous case, but which were forced to share a certain number of particles with their ancestors, which property is the key to build their evolution history.

After building these artificial evolutions, ASOHF was applied to this mock universe to obtain the merger trees of the involved haloes.

As we can see in the upper-middle plot (case II) of Fig. 6.4, the halo finder again provides very accurate results, in perfect agreement with those exposed before. In all cases the obtained percentages are between 99.9% and 100%. Again, the value of the percentages can be explained if we take into account that each halo has been populated with particles randomly placed. Then, the particles positions are not always the same and small deviations are expected.

If we compare the upper-middle plot of Fig. 6.4 (complete merger tree) with the lower-middle plot (reduced merger tree), the results completely agree but in the lower plot each halo is only allowed to have one descendant at maximum.

6.4.3.3 Case III

Here the response of the halo finder in a merger between two or more haloes is checked.

To analyse this, we started again with the same haloes and time steps as before. Now, the different evolutions can be summarized with the following links. In a first step the connections between the haloes of the third ($z \sim 0.5$) and the second ($z \sim 0.3$) iterations are (the same as in the previous case)

- $h_{31} \Longrightarrow h_{21}[100\%]$
- $h_{32} \Longrightarrow h_{22}[100\%], h_{23}[100\%]$
- $h_{33} \Longrightarrow h_{24}[100\%]$
- $h_{34} \Longrightarrow h_{25}[100\%]$.

But now the links between the haloes of the second ($z \sim 0.3$) and first ($z = 0$) iterations are

- $h_{21} + h_{24} + h_{25} \Longrightarrow h_{12}[74.49\% + 9.48\% + 16.03\%]$
- $h_{22} \Longrightarrow h_{11}[100\%]$
- $h_{23} \Longrightarrow h_{13}[100\%]$.

In the end three haloes are obtained as a result of the different processes that happened during their evolution.

From the right panels of Fig. 6.4 (top and bottom plots), we can deduce that despite the triple merger that has taken place in the last time step, the halo finder provides very accurate results. Indeed, the results obtained for this merger event are

- $h_{21} + h_{24} + h_{25} \Longrightarrow h_{12}[74.45\% + 9.45\% + 16.08\%]$,

where the percentages perfectly agree with the expected ones.

6.4.4 Test 4: Analysing a sample of haloes

The analysis of big samples of haloes is crucial in cosmological applications. Therefore, once we checked the halo finder works correctly looking for single haloes and constructing their merger trees, we should check what its response is when working with a large sample of haloes and computing all their properties. Once this sample of haloes is built, an academic mass function, i.e., the mass distribution of all the generated haloes, is computed.

For the sake of simplicity, only one time step corresponding to $z = 0$ was considered. Then a sample of 100 haloes with masses randomly distributed between $1.0 \times 10^{13}\, M_\odot$ and $1.0 \times 10^{15}\, M_\odot$, was generated. The position of the centre and the radius of each halo are obtained randomly, whereas the number of particles belonging to each one of them is derived from their masses.

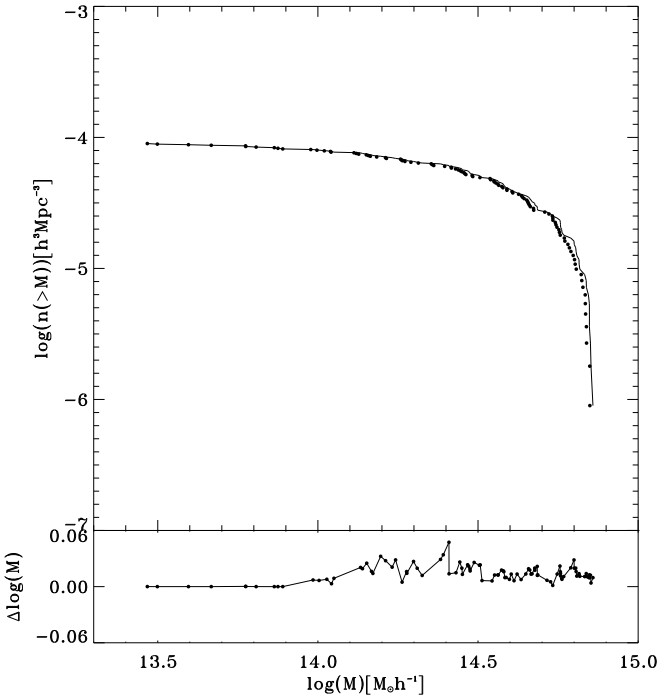

Figure 6.5: Top panel: academic mass function corresponding to the generated sample of 100 haloes for test 4. Dots represent the mass function obtained by ASOHF, whereas the continuous line corresponds to the function generated by hand. Bottom panel: relative error or difference in mass between the two distributions shown in the upper plot.

Once this mock universe was generated, the ASOHF finder was applied. Then the academic mass function of the well-known distribution of haloes is compared with the mass function of the sample of haloes obtained by ASOHF.

The results obtained in this case are shown in Fig. 6.5, in which the number of objects of a given mass is plotted as a function of the mass. This plot shows the theoretical or academic mass function (continuous line) and the one obtained by ASOHF (filled dots). As we can see, these two distributions are almost completely superposed. As a proof of the precision of the finder we can compare the masses of the most and less massive haloes of the sample obtained by the two methods. Thus, the most massive halo found by the finder has a mass of $9.8622 \times 10^{14}\, M_{\odot}$, whereas this halo was supposed to have a mass of $9.8623 \times 10^{14}\, M_{\odot}$. The same occurs for the less massive halo, which was found by the finder to have a mass of $1.48 \times 10^{13}\, M_{\odot}$, whereas it was supposed to have a mass of $1.49 \times 10^{13}\, M_{\odot}$. In addition, as we can see in the bottom panel of Fig. 6.5, the maximum value of the relative error in mass between the theoretical and the obtained mass functions is $\sim 5\%$.

6.5 Comparison with other halo finders

In this Section we compare the results of ASOHF with two other halo-finding mechanisms, namely AFoF (van Kampen, 1995) and AHF (Knollmann & Knebe, 2009). We applied these three halo finders to a cosmological simulation carried out with the cosmological code MASCLET. The main properties of this simulation are explained below.

For the AFoF run, a linking length of 0.16 times the mean DM particle separation was used, yielding an overdensity at the outer radius comparable to the virial overdensity used in the ASOHF run. This linking length is obtained when scaling the standard linking length of 0.2 by $(\Delta_c/\Omega)^{-1/3}$ according to the adopted cosmology (Eke et al., 1996).

For the run with AHF, we used a value of 5 for the parameters with regard to the refinement criterion on the domain grid (DomRef) and on the refined grid (RefRef), respectively. To understand the role of these parameters we need to explain briefly how AHF operates. Once the user has provided the particle distribution, the first step in AHF consists in covering the whole simulation box with a regular grid of a user-supplied size. In each cell the particle density is calculated by means of a triangular shaped cloud (TSC) weighting scheme (Hockney & Eastwood, 1988). If the particle density exceeds a given threshold (the refinement criterion on the domain grid, DomRef), the cell is refined and covered with a finer grid with half the cell size. On the finer grid (where it exists), the particle density is recalculated in every cell and then each cell exceeding another given threshold (the refinement criterion on refined grids, RefRef) is refined again. This is repeated until a grid is reached on which no further cell needs to be refined. Following this procedure yields a grid hierarchy constructed in a way that it traces the density field and can then be used to find haloes and subhaloes in a similar way to that used by ASOHF.

In all the runs, an equal minimum number of dark matter particles per halo was considered. This number has been set to 50 particles per halo. In spite of this consideration, we expect some differences in the final results obtained with the different halo finders. The main explanation for these expected discrepancies has to do with the different techniques used by the three methods in the generation of the density field and hence in the definition of the haloes. However, general properties of the simulation should be well described by the three finders.

6.5.1 Simulation details

The simulation analysed in this Chapter was carried out with the cosmological code MASCLET (Quilis, 2004).

The numerical simulation was performed assuming a spatially flat ΛCDM cosmology with the following cosmological parameters: matter density parameter, $\Omega_m = 0.25$; cosmological constant, $\Omega_\Lambda = \Lambda/3H_o^2 = 0.75$; baryon density parameter, $\Omega_b = 0.045$; reduced Hubble constant, $h = H_o/100km\,s^{-1}\,Mpc^{-1} = 0.73$; power spectrum index, $n_s = 1$; and power spectrum normalization, $\sigma_8 = 0.8$. The initial conditions were set up at $z = 50$, using a CDM transfer function from Eisenstein & Hu (1998) for a cube of a comoving side length $47\,h^{-1}\,Mpc$. The

Halo Finder	N_{haloes} ($M > 10^{12}\,M_{\odot}h^{-1}$)	M_{min} ($10^{9}\,M_{\odot}h^{-1}$)	M_{max} ($10^{14}\,M_{\odot}h^{-1}$)
ASOHF	157	4.5	5.9
AFoF	130	7.3	6.4
AHF	181	4.9	5.9

Table 6.2: General results obtained by ASOHF, AFoF and AHF at $z = 0$. Column 2 stands for the number of detected haloes with masses $\geq 1.0 \times 10^{12}\,M_{\odot}h^{-1}$, whereas Cols. 3 and 4 represent the minimum and maximum masses of all the found haloes in units of 10^{9} and $10^{14}\,M_{\odot}h^{-1}$, respectively.

computational domain was discretised with 256^3 cubical cells.

This simulation uses a maximum of six levels of refinement, which gives a peak spatial resolution of $3\,h^{-1}\,kpc$. For the dark matter two particles species were considered to be the best mass resolution $\sim 4 \times 10^{7}\,h^{-1}\,M_{\odot}$, equivalent to distribute 256^3 particles in the whole box.

6.5.2 Halo mass function

Here we present the sample of haloes obtained from the cosmological simulation by the three halo finders used in the present study, that is, ASOHF, AFOF and AHF. Their main properties and differences are discussed.

The three halo finders obtained a relatively large sample of galaxy clusters and groups spanning an approximated range of masses from $1.0 \times 10^{9}\,M_{\odot}h^{-1}$ to $2.0 \times 10^{14}\,M_{\odot}h^{-1}$. The total number of structures identified by ASOHF, AFoF, and AHF has been 1339, 7448, and 1712, respectively. Although the numbers and masses of the detected haloes are roughly consistent, they are, as expected, slightly different among them. These results are more similar between ASOHF and AHF, whereas AFoF identifies more smaller haloes.

To analyse the simulation mass function, we restricted ourselves to study the best-resolved haloes, that is those haloes with masses above $1.0 \times 10^{12}\,M_{\odot}h^{-1}$. The number of haloes with masses above this limit and the maximum and minimum masses (in all the sample) of the found haloes by the different halo finders are summarized in Table 6.2. The obtained results by the three finders, although very similar, are not exactly the same. This was expected because each halo finder uses different approximations and techniques. ASOHF uses the grid hierarchy generated by the cosmological simulation itself, whereas AHF has to construct a new set of grids with different criteria because only a list of particles is provided to them which is consequently not identical with that used by ASOHF.

In Fig. 6.6 we compare the mass functions at $z = 0$ of the simulation as obtained by the different halo finders in this study. We also present a comparison with the mass function proposed by Sheth & Tormen (1999) (ST).

The obtained mass functions show a considerable dispersion mainly in the lower limit of mass compared with the ST prediction. Note though that the theoretical mass function proposed by ST has been calibrated using an overdensity of $\Delta_c = 174$ (Tormen, 1998), whereas in our case this overdensity is ~ 374. The bottom panel of Fig. 6.6 displays the relative deviation of the mass functions

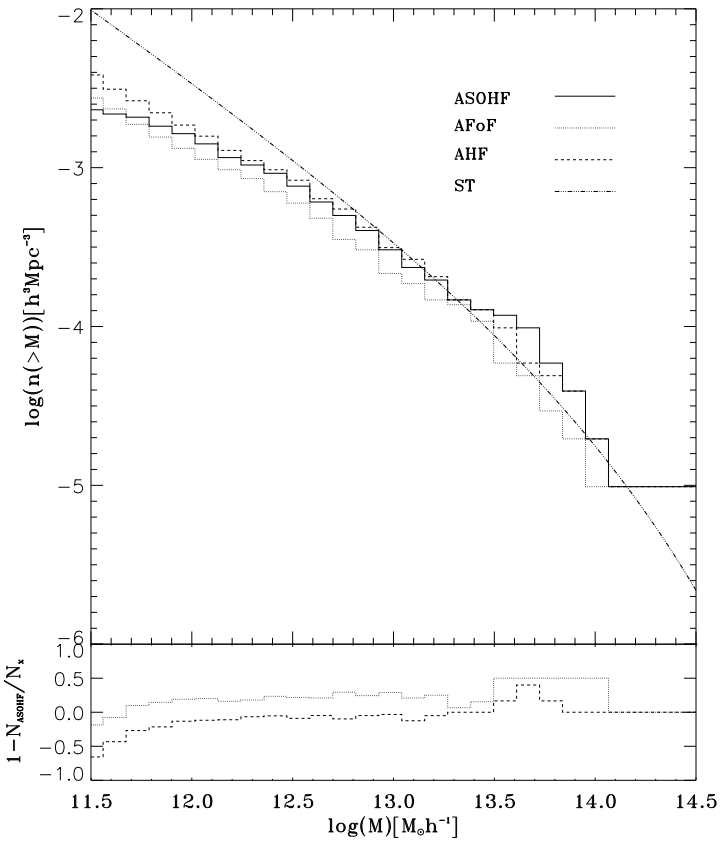

Figure 6.6: Top panel: comparison of the mass functions obtained by ASOHF, AHF and AFoF at $z = 0$. The mass function predicted by Sheth & Tormen (1999) is also shown. Bottom panel: relative difference in the number of haloes between AFoF and AHF compared to ASOHF.

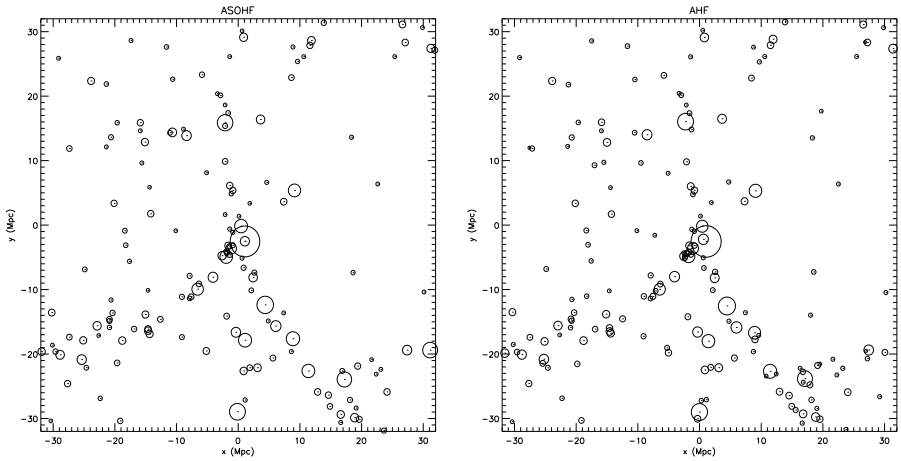

Figure 6.7: 2-D projection for haloes at $z = 0$. Only haloes with masses above $1.0 \times 10^{12}\, M_{\odot} h^{-1}$ are shown. Left panel stands for haloes and subhaloes found by ASOHF, whereas right panel corresponds to those found by AHF. The size of the different haloes is given by their virial radii.

obtained by AFoF and AHF with respect to the results produced by ASOHF. Hence, a positive deviation means that the ASOHF run found more haloes in the given bin than the halo finder it is compared with. Generally speaking, we find good agreement between the three mass functions, although ASOHF and AHF results exhibit a better resemblance, which is expected because the similarities of both methods.

Let us point out that the dispersion of the mass function when compared with the reference mass function (ST) is a well-known issue. We stress that is out of the scope of this work to discuss how representative the considered simulation is. Instead, we use this simulation to test whether the different halo finders produce similar results. In this sense, we emphasize that the three algorithms compared agree very well.

For the sake of completeness, we mention that the dispersion of the mass function is a complex topic that is abundantly discussed in the literature. A few examples, among many others, could be: (i) the work by Reed et al. (2007), where the authors study the dispersion of the mass function for several simulations depending on the redshift, (ii) the results of the GIMIC project (Crain et al., 2009), where an important dispersion in the mass function is shown depending on the considered region, and (iii) the dispersion of the mass function found by Yaryura et al. (2010) related with very large structures.

From now on, we restrict ourselves to analyse only the main differences between the AHF and the ASOHF codes, that is, between the "grid based on halo finders". The reason is that these methods are more directly comparable with each other. Still, given that we use AHF as a stand-alone halo finder, differences are expected.

To have a first order comparison of the spatial distribution of the haloes encountered by both codes, Fig. 6.7 shows the 2-D projection along the z axis of the

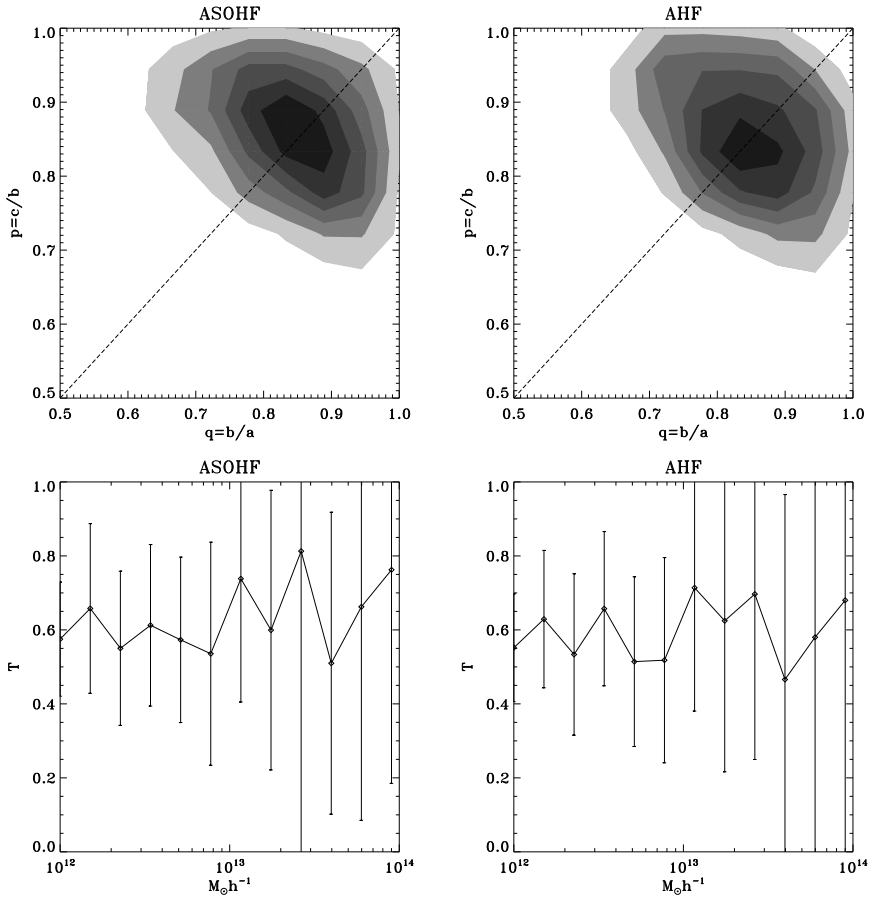

Figure 6.8: Distribution of the halo shapes at $z = 0$ as found by ASOHF (left panels) and AHF (right panels), respectively. Only haloes with masses above $1.0 \times 10^{12}\, M_{\odot} h^{-1}$ are taken into account. The top plots show the distribution of $p = c/b$ against $q = b/a$. The dashed line represents the division between oblate and prolate haloes. The shaded grid was computed by binning individual haloes to a two-dimensional grid. Six contour lines equally spaced are plotted to highlight the shape of the two-dimensional distributions. The bottom panels show the triaxiality parameter as a function of the halo masses. The error bars represent $\sqrt{N}$ uncertainties due to the number counts in the different mass bins.

simulated box of all haloes (and/or subhaloes) found by ASOHF and by AHF at $z = 0$. We only show those haloes or subhaloes with masses larger than $1.0 \times 10^{12}\, M_{\odot} h^{-1}$. Both panels are highly consistent. All relevant features of the halo distribution were caught with both methods, and therefore they seem perfectly comparable.

The main differences between both methods arise when the smallest structures found are taken into account. Whereas the biggest structures are perfectly recognized in both plots, the smallest represent the main source of disagreement. These discrepancies may have a variety of causes, of which the most important is that the finders make use of very different techniques to compute the dark matter density distributions. Both codes create their structures of nested grids according to different criteria. Therefore, a slight change in the number of grids, especially for the small objects, could alter the way in which these objects are resolved, making them detectable or not. Leaving this issue aside, both distributions are fully comparable.

6.5.3 Halo shapes

The shapes of haloes are described by the axes, $a \geq b \geq c$, of the ellipsoid derived from the inertia tensor, as described in Section 6.3.3. For the sake of completeness, we have compared the distribution of halo shapes obtained by ASOHF and AHF for haloes with masses above $1.0 \times 10^{12}\, M_{\odot} h^{-1}$. The obtained results are shown in Fig. 6.8. As we can deduce from these results, haloes are generally triaxial but with a large variation in shapes. Prolate objects have $p = 1$, oblate objects have $q = 1$, and spherical objects have $p = q = 1$.

Our results show that the haloes are mainly spherical but with a slight preference for prolateness over oblateness. This distribution qualitatively agrees with previous results (e.g., Frenk et al., 1988; Cole & Lacey, 1996; Bailin & Steinmetz, 2005).

Bottom panels of Fig. 6.8 show the triaxiallity parameter, T, of the haloes found by ASOHF (left plot) and AHF (right plot) as a function of halo masses. In this figure the x-axis was divided into 12 mass bins equally spaced in logarithmic scale, and the error bars represent $\sqrt{N}$ uncertainties due to the number counts. The general trends obtained from these plots agree with previous results (e.g., Warren et al., 1992; Shaw et al., 2006; Allgood et al., 2006). As it would be naively expected, more massive haloes tend to be less spherical and more prolate. In a hierarchical model of structure formation, more massive haloes form later, and have less time to relax and to form more spherical configurations. In addition, because haloes tend to be formed by matter collapsing along filaments, they generally lead to prolate rather than oblate structures. Because our halo sample is statistically small, the general trend obtained for the shape of the haloes must be taken with caution although it agrees with previous results. Nevertheless, even when the sample can be limited, results from ASOHF and AHF are completely consistent.

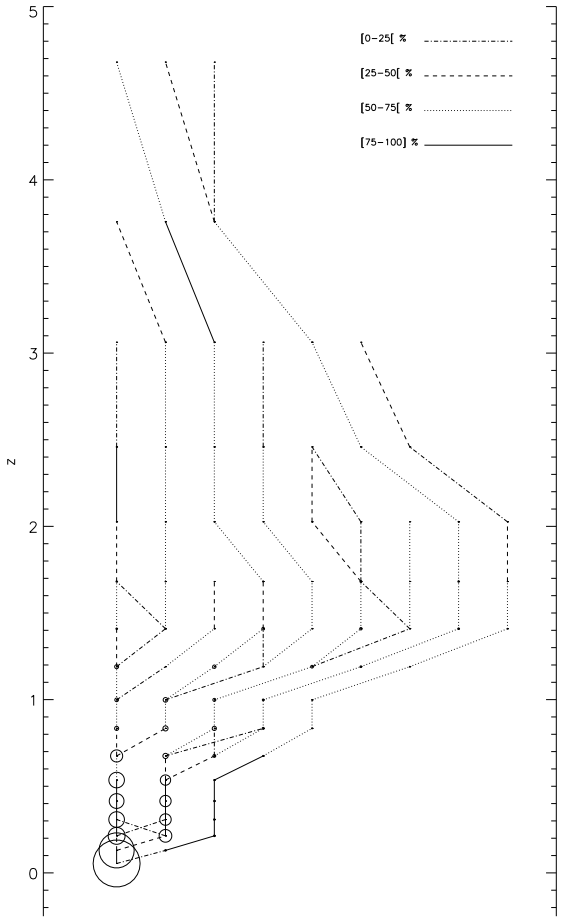

Figure 6.9: Merger tree of the analysed host halo. Cluster haloes are represented by circles whose sizes are normalized to the final mass at z = 0. Lines connecting haloes at different times indicate the amount of mass transferred from the progenitors to their descendants. Only the contribution of the most massive progenitors is displayed.

6.5.4 Subhaloes

One of the main features of the ASOHF finder is its capacity to deal with haloes and subhaloes. In this Section we compare the abundance and distribution of substructures given by ASOHF and AHF.

For the sake of comparison, we focus on the detailed analysis of the most massive halo in the cosmological simulation previously described. This halo has a virial mass of $\sim 8.0 \times 10^{14}\, M_{\odot}$ and a virial radius of ~ 2.4 Mpc. To illustrate the time evolution of the chosen halo, we constructed its merger tree by tracking all its particles backwards in time. In Fig. 6.9 we display the merging history of the halo. To facilitate the reading of this figure, we only show the mergers among the most massive haloes that contribute to build up the final halo at $z = 0$. Otherwise, the plot would be saturated by the amount of mergers due to small structures, which are not very relevant from the dynamical point of view, though. The merger tree starts at $z = 0$ and it plots all the most massive progenitors of the final halo in previous time-steps over several output times of the simulation. The total mass of each halo is represented by a circle, whose size is normalized to the mass of the final halo at $z = 0$. The meaning of the different line types remains the same as in Section 6.4.3 (Fig. 6.4), that is the amount of mass received by any of the progenitors. This kind of plot not only shows the merger history, but also the different interconnections over time. Although this halo is the most massive in the simulation, it is far from being virialized because, as we can see in Fig. 6.9, it has suffered several major mergers during its evolution, one of which happened very recently. This makes the process of the substructure analysis more challenging.

In Fig. 6.10 we present the analysis of this particular halo with its substructures as found by ASOHF (upper plots) and AHF (lower plots), respectively. The left column of the panel displays the 2-D projection of the halo with its subhaloes. The x and y axes show the coordinates in Mpc of the haloes within the computational box. The comparison of the haloes identified by both codes deserves some comments. The main halo is located at the same coordinates and with the same mass and size in both cases. There is also a clear correlation among the largest subhaloes in both subhalo samples in sizes and masses. However, there seem to be important differences in the smallest substructures. As we mentioned above, the explanation of this different performance detecting small structures is directly linked with the structure of nested grids built by the algorithms.

Subhalo mass functions have been widely studied in previous works (e.g., Ghigna et al., 2000; de Lucia et al., 2004; Gao et al., 2004; Giocoli et al., 2008; Knollmann & Knebe, 2009), leading to the conclusion that they can be described with a power law, $N_{sub}(> M) \propto M^{-\alpha}$, with a logarithmic slope α in the range from 0.7 to 0.9. We computed the subhalo mass function of the cosmological simulation used for the comparison of both halo finders. The results are shown in the panels of the right column in Fig. 6.10. These plots show the cumulative mass functions of the subhaloes for the considered main halo as obtained by ASOHF (top) and AHF (bottom). To facilitate the comparison with previous results, two lines corresponding to the power laws with values of α equal to -0.7 and -0.9 are plotted. The masses of subhaloes are normalized to the mass of the main halo. The error bars show $\sqrt{N}$ uncertainties due to the number counts.

From a statistical point of view, the comparison of both mass functions shows

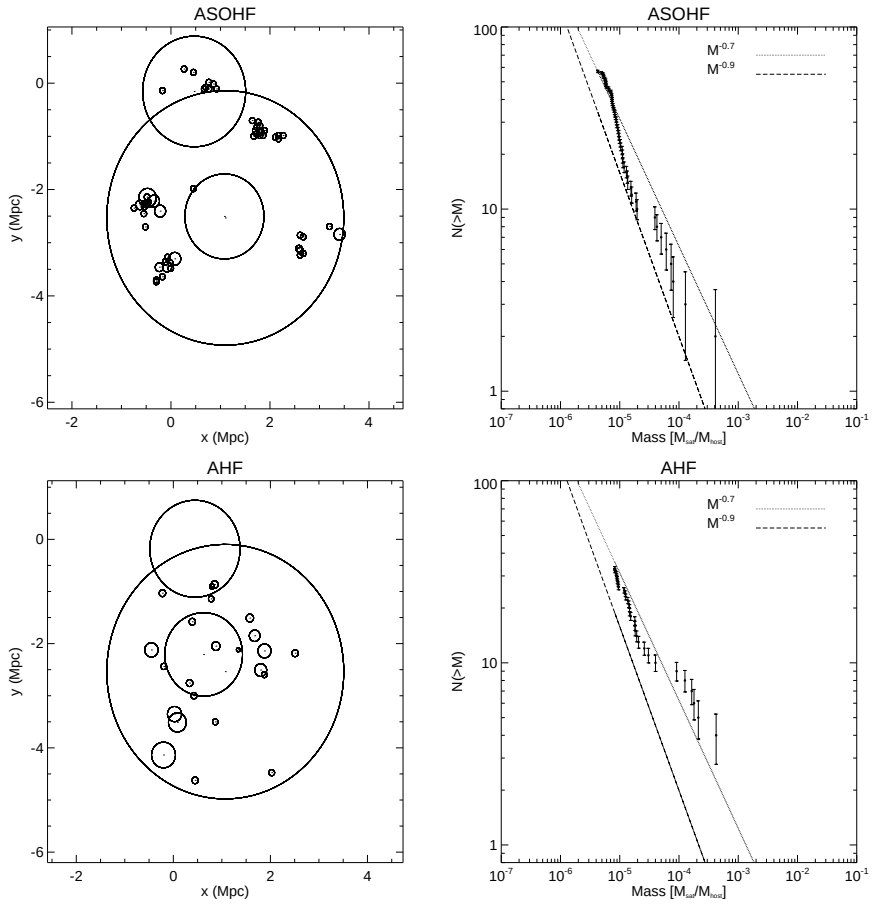

Figure 6.10: Analysis of the subhalo population of the most massive halo in our simulation. Left panels (top and bottom plots): subhalo population within the most massive host halo in our simulation as found by ASOHF and AHF. The size of the circles represents the virial radius of the different haloes. Right panels: cumulative subhalo mass function for the most massive halo in our simulation as found by ASOHF (upper plot) and AHF (lower plot). Two power law fits with slopes of -0.7 and -0.9 are also shown in these panels. Error bars show $\sqrt{N}$ uncertainties due to the number counts.

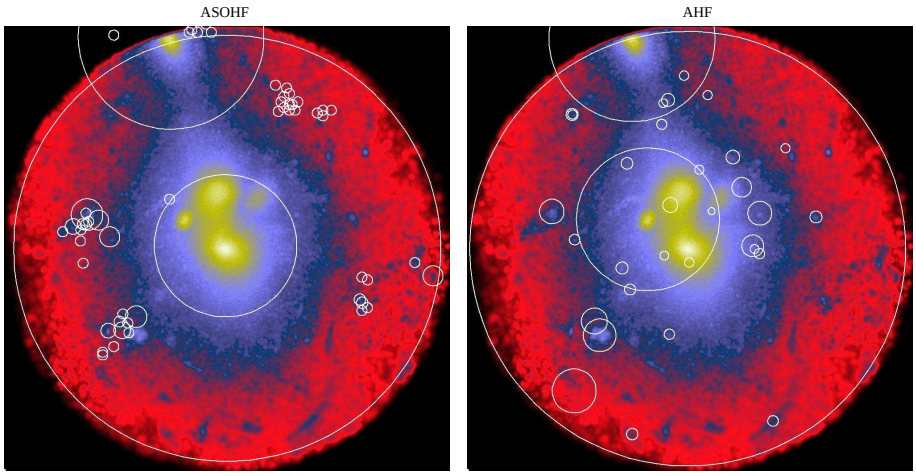

Figure 6.11: 2-D projection of the dark matter density field around the biggest halo in the simulation. The colour scale represents the logarithmic of the density field. Subhaloes found by ASOHF (left panel) and AHF (right panel) are superimposed being the white circles the radii of these haloes.

that both codes have similar capabilities when dealing with finding substructures. The fitting to a power law of the analysed data gives a slope of 0.9 for ASOHF and 0.7 for AHF. This would render the ASOHF and AHF mass functions completely consistent with previous results, because they are well fit between the two limiting power laws for substructure in haloes. Nevertheless, this conclusion must be taken with caution because, as we saw, a direct comparison of the smallest substructures is not straightforward.

We proceed to compare identified subhaloes with the real mass distribution in the main halo to deepen in the comparison of the encountered subhalo samples and assuming that a direct comparison between both methods is not always completely meaningful. Therefore, Fig. 6.11 shows the colour-coded dark matter column density in the main halo considered in this Section together with the detected subhaloes overplotted as circles with their radii normalized to the main halo radius. The left panel of the figure corresponds to the sample obtained by ASOHF, whereas the right panel displays subhaloes identified by AHF. As we previously discussed when analysing Fig. 6.10, most of the substructures are unambiguously identified by both codes and with very similar features (sizes and masses). However, the smallest subhaloes are not well identified either with ASOHF or AHF. Moreover, it is striking that some of these small substructures do not match not only between both halo finders, but more intriguing, with the real mass distribution.

6.6 Summary and conclusions

In the last years cosmological simulations have experienced an astonishing development, producing a huge amount of computational data. Intimately related to

the development of simulations, all kinds of analysis tools have arisen too. One of the most important analysis tools have become the halo finder algorithms, whose relevance is crucial when comparing simulations with observation.

The halo-finding issue has revealed itself as not trivial at all. When cosmological simulations have increased their resolution and complexity and the amount of data have grown exponentially, to find haloes can itself be an intensive computational work. Moreover, the different techniques and implementations used in the halo finders developed so far can show important differences, particularly when looking at the features of the smallest objects in the simulations.

In this Chapter we have presented and tested the ASOHF halo finder. We developed a new halo-finding code with the main idea of contributing towards constraints for a field in which only a limited number of algorithms are available and differences among codes are still relevant.

The ASOHF code was especially designed to overcome some limitations of the original SO technique and to exploit the benefits of having a set of nested grids that track the density distribution in the analysed volume. By treating all AMR grids at a certain level of refinement (same numerical resolution) independently, the code is able to find haloes at all levels. This procedure can identify haloes in haloes in a natural way and therefore describe the properties of the substructure in cosmological objects.

The numerical scheme is also prepared to compute the merger tree of the haloes in the computational box as well as some other usual properties of these haloes such as their shapes, and density and velocity radial profiles.

We set up several idealised and controlled tests to check the capabilities of the halo finder. Although most of these tests are unreal, they allow us total control of every part of the halo-finding process. In all tests, the performance of the finder algorithm has been correct.

The next step to calibrate and test the ASOHF finder was to apply it to the outcome of a cosmological simulation and compare its results with other halo finders widely used like AHF and AFoF.

In a first instance, we compared the sample of haloes encountered by the three codes in a given cosmological simulation. A coarse comparison showed a good agreement among them. The mass functions obtained by the three finders were also very similar. We looked at the shape of the encountered haloes, finding a reasonable concordance between the results obtained by ASOHF and AHF and with previous studies.

More interestingly, we tested the abilities of ASOHF dealing with substructure in not idealised simulations. In order to check this issue, we picked up the most massive halo in the considered computational box. This halo was throughly analysed using both grid based on finders, namely, ASOHF and AHF. From the statistical point of view, the results are comparable because the subhalo mass functions are reasonably consistent. Still, the comparison object by object was not as successful because there are several noticeable differences concerning the smaller objects. To clarify this, we compared the samples of haloes obtained by both algorithms with the real mass distribution. Apparently, both codes agree among themselves and match the mass distribution for the most relevant features. However, both algorithms miss small objects when they are compared with the

mass distribution. Surprisingly, the two codes do not miss the same small objects.

The explanation for this behaviour for the ASOHF finder is related to how the hierarchy of nested grids is created. We checked that some of those smaller objects are not always covered by a high resolution grid. In that case the halo finder does not identify the small haloes because it is necessary to have them defined in grids with enough numerical resolution. Although the detailed description of the AHF algorithm is out of the scope of the present work, given that it is also a grid based on halo finder, it is very likely that the differences affecting the detection of small substructures could be caused by the same reasons as in the ASOHF code.

The ASOHF code has been used to study the role of galaxy cluster mergers in a cosmological context (Planelles & Quilis, 2009) (see next Chapter for further explanations). The working version of the code it is still serial and it is written in FORTRAN 95. At present we are working on the parallel OpenMP version of the code which will be publicly released in due course.

6.7 Recent improvements on ASOHF

During May 2010 we were invited to participate in the conference *Haloes going MAD* devoted to carried out the first large project of comparison among the most popular and used halo finder codes. The aim of this meeting was to define a unique set of test scenarios that all the halo finders had to pass and cross-compared their results. A total number of 17 different halo finders participated in this project which represents the largest *Halo Finder Comparison Project* to date. See Appendix A for further details on the different halo finders used in the comparison and the obtained results.

Motivated by this project, during the last period of this Thesis we implemented several improvements in ASOHF in order to use it as a stand-alone halo finder. Although ASOHF was originally created to be coupled to an Eulerian cosmological code, in its actual version, it is a stand-alone halo finder capable of analysing the outputs from cosmological simulations including different components, i.e., dark matter, gas, and stars.

When using ASOHF as a stand-alone halo finder it can be applied to a continuous density on a grid or to a discrete set of particles. The first step consists therefore in translating this information into a continuous density field on a new grid or set of nested grids. When dealing with particles, in order to obtain a continuous density field on a grid, the TSC method is used. The code takes advantage of an AMR subroutine able to create a hierarchy of nested grids placed at different levels of refinement (this method of grid generation follows the main procedure described for the MASCLET code in Section 5.3 of Chapter 5). All the grids at a certain level, named patches, share the same numerical resolution. The higher the level of refinement the better the numerical resolution, as the size of the numerical cells gets smaller.

The refining criteria used in the generation of the grid are open and can be chosen depending on the application: number of particles per cell, density threshold, etc. For a general purpose, ASOHF refines when the number of particles (of any kind) per cell exceeds a user defined parameter. This refinement method

naturally supports different species of particles (particles with different masses). In addition, it is able to build the hierarchical mesh looking only at one of the existing species of particles (of any nature).

Once the hierarchy of nested grids is built according to the new refinement criteria, the code works as explained throughout this Chapter.

Chapter 7

Galaxy cluster mergers *

Galaxy clusters are structures of crucial relevance for a complete understanding of the Universe. They are perfect systems to be studied by numerical simulations. In this Chapter, taking advantage of the codes developed so far, we analyse the role that galaxy cluster mergers play as a source of feedback and reheating of the ICM in a full cosmological context.

7.1 Introduction

Non-gravitational processes have been included in simulations trying to solve the self-similarity breaking observed in the scale relations (see Section 4.4). In the case of galaxy clusters, however, the processes of hierarchical merging and accretion are particularly energetic due to the large masses of the involved systems and the filamentary structures that surround them. Therefore, in the case of galaxy clusters, merger events can also be an important source of feedback. They can produce shocks and compression waves in the haloes which eventually can release part of the energy associated with the collision as thermal energy in the final system (McCarthy, 2007).

Actually, major cluster mergers are the most energetic events in the Universe since the Big Bang (Sarazin, 2002). In these mergers, the subclusters collide at velocities of $\simeq 2000\ km/s$ releasing gravitational binding energies of as much as $\geq 10^{64} ergs$. During these mergers, shocks are driven into the ICM dissipating energies of $\simeq 3 \times 10^{63} ergs$. Such shocks are the major heating source for the X-ray emitting ICM. It is likely that turbulence and mixing could also play an important role in how this energy is mixed and released in the ICM of the final halo after the merger.

Regarding the simulations, it is well known that some results could depend on the ability of different numerical techniques to describe shock waves, strong gradients, turbulence, and mixing, which can be very different depending on the used numerical approach. Although is still a matter of debate, it has been shown, at least for some idealised tests, that the comparison between grid codes and SPH

*This Chapter is based on Planelles & Quilis (2009)

codes – when numerical resolution is similar – can give substantial differences in the results (Frenk et al., 1999; Agertz et al., 2007). It seems reasonable to think that these inherent numerical differences could translate into relevant differences when they are applied to more complex and realistic scenarios like galaxy clusters. This situation makes interesting, necessary, and complementary, to increase the number of studies using the different numerical strategies available.

In this Chapter, we want to investigate the role of the galaxy cluster mergers as a source of feedback and reheating in a complete general cosmological framework. The galaxy clusters form and evolve due to the non-linear evolution of primordial perturbations and, therefore, no special symmetry or idealised clusters are considered. In this scenario, the merger events naturally take place according to the hierarchical evolution. Previous works have extensively studied the mergers of galaxy clusters using controlled collisions (e.g., Ricker & Sarazin, 2001; Poole et al., 2006, 2007; McCarthy, 2007; Poole et al., 2008). The approach adopted in the present study could be considered as complementary to the studies using controlled mergers. It is clear that our approach has some important weaknesses, when it is compared with controlled mergers, like the worst resolution or the impossibility to control the different parameters involved in the problem. However, it gives a description of the problem in a cosmological context, without symmetries, including the presence of substructures and taking into account the effects of the different environments.

In order to study the role of mergers fulfilling all the previous requirements, we have carried out a simulation of a moderate size box of side length $100\,h^{-1}\,Mpc$. The simulation, performed with MASCLET, includes the usual processes of cooling and heating for primordial gas, and a phenomenological star formation treatment. We have identified and followed the evolution of the different galaxy cluster haloes. Once the evolutionary history of the haloes is known, we have classified them into three broad categories depending on the features of the merger events in which they have been involved. These mergers are the ones naturally happening in the building up of the galaxy clusters. We will discuss their effects on cluster properties.

7.2 The simulation

7.2.1 Simulation details

The numerical simulation has been performed with the MASCLET code assuming a spatially flat ΛCDM cosmology with the following cosmological parameters: matter density parameter, $\Omega_m = 0.25$; cosmological constant, $\Omega_\Lambda = \Lambda/3H_o^2 = 0.75$; baryon density parameter, $\Omega_b = 0.045$; reduced Hubble constant, $h = H_o/100km\,s^{-1}\,Mpc^{-1} = 0.73$; power spectrum index, $n_s = 1$; and power spectrum normalisation, $\sigma_8 = 0.8$.

The initial conditions were set up at $z = 50$, using a CDM transfer function from Eisenstein & Hu (1998), for a cube of comoving side length $100\,h^{-1}\,Mpc$. The computational domain was discretized with 512^3 cubical cells.

A first level of refinement (level 1) for the AMR scheme was set up from the initial conditions by selecting regions satisfying certain refining criteria, when

evolved – until present time – using the Zel'dovich approximation. The volumes selected as *refinable* were covered by grids (patches) with numerical cells selected from the initial conditions. The regions of the box not eligible to be refined were degraded in resolution by averaging the quantities obtained on the initial grid. This procedure creates the coarse grid (level 0) for the AMR scheme. These coarse cells have a volume eight times larger than the first level ones. In the same manner, the dark matter component within the refined regions was sampled with dark matter particles eight times lighter than those used in regions covered only by the coarse grid. During the evolution, regions on the different grids are refined based on the local baryonic and dark matter densities. Any cell with a baryon mass larger than $5.6 \times 10^8 M_\odot$ or a dark matter mass larger than $2.5 \times 10^9 M_\odot$ was labelled as *refinable*. The ratio between the cell sizes for a given level $(l+1)$ and its parent level (l) is, in our AMR implementation, $\Delta x_{l+1}/\Delta x_l = 1/2$. This is a compromise value between the gain in resolution and possible numerical instabilities. This method produces patches with a boxy geometry and cubic cells at any level.

The simulation presented in this Chapter has used a maximum of seven levels $(l = 7)$ of refinement, which gives a peak spatial resolution of $3\,h^{-1}\,kpc$. For the dark matter we consider two particles species, which correspond to the particles on the coarse grid and the particles within the first level of refinement at the initial conditions. The best mass resolution is $5.75 \times 10^8\,h^{-1}\,M_\odot$, equivalent to distribute 512^3 particles in the whole box.

Our simulation includes cooling and heating processes which take into account Compton and free-free cooling, UV heating (Haardt & Madau, 1996), and atomic and molecular cooling for a primordial gas. In order to compute the abundances of each species, we assume that the gas is optically thin and in ionization equilibrium, but not in thermal equilibrium (Katz et al., 1996; Theuns et al., 1998). The tabulated cooling rates were taken from Sutherland & Dopita (1993) assuming a constant metallicity 0.3 relative to solar. The cooling curve was truncated below temperatures of $10^4\,K$. The cooling and heating were included in the energy equation (Eq. 4.8) as extra source terms.

The star formation has also been modelled with a phenomenological approach commonly used in cosmological simulations (Yepes et al., 1997; Springel & Hernquist, 2003) as explained in Section 5.2.3 of Chapter 5. Despite the use of an AMR code to perform the simulation described in the present Chapter, we have still had numerical limitations, namely, the number of patches placed at the highest level of refinement. Although this limitation has been not crucial for the description of clusters, it has translated into a poor star formation efficiency as the analysed run only allowed star formation at the highest level of refinement. This apparent drawback of our simulation is not dramatic for the purpose of the present study where we focus in the effect of mergers on the ICM properties. Thus, the stellar feedback has turned out to be very low and, consequently, it does not alter the pure effect of the mergers.

7.2.2 Cluster identification

As explained in the previous Chapter, a crucial issue in the analysis of our simulation has to do with the cluster identification. In order to do so, we have made use

of the ASOHF halo finder to analysed the outputs generated by the MASCLET code.

Therefore, we define the viral mass of a halo, M_{vir} (Eq. 6.2), as the mass enclosed in a spherical region of radius, r_{vir}, having an average density Δ_c times the critical density $\rho_c(z) = 3H(z)^2/8\pi G$.

For the cosmological parameters considered in our simulation, the over-density Δ_c, approximated by Eq. 6.1, has a value of $\Delta_c \simeq 373$.

After applying ASOHF to the simulation and once the haloes are found, the different progenitors are identified by following all particles belonging to a given halo backwards in time. This procedure is repeated until the first progenitor of a certain halo is found. As explained in Chapter 6 (Section 6.3.2), this method, which is essential for the present study, allows us not only to know all the progenitors of each halo but the amount of mass received from each one of its ancestors.

7.3 Results

In our simulation, we have identified more than three hundred galaxy clusters and groups spanning a range of masses from $1.0\times10^{13}\,M_{\odot}$ to $2.0\times10^{15}\,M_{\odot}$. We refer to this set of clusters as the complete sample. We have constructed their evolutionary histories and, based on their merging histories, we have classified them into three categories according to the mass ratio of the haloes involved in the collision.

It is also convenient to adopt a timescale limit since mergers occurring at a very early epoch would not have any important consequence on the present properties of the clusters. In this sense, and only for the purpose of delimiting the merger events happening recently, we have defined the formation redshift of a cluster, z_{for}, as the redshift at which the cluster mass is half of its present virial mass (Lacey & Cole, 1993). Thus, we consider for each cluster only those mergers that have relevant effects on its recent past.

Therefore, taking into account the formation redshift of the clusters, z_{for}, and the masses of the most (less) massive halo, m_2 (m_1), involved in the merger, we have classified the clusters into three categories:

- Major mergers. Those systems where the mass ratio $m_2 : m_1$ is smaller than $3 : 1$. Therefore, a major merger involves clusters with similar masses.

- Minor mergers. Those systems where the mass ratio is $3 : 1 < m_2 : m_1 < 10 : 1$.

- Relaxed haloes. Those systems which have suffered mergers with very small haloes, $10 : 1 < m_2 : m_1$, or smooth accretion.

Out of the complete sample, we have picked up a subsample which contains the sixteen most massive galaxy clusters in the computational box. They constitute what it would be referred to as the reduced sample, and their main features are summarised in Table 7.1. Depending on the particular analysis, that we will be interested in the following sections, we will use the complete or the reduced sample, respectively. Concerning their merging classification, in the reduced sample we

cluster	r_{vir} $(h^{-1}\,Mpc)$	M_{vir} $(10^{14}\,M_\odot)$	T (keV)	m_{gas} $(10^{14}\,M_\odot)$	S $(keVcm^2)$	type
CL01	2.32	18.61	7.02	3.45	2601.06	MA
CL02	2.22	15.83	5.99	4.89	2130.17	MA
CL03	1.58	5.68	3.24	1.08	919.34	MA
CL04	1.48	4.70	3.80	0.79	998.65	MA
CL05	1.39	3.93	2.29	0.70	1063.19	MA
CL06	1.07	1.86	1.26	0.37	510.01	MA
CL07	1.01	1.53	1.01	0.25	846.33	MA
CL08	0.93	1.14	0.87	0.21	422.39	MA
CL09	1.51	5.19	3.09	1.03	1166.28	MI
CL10	1.51	5.11	2.18	0.92	1126.22	MI
CL11	1.36	3.76	2.55	0.49	862.07	MI
CL12	1.45	4.40	2.52	0.97	980.39	R
CL13	1.10	1.99	1.40	0.41	409.21	R
CL14	0.99	1.39	1.18	0.29	362.36	R
CL15	0.89	1.02	0.97	0.22	554.70	R
CL16	0.89	1.01	0.90	0.22	386.56	R

Table 7.1: Cluster sample. Main features of selected clusters at $z = 0$. Column 2, virial radius in units of $h^{-1}\,Mpc$; Col. 3, total mass within the virial radius in units of $10^{14}\,M_\odot$; Col. 4, mass-weighted temperature within the virial radius in keV; Col. 5, gaseous mass within the virial radius in units of $10^{14}\,M_\odot$; Col. 6, average entropy within the virial radius in units of $keVcm^2$; Col. 7, type classification: relaxed or with no important mergers (R), minor mergers (MI), and major mergers (MA).

have found five relaxed clusters (R), three have been categorised as clusters with minor mergers (MI), and eight have been classified as major merger systems (MA).

Despite we have used an AMR code to carry out the simulation described in this work, due to numerical limitations, a biased sample of clusters – with a tendency to better describe the most massive ones – has been produced. These artificial results could be overcome, in future applications, by performing resimulations of the selected clusters in the sample, although this could prevent us from following the mergers in a cosmological context. In any case, we consider that the effects of mergers would be more important in those systems with higher masses – well-described in the present simulation – and therefore, we believe that this bias has only minor consequences.

In order to analyse the results of our simulation, we will study several thermodynamical properties which can be directly connected with observational data, and which have been widely studied by all sort of different simulations. In addition to the common plots of density, we will also study the behaviour of the ICM temperature, X-ray luminosity, entropy, and the internal and kinetic energies.

The ICM temperature will be defined as:

$$T = \frac{\sum_i T_i w_i}{\sum_i w_i}, \tag{7.1}$$

where T_i and w_i are the temperature and the weight given to each cell. In most of the applications in the present work, the weight will be the cell mass, $w_i = m_i$, and

therefore, this will be a mass-weighted temperature. In some particular cases, and for the sake of comparison with observational data, we will also use the so called spectroscopic-like temperature (Mazzotta et al., 2004), T_{sl}, where the weight is $w_i = m_i \rho_i T_i^{-3/4}$ with ρ_i the density at the cell i.

A crucial observable quantity, directly related with the temperature and the density of the gas, is the bolometric X-ray luminosity. In simulations, this quantity can be computed by adding up all the contributions from each elemental volume of gas:

$$L_x = \int_V n_e n_i \Lambda(T, Z)\, dV \quad , \tag{7.2}$$

where n_e and n_i are the electron and ion density, respectively, and $\Lambda(T, Z)$ is the normalised cooling function depending on the temperature (T) and metallicity (Z) from Sutherland & Dopita (1993) (see Section 7.2.1).

The next thermodynamical quantity we will pay a special attention is the entropy, which is an extremely useful quantity providing a lot of information (Voit, 2005) about the evolutionary state of the clusters, since it records the thermodynamical history of the ICM produced by the gravitational and non-gravitational processes. We will adopt the following common definition for the entropy given by Eq. 3.11:

$$S = k_B T n_e^{-2/3}, \tag{7.3}$$

where n_e is the electron number density and k_B is the Boltzmann constant.

Other thermodynamical quantities useful to quantify the effects of mergers and shocks as a source of feedback are the total internal energy, E_u, and the total kinetic energy, E_k, which are given by the following expressions:

$$E_u = \int_{V_{vir}} \rho \epsilon \, dV \tag{7.4}$$

$$E_k = \frac{1}{2} \int_{V_{vir}} \rho v^2 \, dV \tag{7.5}$$

where ρ, ϵ and v are the gas density, specific internal energy and the peculiar velocity of the gas fluid element, respectively.

For the sake of comparison with observational data, it is also useful to define some characteristic quantities widely used in the literature. Similar to the definition of the virial quantities (see Section 7.2.2), we introduce a characteristic radius, r_Δ, such that the mean density enclosed within this radius is Δ times ρ_c, and therefore, the mass is:

$$M_\Delta (< r_\Delta) = \frac{4}{3} \pi r_\Delta^3 \Delta \rho_c. \tag{7.6}$$

Consequently, we follow the common definition for the temperature,

$$T_\Delta = \frac{G M_\Delta}{2 r_\Delta} \frac{\mu m_p}{k_B}, \tag{7.7}$$

where μ and m_p are the mean atomic weight and the proton mass. In the same manner, we define the entropy,

$$S_\Delta = k_B T_\Delta \left(\frac{\mu m_p}{f_b \rho_\Delta} \right)^{2/3}, \tag{7.8}$$

with $f_b = \Omega_b/\Omega_m$.

In the following sections, and in order to compare with previous works, we will consider $\Delta = 200$ or $\Delta = 500$ depending on the particular case we compare with. All the quantities we have just described are going to be used to analyse the results of the simulation.

7.3.1 Merger history of selected clusters

We have constructed the merger tree of the selected galaxy clusters tracking all the dark matter particles that belong to a given cluster backwards in time. Figure 7.1 displays the merger trees of three haloes, which could be considered as prototypical ones of each category (i.e., relaxed, minor merger, and major merger). The clusters have been selected such that they have very similar masses and sizes at $z = 0$. The merger trees start at $z = 0$ and plot all the parent haloes of the final ones in previous time steps over several output times of the simulation.

The total mass of each halo is represented by a circle, whose size is normalised to the mass of the final halo at $z = 0$. The lines connecting circles between different times inform us about the progenitors of a given halo at a given time. In addition, the type of line tells us the amount of mass transferred from the progenitor to the halo at the considered time. Thus, a halo at a certain time connected with a progenitor halo at earlier time by a dash-dotted line, means that up to 25% of its mass is due to the contribution of that progenitor. The same idea follows for other line types. The aim of this kind of plot is to show the merger history and the different interconnections over time. The horizontal axis is designed to separate haloes for plotting purpose only, and it has no direct implication on the position of haloes in real space. Vertical axes show the redshift.

In Fig. 7.1 the different merger events can be easily identified. Whereas the relaxed cluster (right panel) has a quiet evolution, the middle panel shows a cluster suffering three mergers between $z = 0.79$ and $z = 0.65$. By comparing the masses of the different haloes involved in these processes, all the events are classified as minor mergers. In the left panel, a cluster undergoing several mergers at different times is presented. Some of the mergers are minor ones, but there are major collisions at $z = 0.99, z = 0.79$ and $z = 0.72$. In order to quantify the effect of mergers, we will correlate all these phases of activity in the clusters evolution with changes and effects on the different physical quantities.

It is important to notice that some of the merger trees also show haloes that break apart, that is, lose mass and reduce their sizes. This process operates at two well-separated regimes with different causes. The first group is formed by very small size haloes. These haloes are not really gravitationally bound and they can be easily disrupted by interactions with environment or with other haloes. For the haloes with larger masses, those mass losses are small, and they are associated with tidal interactions.

7.3.2 Average radial profiles

In order to analyse the main properties of the simulated galaxy clusters, we compute radial profiles for several quantities. These profiles are centred at the centre

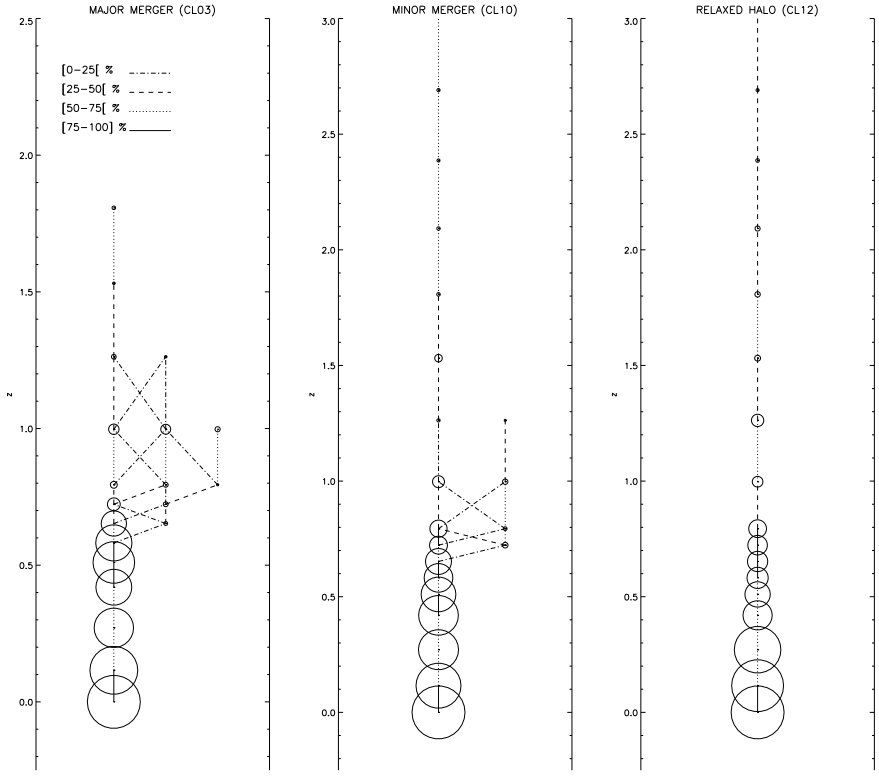

Figure 7.1: Merger tree for one cluster of each category: left panel shows a major merger cluster, central panel represents a minor merger cluster, and right panel stands for a relaxed cluster. Cluster haloes are represented by circles whose sizes are normalised to the final mass at $z = 0$. Lines connecting haloes at different times indicate the amount of mass transferred from the progenitors to their descendants.

of mass of each halo and run outwards from the centre to a distance slightly larger than the radius, r_{200}. The bins are equispaced in logarithmic scale with widths 0.1 dex. In all the plots displaying radial profiles, the radial coordinate is normalised to the r_{200} at this time.

In Fig. 7.2, we plot averaged radial profiles for several quantities for the clusters in the reduced sample (see Table 7.1). All the profiles are scaled by the plotted quantities at r_{200} defined according to Eqs. (7.6–7.8). The mean profiles (continuous lines) are computed by averaging all the profiles of the clusters of each class. The right column stands for the relaxed clusters, the central column represents the minor merger clusters, and the left column displays the major merger clusters. The plotted quantities are gas (ρ/ρ_{200}) and dark matter (ρ_{dm}/ρ_{200}) densities, temperature (T/T_{200}), and entropy (S/S_{200}). The continuous lines stand for results at $z = 0$ and shadowed regions mark one σ deviation. Let us stress that, in Fig. 7.2 and in the following ones – unless explicitly stated –, we consider mean profiles rather than median profiles.

A detailed analysis of Fig. 7.2 shows the main features of the three categories in which we have classified the different clusters. The comparison of gas and dark-matter density profiles does not show notable differences. Whereas for the gas density, the relaxed clusters exhibit a slightly higher density at the centre compared with the minor and major merger clusters, the behaviour for the dark matter is the opposite, having the major merger clusters a higher density. In any case, the profiles are consistent with the expected characteristics of density profiles for galaxy clusters.

Concerning the temperature profiles, there are no dramatic differences either. All clusters, in the reduced sample, show a central core with an almost constant temperature and a declining profile outwards. This result is compatible with observational data (e.g., de Grandi & Molendi, 2002), and with the idea of a quite universal temperature profile for the galaxy clusters (Loken et al., 2002). The major and minor merger cluster profiles have very similar central temperatures, although the isothermal core is larger for the major merger clusters. The relaxed clusters have a bigger isothermal core with a slightly lower value of the temperature compared with the major and minor merger clusters.

The temperature profiles of the most massive clusters in our reduced sample do not exhibit a drop in the temperature in their central regions. Apparently, this could seem to differ from the results of the simulations by Kay et al. (2007) or the observational data presented by Vikhlinin et al. (2005) or Pratt et al. (2007). These last observational results show clusters with temperature profiles with drops in their central temperatures. This effect is more outstanding in the case of Vikhlinin et al. (2005). The nature of this discrepancy amid both observational results could be related with the use of different instrumentation in order to obtain the data of both samples. It must be noticed that whereas Pratt et al. (2007) used XMM-Newton, the results of Vikhlinin et al. (2005) were obtained using CHANDRA – with higher angular resolution. This could explain that some cool cores in the Pratt et al. (2007) sample were not properly resolved. In order to compare with the results in Pratt et al. (2007) and Vikhlinin et al. (2005), we have calculated the spectroscopic-like radial temperature profile for each cluster of our reduced sample (clusters listed in Table 7.1) and normalised them to their respective mean

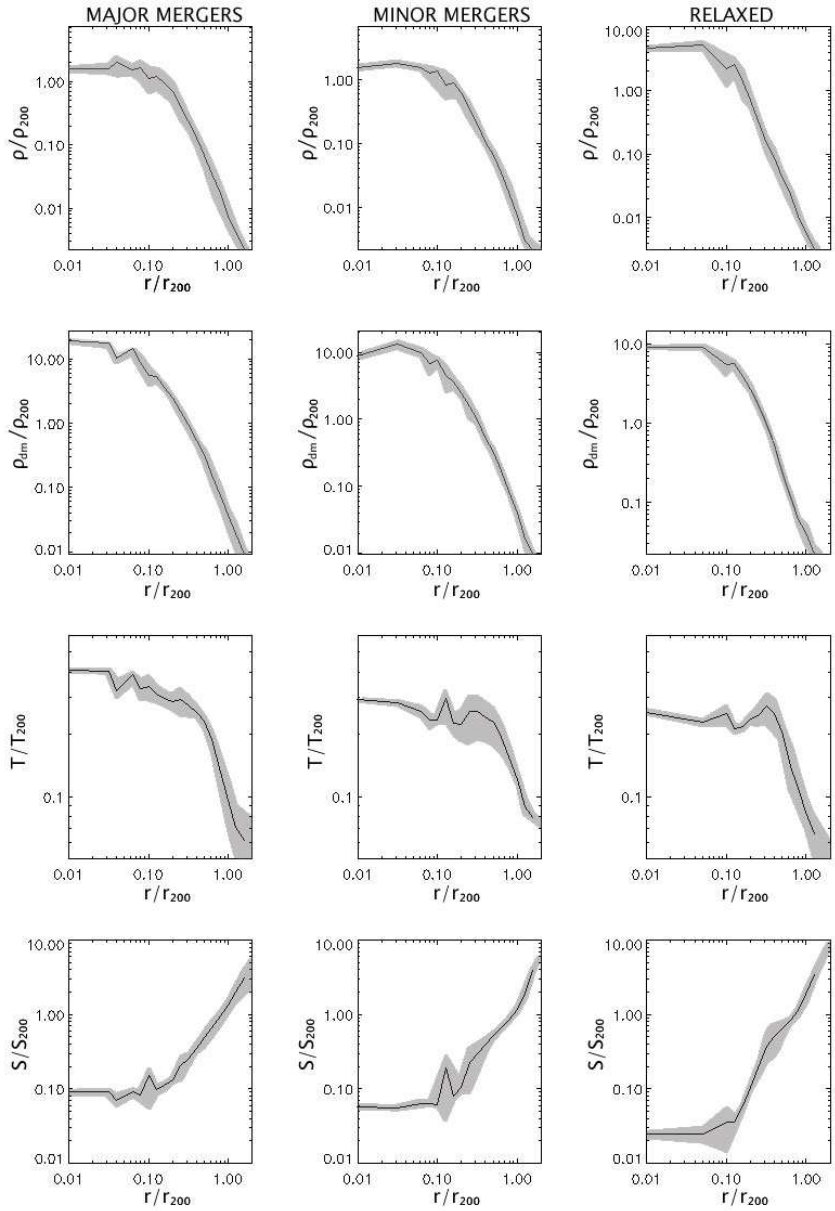

Figure 7.2: Average radial profiles for all clusters belonging to each class: major mergers (left column), minor mergers (central column), and relaxed (right column). From top to bottom, the first and second rows display gas (ρ/ρ_{200}) and dark matter (ρ_{dm}/ρ_{200}) densities, respectively, the third row shows mass-weighted temperature (T/T_{200}), and the fourth row represents entropy (S/S_{200}). All profiles have been scaled by the mean value of the plotted quantities within the scale radius, r_{200}. Continuous lines show the average for all the individual profiles of each class of clusters. Shadowed regions represent one σ deviation.

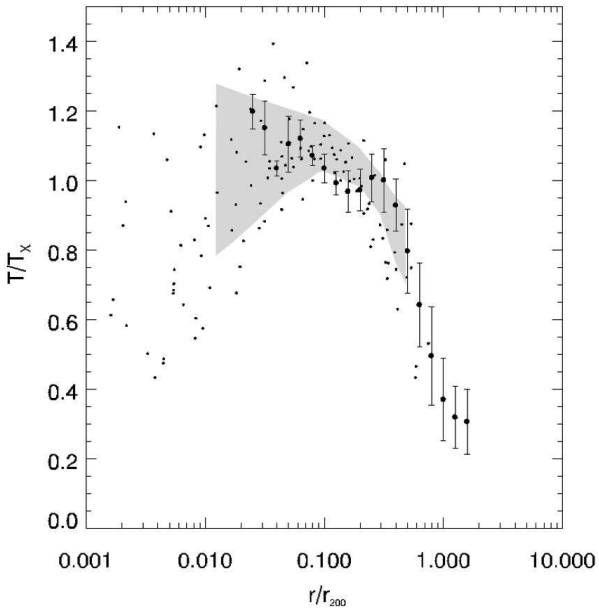

Figure 7.3: Mean spectroscopic-like temperature profile for all the clusters in Table 7.1. Each cluster profile is normalised by its mean spectroscopic-like temperature (T_X) within r_{200}. The normalised profiles are averaged in order to obtain the plotted mean profile. Dots represent the different bins equispaced in logarithmic scale with width 0.1 dex, and error bars are 1 σ s.d. The shaded region encloses the mean and 1 σ s.d. temperature profiles from a representative sample of nearby clusters by Pratt et al. (2007). The small black dots correspond to the temperature profiles of the clusters in the sample of Vikhlinin et al. (2005).

T_{sl} within r_{200}, that we denote as T_X. In Fig. 7.3, we compare the mean of all these radial temperature profiles, represented by dots with error bars (one σ standard deviation), with the observational results in Pratt et al. (2007) marked as the shaded region, and the results in Vikhlinin et al. (2005) represented by small dots[1]. Our results are consistent with these observational data in an average sense, being slightly more similar to the data of Pratt et al. (2007).

We can understand our result if we keep in mind that the clusters we are considering are the most massive ones in our sample. As we will discuss in more detail in Section 7.3.4, we have found that there is a strong anticorrelation between the drop of temperature in the central region and the mass of the cluster. Therefore, the larger the mass of the cluster the smaller the number of clusters with central gradients of temperature. However, if all the clusters in the complete sample are considered, then a relevant fraction of the population ($\sim 16\%$) shows temperature profiles with central gradients (read Section 7.3.4 for more details).

More interesting is the analysis of the entropy profiles. In all cases, the clusters

[1]It must be mentioned that in Vikhlinin et al. (2005), the temperature profiles are plotted against radial coordinate normalized to r_{180}. We have ignored this small correction without relevant effects for the purpose of the actual comparison.

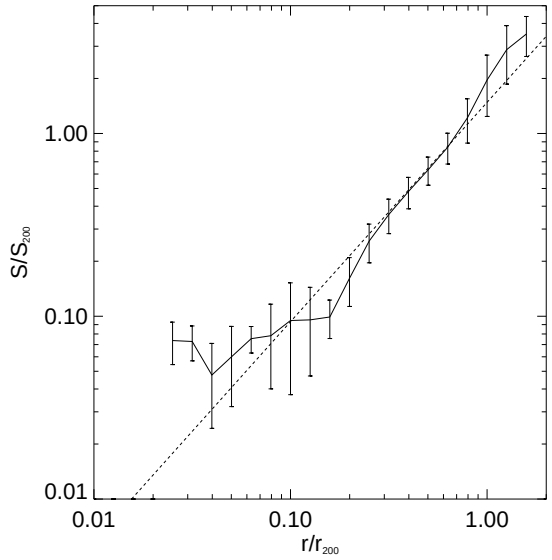

Figure 7.4: Mean entropy profile for all clusters in Table 7.1 compared with the fitting in Voit et al. (2005). The radial profiles for each cluster are obtained using equispaced logarithmic bins. All of them are normalised to their respective values of S_{200}, and then, the mean profile is obtained. Continuous line represents the mean profile and error bars show 1 σ s.d. Dashed line shows the fitting by Voit et al. (2005).

have entropy cores and profiles outside $0.2\,r_{200}$ compatible with a power law $S(r) \propto r^{\alpha}$ (Tozzi & Norman, 2001). In previous work carried out by Voit et al. (2005), the authors performed several non-radiative SPH and AMR simulations, and studied the main features of the entropy profiles of the galaxy clusters in their numerical samples. Besides several differences in the inner cores, all clusters in their sample, regardless of the numerical technique used, showed very similar entropy profiles outside a region around $0.2\,r_{200}$. In particular, for the AMR simulation, they found that the entropy profile in the outer regions can be better fitted by the power law $S(r) = 1.43\,S_{200}(r/r_{200})^{1.2}$. In Fig. 7.4, we compare the mean entropy profile of all the clusters in Table 7.1 with the fitting by Voit et al. (2005). Continuous line represents our mean entropy profile with 1σ error bars. Dashed line stands for Voit et al. (2005) fitting. Our results seem to be compatible with the fitting in the outer part of the profiles, whereas in the inner region, where cooling and feedback processes could be relevant, differences are expected.

In order to compare our results with observational data, we have looked at the values of the entropy at $0.1\,r_{200}$, $S_{0.1\,r_{200}}$, and compared them with previous data by Ponman et al. (2003). In Fig. 7.5 we plot the observational data (with error bars) by Ponman et al. (2003) together with the values for the clusters in our reduced sample with temperatures higher that $1\,keV$ (red filled circles). The points representing simulated clusters match well with the observational data apart

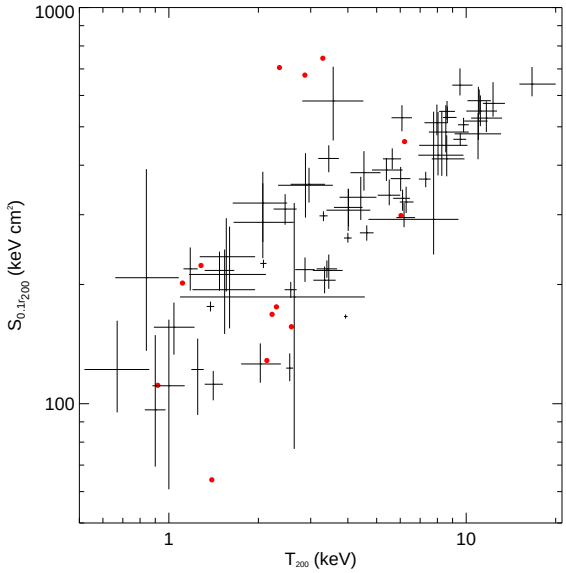

Figure 7.5: Gas entropy at $0.1\,r_{200}$ as a function of temperature, T_{200}. Simulated clusters are represented by red filled circles, whereas observational data with error bars stand for the Ponman et al. (2003) sample. In order to compare simulations and observations, $T_{200} \equiv T_X$ has been assumed.

from three clusters that are marginally compatible. These three objects turn out to have some peculiarities as they have suffered quite recent merger events. The values of the entropy at the very centre of the simulated clusters are also similar to recent CHANDRA observations (Morandi & Ettori, 2007). Therefore, our results seem to be reasonably compatible with the observations taking into account all the simplifications and limitations of our approach.

Coming back to the comparison of the results according to the merger history of the clusters, the generic shape of the entropy profiles does not depend systematically on the mass or temperature of the clusters, in agreement with observations (Ponman et al., 2003). The sizes of the cores are similar in the relaxed and minor merger clusters and slightly larger in the major merger ones. As it would be naively expected, the entropy floor in the relaxed clusters is lower than for the minor merger clusters, and this one is also lower than for the major merger clusters. Although the differences seem not to be dramatic, they are clearly visible in the mean profiles. These differences in the value of the entropy in the core, would be a clear consequence of the different evolutionary histories of each cluster.

7.3.3 Merger effects

Merger events can produce shocks and compression waves in haloes. Their effects could be an efficient way to transfer part of the gravitational energy associated to the collisions to the ICM of the final halo after the mergers. In this picture, the

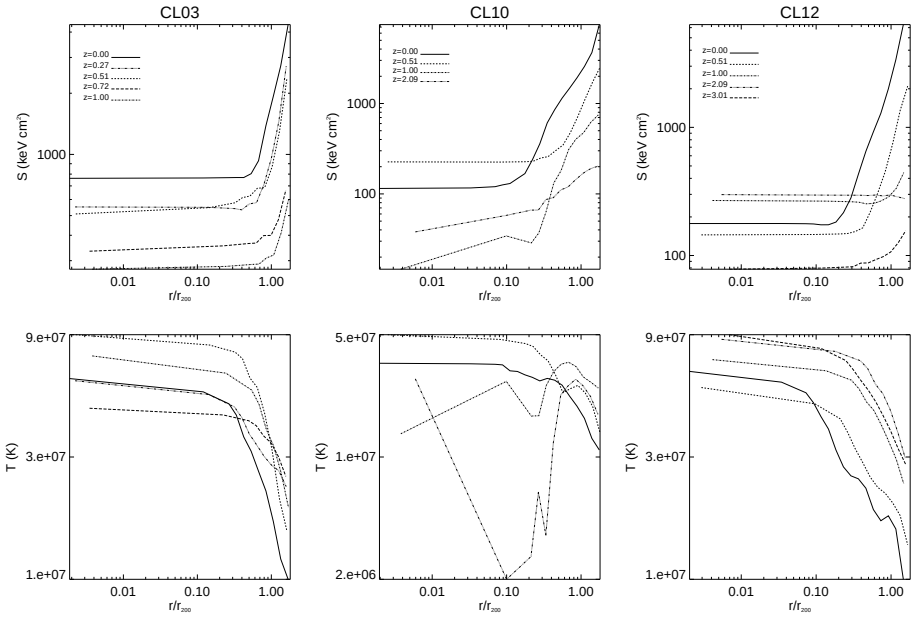

Figure 7.6: Radial profiles of entropy (S) and temperature (T) at different redshifts. Left column shows the result for a cluster representing the major merger clusters, central column for a minor merger cluster and right column for a relaxed cluster.

role of turbulence and mixing phenomena is crucial as a way to redistribute this energy into the ICM.

The study of these scenarios requires a numerical scheme able to tackle with an accurate description of shock waves, strong gradients as well as to describe the turbulence associated to those violent events. As it has been discussed in Section 7.1, the ability of different numerical techniques to describe these phenomena is still a matter of debate.

We focus in this Section on the effects of different merger events in the thermodynamical properties of the ICM. In order to do so, we select the same three clusters than in Section 7.3.1. Each one of them represents one of the three groups of clusters and, as it was already mentioned, they have been chosen in such a way that they have similar masses and sizes at $z = 0$.

In order to discuss the effects of different merger events in the thermodynamical properties of the ICM, we show in Figure 7.6 the radial profiles of entropy (S) and temperature (T) at several redshifts for the selected clusters. This figure can be correlated with Fig. 7.1 to detect the effect produced by the merger events. Lines representing high redshifts must be taken carefully. They correspond to early stages of the clusters formation when these structures are far from being relaxed and, therefore, the radial profiles are not really meaningful.

The relaxed cluster shows a higher entropy and temperature at high redshifts, with a tendency to reach a relaxed state around $z \sim 0.5$ with small changes. The tendency for the minor merger cluster is similar for the lines displaying $z \sim 2$ and

$z \sim 1$, that is, a reduction of the value of the entropy core. However, associated with the minor merger events, there is a significant increase in the value of the entropy core which, eventually, ends up in a reduction of the temperature and entropy at $z \sim 0$ with respect to the values at $z \sim 0.5$. In the case of the major merger cluster, between $z \sim 1$ and $z \sim 0.6$ when the major mergers take place, there is an increase in the entropy and a reheating as the temperature also increases. Later on, the cluster cools to a lower temperature but part of the energy of the merger has been released in the cluster which has a higher entropy. It must be noticed that the values for the entropy are considerably larger than for the other two clusters previously discussed.

So as to assess more clearly the effects of mergers in the thermodynamical properties of ICM, we show in Fig. 7.7 the time evolution of several quantities: the averaged entropy within the 10% of r_{200} ($S_{0.1r_{200}}$), the ratio of the total internal to kinetic energies (E_U/E_K), and the integrated X-ray luminosity (L_X), both within the radius r_{200}. As in previous plots, each column represents the results of a cluster representing one of the three classes.

For the relaxed cluster, the situation is simple. The early stages of cluster formation have left high entropy and internal energy. However, with the time evolution, the cluster cools and loses internal energy, creating a lower entropy core, and increasing the X-ray luminosity. The minor merger cluster exhibits a different history. As the cluster forms a bit later than the previous one, it begins with a lower entropy and internal energy compared with the relaxed cluster. The time zone when mergers happen – delimited by the vertical lines – can be clearly connected with important changes in the cluster evolution. The first minor merger boosts the entropy level and the internal energy, indicating that some energy has been injected in the system. This energy reheats the ICM and produces a decrease in the luminosity by delaying the cooling. Later on, the cooling takes over again dumping part of the energy, but leaving a net increase in the entropy. The history of the major merger cluster is slightly different. At the initial phase, the smooth accretion has produced an increasing trend in the core entropy, the internal energy and the luminosity. After the major merger the situation is different. Due to the more dramatic effects of the major mergers (higher disruption, stronger shock waves, and more turbulence and mixing) there is an increase in the entropy level, but associated with an immediate loss of energy due to radiation. Another minor merger produces some minor changes but the final state is a cluster pretty similar to the previous ones but with a significantly higher entropy.

7.3.4 Cool cores and cluster mergers

It is well known that clusters of galaxies exhibit an important feature that allows to classify them into two separate populations, those having cool cores (CC) and those others not having cool cores (NCC).

Recently, Chen et al. (2007) concluded that, roughly, half of the population observed in a sample with more than hundred clusters have CCs. The explanation for this dichotomy is not clear and it remains a matter of debate. Several authors have studied this problem by means of numerical simulations. Thus, Kay et al. (2007) overestimate the number of CC clusters since almost all their clusters show

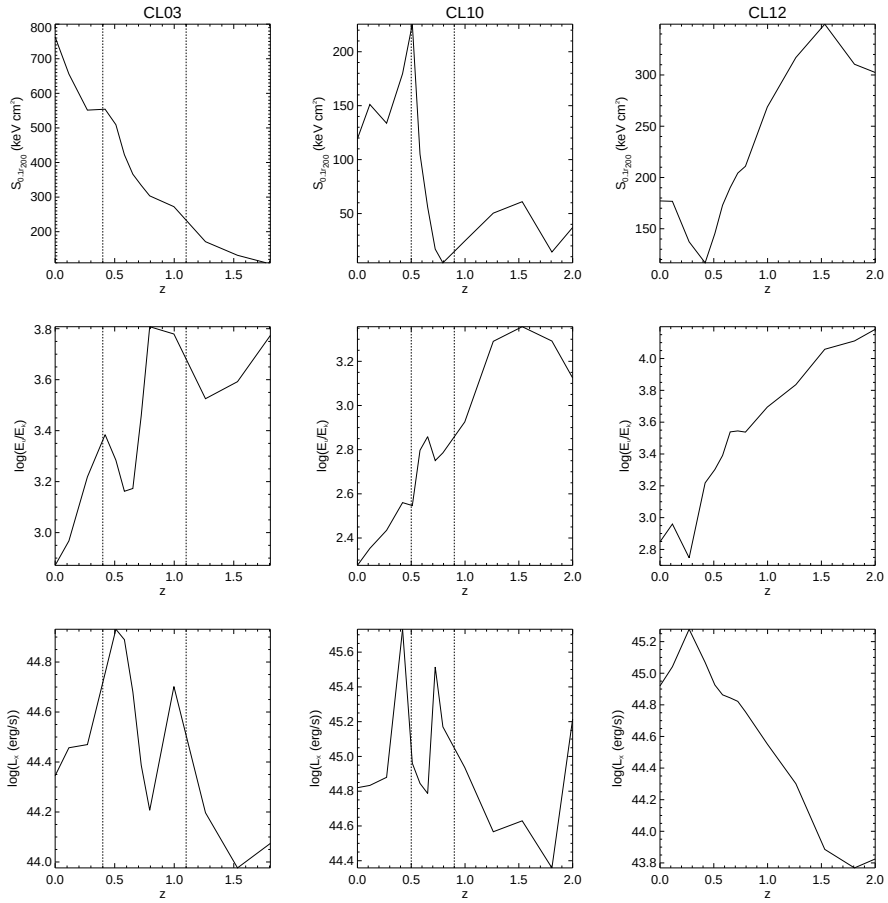

Figure 7.7: Time evolution of the average entropy ($S_{0.1r_{200}}$) within the inner 10% of the radius r_{200}, the ratio between total internal (E_U) and kinetic (E_K) energies, and the X-ray luminosity (L_X), both evaluated within r_{200}. Left column shows the result for a cluster representing the major merger clusters, central column for a minor merger cluster and right column for a relaxed cluster. Vertical lines delimit the time interval when mergers occur.

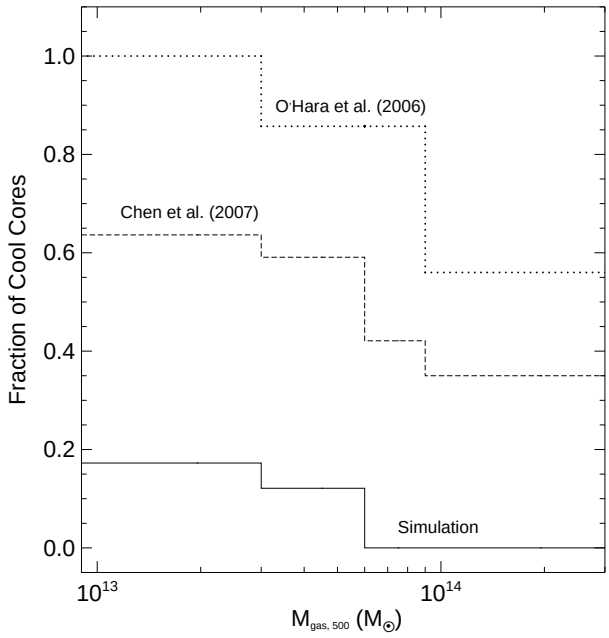

Figure 7.8: Fraction of all galaxy clusters in our simulation that have CC vs the gaseous mass of the clusters. The simulated clusters (continuous line) and the observed clusters from Chen et al. (2007) (dashed line) and O'Hara et al. (2006) (dotted line) are binned in five linearly equispaced bins.

the presence of CCs. However, Burns et al. (2008) claimed to be the first authors producing a simulation with CC and NCC clusters in the same numerical volume, although their abundance at $z \sim 0$ of CC clusters, $\sim 16\%$, seems to be lower than the observed fraction by Chen et al. (2007), $\sim 46\%$. Interestingly, the results presented by Kay et al. (2007) are based on SPH simulations, whereas those of Burns et al. (2008) are obtained using an Eulerian AMR code. It is likely that feedback processes could be directly involved in the survival of CCs in clusters, but it is also possible that mergers could play an important role erasing the presence of CCs (Poole et al., 2006; Burns et al., 2008). In this Section, we analyse our simulation paying special attention to the presence of CCs and their relative abundances.

Following Burns et al. (2008), we define a CC cluster as one with a $\geq 20\%$ reduction of its central temperature compared with the surrounding region. Using this definition, we have classified all the clusters in our complete sample – an extended sample containing all the clusters in the simulation – into two groups: CCs and NCCs.

In Fig. 7.8, we plot the fraction of CCs as a function of gaseous mass at $z = 0$. We have binned the clusters using five linearly equispaced bins in the range $[10^{13}, 10^{15}]\, M_{\odot}$. The continuous line shows our results. For the sake of comparison, we have used the samples of O'Hara et al. (2006) and Chen et al.

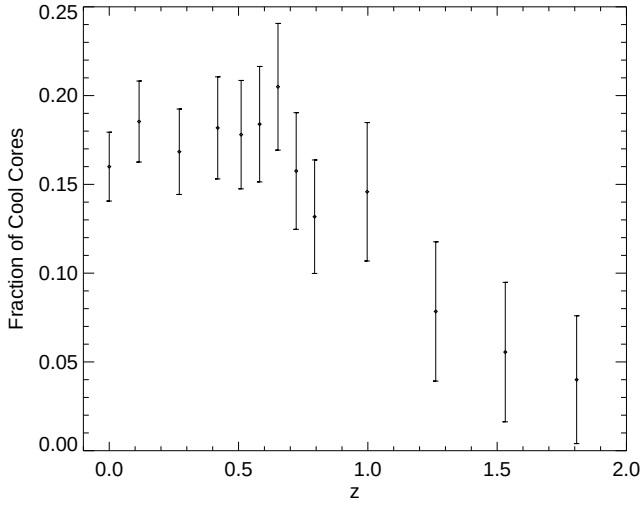

Figure 7.9: Fraction of CCs as function of redshift for the simulated clusters in our complete sample. Error bars show $\sqrt{N}$ uncertainties due to the number counts.

(2007), and we have binned the clusters in these samples using the same bins than for our results. The dashed and dotted lines correspond to Chen's and O'hara's results, respectively.

Our results are extremely similar to those of the Burns et al. (2008) simulation, where they found a total fraction of $\sim$ 16% CC clusters (see figure 8 in this reference) and in our case the number is also $\sim$ 16%. As in Burns et al. (2008), our results differ in the absolute numbers from the observational data, but more interestingly, we have confirmed the general trend of a decreasing number of CC clusters with cluster mass.

Although, we have no clear explanation for the discrepancy between the absolute number of CC clusters in our simulation and the observational data by Chen et al. (2007), two plausible explanations can be given in order to interpret these results. The first one has to do with the fact that no metal-dependent cooling has been considered in the simulation. It is known (see, for instance, de Grandi & Molendi, 2002; Vikhlinin et al., 2005) that some clusters can show strong metallicity gradients, with metallicities rising to solar in the central regions. This limitation of the present simulation could produce some artificial reduction of the cooling, especially in systems where $kT < 2\,keV$. Therefore, this shortcoming could mimic, effectively, some sort of uncontrolled non-gravitational feedback. The second possibility is related with a resolution issue, as no resimulations of the clusters have been performed. Therefore, despite the use of an AMR code, there could exist some resolution limitations. This last possibility seems much less important, though.

We have also looked at the time evolution of the fraction of CC clusters. In Fig. 7.9, we plot the fraction of CCs in our sample as a function of the redshift from

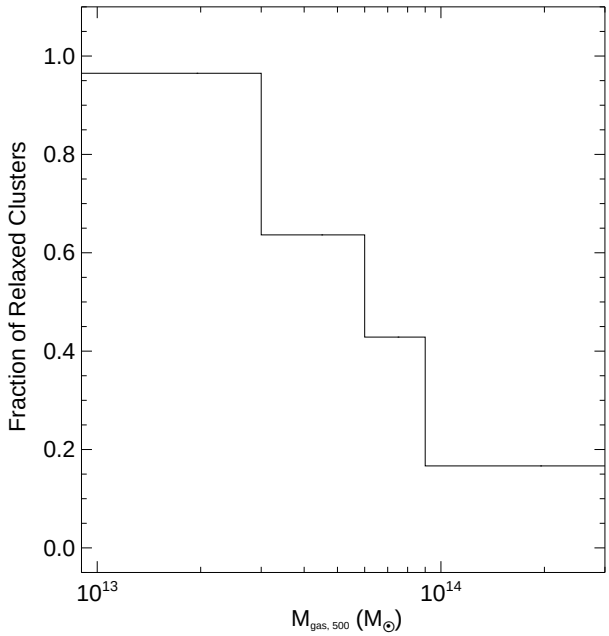

Figure 7.10: Fraction of all the relaxed galaxy clusters in our simulation vs the gaseous mass of the clusters. As in Fig. 7.8, data is binned in five linearly equispaced bins.

$z \sim 2$ until $z = 0$. Again, our results are fully consistent with the simulations by Burns et al. (2008) and show no important change in the fraction of CCs backwards in time, at least back to $z \sim 1$. Our results are in contradiction with observational evidences showing an important variation in the fraction of CCs from $z = 0.5$ (Vikhlinin et al., 2006a).

Before $z \sim 1$, we find a dramatic reduction in the fraction of CCs with time. As it would be expected, the abundance of CCs would be directly correlated with the hierarchical formation of the clusters. At the epoch of cluster formation, almost none of the clusters would have a CC. The formation of CCs would require the establishment of cooling flows which, eventually, and through a slow process will form the cool cores. However, once the clusters were fully formed, the major mergers would destroy the CCs, creating a population of NCC clusters. It is clear that feedback processes would also play a crucial role in this mechanism, but in the present simulation, where no relevant feedback mechanism – apart of the gravitational heating – has been taken into account, the effect of mergers on the existence of CCs is more outstanding. As the mergers are more dramatic in the more massive systems, this would explain the anticorrelation of the fraction of CCs and the mass of the clusters (see Fig. 7.8).

In order to deepen our knowledge of the connection between merger activity and the presence of CCs in clusters, we have studied the dependence of the fraction of relaxed clusters with the cluster mass (Fig. 7.10). If mergers play an important

role in the existence of CCs, one would expect that the systems that have evolved quietly (no recent mergers) do have cool cores. The comparison between the fractions of CC clusters and relaxed clusters is not direct as the establishment of cooling flows and the subsequent formation of CCs could require long time scales, especially for the smaller systems. In any case, and taking the result with caution due to all the uncertainties, we have computed the fraction of relaxed clusters which have central cores with cooling times shorter or comparable to the elapsed time from the clusters formation (z_{for}, see Section 7.3) until the actual time ($z = 0$). Therefore, these clusters would have had time to set up a CC. The result shows the same trend than that in Fig. 7.8, that is, the number of relaxed cluster (no mergers) decreases with the cluster mass. This comparison would show that the smaller systems tend to have a CC and a quiet evolution (no merger events), whereas the larger systems suffer the most important merger events and are NCC systems.

7.3.5 Scaling relations

The scaling relations are crucial tools to study the galaxy clusters, as they connect observables like X-ray luminosities, with cluster properties, namely, masses and temperatures. Moreover, they can be an excellent way to check the behaviour and consistency of the simulations, by comparing with the scaling relations obtained in other simulations or with observations.

The galaxy cluster reduced sample studied in this work is biased towards the most massive clusters of our simulation. Therefore, the statistical properties of this sample must be taken with caution as the sample is far from being complete, due to the numerical limitations. In the present subsection, we have extended the reduced sample (see Table 7.1) by considering all clusters, in the complete sample, with temperature, $T_{500} \geq 1\ keV$ (see Eq. 7.7).

In Fig. 7.11, several scaling relations at $z = 0$ are plotted: X-ray luminosity (upper panel), mass (middle panel), and mean entropy (bottom panel) within the radius r_{500}. All these three quantities are plotted against the temperature T_{500}. Our results can be fitted by the following scaling relations: $L \propto T^{2.5}$, $M \propto T^{1.5}$, and $S \propto T^{0.9}$. In the three relations, we have plotted all the clusters with temperatures $T_{500} \in [1.0, 8.0]\, keV$. This choice slightly increases the number of clusters of the original sample presented in Table 7.1. For completeness, and in order to compare with observational data, we have compared our scaling relations with data by Horner (2001) for the $L - T$ relation and by Ponman et al. (2003) for the $S - T$ relation, respectively. These data are displayed as small dots in the top and bottom panels in Fig. 7.11. The results for our simulated sample seem to be consistent with observational data, leaving aside all the uncertainties of such direct comparison.

Focusing on the effect of mergers, and for the sake of comparison with previous works, let us assume that clusters that have had a relatively quiet evolution would likely develop a CC, whereas those clusters involved in merger events would see their cool cores distorted, turning into NCC clusters (see Section 7.3.4). Under this assumption, we could consider that the galaxy clusters in our sample, labelled as major and minor mergers, could be identified, broadly speaking, with NCC clusters

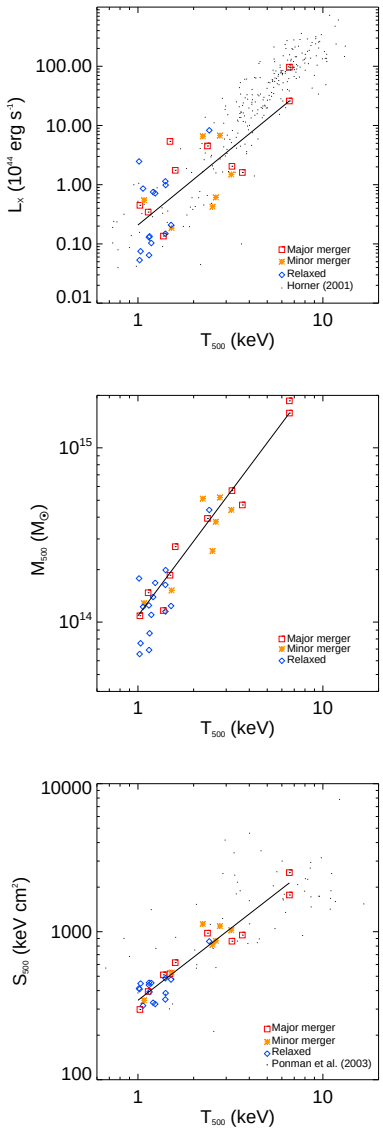

Figure 7.11: Scaling relations for our galaxy cluster sample at $z = 0$. The panels display, from top to bottom: integrated X-ray luminosity, mass, and mean entropy within the radius r_{500}. In all the panels, the previous quantities are plotted against the temperature, T_{500}, computed according to Eq. 7.7. The different symbols represent the clusters in the sample, the continuous lines stand for the proper fittings, and the small filled dots represent observational data by Horner (2001) and Ponman et al. (2003), respectively.

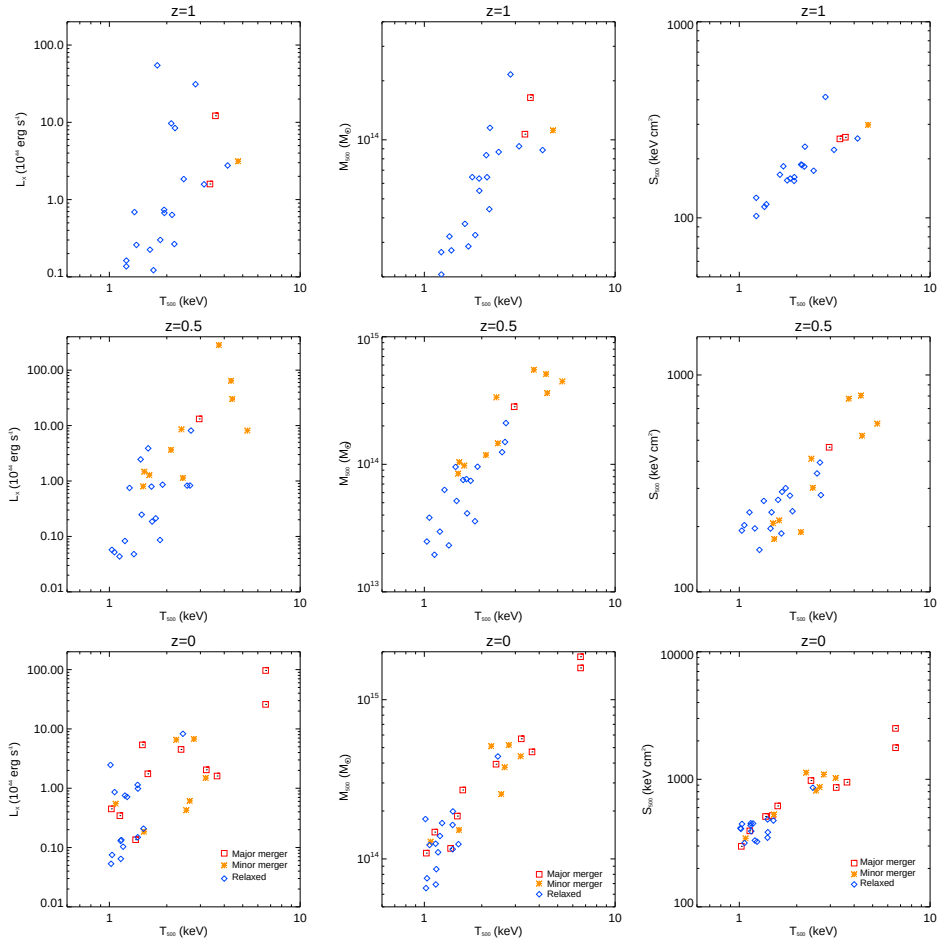

Figure 7.12: Scaling relations at several redshifts for our galaxy cluster sample at $z = 0$. The panels display, from top to bottom, the relations obtained at $z = 1, 0.5$ and 0. Left, middle and right columns show, respectively, the integrated X-ray luminosity, mass, and mean entropy within the radius r_{500}. All these quantities are plotted against the temperature, T_{500}. The different symbols represent the clusters in the sample.

like the ones studied by Poole et al. (2008) and, analogously, our relaxed clusters would be the CC clusters in this reference. The results displayed in Fig. 7.11 show some degree of segregation, with most of the major and minor merger clusters located at well-separated regions on the scaling relation plots. The minor merger clusters sit, preferentially, at an intermediate region between the major merger clusters and the relaxed clusters. As a gross trend, the majority of clusters which have suffered mergers, are placed in zones with higher temperature and higher luminosity, mass, and entropy, respectively.

Understanding the temporal evolution of the scaling relations is crucial for constraining cosmological parameters with cluster surveys. In addition, it also offers a powerful probe of the cooling and heating processes operating in clusters.

For the sake of completeness, we plot in Fig. 7.12 our scaling relations for X-ray luminosity, mass, and mean entropy within the radius r_{500} at several redshifts, namely, $z = 1, 0.5$ and 0, respectively[2]. Again, all these three quantities are plotted against the temperature T_{500}. The sample of clusters represented at $z = 0$ is the same than that in Fig. 7.11. To plot the scaling relations at higher redshift ($z = 0.5$ and 1), we have followed backwards in time the evolution of the clusters considered at $z = 0$ and we have taken their main progenitors at the considered redshift. For the three epochs, only objects with temperatures $T_{500} \geq 1\ keV$ are considered. However, since our sample of clusters is statistically limited, we will only do a qualitative analysis of these scaling relations. As for the $M - T$ relation at high redshift, some observations (e.g., Maughan et al., 2006) are consistent with a self-similar evolution. Our results are compatible with this behaviour since we obtain, at all epochs, a slope for the $M \propto T^{\alpha}$ relation comparable with that expected by the self-similar model. Correspondingly, the $S - T$ relation is also consistent with a self-similar evolution. Attending to the $L - T$ relation, clusters are, in general, brighter at higher redshifts. Our results, neither show a significant change in the slope of this relation, at least back to $z = 0.5$. However, at $z = 1$, there is an important scatter in this relation. The main source of this scatter could be the effect of radiative cooling, which is more prominent at high redshift. As explained in Section 3.3, this result seems to be consistent with previous studies supporting the idea that, because of the increasing importance of radiative cooling and feedback from galaxy formation, the self-similar evolution cannot persist to arbitrarily high redshift (Voit, 2005).

More interestingly, focusing on the effect of mergers and following the above discussion at $z = 0$, a segregation between merging (major or minor merger systems) and relaxed clusters is clearly observed even at high redshift. In all cases, systems which have experimented merger events tend to be placed in regions of higher temperature, luminosity, mass, and entropy, respectively. As it was nearly expected, this result demonstrates that mergers play a relevant role in the physical properties of clusters even at moderately high redshifts.

Mergers, especially the major ones, typically boost clusters along the $L - T$ relation but not parallel to this relation. In Fig. 7.13, we plot – for the major merger clusters in Table 7.1 – the overall drifts experienced by these clusters from

[2]Any of the scaling relations presented in this Section is corrected by redshift. To apply the redshift scaling, they need to be multiplied by the corresponding $E(z)^{\alpha}$ value. See Section 3.3 for further details on the different values of α for each scaling relation.

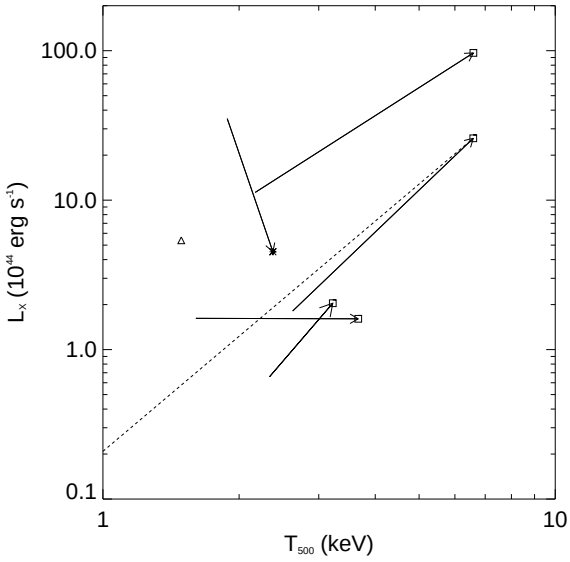

Figure 7.13: The X-ray luminosity vs the temperature, T_{500}, within radius, r_{500}. The plot shows, as vectors, the overall drifts experienced by the most massive major merger clusters in their positions at the $L-T$ relation from $z = 1.5$ until $z = 0$. The clusters, at $z = 0$, are labelled by squares, except two particular cases, identified by a triangle and a star, discussed in the text. Dashed line stands for the fitting of the $L - T$ relation for the whole sample.

$z = 1.5$ until $z = 0$. This evolution is illustrated by vectors starting (finishing) at the values for L and T at $z = 1.5$ ($z = 0$). All the vectors could be decomposed in two components representing the change in temperature and luminosity. Two special clusters deserve a particular discussion. The first one, represented by a triangle, has no arrow associated. This is due to the fact that this cluster has been classified as major merger but it marginally satisfies the 1:3 condition in the mass ratio. Therefore, it is a transition case between major and minor clusters, according to our definition of merger. However, as we will discuss later, consistently with its evolution in the $L - T$ plane, it behaves like the minor merger clusters. The second particular case, represented in the plot by a star, shows the evolution of a cluster with an extremely strong cooling flow at $z = 1.5$. A careful study of the radial temperature of this cluster at that time, shows an extremely relevant CC. During the evolution, the merger event substantially reduces the cooling flow, and disturbs the CC, although the cluster remains radiating. Interestingly, all clusters, except the one represented by the triangle, show a net increase in temperature. Concerning luminosity, letting aside the two particular cases just mentioned, the rest of clusters shows an increase in luminosity. We have performed a similar analysis for the minor merger clusters, and they do not show any clear trend and seem to behave very similar to the relaxed clusters.

There is a clear bias in the treatment of small clusters and groups. Nevertheless the results of our simulation are consistent with previous results, especially considering that it has not been introduced any other preheating or feedback mechanism, besides the one from the star formation (very poor in the present simulation) and the so-called gravitational heating (shock waves, mergers, etc). In any case, even though the sample can be limited, we wish to stress that the individual properties of each of the most massive clusters are well defined.

7.4 Discussion and conclusions

We have presented the results of a hydro and dark matter simulation of a moderate size volume of the Universe in the framework of a concordance cosmological model. The simulation follows the evolution of gaseous and dark matter components. Other relevant processes, like heating and cooling for a primordial gas, have been also taken into account.

The main idea of the present work has been to study the role of galaxy cluster mergers as source of heating of the ICM. The general picture of our simulation shows how mergers stirred the ICM by producing shocks and sound waves in scales comparable to the dimension of the cluster. These phenomena produce turbulence in the form of large eddies characterised by Reynolds numbers, $Re \sim 10^3$, which are values accessible to present-day numerical simulations (Ricker & Sarazin, 2001).

Recent work by Agertz et al. (2007) has shown, in some idealised situations, how the different numerical techniques, namely SPH and AMR, produce different results when describing the formation and evolution of eddies (Kelvin-Helmholtz) instabilities. According to this last reference, there are no substantial differences in results obtained with both techniques if the evolution time is smaller than the characteristic time of formation for Kelvin-Helmholtz instabilities, τ_{KH}. This characteristic time can be estimated for the case of a cluster merger assuming similar densities for the clusters, a characteristic length scale of a few hundred of kpc, and a relative velocity of the order of one thousand km/s; with all this conditions, τ_{KH} turns to be of the order of a few hundreds of millions of years.

In the particular case of galaxy cluster mergers, the typical time scales of evolution after a merger are much larger than this τ_{KH} and, therefore, it is likely that the particular numerical scheme used to simulate such scenario could play some role in the results. This has motivated us to study this problem by means of an AMR technique, and as a complementary work to the studies already published. Therefore, we have used an AMR Eulerian code especially designed for cosmological applications, with excellent capabilities to deal with strong gradients, shock waves, and low density regions. These kind of codes also describe properly some instabilities phenomena such as Kelvin-Helmholtz, Rayleigh-Taylor and, in general, turbulence and mixing processes (see the recent work by Mitchell et al., 2009).

In order to study the effect of mergers as heating source, we have extracted and followed the evolution of the galaxy cluster like haloes in our simulation. These haloes have been studied directly from the simulation and without any resimulating scheme. This has implied a limitation due to numerical restrictions. Since the numerical scheme has the tendency to better resolve the most massive

haloes, our sample is biased towards these systems. However, it is in those large systems where the effects of mergers would be more relevant. On the other hand, this apparently drawback of lack of resolution on small haloes, is compensated by the advantage that mergers can be followed in a consistent way as they naturally occur in the evolution of the simulated volume of the Universe. Thus, no controlled collisions have to be imposed beforehand.

We have assumed a definition of galaxy cluster merger depending on the mass ratio of the haloes involved in the merger. As additional condition, we have introduced a time limitation, in such a way that only mergers occurring in the recent past are taken into account. Thus, if masses are similar – between 1 and 1/3 – we define those events as major mergers. Events with larger ratios in masses are classified as minor mergers. Finally, clusters evolving without relevant merger events are designed as relaxed. Once we have assumed this criterion to group the clusters in our simulation, we have studied the radial profiles of each cluster for the gas and dark matter densities, temperature and entropy. In order to compare the main differences among the three classes, we have computed average profiles for each group. The forms of the different profiles are basically the same for the three categories, indicating no substantial changes in the physics of clusters. However, there is a trend in the normalisation. The relaxed and minor merger clusters have similar values of all quantities, whereas the major merger clusters are slightly hotter and with higher entropy.

The previously mentioned trends in entropy and temperature of clusters depending on their evolutionary history, can be quantify by looking at a representative cluster of each class and comparing the time evolution of their profiles of temperature and entropy.

In the same manner, the effects associated with cluster mergers can be traced in the time evolution of global quantities like the entropy in the inner 10% of the virial radius, the ratio of internal to kinetic energy, or the X-ray luminosity.

In all cases, cluster mergers release energy which ends up partially in the final object. The amount of energy locked in the final cluster is significantly larger for cluster mergers of similar masses (major mergers).

We have also considered all the clusters in the simulation without differentiating amid the merging activities. These results have been compared with previous simulations (Voit et al., 2005; Burns et al., 2008; Kay et al., 2007) and with observational data (Ponman et al., 2003; Vikhlinin et al., 2005; Pratt et al., 2007), paying special attention to the entropy and temperature profiles. Our results seem to be consistent with both, simulations and observations, in an average sense. However, there are still important differences like the lack of central drops in the temperature profiles of the most massive clusters.

The fraction of clusters in our sample that has cool cores has been computed at several redshifts. At $z = 0$, our results are fully compatible with previous AMR simulations by Burns et al. (2008), although seem to differ with the results of the SPH simulation by Kay et al. (2007). We have compared the fraction of cool cores in our simulation with the observational data by Chen et al. (2007) showing a similar trend, that is, the number of clusters with cool cores decreases with the cluster mass.

Given the fact that in our simulation the gravitational heating is the relevant

feedback mechanism, we have tried to correlate the merger events with the existence of cool cores. In order to do so, we have computed the fraction of relaxed clusters (no merger activity) as a function of the cluster mass. Interestingly, the fraction of clusters with cool cores, and the fraction of relaxed clusters as function of the cluster mass, show a very similar trend. Unfortunately, the absolute numbers of CCs in our simulation and the observations are quite different. We suggest two possibilities explaining this discrepancy. The first one would be related with the fact that no metal-dependent cooling has been considered in the simulation. This simplification could make the cooling more inefficient, especially at the central regions of the clusters. The second reason would be linked with a lack of resolution, which appears to be quite unlikely given the actual features of the considered simulation. In any case, it seems clear that there is an evident link between the merger events and the no existence of cool cores.

On the other hand, the time evolution of the fraction of cool cores shows that this quantity has not changed substantially from $z \sim 0$ to $z \sim 1$. This result is compatible with previous simulations (Burns et al., 2008) but in disagreement with observational data (Vikhlinin et al., 2006a).

The cluster sample analysed in this application is limited due to the fact that no resimulations have been done and, therefore, although an AMR code has been used, there are still resolution limitations. Nevertheless, we have analysed the scaling relations derived from our sample. At $z = 0$, our results for $L \propto T^{2.5}$, $M \propto T^{1.5}$, and $S \propto T^{0.9}$ are consistent with previous results that do not introduce any extra reheating or feedback.

We have found some degree of segregation in the scaling relations (even at moderate high redshifts) depending on whether the clusters have or have not undergone a recent merger. The systems that have experienced merger events are usually located at high temperatures, luminosities, masses, and entropies, respectively, at the different scaling relation plots. These results could be comparable with recent works looking at the existence or not of cool cores in clusters (Burns et al., 2008; Poole et al., 2008). The analysis of the time evolution of major merger clusters in the $L-T$ relation, has shown that these clusters have a tendency to move towards regions of this relation with higher temperature and luminosity. This tendency is similar to that found in Hartley et al. (2008), where authors investigate the $L-T$ relation in a large simulation with a strong preheating.

A clear improvement for future work would be to increase the number of clusters in the sample by simulating larger volumes with higher resolution. Therefore, it would be feasible to reliably study the scaling relations for each one of the three families of clusters that we have considered. In any case, even when the sample can be limited, the individual properties of each of the most massive clusters are well defined.

The role of mergers as source of heating, transferring part of the gravitational energy to the thermal energy, is still a matter of debate and study. Mergers are crucial to understand galaxy cluster formation and galaxy formation scenarios as they influence directly the ICM properties. Simulations with higher resolution and including more physical processes are needed in order to keep on quantifying the role of mergers in the hierarchical scenario of structure formation. In parallel, some results from simulations, like the ones presented here, can be considered in

semi-analytical models in order to improve their description of the gas component.

We would like to emphasize that our main approach in this Thesis, analysing the effect of a source of gravitational heating like galaxy cluster mergers in a full cosmological scenario, is completely complementary, and not excluding, of other works including different feedback processes both in a full cosmological context or in idealised and isolated experiments. All these approaches are extremely useful and necessary. However, we strongly believe that, with the recent advancements in theoretical, computational, and observational facilities, it is extremely important to increase the number of numerical studies following this line, that is, an strictly self-consistent cosmological approach. In the next years, an interesting challenge for current cosmological simulations would be to include and describe as many physical processes as possible with an improved resolution and in a full cosmological context in order to bring closer theoretical results with the next generation of observational data to come. In this sense, an accurate numerical description of gravitational processes inherent to the cosmic evolution itself will be also crucial.

Chapter 8

Cosmological shock waves

After analysing the role that galaxy cluster mergers play in the thermodynamical properties of the ICM, we begin a new but natural line of research devoted to analyse the role that shock waves have in the hierarchical model of structure formation. In the present Chapter, we focus on the qualitative description of structure formation shock waves in cosmological simulations.

8.1 Introduction

According to N-body/hydrodynamical simulations, cosmological shock waves develop as a consequence of the hierarchical formation of structures in the Universe. In addition, shocks produce heating, in a sense of energy redistribution, as they travel through the surrounding medium. Consequently, they encode information about structure formation and their thermal effects on the gas.

We classify cosmological shocks in two broad categories: external and internal shocks. External shocks surround filaments, sheets, and haloes, while internal shocks are located within the regions bound by external shocks and are created by flow motions correlated with structure formation and evolution. On large scales, the thermal history of galaxy clusters is dominated by the infall of material onto dark matter haloes and the conversion of gravitational potential energy into thermal energy of the gas. This process occurs through the heating of the gas via strong (external) accretion shocks surrounding galaxy clusters and filaments (e.g., Ryu et al., 2003; Miniati et al., 2001; Pfrommer et al., 2006). Inside collapsed structures, weaker (internal) shocks can be subdivided in three different classes: (i) accretion shocks caused by infalling gas between different cosmic structures, (ii) merger shocks resulting from merging haloes, and (iii) random flow shocks inside nonlinear structures produced during hierarchical clustering. These internal shocks contribute to the virialization of haloes.

The existence and characterization of these cosmological shocks is important for the following reasons, among others:

1. Shock waves can transfer the most part of the gravitational energy associated with the hierarchical formation into thermal energy of the ICM, thus

increasing its entropy and its pressure support.

2. The warm-hot intercluster medium (WHIM), at temperatures of $10^5K - 10^7K$, (Davé et al., 1999; Cen & Ostriker, 1999) is produced by the thermalization of gas at the accretion shocks surrounding large scale filaments and sheets. The evolution of gas in the WHIM phase is given, among other factors, by the history of the mass flux through these shocks (Pfrommer et al., 2008).

3. In some applications taking into account electromagnetic fields, it is possible for thermal particles to be accelerated and transformed into non-thermal populations of cosmic rays (CRs) through the process of diffusive shock acceleration (DSA; e.g. Drury & Falle, 1986; Blandford & Eichler, 1987). As a result of this process, a fraction of the kinetic energy of shocking gas can be converted into both thermal and non-thermal components (Kang et al., 2002; Kang & Jones, 2005; Kang et al., 2007). The CR electron populations are likely sources of radio haloes and radio relics in galaxy clusters (Pfrommer et al., 2008), while the CR protons may be sources of γ-ray emission through their interactions with gas protons. Therefore, simulating realistic CR distributions within galaxy clusters will provide detailed predictions for the expected radio synchrotron and γ-ray emission.

To date, studies of cosmological shocks have included observational, theoretical, and numerical approaches:

Observational approach. Strong shocks usually develop in the external low-density regions of galaxy clusters where the X-ray emission is weak. As a consequence, from an observational point of view, detecting shocks in the LSS is still challenging. From this approach, the most part of the work surrounding cosmic shocks is related to radio relics (e.g., Ensslin et al., 1998), of which only a few have been studied in detail. In a few cases, however, internal shocks driven by merging events have been observed with very low ($\approx 1.5 - 3$) Mach numbers[1] (e.g., Markevitch et al., 1999, 2002; Markevitch & Vikhlinin, 2007).

Theoretical approach. There are basically two methods: (i) modifying the Press-Schechter formalism (Press & Schechter, 1974; Sheth & Tormen, 1999; Pavlidou & Fields, 2006) to deduce the mass function of accreting objects and their interactions with infalling material; (ii) semi-analytical attempts to describe merger shocks (e.g., Fujita & Sarazin, 2001; Gabici & Blasi, 2003). These approaches however are limited as they treat cluster mergers as binary encounters between ideally virialized spherical systems. In addition, it is quite difficult to account for the complex morphologies that arise during structure formation using purely analytical frameworks.

Numerical approach. Numerical techniques using hydrodynamical simulations are essential to deepen in the understanding of cosmological shock waves.

[1]The Mach number, which characterizes the strength of shocks, is defined in Eq. 8.1.

There have been numerical studies of shocks using both Eulerian, "single-grid" (e.g. Quilis et al., 1998; Miniati et al., 2000; Ryu et al., 2003; Kang et al., 2007; Vazza et al., 2009) and "AMR-grid" approaches (Skillman et al., 2008), as well as SPH codes (e.g., Pfrommer et al., 2006, 2008). As explained in previous chapters, there are advantages and disadvantages of both methods. However, the main advantage of an Eulerian over a Lagrangian code is its excellent shock-capturing properties.

First attempts to characterize shock waves in cosmological simulations were produced by Quilis et al. (1998) and Miniati et al. (2000). They employed fix grid Eulerian simulations and shock detecting schemes based on jumps in the main thermodynamical quantities. Later works adopted more refined shock-detecting algorithms and were more focused onto the distribution of energy dissipated at shocks (e.g., Ryu et al., 2003; Pfrommer et al., 2006; Vazza et al., 2009). However, in these first works using uniform grid-based codes, it was not possible to recover the spatial resolutions required to describe both the complex flow within haloes and their coupling to large scale structures. Further improvement has been reached by Skillman et al. (2008) using a shock detecting scheme looking for shocks in the direction of the temperature gradients on an AMR grid.

In spite of all these works, the identification and characterization of shocks is still challenging because of the complex dynamics involved in the formation and evolution of cosmological structures. In addition, if we have into account the physical and numerical limitations that affect present-day cosmological simulations, the problem becomes even more difficult.

In this Chapter, our purpose is to analyse the main qualitative and statistical properties of shock waves developed during the evolution of a large cosmological simulation performed with the MASCLET code. In particular, the simulation that we will analyse is the one described in Section 6.5.1 (see this section for further details on the performance and the results of the simulation). To study the shock waves we have developed a numerical algorithm able of detecting and characterizing shocks in 3-D AMR simulations. The use of AMR allows us to obtain very good dynamic ranges with an advanced hydrodynamical code that is able to capture shocks very accurately.

8.2 Detecting shock waves

8.2.1 Basic relations

Shocks produce irreversible changes in the gas in galaxy clusters. As a consequence, the evolution of a shock in a simulated volume produces a jump in all the thermodynamical quantities. If we assume that the pre-shocked medium is at rest and in thermal and pressure equilibrium, the pre-shock and post-shock values for any of the hydrodynamical variables are unambiguously related to the shock Mach number, $\mathcal{M}$. The Mach number, which characterizes the strength of a shock, is given by

$$\mathcal{M} = v_s/c_s, \tag{8.1}$$

where v_s is the shock speed in the region, and c_s is the sound speed ahead of the shock itself.

All the information needed to evaluate $\mathcal{M}$ is contained in the Rankine-Hugoniot jump conditions. If the adiabatic index is set to $\gamma = 5/3$ we obtain, for the density (ρ), the temperature (T), and the entropy ($S = T/\rho^{\gamma-1}$), the well-known relations:

$$\frac{\rho_2}{\rho_1} = \frac{4\mathcal{M}^2}{\mathcal{M}^2 + 3} \tag{8.2}$$

$$\frac{T_2}{T_1} = \frac{(5\mathcal{M}^2 - 1)(\mathcal{M}^2 + 3)}{16\mathcal{M}^2} \tag{8.3}$$

$$\frac{S_2}{S_1} = \frac{(5\mathcal{M}^2 - 1)(\mathcal{M}^2 + 3)}{16\mathcal{M}^2}\left(\frac{\mathcal{M}^2 + 3}{4\mathcal{M}^2}\right)^{2/3} \tag{8.4}$$

with indices $1, 2$ referring to pre and post-shock quantities, respectively.

The Mach number can be obtained from the jumps in any of the hydrodynamical variables (Eqs. 8.2–8.4) or from a combination of them. In the case of relatively large Mach numbers, since the value of the density jump saturates at $\rho_2/\rho_1 = 4$ (Eq. 8.2), strong shocks cannot be detected from density jumps. As a consequence, the most effective methods to measure $\mathcal{M}$ are those considering temperature and entropy jumps.

Nevertheless, because of the limitations of the considered numerical schemes, the estimate of the shock Mach numbers in simulations by means of these equations is subjected to unavoidable uncertainties with respect to the ideal case (Eqs. 8.2–8.4).

8.2.2 Shock-finding algorithm

The objective of any shock-finding method relies on accurately identifying and quantifying the strength of shocks. During the simulations, shocks are automatically detected by the Riemann solver within the hydrodynamical routine. However, to perform an analysis of these shocks, additional considerations are necessary.

Our shock-finding algorithm proceeds according to the following steps:

1. The first step consists in classifying all the cells within the computational volume as shocked or not shocked cells. A cell is labelled as shocked if the fluid inside the cell meets the following requirements:

$$\nabla \cdot \mathbf{v} < 0 \tag{8.5}$$

$$\nabla T \cdot \nabla S > 0 \tag{8.6}$$

   where $\mathbf{v}$, T and S are, respectively, the velocity field, the temperature and the entropy of the fluid (gas) within the cell.

2. Among all the shocked cells, we identify the first shock centre with the position of the shocked cell where $\nabla \cdot \mathbf{v}$ is minimum.

3. Now, a directional splitting approach is applied: moving outwards from the shock centre, and along each of the coordinate axes, we look for the sense of shock propagation and define the limits of the shocked region along each axis. These limits are given by the first cells outside (behind and ahead) of the shocked region. In order to fit properly the extension of the shock along each coordinated direction, the temperature and the density in the pre- and post-shock regions must satisfy the following conditions:

$$T_2 > T_1 \tag{8.7}$$

$$\rho_2 > \rho_1. \tag{8.8}$$

   The shock discontinuity in the simulation is typically spread over a few cells.

4. Once the furthest pre- and post-shock cells in each coordinated direction are found, the temperatures T_1 (pre-shock) and T_2 (post-shock) are taken and three different Mach numbers (one for each direction) are calculated from Eq. 8.3.

5. Finally, the Mach number of the shocked region (associated to the shock centre) is computed by combining the Mach numbers measured along the three coordinate axes: $\mathcal{M} = (\mathcal{M}_x^2 + \mathcal{M}_y^2 + \mathcal{M}_z^2)^{1/2}$, which minimizes projection effects in case of diagonal shocks (e.g., Vazza et al., 2009).

In this way, all the shock centres within the computational box are characterized by a Mach number. The assembly of all these shocks defines the characteristic shock surfaces associated to shock waves.

We perform this analysis on the most highly refined grids first and move down to progressively coarser levels of resolution. Given that this procedure is applied, independently, at each level of refinement of the simulation, the algorithm is able to find, in a natural way, shock waves related to different cosmological scales provided by the simulation itself. However, the use of an AMR grid makes the process slightly more complicated, especially when a shock is extended along more than one patch in a given level of resolution. Thus, some caution must be taken when defining the extension of shocks on the different levels of refinement.

In the analysis performed below, in order to avoid noisy shock patterns with very low Mach numbers, we have considered a Mach number minimum threshold equal to 1.3.

8.3 Results

8.3.1 Distribution of large scale shocks

Shocks fill the simulated volume in a very complex pattern (e.g., Miniati et al., 2000; Ryu et al., 2003). Figure 8.1 illustrates typical structures found in large scale cosmological simulations. The different panels represent slices of 10 Mpc thickness and 64 Mpc side length showing the gas density contrast (upper left), the gas temperature (upper right), the gas entropy (lower left) and the Mach number (lower right) distributions at $z = 0$. All the panels show the logarithm of the

different quantities. All these projections are centred at the position of the largest cluster in the simulation ($M_{vir} \sim 8.0 \times 10^{14}\, M_{\odot}$) which is almost in the centre of the box. A global inspection of this figure provides a lot of information. For instance, the galaxy clusters, located in large high-density regions with high temperatures ($\geq 10^7 K$), are clearly visible. Contrarily, large black regions in the density and temperature maps show voids which cool down during cosmic evolution. On the other hand, the spatial Mach number distribution, which reflects the nonlinear structures and voids of the density and temperature maps, allows us to see the structure of cosmological shocks showing both the external high-Mach number shocks as well as the internal shocks.

The cosmic evolution of shock strengths provides valuable information about the thermal history of the baryonic component of the Universe. Figure 8.2 shows the evolution with redshift of the fraction of the shocked simulated volume (left panel), together with the volume-weighted mean Mach number (right panel) for each epoch. We find that at high redshift ($z \geq 6$), approximately the 30% of the simulated volume is shocked. Although the shocked cells are distributed throughout the volume, the number of shocked cells increases in denser environments. As the temperature of the gas in the simulated volume increases, the Mach number distribution at redshift $z \sim 2-6$ becomes steeper and dominated by weak shocks. As the evolution advances, temperature in low density regions gradually decreases and the Mach number distribution becomes gradually flatter. Simultaneously, the fraction of the simulated volume that is shocked reaches a value of $\sim 20\%$ at $z = 0$. This general behaviour is consistent with previous results obtained by Vazza et al. (2009).

Another interesting issue concerning the distribution of shock waves has to do with the distribution function of shocks as a function of their Mach number. In Fig. 8.3 we show the Mach number distribution of the shocks detected in our simulated volume at $z = 0$. Logarithmic bins for the Mach number are considered. The differential distribution shown in this figure is quite steep and dominated by weak shocks. Moreover, it clearly presents two different trends which can be perfectly fitted by two different power laws of the form $dN(\mathcal{M})/d\mathcal{M} \propto \mathcal{M}^{\alpha}$. For low Mach numbers (up to $\simeq 20$) we obtain a slope of $\alpha \simeq -1.7$, whereas for stronger shocks a steeper relation ($\alpha \simeq -4.1$) is found. This turn in the Mach number distribution function of shocks, located around $\mathcal{M} \simeq 20$, clearly shows the transition between two different regimes. As we will deduce from the analysis of Fig. 8.7, shocks with Mach numbers lower than $\simeq 20$ correspond, mainly, to internal shocks placed within the virial regions of galaxy clusters. Contrarily, the most part of the stronger shocks (above $\mathcal{M} \simeq 20$) could be associated to outer, external shocks. For the sake of clarity, Fig. 8.3 only shows the Mach number distribution of shocks at $z = 0$. However, we have also looked at the time evolution of this relation for several redshifts. According to this evolution, we have observed a similar trend in almost all the considered epochs. The main difference between the distributions obtained at different moments is in the high-Mach end of the relation, which slowly moves down to lower values when decreasing redshift. We need to reach quite high redshifts ($z \geq 6$) to appreciate an important change in the shape of this distribution.

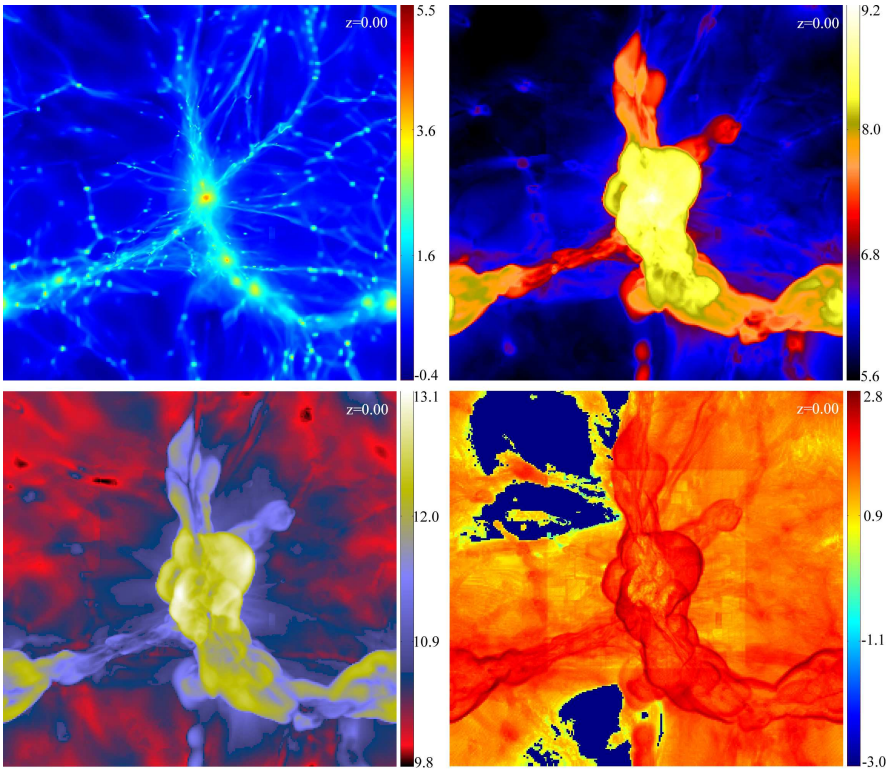

Figure 8.1: Large scale thermodynamical distributions at $z = 0$. Each panel is a slice of 10 Mpc thickness and 64 Mpc side length. They show the gas density contrast (upper left), the gas temperature (upper right), the gas entropy (lower left) and the Mach number (lower right) distributions, respectively. All these quantities are in logarithmic scale.

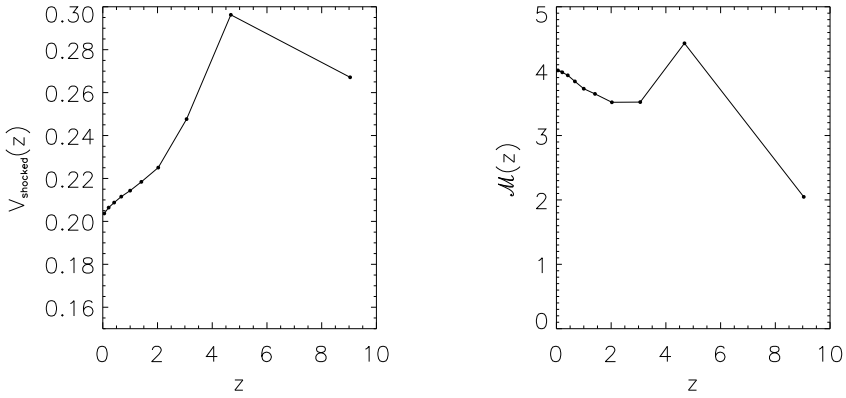

Figure 8.2: Left: fraction of the simulated volume hosting shocks as a function of redshift. Right: mean volume-weighted Mach number as a function of redshift.

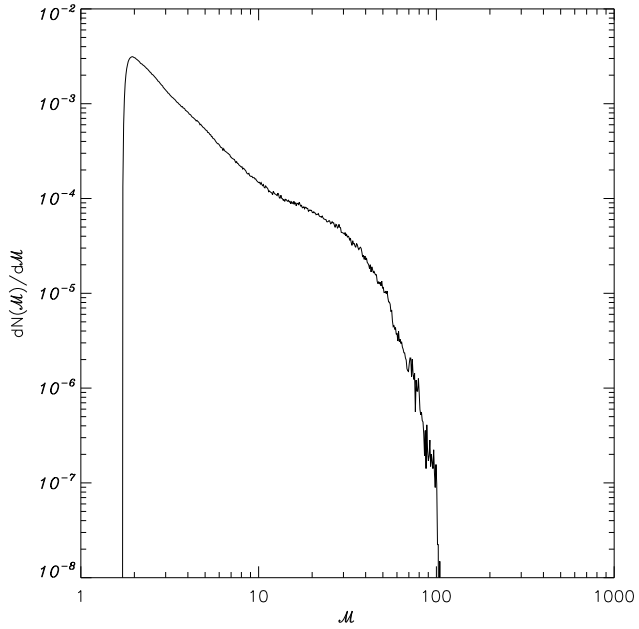

Figure 8.3: Distribution function of shocks at $z = 0$ as a function of their Mach number in logarithmic bins.

8.3.2 Shock waves and galaxy clusters

In this Section we are interested in studying the spatial distribution of cosmological structure formation shocks and the possible correlations with the population of dark matter haloes found within the computational box.

Figure 8.4 shows a 2-D projection along the z axis of the Mach number distribution (upper left panel) and the gas, DM and stellar densities (upper right, lower left, and lower right panels, respectively) at $z = 0$. Each panel represents a slice of 0.2 Mpc thickness and 64 Mpc side length centred at the same position than in Fig. 8.1. All these quantities are in logarithmic scale. In all these panels, the contours of the shock waves with higher Mach numbers are superposed.

A visual inspection of this figure clearly shows how the different shock patterns follow the shape of the cosmic web. Filaments, sheets, and haloes are surrounded by strong ($\mathcal{M} >> 20$) external shocks. The external shocks around galaxy clusters, at a distance of several virial radius from the cluster centre, have typically quasi-spherical shaped boundaries. Moving inwards the virial radius of clusters, more irregular and weak shocks ($\mathcal{M} \leq 5$) are visible. These internal shocks are basically associated to random flow shocks and merger events within the clusters.

This general pattern is also visible in Fig. 8.5 where we compare the distribution of shock waves with high Mach numbers (given by the contour lines) with the spatial distribution of the dark matter haloes found in the simulation at $z = 0$. This figure shows the same slice than in Fig. 8.4. The represented dark matter haloes have been found with the ASOHF code and are those analysed in Section 6.5.1. These haloes are plotted as circles whose sizes represent their virial radius. Only objects with masses larger than $10^{12}\, M_{\odot} h^{-1}$ are considered. We point out in red those haloes whose positions perfectly fit in the considered slice. The most interesting feature of this figure is the complexity of shocks around galaxy clusters. As a consequence of the hierarchical formation of clusters, multiple external shocks form and extend over a region of several Mpc size around them.

The distribution of Mach numbers within the virial radius of the haloes is shown in Fig. 8.6. In this figure we plot an histogram of the distribution, at redshift zero, of the number of haloes (N) as a function of the Mach number ($\mathcal{M}$) of the shocks within the virial radius of haloes. Since these internal shocks are spread over a quite wide region within the haloes, we note that their associated Mach numbers are relatively small, mostly in the range $\sim$ 1–10, with several important peaks between 1 and 5. The mean mass-weighted Mach number within the virial radius for all the sample of haloes is $\mathcal{M} \simeq 5.1$.

From the analysis of these figures, we can deduce that the most part of shocks in the Universe are relatively weak although there is also an important population of stronger shocks surrounding large scale structures. These results are broadly consistent with previous works in literature (e.g., Ryu et al., 2003; Pfrommer et al., 2006; Vazza et al., 2009).

Figure 8.7 shows the distribution of the virial mass of haloes as a function of the mean volume-weighted Mach number within their virial radius. The different panels of this figure show this distribution at $z \simeq 2, 1, 0.4$, and 0, respectively. In all the panels, the shaded regions have been computed by binning individual haloes into a two-dimensional grid. Six contour lines equally spaced are plotted to highlight the two-dimensional distributions. Again, only haloes with $M_{vir} >$

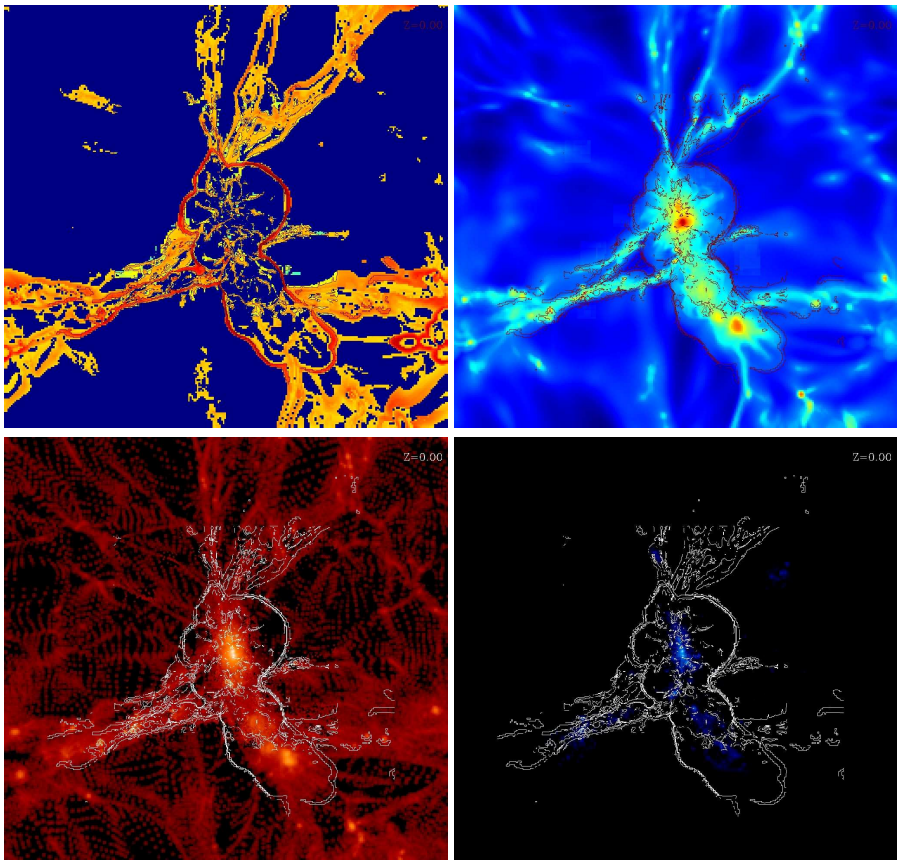

Figure 8.4: Distributions of Mach number vs DM, gas and stellar densities at $z = 0$. Each panel is a slice of 0.2 Mpc thickness and 64 Mpc side length. They show the Mach number distribution (upper left) and the gas, DM and stellar densities (upper right, lower left, and lower right panels, respectively). All these quantities are in logarithmic scale. In all the panels, we overplot the contours of the shock waves with high Mach numbers.

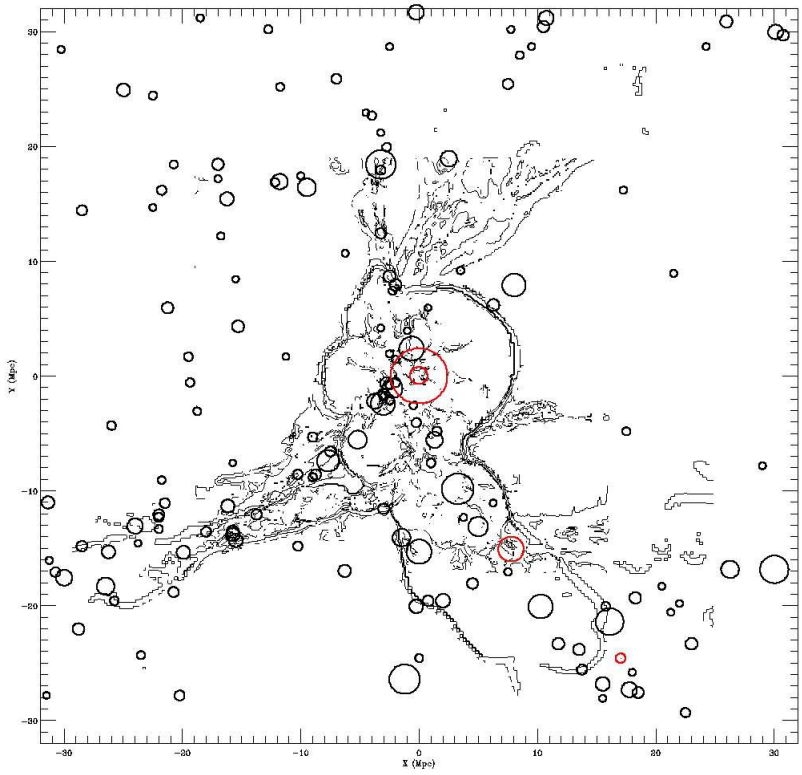

Figure 8.5: Distribution of dark matter haloes together with shock waves at $z = 0$. The solid lines represent six contour levels of the shock waves of higher Mach numbers. This contour has been computed for a slice of the simulated box of 0.2 Mpc depth and 64 Mpc side length. Circles stand for all the found haloes with masses larger than $\geq 10^{12}\, M_{\odot} h^{-1}$. We point out in red those haloes whose positions fit in the considered slice. The size of the circles represent the virial radius of the haloes.

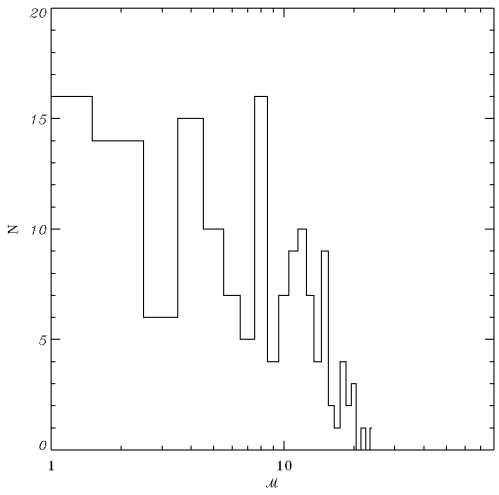

Figure 8.6: Histogram showing the distribution of haloes with masses larger than $\geq 10^{12}\, M_{\odot} h^{-1}$ at $z = 0$ as a function of the mean volume-weighted Mach number within their virial radius.

$10^{12}\, M_{\odot}$ are considered. Several conclusions can be obtained from an inspection of these panels. If we analyse the distribution at $z = 0$ (lower right panel), there are two clearly differentiated trends. On the one hand, there is an almost constant region, for low Mach numbers between $\mathcal{M} = 1.3 - 5$, which seems to be no-dependant on the mass of the haloes. These low Mach number shocks could stem from the primordial formation of clusters and are more visible in structures which have reached an equilibrium state. On the other hand, a steeper trend along all the range of Mach numbers seems to be correlated with halo masses and could represent the shocks taking place during the hierarchical evolution of the structures as a consequence of mergers and accretion processes.

If we make a global analysis of all the panels, a bimodal distribution is also observed through the evolution. At the epoch of cluster formation, $z \sim 2$, an L-like pattern in the plane $\mathcal{M} - M_{vir}$ has been developed. In general, complex shock waves are already formed at high redshifts within the virial region of protoclusters. When advancing in time, the initial pattern tends to progressively fall down to higher masses but lower Mach numbers, reaching the bimodal distribution explained at $z = 0$.

In order to understand this behaviour, we have followed the global evolution of individual haloes looking at their overall drifts along the plane $\mathcal{M} - M_{vir}$. We have studied this evolution for the 16 more massive haloes in the simulation which, indeed, are the best numerically resolved. The haloes in this subsample evolve according to two different behaviours. Roughly the 60% of this subsample of haloes begin, at high redshift, with a relatively high Mach number and evolve to progressively lower Mach numbers while increasing their mass. The remaining

percentage of haloes depart from a low ($\mathcal{M} < 5$) Mach number and tend to move, during their evolution, almost parallel to the x-axis while augmenting their mass. Since our sample of haloes is far from being statistically complete we can not make a robust conclusion. However, our hypothesis to explain this behaviour is that the evolution of haloes along the plane $\mathcal{M} - M_{vir}$ is intimately related with their dynamical history. Like a gross trend, those haloes suffering important merger events (major mergers) early in their evolution only can evolve towards lower Mach numbers while reaching an equlibrium state, producing, therefore, the decline of the initial L-like pattern into the flatter final distribution. On the other hand, haloes with a relatively quiet evolution evolve without significant changes in their virial Mach number and, consequently, they move almost parallel to the M_{vir}-axis while increasing their mass.

Another interesting feature of this figure is that the mean Mach number of the overall sample of haloes at different redshifts tends to move progressively from higher values ($\mathcal{M} \simeq 10$), at high redshift, down to lower values ($\mathcal{M} \simeq 5$), at $z = 0$. This decrease of the mean Mach number is consistent with the picture in which haloes evolve towards an equilibrium state. In any case, independently of the considered epoch, the mean Mach number of the bulk of haloes is lower than 20. This value, which perfectly correlates with the turn observed in the Mach number distribution function shown in Fig. 8.3, clearly shows the transition between external and internal shocks.

8.4 Conclusions and future directions

In this Chapter we have studied some qualitative and statistical properties of the shock waves developed during the hierarchical evolution of the Universe in a large cosmological simulation. The simulation, performed with the MASCLET code, assumes a ΛCDM model.

To analyse the shock waves we have developed a numerical algorithm able of identifying shocks in 3-D AMR simulations. After labelling all the shocked cells (compression regions with $\nabla \cdot \mathbf{v} < 0$) within the computational box, the Mach numbers of the shocks are computed by means of the Rankine-Hugoniot temperature-jump condition. An important point here is that, thanks to the Eulerian scheme of the MASCLET code, we are able to obtain a good dynamical range and detect shocks with a good accuracy.

We have analysed several aspects of interest associated to the detected shock waves:

- In agreement with previous studies, the morphology of the different shock patterns detected in our simulated volume is quite complex. These patterns follow the shape of the cosmic web: filaments, sheets, and haloes are surrounded by strong external shocks while more irregular and weak shocks are found within the virial region of galaxy clusters. External shocks surrounding galaxy clusters show quasi-spherical shaped boundaries.

- At $z = 0$ we find that roughly the 20% of the simulated volume is shocked with a mean Mach number of $\simeq 4$.

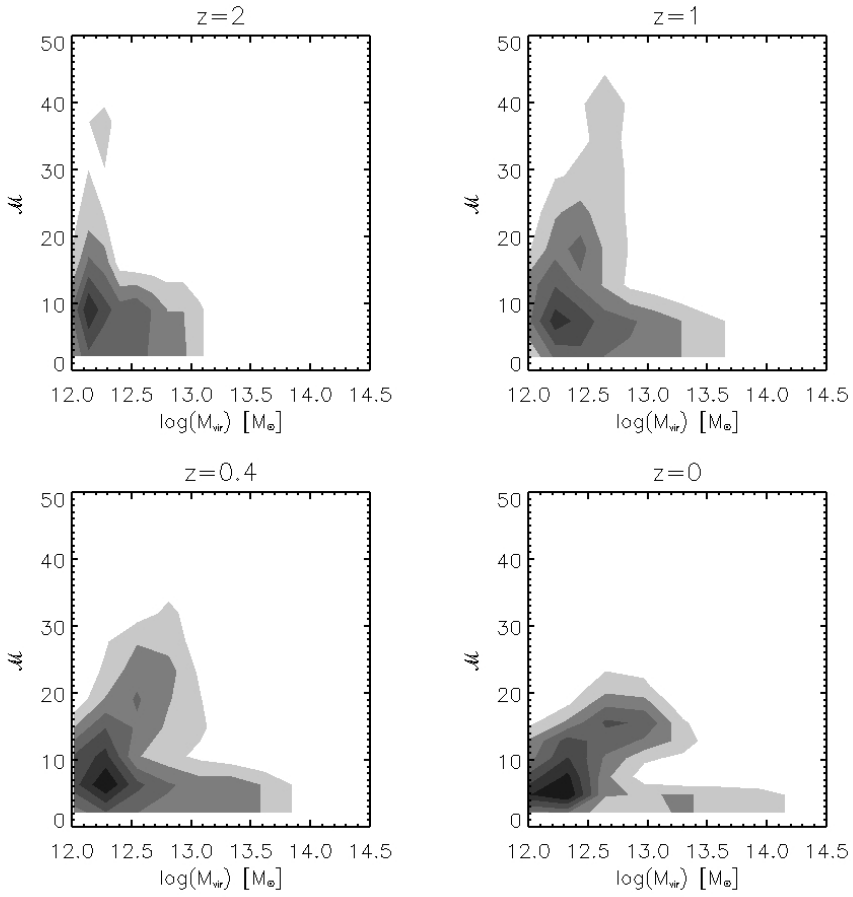

Figure 8.7: Distribution of the virial mass of haloes as a function of the mean Mach number within their virial radius. Results at $z \simeq 2, 1, 0.4$, and 0, are shown. The shaded regions have been computed by binning individual haloes into a two-dimensional grid in the plane $\mathcal{M} - M_{vir}$. Six contour lines equally spaced are plotted to highlight the two-dimensional distributions.

- We have also studied, at $z = 0$, the differential number distribution of shocked cells within the simulated volume as a function of the shock Mach numbers. We find that the most part of cosmological shocks are essentially weak shocks ($\mathcal{M} \leq 2$). In addition, we have fit this distribution by two different power laws with this form $dN(\mathcal{M})/d\mathcal{M} \propto \mathcal{M}^{\alpha}$. For low Mach numbers (up to $\simeq 20$) we obtain a slope of $\alpha \simeq -1.7$, whereas a steeper relation ($\alpha \simeq -4.1$) is found for stronger shocks. This turn shows the transition between the scales associated to internal and external shocks, respectively.

- We have also tried to correlate the shock waves with the population of galaxy clusters within the computational box.

  In this sense, we have found that the mean Mach number within the virial radius of haloes at $z = 0$ is $\mathcal{M} \approx 5$. Attending to the evolution, the mean Mach number of the population of haloes at a given epoch is always below a value of ≈ 20. This value is in agreement with the turn observed in the Mach number distribution function and indicates the transition between two different scales.

  When representing the mean Mach number inside the virial radius of haloes as a function of their masses, we have found at $z = 0$ two well-separated trends. On the one hand, there is an almost constant line for low Mach numbers (up to 5) which seems to be no-dependant on the mass of the haloes. These low Mach number shocks could stem from the primordial formation of clusters and are more visible in structures which have reached an equilibrium state. On the other hand, a steeper trend along all the range of Mach numbers seems to be correlated with halo masses and could represent the shocks taking place during the hierarchical evolution of the structures as a consequence of mergers and accretion processes. Our hypothesis to explain this behaviour is that the evolution of haloes along the plane $\mathcal{M} - M_{vir}$ is intimately related with their merging history.

According to these preliminary results, several projects need to be addressed in the near future. For instance, the role played by cosmological shock waves from an energetic point of view and their consequences for cosmology will be an interesting topic for future works. It would be also very important to analyse how the mass and spatial resolutions of the considered simulation can affect the obtained results. Another interesting point could be to correlate more directly the events of shock formation with the cluster dynamics. Linking with the observations, since the strength of the outer accretion shocks onto haloes depends on the mass of the gravitating object, it can be used as an independent measure of cluster mass. This could be a powerful new tool for cluster mass estimation if we are able to observe the accretion shocks with radio observations (e.g., Giacintucci et al., 2008).

What is obvious is that shock waves play a crucial role in galaxy clusters as well as in the thermalization of the ICM. However, direct evidence of shocks, both from the cosmic web formation processes and those due to cluster merging activity, has been found only in a small number of clusters thanks to observations of radio relics and temperature jumps in X-rays. Thus, we need more observations together with theoretical and numerical predictions to deepen in the role that shock waves have in the hierarchical assembly of cosmic structures.

Chapter 9

Summary and future directions

During the period of time spent in this Thesis I have been involved in both theoretical and numerical research, as two important and complementary ingredients, focusing on the characterization, formation and evolution of clusters of galaxies as well as in the physical properties of the ICM. All my work has been framed in the field of Numerical Cosmology and devoted to compare numerical results with observational data.

Regarding the numerical part of the Thesis, I have made progress in several lines:

- **Cosmological simulations.** I have become an advanced user and developer of the cosmological code MASCLET (Quilis, 2004). MASCLET is an Eulerian coupled hydrodynamical and N-body code for cosmological applications based on an AMR scheme. During the last years, I have been directly involved in the new developments carried out in the MASCLET code, namely, the inclusion of star formation and the metal-dependent cooling. In addition, I have personally carried out several simulations which have been used for the study of different physical scenarios.

- **The ASOHF halo finder.** To benefit from the use of a cosmological code like MASCLET, I have developed from scratch a new halo finder algorithm able to analyse the outputs of such complex cosmological codes. This Adaptive Spherical Overdensity Halo Finder (ASOHF; Planelles & Quilis, 2010) was originally designed to be coupled to an Eulerian cosmological code. However, in its actual version it is a stand-alone halo finder capable of analysing the outputs from cosmological simulations including different components, i.e., dark matter, gas, and stars.

  The ASOHF halo finder has been intensively and extensively tested and compared with other well-known halo finder algorithms in the largest halo-finder comparison project to date (*Haloes gone MAD: The Halo-Finder Comparison Project*, submitted by Knebe et al., 2010).

Besides this numerical part, I have also analysed some physical processes affecting the ICM properties and hence galaxy clusters:

- **Galaxy cluster mergers.** Making use of MASCLET and ASOHF, the first physical application was devoted to discuss the role that galaxy cluster mergers play as a source of feedback and reheating of the ICM in a full cosmological context (Planelles & Quilis, 2009).

  Different mechanisms of heating as well as non-gravitational processes have been included in simulations trying to solve the self-similarity breaking observed in the scaling relations. In the case of galaxy clusters, the processes of hierarchical merging and accretion are particularly energetic and, therefore, merger events can also be an important source of gravitational heating. They can produce shocks and compression waves in the haloes which eventually can release part of the energy associated with the collision as thermal energy in the final system.

  As for the simulations, although is still a matter of debate, it has been shown, at least for some idealised tests, that some results could depend on the ability of different numerical techniques – namely, SPH or grid codes – to properly describe some of these phenomena. Then, it seems reasonable to think that these inherent numerical discrepancies could translate into relevant differences when they are applied to more complex and realistic scenarios like galaxy clusters. This has motivated us to study this problem by means of an AMR technique, and as a complementary work to the studies already published.

  In this study, in which a simulation with only gravitational heating was analysed, we payed special attention to discuss the role of merger events on the existence of CCs in clusters and their relative abundances. In this regard, we have obtained several relevant results. The fraction of CC clusters in our sample was computed at several redshifts. At $z = 0$, our results are fully compatible with previous AMR simulations by Burns et al. (2008), although seem to differ with the results of the SPH simulation by Kay et al. (2007). When comparing with observational data by Chen et al. (2007), our results show a similar trend, that is, the number of clusters with CCs decreases with the cluster mass. Unfortunately, the absolute numbers of CCs in our simulation are lower than those by Chen et al. (2007). The most plausible explanation that we suggest for this discrepancy would be related with the fact that no metal-dependent cooling was considered in the simulation. This simplification could make the cooling more inefficient, especially at the central regions of the clusters.

  On the other hand, the time evolution of the fraction of CCs shows that this quantity has not changed substantially from $z \sim 0$ back to $z \sim 1$. This result is compatible with previous simulations (Burns et al., 2008) but in disagreement with observational data (Vikhlinin et al., 2006a).

  As for the different scaling relations, we have also found some degree of segregation (even at moderate high redshifts) depending on whether the clusters have or have not undergone a recent merger event. The systems that have

experienced merger events are usually located at high temperatures, luminosities, masses, and entropies, respectively, at the different scaling relation plots. These results could be comparable with recent works looking at the existence or not of CCs in clusters (Burns et al., 2008; Poole et al., 2008). The analysis of the time evolution of major merger clusters in the $L-T$ relation, has shown that these clusters have a tendency to move towards regions of this relation with higher temperature and luminosity. This tendency has also been confirmed in other simulations (e.g., Hartley et al., 2008).

In our simulation the gravitational heating is the relevant feedback mechanism. Our results clearly show that galaxy cluster mergers are an important source of heating affecting the ICM properties. Nevertheless, this gravitational source of heating is completely complementary to other forms of feedback. However, its relevance strongly depends on the numerical modelling employed in its description. Therefore, we wish to stress that a proper inclusion of gravitational heating requires not only a self-gravitating simulation, but a suitable description of the complex phenomena onto the ICM component (turbulence, heating, mixing,...) associated with mergers.

- **Cosmological shock waves.** As a natural extension of the previous study, we have also begun a new line of research devoted to analyse the role that cosmological shock waves have in the hierarchical model of structure formation. In particular, we have focused on the study of some qualitative and statistical properties of the structure formation shock waves developed during the evolution of a cosmological simulation. In order to do so, we have developed a numerical algorithm able of identifying shocks in 3-D AMR simulations. The analysis of these cosmological shock waves have produced several important results.

  In agreement with previous studies, we have confirmed that the morphology of the detected shock patterns is quite complex and it perfectly traces the cosmic web.

  We have also studied, at $z = 0$, the differential number distribution of shocked cells within the simulated volume as a function of the shock Mach numbers. We find that the most part of cosmological shocks are essentially weak ($\mathcal{M} \leq 2$), although there is also a population of stronger shocks mainly around filaments and haloes. In addition, by fitting this distribution to a double power law we have obtained two slopes clearly differentiated: for low Mach numbers (up to $\simeq 20$) we obtain a slope much less steeper than that found for stronger shocks. This turn shows the transition between the scales associated to internal and external shocks, respectively.

  We have also tried to correlate the shock waves with the population of galaxy clusters within the computational box. In this sense, we have found that the mean Mach number within the virial radius of haloes at $z = 0$ is $\mathcal{M} \approx 5$. Attending to the evolution, the mean Mach number of the population of haloes at a given epoch is always below a value of ≈ 20. This value, which is in agreement with the turn observed in the Mach number distribution function, indicates the transition between two different scales.

When representing the mean Mach number inside the virial radius of haloes as a function of their masses, we have found at $z = 0$ two well-separated trends. On the one hand, there is an almost constant line for low Mach numbers (up to 5) which seems to be no-dependant on the mass of the haloes. These low Mach number shocks could stem from the primordial formation of clusters and are more visible in structures which have reached an equilibrium state. On the other hand, a steeper trend along all the range of Mach numbers seems to be correlated with halo masses and could represent the shocks taking place during the hierarchical evolution of the structures as a consequence of mergers and accretion processes. Our hypothesis to explain this behaviour is that the evolution of haloes along the plane $\mathcal{M} - M_{vir}$ is intimately related with their merging history.

According to these preliminary results, several projects need to be addressed in the near future like, for instance, the role played by cosmological shock waves from an energetic point of view, or a detailed analysis of the correlation between shock formation events and cluster dynamics. In any case, it is clear that shock waves play a crucial role in galaxy clusters as well as in the thermalization of the ICM.

Up to now, we have exposed the main goals of our work. Nevertheless, the great challenge arise just after this point. Hence, I foresee a set of possible extensions or applications of this work in different subfields intimately related.

In fact, some of these applications are already ongoing projects. In particular, I am involved in the OpenMp parallelization of the ASOHF halo finder. I consider this task very important as well as quite urgent. The huge dynamical ranges and the small resolutions reached by the present-day cosmological simulations demand sophisticated and capable halo finders to deal efficiently with the huge amount of data they generate.

From a physical point of view, since the complete physical description of the ICM is far from being finished, the accurate description of the hydrodynamical processes from a cosmological point of view turns out to be crucial. In this regard, I am analysing a new set of high resolution cosmological simulations especially devoted to quantify the role of shock waves generated during the formation of the different cosmological structures.

Linking the scale of galaxy clusters and galaxies, I am also involved in a project to study the feedback processes associated to AGN in a full cosmological context. In order to do so, a new module, especially designed to mimic the formation of galactic jets, will be included in the MASCLET code. Our idea for introducing this new module is to describe the jets phenomenologically. In order to do this, we will use their general properties as they are observed in different galaxies. This project is a natural extension of a recent work presented by Perucho et al. (2011).

Besides all these ongoing projects, many physical and numerical applications remain to be done. I am particularly interested in the study of different feedback processes and how they connect galactic and cosmological scales. In this sense, several topics could be addressed: (i) the description of cluster reheating due to AGN activity and all its implications, especially, in the scaling relations; (ii) the morphological transformations experimented by galaxies in clusters due to the

properties of the environment; (iii) the effects of the cluster environment on the properties of the galaxies, especially, on their stellar populations.

In addition, as a by-product of the analysis performed on galaxy cluster mergers in a cosmological context, it would be very interesting to set up controlled merger events. With this study we would be able to analyse in detail how different orbital parameters affect the properties of the ICM as well as the condition of hydrostatic equilibrium in galaxy clusters.

Another very interesting long-term numerical project could be the inclusion of magnetic fields and chemical enrichment in the MASCLET code.

I am also very interested in the numerical challenges that future advances could open in Computational Cosmology. In this line, cosmological codes not only have to meet the requirements of the new supercomputers, but to improve their algorithms and their description of relevant physical processes. Therefore, I consider essential to compare numerical results with different codes as well as with observations so as to tackle the scientific projects from a full description both theoretical and observational.

Appendices

Appendix A

Haloes gone MAD: The Halo-Finder comparison project *

Abstract: We present a detailed comparison of fundamental dark matter halo properties retrieved by a substantial number of different halo finders. These codes span a wide range of techniques including friends-of-friends (FOF), spherical-overdensity (SO) and phase-space based algorithms. We further introduce a robust (and publicly available) suite of test scenarios that allows halo finder developers to compare the performance of their codes against those presented here. This set includes mock haloes containing various levels and distributions of substructure at a range of resolutions as well as a cosmological simulation of the large-scale structure of the universe.

All the halo finding codes tested could successfully recover the spatial location of our mock haloes. They further returned lists of particles (potentially) belonging to the object that led to coinciding values for the maximum of the circular velocity profile and the radius where it is reached. All the finders based in configuration space struggled to recover substructure that was located close to the centre of the host halo and the radial dependence of the mass recovered varies from finder to finder. Those finders based in phase space could resolve central substructure although they found difficulties in accurately recovering its properties. Via a resolution study we found that most of the finders could not reliably recover substructure containing fewer than 30-40 particles. However, also here the phase space finders excelled by resolving substructure down to 10-20 particles. By comparing the halo finders using a high resolution cosmological volume we found that they agree remarkably well on fundamental properties of astrophysical significance (e.g. mass, position, velocity, and peak of the rotation curve).

We further suggest to utilize the peak of the rotation curve $v_{\rm max}$ as a proxy for mass given the arbitrariness in defining a proper halo edge.

Keywords: methods: N-body simulations – galaxies: haloes – galaxies: evolution – cosmology: theory – dark matter

*This Appendix corresponds to a paper submitted to MNRAS by Knebe et al. (2010).

A.1 Introduction

While recent decades have seen great progress in the understanding and modelling of the large- and small-scale structure of the Universe by means of numerical simulation there remains one very fundamental question that is yet to be answered: "How to find a dark matter halo?" The comparison of any cosmological simulation to observational data relies upon reproducibly identifying "objects" within the model. But how do we identify "dark matter haloes" or even "galaxies" in such simulations? Researchers in the field have developed a wide variety of techniques and codes to accomplish this task. But how does the performance of these various techniques and codes compare? While we still may argue about the proper definition of an "object" the various approaches should nevertheless agree once the same recipe for defining a (dark matter) halo is used.

This introduction begins by establishing why it is important to have "The Halo-Finder Comparison Project" before continuing by laying out the groundwork for the comparison we have undertaken. It is therefore subdivided into a first subsection where we highlight the necessity for such a comparison and summarise the recent literature in this area. This section also includes a brief primer on halo finders and their history. The second part introduces the design of the test cases, illustrated with some analysis. The last part then raises the question "how to cross-compare haloes?" as well as "what is actually a halo?" and presents a possible answer the authors agreed upon.

A.1.1 The Necessity for a Comparison Project

Over the last 30 years great progress has been made in the development of simulation codes that model the distribution of dissipationless dark matter while simultaneously following the (substantially more complex) physics of the baryonic component that accounts for the observable Universe. Nowadays we have a great variety of highly reliable, cost effective (and sometimes publicly available) codes designed for the simulation of cosmic structure formation (e.g. Couchman et al. 1995; Pen 1995; Gnedin 1995; Kravtsov et al. 1997; Fryxell et al. 2000; Bode et al. 2000; Springel et al. 2001; Knebe et al. 2001; Teyssier 2002; O'Shea et al. 2004; Quilis 2004; Dubinski et al. 2004; Merz et al. 2005; Springel 2005; Bagla & Khandai 2009; Springel 2010; Doumler & Knebe 2010).

However, producing the (raw) simulation data is only the first step in the process; the model requires reduction before it can be compared to the observed Universe we inhabit. This necessitates access to analysis tools to map the data onto "real" objects; traditionally this has been accomplished via the use of "halo finders". Conventional halo finders search the (dark) matter density field within the simulations generated by the aforementioned codes to find locally over-dense gravitationally bound systems, which are then tagged as (dark) matter haloes. Such tools have led to critical insights into our understanding of the origin and evolution of cosmic structure. To take advantage of sophisticated simulation codes and to optimise their predictive power one obviously needs equally sophisticated halo finders! Therefore, this field has also seen great development in recent years (e.g. Gelb & Bertschinger 1994; Klypin & Holtzman 1997; Eisenstein & Hut 1998; Stadel 2001; Bullock et al. 2001; Springel et al. 2001; Aubert et al. 2004; Gill et al. 2004; Weller et al. 2005; Neyrinck et al. 2005; Kim & Park 2006; Diemand et al. 2006; Shaw et al. 2007; Gardner et al. 2007a,b; Maciejewski et al. 2009; Habib et al. 2009; Knollmann & Knebe 2009; Ascasibar 2010; Behroozi 2010; Planelles & Quilis 2010; Sutter & Ricker 2010; Rasera et al. 2010; Skory et al. 2010; Falck et al. 2011, see also Fig. A.1 noting that for some halo finders no code paper exists yet). But so far comparison projects have tended to focus on the simulation codes themselves rather than the analysis tools.

The increasing demand for halo finders is schematically presented in Fig. A.1 where we show the (cumulative) number of codes as a function of time, binned in ten year intervals since 1970. We can clearly see the increasing pace of development in the past decade reflecting the necessity for sophisticated codes: in the last ten years the number of existing halo finding codes has practically tripled. While for a long time the spherical overdensity method first mentioned by Press & Schechter (SO, 1974) as well as the friend-of-friends algorithm introduced by Davis et al. (FOF, 1985) remained the standard techniques, the situation changed in the 90's when new methods were developed (Gelb 1992; Lacey & Cole 1994; van Kampen 1995; Pfitzner & Salmon 1996; Klypin & Holtzman 1997; Eisenstein & Hut 1998; Gottlöber et al. 1999).

While the first generation of halo finders primarily focused on identifying isolated field haloes the situation dramatically changed once it became clear that there was no such thing as "overmerging", i.e. the premature destruction of haloes orbiting inside larger host haloes (Klypin et al. 1999) was a numerical artifact rather than a real physical process. Now codes

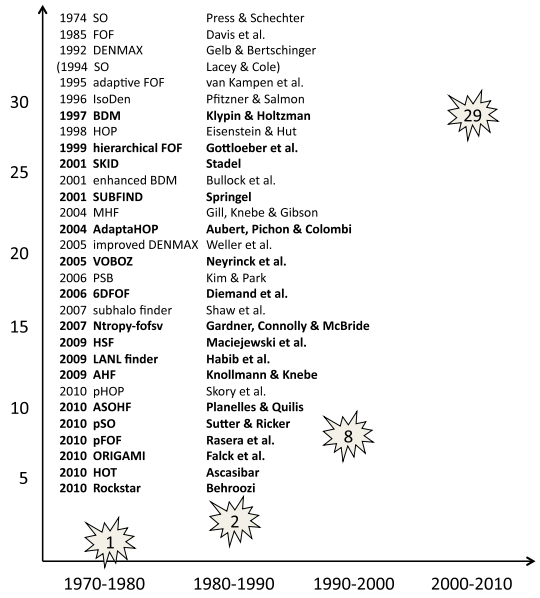

Figure A.1: Schematic presentation of the (cumulative) number of halo finders as a function of time, binned in ten-year intervals since 1970. The codes participating in this comparison project have been highlighted in bold font.

faced the challenge of finding both haloes embedded within the (more or less uniform) background density of the Universe as well as subhaloes orbiting within a density gradient of a larger host halo. The past decade has seen a substantial number of codes and techniques introduced in an attempt to cope with this problem (Stadel 2001; Bullock et al. 2001; Springel et al. 2001; Aubert et al. 2004; Gill et al. 2004; Weller et al. 2005; Neyrinck et al. 2005; Kim & Park 2006; Diemand et al. 2006; Shaw et al. 2007; Gardner et al. 2007a,b; Maciejewski et al. 2009; Knollmann & Knebe 2009; Planelles & Quilis 2010). Along with the need to identify subhaloes simulations became much larger during this period and this led to a drive towards parallel analysis tools. The simulation data had become too large to be analysed on single CPU architectures and hence halo finders had to be developed to cope with this situation, too.

Nevertheless, the first two halo finders mentioned in the literature, i.e. the spherical overdensity (SO) method (Press & Schechter 1974) and the friends-of-friends (FOF) algorithm (Davis et al. 1985) remain the foundation of nearly every code: they often involve at least one phase where either particles are linked together or (spherical) shells are grown to collect particles. While we do not wish to invent stereotypes or a classification scheme for halo finders there are unarguably two distinct groups of codes:

- density peak locator (+ particle collection)
- particle collector

The density peak locators – such as the classical SO method – aim at identifying by whatever means peaks in the matter density field. About these centres (spherical) shells are grown out to the point where the density profile drops below a certain pre-defined value normally derived from a spherical top-hat collapse. Most of the methods utilising this approach merely differ in the way they locate density peaks. The particle collector codes – above all the FOF method – connect and link particles together that are close to each other (either in a 3D configuration or in 6D phase-space). They afterwards determine the centre of this mass aggregation.

After the initial selection has been made most methods apply a pruning phase where gravitationally unbound particles are removed from the object. While this unbinding procedure is not essential for isolated field haloes it

is vital for subhaloes in order to properly alleviate contamination by host halo particles. Furthermore, for subhaloes it appears essential to define the first guess for bound particles upon a stable and reproducible criterion for the subhalo edge. One cannot extend the (spherical) shells out to the point where the density drops below some preselected multiple of the universal background density as this level will not be reached anymore; one needs to "truncate" the object beforehand, usually at the point where the density rises again due to the fact that the subhalo is embedded within a host. Similarly, particle collecting codes which use simple "proximity" as a criterion for grouping particles need to adjust their yardsticks. However, the situation may be a bit more straightforward for 6D phase-space finders as we expect the velocity distributions of the host and the subhalo to be different.

Driven by the explosion of high-quality observational data, simulations of cosmological structure formation have moved to increasingly high mass and force resolution. The simulation codes and techniques have been continuously refined over the past few decades providing us with methods that are akin yet different: they all have to solve the collisionless Boltzmann equation simultaneously with Poisson's equation and the equations that govern gas physics. In order to verify their credibility the past few years have seen substantial efforts to inter-compare the results stemming from these different techniques (cf. Frenk et al. 1999; Knebe et al. 2000; O'Shea et al. 2005; Agertz et al. 2007; Heitmann et al. 2008; Tasker et al. 2008). *However, to date the literature lacks a quantitative comparison of the various halo finding techniques.* While some efforts have been directed towards this goal (e.g. Lacey & Cole 1994; White 2002; Gill et al. 2004; Cohn & White 2008; Lukić et al. 2009; Tweed et al. 2009; Maciejewski et al. 2009; Knollmann & Knebe 2009) these studies primarily scratched the surface and no-one has yet presented a conclusive inter-comparison based upon a well defined test suite. In addition, we would like to stress again that the analysis of massive state-of-the-art simulations is a non-trivial task, especially when it comes to the detailed substructure of the haloes. Furthermore, various definitions of the extent of a halo exist within the literature making comparisons of the results from different groups far from straightforward (cf. White 2001; Lukić et al. 2009).

We though acknowledge that there is a body of literature available that has compared halo finder methods to theoretical predictions (e.g. Press & Schechter 1974; Lacey & Cole 1994; Sheth & Tormen 1999; Jenkins et al. 2001; Robertson et al. 2009; Courtin et al. 2010). While this is important work, it nevertheless rather often leads to halo finders being tuned to match theoretical expectations than testing the validity of the code in the first place; the theories have sometimes been used to answer "what halo definition is required to match theoretical expectations?". This may therefore mask important differences between simple linear theory and the full non-linear growth of structure in the Universe. In this paper, we focus instead on directly comparing different codes for halo finding and leave theoretical expectation aside.

In summary, there is no clear definition of "what is a (dark) matter halo?" never mind "what is a subhalo?". Workers in the field of simulation analysis tend to utilise their own definitions and codes to study the properties of haloes in cosmological simulations. This paper aims at rectifying this situation by presenting the first ever coherent halo-finder comparison involving a substantial number of codes as well as providing the community with a well-defined set of test cases. Although, we would like to caution the reader that the prime objective of this comparison is *codes* and not *algorithms*. Therefore, while certain codes may be based upon the same algorithm they still may yield (marginally) different results due to the individual realisation of that algorithm.

A.1.2 The Workshop

During the last week of May 2010 we held the workshop "Haloes going MAD" in Miraflores de la Sierra close to Madrid dedicated to the issues surrounding identifying haloes in cosmological simulations. Amongst other participants 15 halo finder representatives were present. The aim of this workshop was to define (and use!) a unique set of test scenarios for verifying the credibility and reliability of such programs. We applied each and every halo finder to our newly established suite of test cases and cross-compared the results.

To date most halo finders were introduced (if at all) in their respective code papers which presented their underlying principles and subjected them to tests within a full cosmological environment (primarily matching (sub-)halo mass functions to theoretical models and fitting functions) and hence no general benchmarks such as the ones designed at the workshop and presented below existed prior to our meeting. Our newly devised suite of test cases is designed to be simple yet challenging enough to assist in establishing and gauging the cred-

ibility and functionality of all commonly employed halo finders. These tests include mock haloes with well defined properties as well as a state-of-the-art cosmological simulation. They involve the identification of individual objects, various levels of substructure, and dynamically evolving systems. The cosmological simulation has been provided at various resolution levels with the best resolved containing a sufficient number of particles (1024^3) that it can only presently be analysed in parallel.

All the test cases and the analysis presented here is publicly available from `http://popia.ft.uam.es/HaloesGoingMAD` under the tab "The Data".

A.1.3 How to compare Haloes?

One of the most crucial questions to address is obviously "How to define a halo?". This question is intimately related to "How do we fairly cross-compare the results of the various halo finders?". While we all agreed that the proper definition of a halo should be a "gravitationally bound object", how the size of a halo should be defined proved harder to agree upon. The "virial radius" is not a well-defined property as its precise definition can (and does) vary from halo finder to halo finder.[1] Furthermore, this quantity is ill-defined for subhaloes that live within the environment of a host halo. While there is some work available that allows for a conversion between commonly applied methods to calculate the mass of an isolated field halo (see e.g. White 2001; Lukić et al. 2009), such variations in definition will nevertheless lead to discrepancies in a cross-comparison and hence we decided to abandon the ambiguous definition for the edge of a halo and rather focus on a property that uniquely specifies the halo for the code comparison project: the peak of the rotation curve as characterised by $v_{\rm max}$ and the radial location of this peak $R_{\rm max}$, respectively. It has been argued (e.g. Ascasibar & Gottlöber 2008) that these quantities do indeed provide a physically-motivated scale for dark matter haloes, showing that, in contrast to the inner regions, there is substantial scatter in their physical properties, as well as significant systematic trends with halo mass and cosmic epoch, beyond the radius $R_{\rm max}$.

However, utilizing $v_{\rm max}$ raises two obvious issues: firstly, as $v_{\rm max}$ is reached quite close to the centre of the halo its measurement is obviously sensitive to resolution. Secondly, as the value of $v_{\rm max}$ is set by the central particles it is not very sensitive to tidal stripping. The relationship between $R_{\rm max}$ and $R_{\rm vir}$ for a range of NFW halo concentrations is given in figure 6 of Muldrew et al. 2011. The resolution issue can be addressed by increasing the number of particles required when studying subhalo properties so that $v_{\rm max}$ will always be resolved sufficiently and credibly. The relevance of the stripping issue though depends upon the questions to be asked of the simulation data: are we interested in a (stable) measure of the (original) infall mass of the subhalo or do we want to quantify the mass inside the tidal radius? For the comparison project we decided to evaluate $v_{\rm max}$ in order to have a stable quantity. We further agreed that this quantity is better related to observational data as it is possible to observe rotation curves (and hence $v_{\rm max}$) whereas the same ambiguity applies to observers: what is the (outer) edge of a halo and/or galaxy? Nevertheless, we also decided to include $N_{\rm part}$ (i.e. the total number of gravitationally bound particles as returned by the respective halo finder) in the comparison as a halo is (or should be) a gravitationally bound entity. The values for $N_{\rm part}$ are the ones directly returned by the halo finder and are based upon the internal criteria each code uses. How (and if) to perform the unbinding procedure and what particles to consider as belonging to the (sub-)halo were questions left for each group taking part to answer as they saw fit. For several groups these particle lists would normally be pruned further during an additional post-processing phase prior to obtaining halo properties. The numbers given here therefore serve solely as an indicator of whether or not particles are missing and/or – in case of subhaloes – belong to the host. In addition, we also used the list of particles belonging to each halo to calculate a fiducial M_{200} value (defined via $M(<r)/4\pi r^3 = 200\times\rho_{\rm crit}$) considering the object in isolation, even for subhaloes: there are physical situations – like the dynamical friction on infalling loose groups (e.g. Read et al. 2008; Lux et. al 2010) – where the (total) mass is the physically important quantity. Such examples of the limitation of the $v_{\rm max}$ value as a proxy for mass have also been witnessed in our test cases and we will come back to it in Section A.4.1.3.

The first preliminary comparisons focusing on spatial location, $v_{\rm max}$, and the number of bound particles for the static mock haloes indicate that even though there exist a variety of different approaches for halo finding, most

[1] We like to add the cautionary remark that a lot of the properties and in particular any "radius" is based upon the assumption of spherical symmetry which is not valid for all halo finders presented here.

of the codes agree with the known correct result well. If substructure is located close to the centre of the host halo all the codes tested experienced some difficulties in accurately recovering it, with all the finders based in 3D configuration space missing some material. For subhaloes placed near the very centre of the host halo the more sophisticated 6D finders based in phase space, while correctly noting the existence of a substructure often overestimated the associated mass due to confusion with material in the host halo. After proving to ourselves that we could all successfully reproduce the location and scale of a supplied mock halo we performed a resolution study where the mass and hence number of particles in a subhalo was gradually lowered. We found that practically all halo finders have a completeness limit of 30-40 particles; substructure objects smaller than this are not reliably found. Once we had established a firm baseline for our comparisons we extended the study to consider a full cosmological volume at varying resolution. The results of this comparison are presented in Section A.4 below after we first briefly introduce each of the halo finders involved in the comparison project in Section A.2 and describe the set-up of our mock haloes in Section A.3. Finally we wrap-up and present some conclusions in Section A.5.

A.2 The Codes

In this Section we are going to *briefly* present the codes that participated in the halo-finder comparison project. We highlight their main features allowing for a better understanding of any (possible) differences in the comparison Section A.4. The prime information to be found in each code paragraph should be sufficient to understand how the algorithm works, how the initial particle content of a halo is obtained, the way the the (sub-)halo centre and edge are calculated, how the unbinding is performed and which method of parallelisation has been applied. Please note that not all halo finders perform an unbinding, are parallelized or suitable to detect subhaloes. And we explicitly stress that this Section is neither intended as a review of all available halo finders nor an elaborate exposition of the partaking codes; for the latter we refer the reader to the respective code papers referenced in the subsection of each halo finder.

As much as possible, the halo finders have been organised in terms of their methodology: spherical overdensity finders first followed by FOF-based finders with 6D phase-space finders last. This applies to both the presentation in this Section as well as the comparison in Section A.4.

A.2.1 AHF (Knollmann & Knebe)

The MPI+OpenMP parallelised halo finder `AHF`[2] (`AMIGA` Halo Finder, Knollmann & Knebe 2009), is an improvement of the `MHF` halo finder (Gill et al. 2004), which employs a recursively refined grid to locate local overdensities in the density field. The identified density peaks are then treated as centres of prospective haloes. The resulting grid hierarchy is further utilized to generate a halo tree readily containing the information which halo is a (prospective) host and subhalo, respectively. We therefore like to stress that our halo finding algorithm is fully recursive, automatically identifying haloes, subhaloes, sub-subhaloes, etc. Halo properties are calculated based on the list of particles asserted to be gravitationally bound to the respective density peak. To generate this list of particles we employ an iterative procedure starting from an initial guess of particles. This initial guess is based again upon the adaptive grid hierarchy: for field haloes we start with considering all particles out to the iso-density contour encompassing the overdensity defined by the virial criterion based upon the spherical top-hat collapse model; for subhaloes we gather particles up to the grid level shared with another prospective (sub-)halo in the halo tree which corresponds to the upturn point of the density profile due to the embedding within a (background) host. This tentative particle list is then used in an iterative procedure to remove unbound particles: In each step of the iteration, all particles with a velocity exceeding the local escape velocity, as given by the potential based on the particle list at the start of the iteration, are removed. The process is repeated until no particles are removed anymore. At the end of this procedure we are left with bona fide haloes defined by their bound particles and we can calculate their integral and profiled quantities.

The only parameter to be tuned is the refinement criterion used to generate the grid hierarchy that serves as the basis for the halo tree and also sets the accuracy with which the centres are being determined. The virial overdensity criterion applied to find the (field) halo edges is determined from the cosmological model of the data though it can readily be tailored to specific needs; for the analysis presented here we used $200 \times \rho_{\rm crit}$. For more details on the mode of operation and actual functionality we

[2] `AHF` is freely available from `http://www.popia.ft.uam.es/AMIGA`

refer the reader to the two code description papers by (Gill et al. 2004) and Knollmann & Knebe (2009), respectively.

A.2.2 ASOHF (Planelles & Quilis)

The ASOHF finder (Planelles & Quilis 2010) is based on the spherical overdensity (SO) approach. Although it was originally created to be coupled to an Eulerian cosmological code, in its actual version, it is a stand-alone halo finder capable of analysing the outputs from cosmological simulations including different components (i.e., dark matter, gas, and stars). The algorithm takes advantage of an AMR scheme to create a hierarchy of nested grids placed at different levels of refinement. All the grids at a certain level, named patches, share the same numerical resolution. The higher the level of refinement the better the numerical resolution, as the size of the numerical cells gets smaller. The refining criteria are open and can be chosen depending on the application. For a general purpose, ASOHF refines when the number of particles per cell exceeds a user defined parameter. Once the refinement levels are set up, the algorithm applies the SO method independently at each of those levels. The parameters needed by the code are the following: i) the cosmological parameters when analysing cosmological simulations, ii) the size of the coarse cells, the maximum number of refinement levels (N_{levels}), and the maximum number of patches (N_{patch}) for all levels in order to build up the AMR hierarchy of nested grids, iii) the number of particles per cell in order to choose the cells to be refined, and iv) the minimum number of particles in a halo.

After this first step, the code naturally produces a tentative list of haloes of different sizes and masses. Moreover, a complete description of the substructure (haloes within haloes) is obtained by applying the same procedure on the different levels of refinement. A second step, not using the cells but the particles within each halo, makes a more accurate study of each of the previously identified haloes. These prospective haloes (subhaloes) may include particles which are not physically bound. In order to remove unbound particles, the local escape velocity is obtained at the position of each particle. To compute this velocity we integrate Poisson equation assuming spherical symmetry. If the velocity of a particle is higher than the escape velocity, the particle is assumed to be unbound and is therefore removed from the halo (subhalo) being considered. Following this procedure, unbound particles are removed iteratively along a list of radially ordered particles until no more of them need to be removed. In the case that the number of remaining particles is less than a given threshold the halo is dropped from the list.

After this cleaning procedure, all the relevant quantities for the haloes (subhaloes) as well as their evolutionary merger trees are computed. The lists of (bound) particles are used to calculate canonical properties of haloes (subhaloes) like the position of the halo centre, which is given by the centre of mass of all the bound particles, and the size of the haloes, given by the distance of the farthest bound particle to the centre.

The ability of the ASOHF method to find haloes and their substructures is limited by the requirement that appropriate refinements of the computational grid exist with enough resolution to spot the structure being considered. In comparison to algorithms based on linking strategies, ASOHF does not require a linking length to be defined, although at a given level of refinement the size of the cell can be considered as the linking length of this particular resolution.

The version of the code used in this comparison is serial, although there is already a first parallel version based on OpenMP.

A.2.3 BDM (Klypin & Ceverino)

The Bound Density Maxima (BDM) halo finder originally described in Klypin & Holtzman (1997) uses a spherical 3D overdensity algorithm to identify haloes and subhaloes. It starts by finding the local density at each individual particle position. This density is defined using a top-hat filter with a constant number of particles $N_{\rm filter}$, which typically is $N_{\rm filter} = 20$. The code finds all maxima of density, and for each maximum it finds a sphere containing a given overdensity mass $M_\Delta = (4\pi/3)\Delta\rho_{\rm cr}R_\Delta^3$, where $\rho_{\rm cr}$ is the critical density and Δ is the specified overdensity.

For the identification of distinct haloes, the code uses the density maxima as halo centres; amongst overlapping sphere the code finds the one that has the deepest gravitational potential. Haloes are ranked by their (preliminary) size and their final radius and mass are derived by a procedure that guarantees smooth transition of properties of small haloes when they fall into a larger host) halo becoming subhaloes: this procedure either assigns R_Δ or $R_{\rm dist}$ as the radius for a currently infalling halo as its radius depending on the environmental conditions, where $R_{\rm dist}$ measures the distance of the infalling halo to the surface of the soon-to-be host halo.

The identification of subhaloes is a more complicated procedure: centres of subhaloes are certainly density maxima, but not all density maxima are centres of subhaloes. BDM eliminates all density maxima from the list of subhalo candidates which have less than $N_{\rm filter}$ self-bound particles. For the remaining set of prospective subhaloes the radii are determined as the minimum of the following three distance: (a) the distance to the nearest barrier point (i.e. centres of previously defined (sub-)haloes), (b) the distance to its most remote bound particle, and (c) the truncation radius (i.e. the radius at which the average density of bound particles has an inflection point). This evaluation involves an iterative procedure for removing unbound particles and starts with the largest density maximum.

The unbinding procedure requires the evaluation of the gravitational potential which is found by first finding the mass in spherical shells and then by integration of the mass profile. The binning is done in log radius with a very small bin size of $\Delta \log(R) = 0.005$.

The bulk velocity of either a distinct halo or a subhalo is defined as the average velocity of the 30 most bound particles of that halo or by all particles, if the number of particles is less than 30. The number 30 is a compromise between the desire to use only the central (sub)halo region for the bulk velocity and the noise level.

The code uses a domain decomposition for MPI parallelization and OpenMP for the parallelization inside each domain.

A.2.4 pSO (Sutter & Ricker)

The parallel spherical overdensity (pSO) halo finder is a fast, highly scalable MPI-parallelized tool directly integrated into the FLASH simulation code that is designed to provide on-the-fly halo finding for use in subgrid modeling, merger tree analysis, and adaptive refinement schemes (Sutter & Ricker 2010). The pSO algorithm identifies haloes by growing SO spheres. There are four adjustable parameters, controlling the desired overdensity criteria for centre detection and halo size, the minimum allowed halo size, and the resolution of the halo radii relative to the grid resolution. The algorithm discovers halo centres by mapping dark matter particles onto the simulation mesh and selecting cell centres where the cell density is greater than the given overdensity criterion. The algorithm then determines the halo edge using the SO radius by collecting particles using the FLASH AMR tree hierarchy. The algorithm determines the halo centre, bulk velocity, mass, and velocity dispersion without additional post-processing. pSO is provided as both an API for use in-code and as a stand-alone halo finder.

A.2.5 LANL (Lukić, Fasel & Hsu)

The LANL halo finder is developed to provide on-the-fly halo analysis for simulations utilizing hundreds of billions of particles, and is integrated into the MC^3 code (Habib et al. 2009), although it can also be used as a stand-alone halo finder. Its core is a fast kD-tree FOF halo finder which uses 3D (block), structured decomposition to minimize surface to volume ratio of the domain assigned to each process. As it is aimed at large-scale structure simulations (100+ Mpc/h on the side), where the size of any single halo is much smaller than the size of the whole box, it uses the concept of "ghost zones" such that each process gets all the particles inside its domain as well as those particles which are around the domain within a given distance (the overload size, a code parameter chosen to be larger then the size of the biggest halo we expect in the simulation). After each process runs its serial version of a FOF finder, MPI based "halo stitching" is performed to ensure that every halo is accounted for, and accounted for only once.

If desired, spherical "SO" halo properties can be found using the FOF haloes as a proxy. Those SO haloes are centred at the particle with the lowest gravitational potential, while the edge is at R_Δ – the radius enclosing an overdensity of Δ. It is well known that percolation based FOF haloes suffer from the over-bridging problem; therefore, if we want to ensure completeness of our SO sample we should run FOF with a smaller linking length than usual in order to capture all density peaks, but still avoid over-bridging at the scale of interest (which depends on our choice of Δ). Overlapping SO haloes are permitted, but the centre of one halo may not reside inside another SO halo (that would be considered as a substructure, rather than a "main" halo). The physical code parameters are the linking length for the FOF haloes, and overdensity parameter Δ for SO haloes. Technical parameters are the overload size and the minimum number of particles in a halo.

The LANL halo finder is being included in the standard distributions of PARAVIEW[3] package, enabling researchers to combine analysis and visualization of their simulations. A substructure finder is currently under development.

[3] http://www.paraview.org/

A.2.6 SUBFIND (Iannuzzi, Springel & Dolag)

SUBFIND (Springel et al. 2001) identifies gravitationally bound, locally overdense regions within an input parent halo, traditionally provided by a FOF group finder, although other group finders could be used in principle as well. The densities are estimated based on the initial set of all particles via adaptive kernel interpolation based on a number $N_{\rm dens}$ of smoothing neighbours. For each particle, the nearest $N_{\rm ngb}$ neighbours are then considered for identifying local overdensities through a topological approach that searches for saddle points in the isodensity contours within the global field of the halo. This is done in a top-down fashion, starting from the particle with the highest associated density and adding particles with progressively lower densities in turn. If a particle has only denser neighbours in a single structure it is added to this region. If it is isolated it grows a new density peak, and if it has denser neighbours from two different structures, an isodensity contour that traverses a saddle point is identified. In the latter case, the two involved structures are joined and registered as candidate subhaloes if they contain at least $N_{\rm ngb}$ particles. These candidates, selected according to the spatial distribution of particles only, are later processed for gravitational self-boundness. Particles with positive total energy are iteratively dismissed until only bound particles remain. The gravitational potential is computed with a tree algorithm, such that large haloes can be processed efficiently. If the remaining bound number of particles is at least $N_{\rm ngb}$, the candidate is ultimately recorded as a subhalo. The set of initial substructure candidates forms a nested hierarchy that is processed from inside out, allowing the detection of substructures within substructures. However, a given particle may only become a member of one substructure, i.e. SUBFIND decomposes the initial group into a set of disjoint self-bound structures. Particles not bound to any genuine substructure are assigned to the "background halo". This component is also checked for self-boundness, so that some particles that are not bound to any of the structures may remain. For all substructures as well as the main halo, the particle with the minimum gravitational potential is adopted as (sub)halo centre. For the main halo, SUBFIND additionally calculates a SO virial mass around this centre, taking into account all particles in the simulation (i.e. not just those in the FOF group that is analyzed). There exist both serial and MPI-parallelized versions of SUBFIND, which implement the same underlying algorithms. For more details we refer the reader to the paper by Springel et al. (2001).

A.2.7 FOF (Gottlöber & Turchaninov)

In order to analyse large cosmological simulations with up to 2048^3 particles we have developed a new MPI version of the hierarchical Friends-Of-Friends algorithm with low memory requests. It allows us to construct very fast clusters of particles at any overdensity (represented by the linking length) and to deduce the progenitor-descendant-relationship for clusters in any two different time steps. The particles in a simulation can consist of different species (dark matter, gas, stars) of different mass. We consider them as an undirected graph with positive weights, namely the lengths of the segments of this graph. For simplicity we assume that all weights are different. Then one can show that a unique minimum spanning tree (MST) of the point distribution exists, namely the shortest graph which connects all points. If subgraphs cover the graph then the MST of the graph belongs to the union of MSTs of the subgraphs. Thus subgraphs can be constructed in parallel. Moreover, the geometrical features of the clusters, namely the fact that they occupy mainly almost non-overlapping volumes, allow the construction of fast parallel algorithms. If the MST has been constructed all possible clusters at all linking lengths can be easily determined. To represent the output data we apply topological sorting to the set of clusters which results in a cluster ordered sequence. Every cluster at any linking length is a segment of this sequence. It contains the distances between adjacent clusters. Note, that for the given MST there exist many cluster ordered sequences which differ in the order of the clusters but yield the same set of clusters at a desired linking length. If the set of particle-clusters has been constructed further properties (centre of mass, velocity, shape, angular momentum, orientation etc.) can be directly calculated. Since this concept is by construction aspherical a circular velocity (as used to characterise objects found with spherical overdensity algorithms) cannot be determined here. The progenitor-descendant-relationship is calculated for the complete set of particles by comparison of the cluster-ordered sequences at two different output times.

The hierarchical FOF algorithm identifies objects at different overdensities depending on the chosen linking length (More et al. 2011). In order to avoid artificial misidentifications of subhaloes on high overdensities one can add an

additional criterion. Here we have chosen the requirement that the spin parameter of the subhalo should be smaller than one. All subhaloes have been identified at 512 times the virial overdensity. Thus only the highest density peak has been taken into account for the mass determination and the size of the object, which are therefore underestimated. The velocity of the density peak is estimated correctly but without removing unbound particles.

A.2.8 pFOF (Rasera & Roy)

Parallel FOF (`pFOF`) is a MPI-based parallel Friends-of-Friends halo finder which is used within the DEUS Consortium [4] at LUTH (Laboratory Universe and Theories). It has been parallelized by Roy and was used for several studies involving large N-body simulations such as Courtin et al. (2010); Rasera et al. (2010). The principle is the following: first, particles are distributed in cubic subvolumes of the simulation and each processor deals with one "cube", and runs Friends-of-Friends locally. Then, if a structure is located close to the edge of a cube, `pFOF` checks if there are particles belonging to the same halo in the neighbouring cube. This process is done iteratively until all haloes extending across multiple cubes have been merged. Finally, particles are sorted on a per halo basis, and the code writes two kinds of output: particles sorted per region, particles sorted per halo. This makes any post-processing straightforward because each halo or region can be analysed individually on a single CPU server. `pFOF` was successfully tested on up to 4096 Bluegene/P cores with a 2048^3 particles N-body simulation. In this article, the serial version was used for mock haloes and small cosmological simulations, and the parallel version for larger runs. The linking length was set to $b = 0.2$ (however see Courtin et al. 2010, for a discussion on the halo definition), and the minimum halo mass to 100 particles. And the halo centres reported here are the centre-of-mass of the respective particle distribution.

A.2.9 Ntropy-fofsv (Gardner, McBride & Stinson)

The Ntropy parallel programming framework is derived from N-body codes to help address a broad range of astrophysical problems [5]. This includes an implementation of a simple but efficient FOF halo finder, `Ntropy-fofsv`, which is more fully described in Gardner et al. (2007a) and Gardner et al. (2007b). Ntropy provides a "distributed shared memory" (DSM) implementation of a kD-tree, where the application developer can reference tree nodes as if they exist in a global address space, even though they are physically distributed across many compute nodes. Ntropy uses the kD-tree data structures to speed up the FOF distance searches. It also employs an implementation of the Shiloach & Vishkin (1982) parallel connectivity algorithm to link together the haloes that span separate processor domains. The advantage of this method is that no single computer node requires knowledge of all of the groups in the simulation volume, meaning that `Ntropy-fofsv` is scalable to petascale platforms and handle large data input. This algorithm was used in the mock halo test cases to stitch together particle groups found across many threads into the one main FOF halo. As FOF is a deterministic algorithm, `Ntropy-fofsv` takes a single physical linking length to group particles into FOF haloes without any performing particle unbinding or subhalo identification. The halo centres for the analysis presented here use centre-of-mass estimates based on the FOF particle list. Ntropy achieves parallelisation by calling "machine dependent library" (MDL) that consists of high-level operations such as "acquire_treenode" or "acquire_particle." This library is rewritten for a variety of models (MPI, POSIX Threads, Cray SHMEM, etc.), allowing the framework to extract the best performance from any parallel architecture on which it is run.

A.2.10 VOBOZ (Neyrinck)

Conceptually, a `VOBOZ` (VOronoi BOund Zones, Neyrinck et al. 2005) halo or subhalo is a density peak surrounded by gravitationally bound particles that are down steepest-density gradients from the peak. A statistical significance is measured for each (sub)halo, based on the probability that Poisson noise would produce it.

The only physical parameter in `VOBOZ` is the density threshold characterizing the edge of (parent) haloes (set to 200 times the mean density here), which typically only affects their measured masses. To return a definite halo catalog, we also impose a statistical-significance threshold (set to 4-σ here), although depending on the goal of a study, this may not be necessary.

Density peaks are found using a Voronoi tessellation (parallelizable by splitting up the volume), which gives an adaptive, parameter-free estimate of each particle's density and set

[4] `www.deus-consortium.org`

[5] http://www.phys.washington.edu/users/-gardnerj/ntropy

of neighbours (e.g., Schaap & van de Weygaert 2000). Each particle is joined to the peak particle (whose position is returned as the halo centre) that lies up the steepest density gradient from that particle. A halo associated with a high density peak will also contain smaller density peaks. The significance of a halo is judged according to the ratio of its central density to a saddle point joining the halo to a halo with a higher central density, comparing to a Poisson point process. Pre-unbinding (sub)halo boundaries are defined along these density ridges.

Unbinding evaporates many spurious haloes, and often brings other halo boundaries inward a bit, reducing the dependence on the outer density contrast. Particles not gravitationally bound to each halo are removed iteratively, by comparing their potential energies (measured as sums over all other particles) to kinetic energies with respect to the velocity centroid of the halo's core (i.e. the particles that directly jump up density gradients to the peak). The unbinding is parallelized using OpenMP. In the cosmological test, we remove haloes with fewer than 20 particles from the `VOBOZ` halo list.

A.2.11 ORIGAMI (Falck, Neyrinck & Aragon-Calvo)

`ORIGAMI` (Order-ReversIng Gravity, Apprehended Mangling Indices, Falck et al. 2010) uses a natural, parameter-free definition of the boundary between haloes and the non-halo environment around them: halo particles are particles that have experienced shell-crossing. This dynamical definition does not make use of the density field, in which the boundary can be quite ambiguous. In one dimension, shell crossings can be detected by looking for pairs of particles whose positions are out-of-order compared with their initial positions. In 3D, then, a halo particle is defined as a particle that has undergone shell crossings along 3 orthogonal axes. Similarly, this would be 2 axes for a filament, 1 for a wall, and 0 for a void. There is a huge number of possible sets of orthogonal axes in the initial grid to use to test for shell-crossing, but we only used four simple ones, which typically suffice to catch all the shell-crossings. We used the Cartesian x, y, and z axes, as well as the three sets of axes consisting of one Cartesian axis and two (45°) diagonal axes in the plane perpendicular to it.

Once halo particles have been tagged, there are many possible ways of grouping them into haloes. For this paper, we grouped them on a Voronoi tessellation of final-conditions particle positions. This gives a natural density estimate (e.g. Schaap & van de Weygaert 2000, `VTFE`, Voronoi Tessellation Field Estimator) and set of neighbours for each particle. Haloes are sets of halo particles connected to each other on the Voronoi tessellation. To prevent haloes from being unduly linked, we additionally require that a halo contain at most one halo "core", defined as a set of particles connected on the tessellation that all exceed a `VTFE` density threshold. This density threshold is the only parameter in our algorithm, since the initial tagging of halo particles is parameter-free; for this study, we set it to 200 times the mean density. We partition connected groups of halo particles with multiple cores into haloes as follows: each core iteratively collects particles in concentric rings of Voronoi neighbours until all halo particles are associated. The tagging procedure establishes halo boundaries, so no unbinding procedure is necessary. Also, we note that currently, the algorithm does not identify subhaloes. We remove haloes with fewer than 20 particles from the `ORIGAMI` halo catalogue, and the halo centre reported is the position of the halo's highest-density particle.

Please note that due to its nature ORIGAMI is only applicable to cosmological simulations and hence only enters the comparison project in the respective Section A.4.2.

A.2.12 SKID (Stadel & Potter)

`SKID` (Spline Kernel Interpolative Denmax)[6], first mentioned in Governato et al. (1997) and extensively described in Stadel (2001), finds density peaks within N-body simulations and subsequently determines all associated bound particles thereby identifying haloes. It is important to stress that `SKID` will only find the smallest scale haloes within a hierarchy of haloes as is generally seen in cosmological structure formation simulations. Unlike original DENMAX (Bertschinger & Gelb 1991; Gelb 1992) which used a fixed grid based density estimator, `SKID` uses SPH kernel averaged densities which are much better suited to the Lagrangian nature of N-body simulations and allow the method to locally adapt to the large dynamic range found in cosmological simulations.

Particles are slowly slid (each step moving the particles by a distance of order the softening length in the simulation) along the local density gradient until they pool at a maximum, each pool corresponding to each initial group. This first phase of `SKID` can be computation-

[6]The OpenMP parallelized version of `SKID` can be freely downloaded from `http://www.hpcforge.org`

ally very expensive for large simulations, but is also quite robust.

Each pool is then "unbound" by iteratively evaluating the binding energy of every particle in their original positions and then removing the most non-bound particle until only bound particles remain. This removes all particles that are not part of substructure either because they are part of larger scale structure or because they are part of the background.

SKID can also identify structure composed of gas and stars in hydrodynamical simulations using the dark matter only for its gravitational binding effect. The "Haloes going MAD" meeting has motivated development of an improved version of the algorithm capable of also running on parallel computers.

A.2.13 AdaptaHOP (Tweed & Colombi)

The code AdaptaHOP itself is described in the Appendix A of paper Aubert et al. (2004). It simply consist in computing a SPH density for each particles. We use the 20 closest neighbours to for the purpose of estimated the SPH density. Haloes are first described as groups of particles above a density threshold ρ_t, this parameter is set to 80 which closely match results of a FOF group finder with parameter $b = 0.2$. Within those groups, local density maxima and saddle points are detected. Then by increasing the density threshold, it is a simple matter to decompose haloes into nodes which are either density maxima or groups of particles whose density is included between two values of saddle points. A node structure tree is then created to detail the whole structure of the halo itself. Each leaf of this tree is a local density maxima and can be interpreted as a subhalo, however further post-processing is needed to define the halo structure tree, describing the host halo itself, its subhaloes and subhaloes within subhaloes. This part of the code is detailed in paper Tweed et al. (2009), the halo structure tree is constructed so that the halo itself contains the most massive local maxima (Most massive Sub maxima Method: MSM). This method giving the best result for isolated snapshots as used in this paper.

In a more detailed manner, AdaptaHOP needs a set of seven parameters. The first parameter is the number of neighbors n_{nei} searched using a kD-tree scheme in order to estimate the SPH density. Among these n_{nei} neighbors the n_{hop} closest are used to run through the density field and detect both density maxima and saddle points. As we previously mentioned, parameter ρ_t set the halo boundary. The decomposition of the halo itself into leaves which are to be redefined as subhaloes has to fill in criteria set by the remaining four parameters. The most relevant being the statistical significance threshold is set via parameter $fudge$ so that $(< \rho > -\rho_t)/\rho_t > fudge/\sqrt{N}$. Where N is he number of particles in the leaves and respect the minimal mass threshold parameter set by the minimum number of particles $n_{members}$. The potential subhalo has also to respect to condition in term of density profile and minimal radius respectively through parameters α and f_ϵ. Thus ensuring that the subhalo has a maximal density ρ_{max} such as $\rho_{max} > \alpha * < \rho >$ and a radius greater than f_ϵ times the mean interparticle distance. We used the following set of parameters ($n_{nei} = n_{hop} = 20$, $\rho_t = 80$, $fudge = 4$, $\alpha = 1$, $f_\epsilon = 0.05$, $n_{members} = 20$). It is important to understand that all nodes are treated as leaves and respect these criteria before being further decomposed into separate structures. As for defining haloes and subhaloes themselves, this is done by grouping linked list of particles corresponding to different nodes and leaves from the node structure tree, the halo and subhaloes centres are defined as the position of the highest density particles the halo edge correspond to the ρ_t density threshold and the saddle points define the subhalo edge.

Please note that AdaptaHOP is a mere topological code that does *not* feature an unbinding procedure. For substructures (whose boundaries are chosen from the saddle point value) this may impact on the estimate of the mass as well as lead to contamination by host particles.

A.2.14 HOT (Ascasibar)

This algorithm, still under development, computes the Hierarchical Overdensity Tree, (HOT), of a point distribution in an arbitrary multidimensional space. HOT is introduced as an alternative to the minimal spanning tree (MST) for spaces where a metric is not well defined, like the phase space of particle positions and velocities.

The method is based on the Field Estimator for Arbitrary Spaces (FiEstAS, Ascasibar & Binney 2005; Ascasibar 2010). First, the space is tessellated one dimension at a time, until it is divided into a set of hypercubical cells containing exactly one particle. Particles in adjacent cells are considered as neighbours. Then, the mass of each point is distributed over an adaptive smoothing kernel as described in Ascasibar (2010), which provides a key step in order to define a metric.

In the HOT+FiEstAS scheme, objects corre-

spond to the peaks of the density field, and their boundaries are set by the isodensity contours at the saddle points. At each saddle point, the object containing less particles is attached to the most massive one, which may then be incorporated into even more massive objects in the hierarchy. This idea can be implemented by computing the MST of the data distribution, defining the the distance between two neighbouring particles as the minimum density along an edge connecting them (i.e. the smallest of the two densities, or the density of the saddle point when it exists). However, this is not practical for two reasons. Firstly, defining a path between two particles is not trivial when a metric is not available. Secondly, finding the saddle points would require a minimisation along the path, which is extremely time consuming when a large number of particles is involved. These problems may be overcome if the distance between two data points is given by the average density within the hyperbox they define.

Once the distances are defined in this way, `HOT+FiEstAS` computes the MST of the data distribution by means of Kruskal's algorithm (Kruskal 1956). The output of the algorithm consists of the tree structure, given by the parent of each data point in `HOT`, and a catalogue containing an estimate of the centroid (given by the density-weighted centre of mass) as well as the number of particles in the object (both including and excluding substructures). In order to discard spurious density fluctuations, a minimum number of points and density contrast are required for an object to be output to the catalogue. Currently, these parameters are set to $N > 20$ particles and a contrast threshold $\rho_{\rm peak}/\rho_{\rm background} > 5$. Although these values seem to yield reasonable results, more experimentation is clearly needed.

In this work, the algorithm is applied to the particle positions only (`HOT3D`) as well as the full set of phase-space coordinates (`HOT6D`). Since it is intended as a general data analysis tool, not particularly optimised for the problem of halo identification, it should not (and does not) take into account any problem-specific knowledge such as the concepts of binding energy or virial radius. The latter quantity, as well as the maximum circular velocity, have been computed from the raw particle IDs returned by the code.

The definition of object boundaries in terms of the saddle points of the density field will have a relatively mild impact in the results concerning the mock haloes, but it is extremely important in the cosmological case. `HOT+FiEstAS` will, for instance, identify large-scale filamentary structures that are not considered haloes by any the other algorithms (although many of these objects are indeed gravitationally bound).

On the other hand, keeping unbound particles will be an issue for subhaloes close to the centre of their host, especially in three dimensions, and a post-processing[7] script will be developed to perform this task.

Please note that due to its nature `HOT` is not yet applicable to cosmological simulations and hence only enters the comparison project in the mock halo Section A.4.1.

A.2.15 HSF (Maciejewski)

The Hierarchical Structure Finder (`HSF`, Maciejewski et al. 2009) identifies objects as connected self-bound particle sets above some density threshold. This method consists of two steps. Each particle is first linked to a local DM phase-space density maximum by following the gradient of a particle-based estimate of the underlying DM phase-space density field. The particle set attached to a given maximum defines a candidate structure. In a second step, particles which are gravitationally unbound to the structure are discarded until a fully self-bound final object is obtained.

In the initial step the phase-space density and phase-space gradients are estimated by using a six-dimensional SPH smoothing kernel with a local adaptive metric as implemented in the `EnBiD` code (Sharma & Steinmetz 2006). For the SPH kernel we use $N_{\rm sph}$ between 20 and 64 neighbours whereas for the gradient estimate we use $N_{\rm ngb} = 20$ neighbours.

Once phase-space densities have been calculated, we sort the particles according to their density in descending order. Then we start to grow structures from high to low phase-space densities. While walking down in density we mark for each particle the two closest (according to the local phase-space metric) neighbours with higher phase-space density, if such particles exist. In this way we grow disjoint structures until we encounter a saddle point, which can be identified by observing the two marked particles and seeing if they belong to different structures. A saddle point occurs at the border of two structures. According to each structure mass, all the particles below this saddle point can be attached to only one of the structures if it is significantly more massive than the other one, or redistributed between both structures if they have comparable masses. This is controlled by a simple but robust cut or grow criterion depending on a *connectivity parameter*

[7] `HOT3D` does not even read particle velocities

α which is ranging from 0.2 up to 1.0. In addition, we test on each saddle point if structures are statistically significant when compared to Poisson noise (controlled by a β parameter). At the end of this process, we obtain a hierarchical tree of structures.

In the last step we check each structure against an unbinding criterion. Once we have marked its more massive partner for each structure, we sort them recursively such that the larger partners (parents) are always after the smaller ones (children). Then we unbind structure after structure from children to parents and add unbound particles to the larger partner. If the structure has less than $N_{\rm cut} = 20$ particles after the unbinding process, then we mark it as not bound and attach all its particles to its more massive partner (note, that a smaller $N_{\rm cut}$ is used for the resolution study in Section A.4.1.4). The most bound particle of each halo/subhalo defines its position centre.

Although `HSF` can be used on the entire volume, to speed up the process of identification of the structures in the cosmological simulation volume we first apply the FOF method to disjoint the particles into smaller FOF groups.

A.2.16 6DFOF (Zemp & Diemand)

`6DFOF` is a simple extension of the well known FOF method which also includes a proximity condition in velocity space. Since the centres of all resolved haloes and subhaloes reach a similar peak phase space density they can all be found at once with `6DFOF`. The algorithm was first presented in Diemand et al. (2006). The `6DFOF` algorithm links two particles if the following condition

$$\frac{(\mathbf{x}_1 - \mathbf{x}_2)^2}{\Delta x^2} + \frac{(\mathbf{v}_1 - \mathbf{v}_2)^2}{\Delta v^2} < 1 \qquad \text{(A.1)}$$

is fulfilled. There are three free parameters: Δx, the linking length in position space, Δv, the linking length in velocity space, and $N_{\rm min}$, the minimum number of particles in a linked group so that it will be accepted. For $\Delta v \to \infty$ it reduces to the standard FOF scheme. The `6DFOF` algorithm is used for finding the phase space coordinates of the high phase space density cores of haloes on all levels of the hierarchy and is fully integrated in parallel within the MPI and OpenMP parallelised code `PKDGRAV` (Stadel 2001).

The centre position and velocity of a halo are then determined from the linked particles of that halo. For the centre position of a halo, one can choose between the following three types: 1) the centre-of-mass of its linked particles, 2) the position of the particle with the largest absolute value of the potential among its linked particles or 3) the position of the particle which has the largest local mass density among its linked particles. For the analysis presented here, we chose type 3) as our halo centre position definition. The centre velocity of a halo is calculated as the centre-of-mass velocity of its linked particles. Since in `6DFOF` only the particles with a high phase space density in the very centre of each halo (or subhalo) are linked together, it explains the somewhat different halo velocities (compared to the other halo finders) and slightly offset centres in cases only a few particles were linked.

Other properties of interest (e.g. mass, size or maximum of the circular velocity curve) and the hierarchy level of the individual haloes are then determined by a separate profiling routine in a post processing step. For example, a characteristic size and mass scale definition (e.g. r_{200c} and M_{200c}) for field haloes based on traditional spherical overdensity criteria can be specified by the user. For subhaloes, a truncation scale can be estimated as the location where the mass density profile reaches a user specified slope. During the profiling step no unbinding procedure is performed. Hence, the profiling step does not base its (sub-)halo properties upon particle lists but rather on spherical density profiles. Therefore, `6DFOF` directly returned halo properties instead of the (requested) particle ID lists.

A.2.17 Rockstar (Behroozi)

`Rockstar` is a new phase-space based halo finder designed to maximize halo consistency across timesteps; as such, it is especially useful for studying merger trees and halo evolution (Behroozi et al. in prep.). `Rockstar` first selects particle groups with a 3D Friends-of-Friends variant with a very large linking length ($b = 0.28$). For each main FOF group, `Rockstar` builds a hierarchy of FOF subgroups in phase space by progressively and adaptively reducing the linking length, so that a tunable fraction (70%, for this analysis) of particles are captured at each subgroup as compared to the immediate parent group. For each subgroup, the phase-space metric is renormalized by the standard deviations of particle position and velocity. That is, for two particles p_1 and p_2 in a given subgroup, the distance metric is defined as:

$$d(p_1, p_2) = \left(\frac{(\mathbf{x}_1 - \mathbf{x}_2)^2}{\sigma_x^2} + \frac{(\mathbf{v}_1 - \mathbf{v}_2)^2}{\sigma_v^2} \right)^{1/2}, \qquad \text{(A.2)}$$

where σ_x and σ_v are the particle position and velocity dispersions for the given subgroup. This metric ensures an adaptive selection of over-

densities at each successive level of the FOF hierarchy.

When this is complete, `Rockstar` converts FOF subgroups into haloes beginning at the deepest level of the hierarchy. For a subgroup without any further sublevels, all the particles are assigned to a single seed halo. If the parent group has no other subgroups, then all the particles in the parent group are assigned to the same seed halo as the subgroup. However, if the parent group has multiple subgroups, then particles are assigned to the subgroups' seed haloes based on their phase-space proximity. In this case, the phase-space metric is set by halo properties, so that the distance between a halo h and a particle p is defined as:

$$d(h,p) = \left(\frac{(\mathbf{x}_h - \mathbf{x}_p)^2}{r_{vir}^2} + \frac{(\mathbf{v}_h - \mathbf{v}_p)^2}{\sigma_v^2} \right)^{1/2}, \tag{A.3}$$

where r_{vir} is the current virial radius of the seed halo and σ_v is the current particle velocity dispersion. This process is repeated at all levels of the hierarchy until all particles in the base FOF group have been assigned to haloes. Unbinding is performed using the full particle potentials (calculated using a modified Barnes & Hut method); halo centres are defined by averaging particle positions at the FOF hierarchy level which yields the minimum estimated Poisson error—which in practice amounts to averaging positions in a small region close to the phase-space density peak. For further details about the unbinding process and for details about accurate calculation of halo properties, please see Behroozi et al. in prep.

`Rockstar` is a massively parallel code (hybrid OpenMP/MPI style); it can already run on up to 10^5 CPUs and on the very largest simulations ($> 10^{10}$ particles). Additionally, it is very efficient, requiring only 56 bytes of memory per particle and 4-8 (total) CPU hours per billion particles in a simulation snapshot. The code is in the final stages of development; as such, the results in this paper (although already excellent) are a minimum threshold for the performance and accuracy of the final version.[8]

A.3 The Data

In order to study, quantify, and assess the differences between various halo finding techniques we first have to define a unique set of test cases. In that regard we decided to split the suite of comparisons into two major parts:

- a well-defined mock haloes consisting of field haloes in isolation as well as (sub-)subhaloes embedded within the density background of larger entities, and
- a state-of-the-art cosmological simulation primarily focusing on the large-scale structure.

We further restricted ourselves to analysing dark matter only data sets as the inclusion of baryons (especially gas and its additional physics) will most certainly complicate the issue of halo finding. As most of the codes participating in this comparison project do not consider gas physics in the process of object identification we settled for postponing such a comparison to a later study.

We further adopted the following strategy for the comparison. For the mock haloes each code was asked to return a list of particles and the centre of the (sub-)halo as derived from applying the halo finder to the respective data set. These centres and particle lists were then post-processed by one single code deriving all the quantities studied below. By this approach we aimed at homogenising the comparison and eliminating subtle code-to-code variations during the analysis process. However, we also need to acknowledge that not all codes complied with this request as they were not designed to return particle lists; those codes nevertheless provided the halo properties in question and are included in the comparison.

For the comparison of the cosmological simulations each code merely had to return those halo properties to be studied, based upon each and every code individually. The idea was to compare the actual performance of the codes in a realistic set-up without interference in the identification/analysis process.

A.3.1 Mock Haloes

In order to be able to best quantify any differences in the results returned by the different halo finders it is best to construct test scenarios for which the correct answer is known in advance. Even though we primarily aim at comparing $v_{\max}$ and the number of gravitationally bound particles we also want to have full control over various definitions of, for instance, virial mass, i.e. we require haloes whose density profile is well known. Additionally, as subhalo detection is of prime interest in state-of-the-art cosmological simulations we also place haloes

[8] Those interested in obtaining a copy of the code as well as a draft of the paper should contact the author at behroozi@stanford.edu. Current acceptable input formats for simulation files are `ART`, `GADGET-2`, and ASCII.

within haloes within haloes etc. Further, sampling a given density profile with particles also gives us the flexibility to study resolution effects related to the number of particles actually used.

We primarily used the functional form for the (dark matter) density profile of haloes originally proposed in a series of papers by Navarro, Frenk & White (Navarro et al. 1995, 1996, 1997, the so-called "NFW profile"),

$$\frac{\rho(r)}{\rho_{\rm crit}} = \frac{\delta_{\rm c}}{r/r_{\rm s}(1+r/r_{\rm s})^2}, \qquad \text{(A.4)}$$

where $\rho_{\rm crit}$ is the critical density of the universe, $r_{\rm s}$ is the scale radius and $\delta_{\rm c}$ is the characteristic density. NFW haloes are characterised by their mass for a given enclosed overdensity,

$$M_\Delta = \frac{4\pi}{3} r_\Delta^3 \Delta \rho_{\rm crit}, \qquad \text{(A.5)}$$

where Δ is a multiple of the critical density that defines the magnitude of the overdensity and r_Δ is the radius at which this occurs. The characteristic density is then defined as,

$$\delta_{\rm c} = \frac{\Delta}{3} \frac{c^3}{\ln(1+c) - c/(1+c)}, \qquad \text{(A.6)}$$

where $c = r_\Delta/r_{\rm s}$ is the concentration. The mock haloes were generated with using a predefined number of particles that reproduced the NFW profile even though the consensus has moved away from the statement that dark matter haloes follow this particular profile all the way down to the centre. We are not interested in probing those very central regions where the density profile starts to deviate from the NFW form as found nowadays in cosmological simulations (Stadel et al. 2009; Navarro et al. 2010). We need to stress that the position and size of the maximum of the rotation curve is in fact unaffected in all tests presented here. The velocities of the particles were then assigned using the velocity dispersion given in Łokas & Mamon (2001) and distributed using a Maxwell-Boltzmann (Hernquist 1993).[9]

In addition to mock haloes whose density profile is based upon the findings in cosmological simulations (at least down to those scales probed here) we also chose to generate test haloes that follow a Plummer profile (Plummer 1911),

$$\rho(r) = \frac{3M}{4\pi r_{\rm s}^3}(1 + r^2/r_{\rm s}^2)^{-\frac{5}{2}}, \qquad \text{(A.7)}$$

where M is the total mass and $r_{\rm s}$ is the scale radius. The mock haloes were then produced again using a predefined number of particles to reproduce the profile, but this time the velocities were obtained using an isotropic, spherically symmetric distribution function (Binney & Tremaine 1987). The two major differences between the Plummer and the NFW density profile are that for the former profile the mass converges and it contains a well defined constant-density core. This constant density may pose problems for halo finders as most of them rely on identifying peaks in the density field as (potential) sites for dark matter haloes. We stress that the Plummer spheres are intended as academic problems with no observed counterpart in cosmological simulations and hence only to be taken lightly and for information purposes; they may be viewed as a stability test for halo finders and as a trial how sensitive halo characteristics are against precise measurements of the centre. We will see that some properties can still be stably recovered even if an incorrect determination of the Plummer halo centre is made.

As we also plan to study the accurate recovery of substructure we generated setups where one (or multiple) subhaloes are embedded within the density profile of a larger host halo. To this end we generate, for instance, two haloes in isolation: one of them (the more massive one) will then serve as the host whereas the lighter one will be placed inside at a known distance to the centre of its host and with a certain (bulk) velocity. The concentrations (i.e. the ratio between the virial and the scale radius) have been chosen in order to meet the findings of cosmological simulations (e.g. Bullock et al. 2001). All our mock haloes are setup with fully sampled 6D initial phase space distributions and every halo (irrespective of it becoming a host or a subhalo) has been evolved in isolation for several Gyrs in order to guarantee equilibrium. The mass of all particles in both the host halo and the subhalo are identical and all haloes have been sampled with particles out to $2 \times R_{100}$ where R_{100} marks the point where the density drops below $100 \times \rho_{\rm crit}$. For more details of the procedure and the generation of the NFW haloes we would like to refer the reader to Muldrew et al. (2011) and for the generation of the Plummer spheres to Read et al. (2006).

[9] We are aware that the velocity distribution is not derived from the full distribution function and that the Maxwell-Boltzmann distribution is only an approximation (cf. Kazantzidis et al. 2004; Zemp et al. 2008). Despite this, it will have no effect on the ability of halo finders to recover the haloes as has been shown in Muldrew et al. (2011) where also more details about the generation of the mock haloes can be found.

The characteristics of the haloes are summarised in Table A.1. We are aware of the fact that even though the radius at which the enclosed overdensity reaches some defined level is well-defined for our subhaloes when they were generated in isolation, such a definition becomes obsolete once they are placed inside a host. However, we nevertheless need to acknowledge that such a definition may serve as a fair basis for the comparisons of the recovery of subhalo properties amongst different halo finders.

Further, placing an unmodified subhalo at an arbitrary radial distance within a parent halo is also in part an academic exercise. It neglects that "real" subhaloes will always be tidally truncated. In that regards, it is not realistic to have an extended/untruncated subhalo at small distances to the host's centre. Some halo finders (e.g. `SUBFIND`) rely on the tidal truncation in order to be able to avoid a very large radially dependent bias in the amount of mass that can be recovered for a subhalo.

For each of the two types of density profile we generated the following setups:

1. isolated host halo
2. isolated host halo + subhalo at $0.5R_{100}^{\rm host}$
3. isolated host halo + subhalo at $0.5R_{100}^{\rm host}$ + subsubhalo at $(0.5R_{100}^{\rm host} + 0.5R_{100}^{\rm subhalo})$
4. isolated host halo + 5 subhaloes at various distances

The (sub-)subhaloes were placed along the x-axis and given radially infalling bulk velocities of 1000 km/sec for the subhalo and 1200 km/sec for the subsubhalo, respectively. These velocities are typical for what you would expect in a dark matter host halo and were set to round numbers to make the analysis easier; their values were motivated by $\sqrt{2GM_{\rm host}(<D)/D}$ where D is the distance of the subhalo to the host's centre.

The first three setups were used to study the overall recovery of (sub-)halo properties presented in Section A.4.1.1. The fourth test has been used to study the radial dependence of subhalo properties introduced in Section A.4.1.2.

Besides of the recovery of (sub-)halo properties we also aim at answering the question "How many particles are required to find a subhalo?". To this end we systematically lowered the number of particles (and hence also the subhalo mass as our particle mass remains constant) used to sample the subhalo listed above as test case #2. The properties of these mock subhaloes are summarised in Table A.2 and the results will be shown in Section A.4.1.4.

Besides these well controlled tests we also performed a so-called "blind test" where the precise set-up of the data to be analysed by each halo finder was unknown to the participants. We introduce this particular experiment alongside its results in a stand-alone Section A.4.1.5. Only a small subset of the halo finders took part in this trial.

We close this section with a cautionary remark that not all halo finders are ab initio capable of identifying subhaloes and hence some of the test cases outlined here were not performed by all the finders. Therefore some of the codes only contribute data points for the host halo in Section A.4.

A.3.2 Cosmological Simulation

The cosmological simulation used for the halo-finder code comparison project is the so-called MareNostrum Universe which was performed with the entropy conserving GADGET2 code (Springel 2005). It followed the nonlinear evolution of structures in gas and dark matter from $z = 40$ to the present epoch ($z = 0$) within a comoving cube of side $500h^{-1}\,$Mpc. It assumed the spatially flat concordance cosmological model with the following parameters: the total matter density $\Omega_m = 0.3$, the baryon density $\Omega_b = 0.045$, the cosmological constant $\Omega_\Lambda = 0.7$, the Hubble parameter $h = 0.7$, the slope of the initial power spectrum $n = 1$, and the normalisation $\sigma_8 = 0.9$. Both components, the gas and the dark matter, were resolved by 1024^3 particles, which resulted in a mass of $m_{\rm DM} = 8.3 \times 10^9 h^{-1}{\rm M}_\odot$ for the dark matter particles and $m_{\rm gas} = 1.5 \times 10^9 h^{-1}{\rm M}_\odot$ for the gas particles, respectively. For more details we refer the reader to the paper that describes the simulation and presents results drawn from it (Gottlöber & Yepes 2007).

For the comparison presented here we discarded the gas particles as not all halo finders yet incorporate proper treatment of gas physics in their codes. The focus here lies with the dark matter structures. However, to avoid that too many particles will be considered "unbound" (for those halo finders that perform an unbinding procedure), the masses of the dark matter particles have been corrected for this, i.e. $m_{\rm DM}^{\rm corrected} = m_{\rm DM}/(1-f_b)$ where $f_b = \Omega_b/\Omega_m$ is the cosmic baryon fraction of our model universe.

In order to allow non-parallel halo finders to participate in this test we degraded the resolution from the original 1024^3 particles down

Table A.1: The properties of the (sub-)haloes for the study of recovered halo properties presented in Section A.4.1.1 and Section A.4.1.2 . The number of particles $N_{\rm xxx}$ counts all particles out to $R_{\rm xxx}$ where the density drops below xxx $\times\, \rho_{\rm crit}$. Masses are given in $h^{-1}{\rm M}_{\odot}$, radii in $h^{-1}\,$kpc, and velocities in km/sec. Please note that all haloes have been sampled out to $2 \times R_{100}$ and that the Plummer subsubhalo does not reach this overdensity and has been truncated at $23.9h^{-1}\,$kpc. The halo type indicates whether the halo is a host, a subhalo or a subsubhalo. $R_{\rm s}$ is the scale length of the appropriate halo type.

profile	type	N_{100}	M_{100}	R_{100}	N_{200}	M_{200}	R_{200}	$R_{\rm s}$	$v_{\rm max}$
NFW	host	10^6	10^{14}	947.4	760892	7.61×10^{13}	689.1	189.5	715
	sub	10^4	10^{12}	204.1	8066	8.07×10^{11}	151.4	17.0	182
	subsub	10^2	10^{10}	44.0	84	8.42×10^{9}	33.1	2.6	43
Plummer	host	10^6	10^{14}	947.0	966326	9.66×10^{13}	760.5	190.0	961
	sub	10^4	10^{12}	204.0	9937	9.94×10^{11}	161.7	17.0	314
	subsub	10^2	10^{10}	23.9	100	10.00×10^{9}	23.9	2.6	79

Table A.2: The properties of the subhaloes for the NFW resolution study presented in Section A.4.1.4. Radii are given in $h^{-1}\,$kpc, and velocities in km/sec.

N_{100}	$N_{\rm tot}$	R_{100}	$v_{\rm max}$	$R_{\rm vmax}$
10	13	20.41	18.24	3.68
20	27	25.72	22.99	4.62
30	41	29.44	26.31	5.30
40	55	32.40	28.96	5.85
50	68	34.90	31.20	6.30
100	137	43.98	39.31	7.93
500	687	75.20	67.21	13.55
1000	1375	94.74	84.68	17.08

to 512^3 as well as to 256^3 particles. The properties to be compared will however be drawn from the highest-resolved data set for each individual halo finder, making the appropriate mass/number cuts when producing the respective plots.

A.3.3 Code Participation

Not all codes have participated in all the tests just introduced and outlined. Hence in order to facilitate an easier comparison of the results and their relation to the particular code we provide in Table A.3 an overview of the tests and the halo finders participating in them. In that regard we also list for the cosmological simulation the respective resolution of the data set analysed by each code. The last two columns simply indicate whether the code performs an unbinding procedure and provided subhalo properties, respectively.

A.4 The Comparison

This Section forms the major part of the paper as it compares the halo catalogues derived with various halo finders when applied to the suite of test scenarios introduced in the previous Section. We first address the issue of the controlled experiments brought forward in Section A.4.1 followed by the analysis of the cosmological simulation introduced in Section A.4.2. As already mentioned before, we are solely addressing dark matter haloes leaving the inclusion of baryonic matter (especially gas) for a later study.

A.4.1 Mock Haloes

Before presenting the results of the cross comparison we need to explain further the actual procedures applied. Each data set was given to the respective code representative asking them to return the centre of each object found as well as a list of the (possible) particles belonging to each (sub)halo. A single code only using that particular list was then used to derive the bulk velocity $V_{\rm bulk}$, the (fiducial) mass M_{200}, and the peak of the rotation curve $v_{\rm max}$ in order to eliminate differences in the determination of said values from code to code. Or in other words, we did not aim at comparing how different codes calculate, for instance, $v_{\rm max}$ or M_{200} and so eliminated that issue. This simple analysis routine is also available from the project website. We were aiming at answering the more fundamental question "Which particles may or may not belong to a halo?" according to each code. However not all representatives returned particle lists as requested (due to a different method or technical difficulties) but rather directly provided the values in question; those codes are `BDM`, `FOF`, and `6DFOF`. Further, `FOF` did not provide values for $v_{\rm max}$.

And when comparing results we primarily focused on fractional differences to the theoretical values by calculating $\Delta x/x_{\rm Model} = (x_{\rm code} - x_{\rm Model})/_{\rm Model}$ where x is the halo property in question.

A.4.1.1 Recovery of Host and Subhalo Properties

For all the subsequent analysis and the plots presented in this subsection A.4.1.1 we used the the setups (i) through (iii) specified in Section A.3.1. In that regard we have three host haloes (one for the host alone, one from the host + subhalo setup, and one from the host+subhalo+subsubhalo configuration); we further have two subhaloes at our disposal (one from the host+subhalo and one from the host+subhalo+subsubhalo tests) as well as one subsubhalo. In all figures presented below the origin of the halo is indicated by the size of the symbol: the largest symbol refers to the host+subhalo+subsubhalo set with the symbol size decreasing in the order of the host+subhalo towards the host test alone. We further always show the results for the NFW mock haloes in the left panel and the Plummer spheres in the right one. As much as possible, the halo finders have been organised in terms of their methodology: spherical overdensity finders first followed by FOF-based finders with 6D phase-space finders last.

Centre Determination We start with inspecting the recovery of the position of the haloes as practically all subsequent analysis as well as the properties of haloes depend on the right centre determination. The results can be viewed in Fig. A.2 where the y-axis represents the halo finder and the x-axis measures the offset between the actual position and the recovered centre in $h^{-1}\,$kpc.

We can clearly see differences for all sorts of comparisons: host haloes vs. (sub-)subhaloes, NFW vs. Plummer model, and – of course – amongst halo finders. While for the NFW density profile the deviations between analytical and recovered centre are for the majority of haloes and codes below $\approx 5h^{-1}\,$kpc there are nevertheless some outliers. For the large halo the 100^{th} particle is $3h^{-1}\,$kpc from the nominal centre. These outliers are primarily for the FOF-based halo finders which are using a centre-of-mass rather than a density-peak as

Table A.3: Brief summary of the codes participating in the comparison project. The first six columns provide a synopsis of the respective tests the code participated in (columns 2–7). The last two columns simply list whether the code performs an unbinding procedure and provided subhalo properties, respectively.

code	participation in test						unbinding	subhaloes
	recovery	rad. depend.	dyn. infall	resolution	blind	cosmology		
AHF	yes	yes	yes	yes	yes	1024^3	yes	yes
ASOHF	yes	yes	yes	yes	yes	256^3	yes	yes
BDM	yes	yes	yes	yes	yes	512^3	yes	yes
pSO	only host	no	no	no	only host	1024^3	no	no
LANL	only host	no	no	no	no	1024^3	no	no
SUBFIND	yes	yes	yes	yes	yes	1024^3	yes	yes
FOF	yes	yes	yes	yes	no	1024^3, no $v_{\rm max}$	no	limited
pFOF	only host	no	no	no	no	512^3	no	no
Ntropy-fofsv	only host	no	no	no	no	1024^3, no $v_{\rm max}$	no	no
VOBOZ	yes	yes	no	yes	yes	512^3	yes	yes
ORIGAMI	no	no	no	no	no	512^3	yes	no
SKID	yes	yes	yes	yes	yes	1024^3	yes	yes
AdaptaHOP	yes	yes	yes	yes	yes	512^3	no	yes
HOT	yes	yes	yes	yes	yes	no	no	yes
HSF	yes	yes	yes	yes	yes	1024^3	yes	yes
6DFOF	yes	yes	yes	yes	yes	1024^3	no	yes
Rockstar	yes	yes	yes	yes	no	1024^3	yes	yes

the centre. However, for a perfectly spherically symmetric setup as the one used here the differences between centre-of-mass and density peak should be small. Some of the finders (pSO, LANL, pFOF, ntropy-fofsv) were not designed to find substructure and so do not return the locations for these. Interestingly HOT6D cannot detect the NFW subsubhalo. The situation is a bit different for the Plummer model that consists of a flat density profile inwards from the scale radius of $190h^{-1}$ kpc. While the centre offset for the FOF finders remains the same we now also observe a shift towards larger offset-values for the majority of the other codes; some codes were even unable to locate the host halo at all (e.g. SKID) while other finders even marginally improved their (sub-)halo centre determination (AHF, ASOHF, HOT3D). Remember that for 6DFOF all positions and velocities were solely determined from the linked particles which explains the slightly offset centres in cases only a few particles were linked (as in the case of the Plummer sphere which had an artificial low phase space density by construction) as well as the somewhat different bulk velocities (when compared to the other halo finders below).

Halo Bulk Velocity A natural follow-up to the halo centre is to ask for the credibility of the bulk velocity of the halo. Errors in this value would indicate contamination from particles not belonging to the halo in question to be studied in greater detail in Section A.4.1.4 below. In our test data the host is always at rest whereas the subhalo (subsubhalo) flies towards the centre with -1000 (-1200) km/sec along the negative x-direction. The fractional difference between the model velocity and the bulk velocity as measured for each halo finder is presented in Fig. A.3. Please note that we have normalised the host's velocities to the rotational velocity at the R_{100}, i.e. $\approx$1000 km/sec, for the two density profiles. Here we find that for practically all halo finders the error in the bulk velocity is smaller than 3%; only some outliers exist. Please note that we used all particles in the determination of the bulk velocities as returned/recovered by the respective halo finder. SKID displays very significant contamination in the recovered subhaloes with a 40% error in the recovered bulk velocity but is also one of the codes whose returned particle lists are intended to undergo significant post-processing. AdaptaHOP and HOT3D have smaller but still significant levels of contamination within the returned substructures. The marginal offset in the bulk velocities of the host Plummer host haloes for 6DFOF and BDM are directly related to the respective centre offsets seen in Fig. A.2: those two codes base their bulk velocities on particles in the central regions.

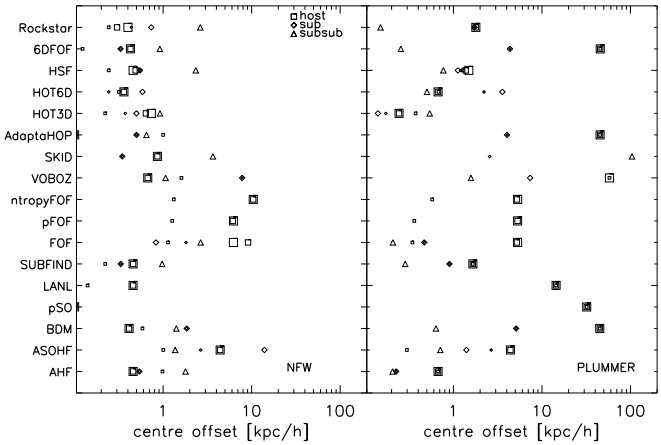

Figure A.2: The offset of the actual and recovered centres for the NFW (left) and Plummer (right) density mock haloes. The symbols refer to either the host halo, subhalo or subsubhalo as indicated while the symbol size indicates the test sequence as detailed in the text (i.e. larger symbols for haloes containing more subhaloes).

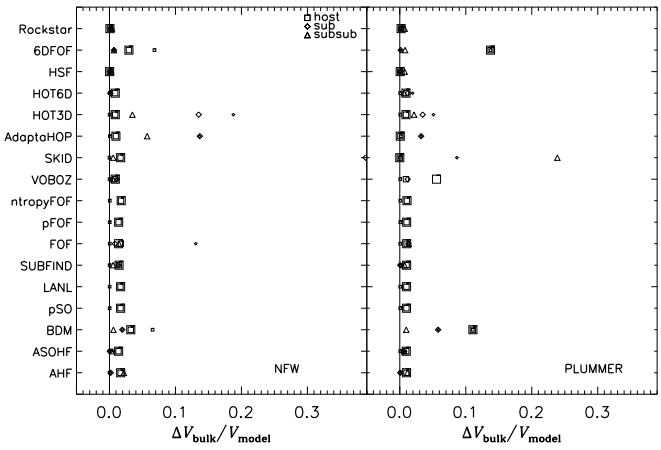

Figure A.3: Recovery of halo bulk velocities in comparison to the analytical input values for the NFW (left) and Plummer (right) density mock haloes. Note that the host halo has been set up to be at rest with $v_{\rm bulk} = 0$. The symbols have the same meaning as in Fig. A.2.

Number of Particles In Fig. A.4 we are comparing the number of particles recovered by each halo finder to the number of particles within M_{200} listed in Table A.1[10]. We are aware that there is no such well defined radius for (sub-)subhaloes, but it nevertheless provides a well-defined base to compare against.

We observe that while the errors are at times substantial for the NFW model the Plummer results appear to be more robust this time. But this is readily explained by the form of the applied density profile: the variations in mass and hence number of particles are more pronounced for the NFW profile than for the Plummer model when changing the (definition of the) edge of a halo. Or in other words, the total mass of a Plummer model is well-defined whereas the mass of an NFW halo diverges. Therefore, (minor) changes and subtleties in the definition of the other edge of a (sub-)halo will lead to deviations from the analytically expected value – at least for the NFW model. To this extent we also need to clarify that each halo finder had been asked to return that set of particles that was believed to be part of a gravitationally bound structure; participants were not asked to return the list of particles that made up M_{200}. Post-processing of the supplied particle lists to apply this criterion results in errors for the NFW profiles that are well below 10% – at least for the host haloes (cf. Fig. A.5 below). However, a straight comparison of the number of recovered particles amongst the codes reveals a huge scatter. This is due to the fact that the individual codes are tuned to different criteria to define the edge of the halo. Clearly some codes (`HSF, HOT, VOBOZ`) have been tuned to extract an effectively smaller overdensity for this test than say `6DFOF, LANL, pSO` or `AHF`. This is a well known issue and all code developers are well aware of it. Perhaps more concerning is the wide scatter in relative mass of the largest subhalo. Here M_{200} is ill-determined but the ratio of the substructure mass to the host halo mass displays a wide scatter. This ratio is a astrophysical importance for several issues.

The difference in host halo seen for `FOF` and `pFOF` is – in general – due to the choice of a linking-length not corresponding to $200 \times \rho_{\rm crit}$. However, with an appropriate linking length the `FOF` algorithm detects the halo at the desired overdensity correctly as can be seen for the host only and host+subhalo data for which there is agreement with the analytical expectation as opposed to the host+subhalo+subsubhalo where the standard linking length has been applied and hence the number of particles (and mass) is over-estimated. As a (down-)tuned linking length has also been utilized for the detection of the (positions of the) subhaloes, the higher overdensity encompassed naturally led to a smaller number of particles (and masses) than assumed in the model.

Again, we stress that Fig. A.4 does not necessarily reflect the number of particles actually used to calculate halo properties; it is the raw number of (bound) particles assigned to the centre of the respective (sub-)halo and used for further post-processing with most of the codes. But the comparison also indicates that neither number of particles nor M as defined by some overdensity criterion (see below) are stable quantities for a fair comparison; this is why we argue in favour of the peak of the rotation curve for cross-comparison as already highlighted in the introduction.

Mass Using the particle lists provided by each halo finder we extract each object and calculate the density profile. From this we determine the point where it drops below $200 \times \rho_{\rm crit}$. This point can then be used as a radial distance within which to define M_{200} which is then compared against the theoretical expectation (cf. Table A.1) in Fig. A.5. Again, we acknowledge that this is not the correct definition for (sub-)subhalo mass, but can regardlessly be used to compare halo finders amongst themselves.

As already outlined in the previous paragraph, the differences to the analytical values (and between the codes) are substantially alleviated now that differences in definition for the edge of each halo have been removed. The apparent underestimation of the (sub-)subhalo masses has also to be taken and digested carefully as the M_{200} values are based upon objects in isolation when these are embedded in a large host halo. However, please recall that the values for `BDM, FOF, 6DFOF` are based upon their respective criteria as these codes did not return particle lists but directly M_{200}.

Amongst those codes that did recover subhaloes and underwent the same processing scheme there remains a surprisingly wide variation in recovered subhalo M_{200} mass. Almost all the codes studied here post-process their subhalo catalogues heavily to alleviate this problem. We would stress however that the precise definition for a subhalo contents can, as demonstrated, lead to a range of recovered subhalo masses, a point users of subhalo catalogues should be well aware of. We will return to the issue of missing subhalo mass in Section A.4.1.3 below, which provides some explanation for the variation.

[10] Please note that in all subsequent plots we are using N_{200} when referring to $N_{\rm model}$.

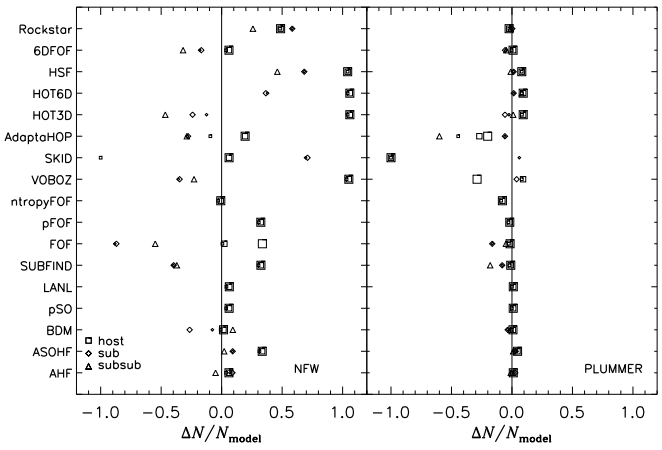

Figure A.4: Total number of particles recovered for the (sub-)halo for the NFW (left) and Plummer (right) density mock haloes with respect to the number of particles within M_{200}. The symbols have the same meaning as in Fig. A.2.

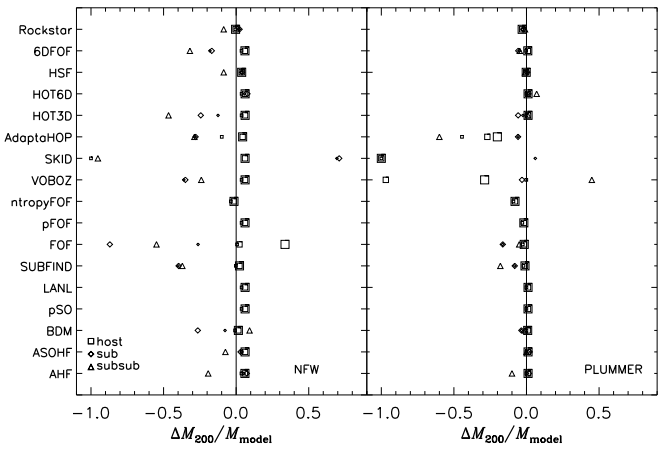

Figure A.5: M_{200} mass (as determined from the supplied particle lists) measured according to the mean enclosed density being $200 \times \rho_{\rm crit}$ criterion for the NFW (left) and Plummer (right) density mock haloes extracted from each finder's list of gravitationally bound particles. The symbols have the same meaning as in Fig. A.2.

Maximum of the Rotation Curve As outlined in Section A.1.3, M_{200} does not provide a fair measure for (sub-)subhalo mass and hence we consider the maximum circular velocity $v_{\rm max}$ as a proxy for mass. The fractional difference between the theoretically derived $v_{\rm max}$ and the value based upon the particles returned by each halo finder are plotted in Fig. A.6. While we now find a considerably improved agreement with the analytical calculation the subsubhalo has still not been recovered correctly in most of the cases. This result is entirely in line with the results of figure 7 of Muldrew et al. (2011) where the error in measuring $v_{\rm max}$ for a range of particle numbers was calculated: we should not be surprised by a 10% underestimate for our subsubhalo as this is well within expected limits.

A.4.1.2 Radial Dependence of Subhalo Properties

The following test aims at studying how the recovered properties of a subhalo change as a function of the distance from the centre of the subhalo to the centre of its host. We always placed the same subhalo (sampled with 10000 particles) at various distances and applied each halo finder to this test scenario, without changing the respective code parameters in-between the analyses. We then focused our attention on the number of gravitationally bound particles in Fig. A.7, the recovered M_{200} masses in Fig. A.8 and the maximum of the rotation curve in Fig. A.9.

We reiterate that this particular test (as well as the following two) is only suited to halo finders that are able to identify substructure embedded within the density profile of a larger encompassing object. Therefore, some of the codes will not appear in this and the following tests in Section A.4.1.4 and Section A.4.1.3. However, we also need to acknowledge that some of the code developers were keen to participate in this venture and manually tuned their halo finders to (at least) provide a centre (and possibly mass) estimate for the subhalo under investigation (e.g. `FOF` by Gottlöber & Turachninov systematically lowered their linking length until an object had been found using the spin parameter as a measure for credibility (cf. Section A.2.7); however, as `FOF` in its basic implementation does not perform any unbinding they did not dispense particle lists and/or internal properties.). Therefore, the results for `FOF` are to be taken lightly and with care.

Number of Particles Aside from the location of the substructure, which we are not investigating in more detail in this particular Subsection, the number of particles recovered by each halo finder is the first quantity to explore as a function of subhalo distance. The results can be viewed in Fig. A.7 with the NFW mock halo in the upper panel and the Plummer sphere in the lower. Recall that there are five subhaloes placed at various distances from the centre of the host with the closest one actually overlapping with the host centre.

As expected from the above results of the previous section (which equate to the middle position of these five haloes) the various halo finders recover a range of number of particles within the halo. Only the phase space based finders are capable of disentangling the subhalo when it is directly in the centre. Even then their particle recovery either indicates that there are too few particles associated with the subhalo or that they found the host. We further observe that, at least for the NFW haloes, the number of recovered particles drops the closer we get to the centre. This is naturally explained by the fact that the density contrast of the subhalo becomes smaller and the point where the host halo's density takes over is closer to the centre of the subhalo. This is another reflection of the fact that the number of particles (or anything based upon a measure of "halo edge") is not a good proxy for the actual subhalo. The situation is obviously different for the Plummer sphere with no pronounced density rise towards the centre; therefore, the subhalo appears to be well recovered in this case. For the low number of particles recovered by `SUBFIND` we refer the reader to an improved discussion and investigation, respectively, in Muldrew et al. (2011).

In any case, these are the still simply particle lists; we continue to check the (hypothetical) M_{200} values as well as the recovery of the maximum of the rotation curve. When defining a (hypothetical) M_{200} value considering the subhalo in isolation we find basically the same trends as for the number of particles. This can be verified in Fig. A.8 where we observe the same phenomena as in Fig. A.7. However, `SKID` is the exception with the M_{200} values closer to the actual model mass across all distances than the number of particles, as expected and as they themselves would obtain during their own post-processing steps.

We note that the discrepancy between the (fiducial) mass and the real mass of the subhalo placed at different radial distances from the centre is more serious in this idealised set-up than it would be in a realistic situation, where the substructures would experience tidal truncation in moving towards the inner regions of

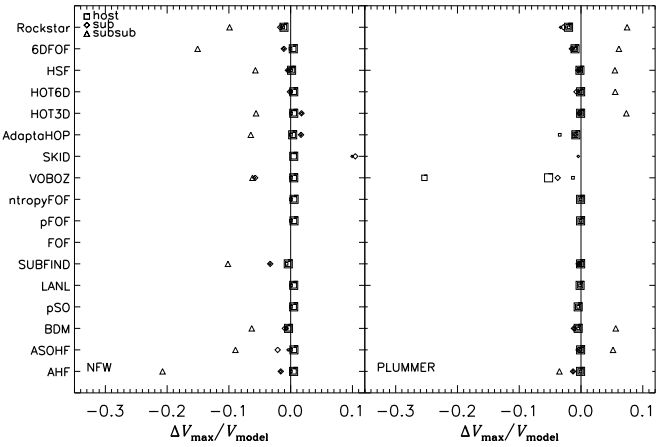

Figure A.6: Recovery of numerical $v_{\rm max}$ values in comparison to the analytical input values for the NFW (left) and Plummer (right) density mock haloes. The symbols have the same meaning as in Fig. A.2.

the halo (see the discussion in Section A.3.1 as well as the study of the dynamical subhalo infall in Section A.4.1.3 below); when considering the mass within the tidal truncation radius, the discrepancy between the "real" and recovered mass would reduce.

The most credible measure of subhalo mass, however, appears to be the maximum of the rotation curve: it hardly changes its value irrespective of the position inside the host halo as can be seen in Fig. A.9. All halo finders perform equally well in recovering the $v_{\rm max}$ value from the list of particles used in Fig. A.7. This then indicates that the only difference amongst the halo finders as seen as a substantial spread in (the upper panel of) Fig. A.7 stems from the outer and less well contrasted regions of the subhalo.

Maximum of Rotation Curve We have seen in Section A.4.1.1 that the maximum of the rotation curve $v_{\rm max}$ serves as an adequate proxy for mass and hence we test its sensitivity to radial position in Fig. A.9. We find that this quantity is, as expected, hardly affected by the actual position of the subhalo within the host. Its value is determined by the more central regions of the subhalo and hence does not change if the object is truncated in the outskirts due to embedding within the host's background density field. Only when the two centres of the sub- and the host halo overlap do we encounter problems again, however, `HOT6D` and `HSF` even masters this situation fairly well (at least for the more realistic NFW test scenario).

A.4.1.3 Dynamical Infall of a Subhalo

The test described and analysed in this Subsection is a dynamic extension of the previously studied radial distance test: we throw a subhalo (initially sampled with 10000 particles inside M_{100}) into a host halo two orders of magnitude more massive. It was initially placed at a distance of $D = 3 \times R_{100}^{\rm host}$ with a radially inwards velocity of $v = \sqrt{2GM(<D)/D} =$ 686km/s and then left to free-fall. During the temporal integration of this system with GADGET-2 the cosmological expansion was turned off so the haloes were only affected by gravity. The orbit of the subhalo takes it right through the host halo centre, exiting on the other side. Due to the tidal forces the subhalo will lose mass and we aim at quantifying how different halo finders recover both the number of (bound) particles as well as the evolution of the peak rotational velocity.

Evolution in Number of Particles In Fig. A.10 we start again with the number of recovered particles this time as a function of time measured in Gyrs since the infalling object passed $2 \times R_{200}^{\rm host}$. Note the fractional difference

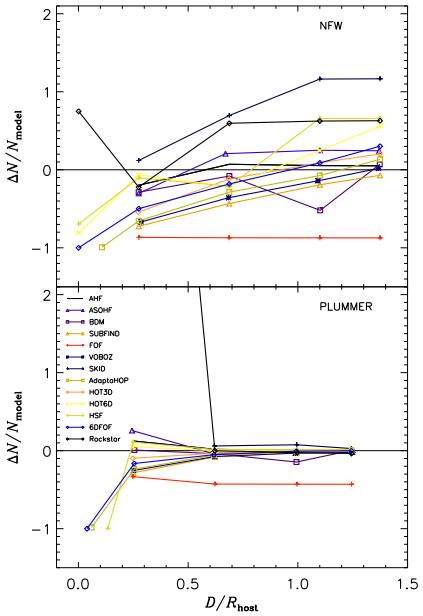

Figure A.7: Number of particles belonging to the subhalo for the NFW (upper) and Plummer (lower) density mock haloes as a function of subhalo distance to the host.

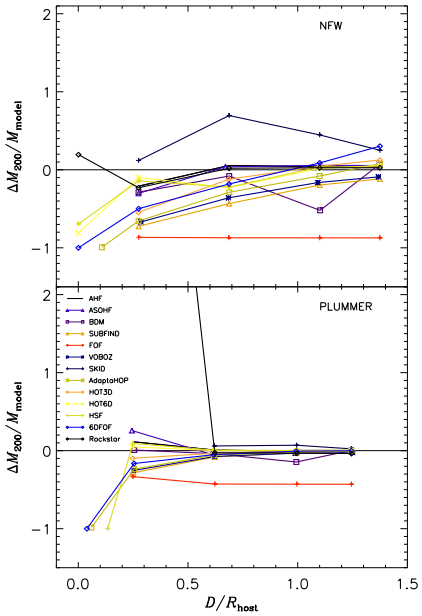

Figure A.8: Hypothetical M_{200} value comparison to the NFW (upper) and Plummer (lower) subhalo as a function of distance to the host. M_{200} was calculated again considering the recovered particles N (as presented in Fig. A.7) in isolation.

$\Delta N/N_{\rm model}$ is measured with respect to the number of particles $N_{\rm model}$ prior to infall and that the analysis has only been performed over a certain number of output snapshots and not every integration step. At the starting point we observe again the same scatter in the number of particles as already found in Fig. A.7.[11] Until the passage through the very centre of the host halo after approximately 1.8 Gyrs we also find the expected drop in number of particles due to the stripping of the subhalo; however, as noted in Fig. A.7 part of this drop can also be attributed to the subhalo moving deeper into the dense region of the host. This drop in particle number has a marginally different shape depending on the halo finder, and for `ASOHF` there is even a marginal rise. But this time actually all halo finders (except the phase-space finders `HOT6D`, `HSF` and `6DFOF`, cf. Fig. A.12 below) do lose the subhalo when it overlaps with the host halo - or at least are unable to determine its properties at that time (e.g. `6DFOF` actually found the objects but could not assign the correct particles to it as the search radius for "subhalo membership" was practically zero). After the passage through the centre all halo finders identify the object again with more particles yet obviously not reaching the original level anymore.

However, we also like to mention that after the core transition of the subhalo we expect to find a more or less constant set of particles that remain bound to the subhalo: as the radial distance increases again there is no reason for the subhalo to lose additional mass. It seems clear that the majority of structure finders agree on this plateau value, but there are also some that

[11] However, when comparing Fig. A.7 and Fig. A.10 one needs to bear in mind that the radial dependence of subhalo properties only extends out to $\approx 1.37 \times R_{200}^{\rm host}$ whereas the first data point in Fig. A.10 is for $2 \times R_{200}^{\rm host}$.

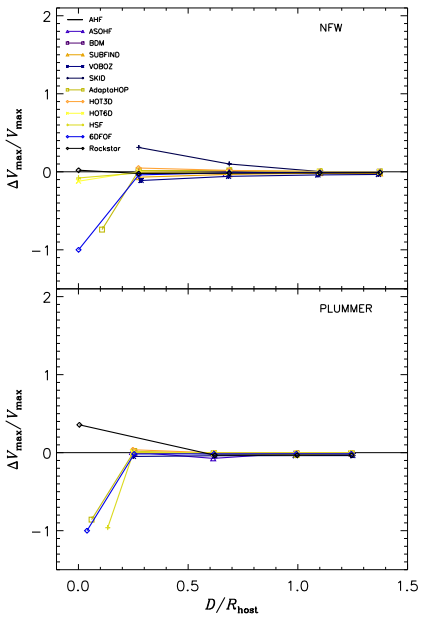

Figure A.9: Recovery of numerical $v_{\max}$ values in comparison to the analytical input values for the NFW (upper) and Plummer (lower) density mock haloes as a function of subhalo distance to the host.

return an unphysical result in this regime (e.g. both `HOT` codes as well as `6DFOF` in the early phases).

Please note again that none of the FOF-based halo finders is ab initio designed to locate substructure, but the `FOF` results have been included as this code was manually tuned to locate subhaloes (cf. Section A.4.1.2).

Evolution of the Maximum of the Rotation Curve As we have seen before a number of times already, the number of particles has to be used with care as the actual halo properties will be based upon them, but the list has undeniably to be pruned and/or postprocessed. We therefore present in Fig. A.11 again the evolution of the maximum of the rotation curve which focuses on the more central regions of the subhalo and its particles. Here we can undoubtedly see that all halo finders perform equally well (again): they all start with a value equal to the analytical input value and drop by the same amount once the subhalo has left the very central regions again. However, the majority of the codes (except `SUBFIND`, `HSF`, and `SKID`) found a sharp rise of $v_{\max}$ right after the central passage.

To gain better insight into this region we show in Fig. A.12 a zoom into the timeframe immediately surrounding the central passage, this time though using the distance (as measured by the respective halo finder) to the host centre as the x-axis. We attribute part of this rise to an inclusion of host particles in the subhalo's particle list to be studied in greater detail below in Section A.4.1.4; we can see that codes having problems with such contamination appear to show this rise too – even though not all of the codes showing this rise are amongst the list of finders showing contamination. However, this rise is also (or maybe even more) indicative of problems with the unbinding procedure: particles who have just left the subhalo (and are then part of the host) may still be considered bound depending on the particulars of the halo finder. For instance, `AHF` assumes a spherically symmetric object during the unbinding process which is obviously not correct for an object heavily elongated by the strong tides during the central passage. However, one should also bear in mind that a rise in $v_{\max}$ also occurs when the subhalo gets (tidally) compressed and hence $R_{\max}$ is lowered (cf. Dekel et al. 2003) even though this has not been seen in all (controlled) experiments of this kind (e.g. Hayashi et al. 2003; Klimentowski et al. 2009).

Finally we point out that the x-axis is based upon the distance to the host centre as measured by each individual halo finder; and it is rather obvious that all halo finders have recovered (more or less) the same distance for the subhalo.

A.4.1.4 Resolution Study of a Subhalo

While we have seen that there is little variation of the most stable subhalo properties with respect to distance to the host (i.e. $v_{\max}$) we now investigate the number of particles required to (credibly) identify a subhalo. To this extent we used setup (ii) from the list in Section A.3.1 where we placed a single subhalo into a host halo at half the host's M_{100} radius. But this time we also gradually lowered its mass and number of particles (keeping the mass of an individual particle constant). Even though it is meaningless to talk about R_{200} radii for subhaloes again, we are nevertheless comparing the number of gravitationally bound particles, as

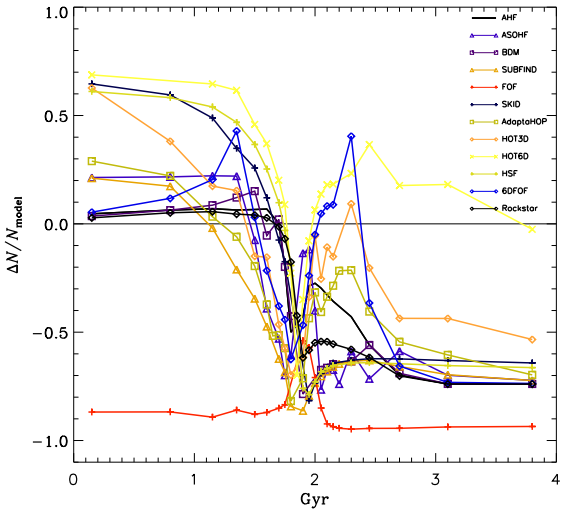

Figure A.10: Temporal evolution of the number of particles belonging to the subhalo for the dynamical infall study.

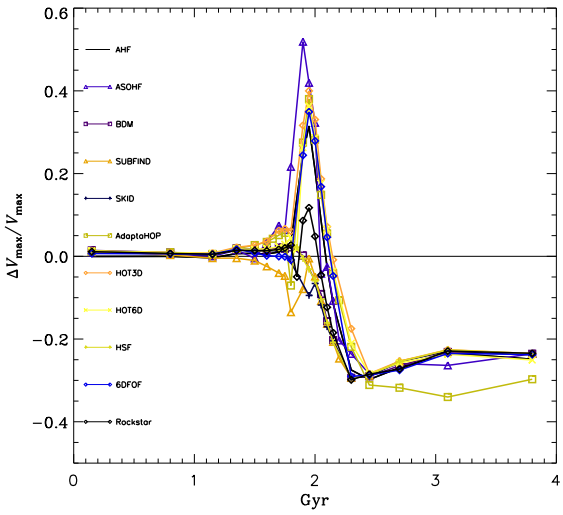

Figure A.11: Temporal evolution of the maximum of the rotation curve for the dynamical infall study.

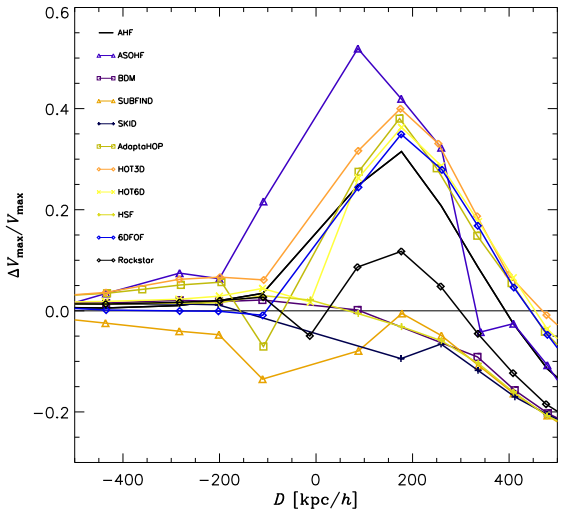

Figure A.12: The maximum of the rotation curve for the dynamical infall study as a function of distance (as measured by the halo finder) to the centre of the host – zooming into the region about the centre.

returned by the respective halo finder, to the number of particles inside the subhaloes' R_{200} radius; remember that the subhaloes were generated in isolation and sampled out to 2× their M_{100} radius (cf. Section A.3.1).

Number of Particles The results of this resolution study can be viewed in Fig. A.13 where we plot the fractional difference in the number of particles within R_{200} against the number of particles in the subhalo. In this figure there are two important things to note and observe: a) the end point of each curve (towards lower particle numbers) marks the point where the respective halo finder was no longer able to identify the object and b) a constant line (irrespective of being above, on top, or below the 0-line) means that for each particle number the error in the determination is equal. Again, practically all halo finders perform equally well, i.e. they recover the input number of particles with a constant error across all values. Only the two `HOT` algorithms show a strong deviation due to the lack of an unbinding procedure. It is also interesting to compare the (inner) end point of the curves marking the number of particles for which a certain code stopped finding the subhalo: all of them were still able to identify the object with 50 particles. `HSF` and `SKID` actually went all the way down to 10 particles with `VOBOZ`, `6DFOF`, and `Rockstar` stopping at 20 particles, and `AHF` at 30. We need to stress that codes were asked not to alter their technical parameters while performing this resolution study and hence some may in fact be able to recover objects with a lower number of particles than presented here. For instance, we are aware that `SUBFIND` (as well as `AHF` and `ASOHF`) is capable of going all the way down to 20 particles, if the technical parameters are adjusted appropriately.

In any case, we also observe that some codes show a rise in $\Delta N/N_{\rm model}$ towards lower particle numbers (e.g. `AdaptaHOP`, `HOT`); could this be due to contamination from host halo particles? We will study this phenomenon in the following Subsection.

Contamination by Host Particles Downsizing a subhalo yet still trying to pinpoint it also raises the question how many of the recovered particles are actually subhalo and how many are host halo particles. We are in the unique situation to know both the id's of the sub- and the host halo and hence studied the "contamination" of the subhalo with host particles as a function of the number of (theoretical) subhalo particles in Fig. A.14. We can

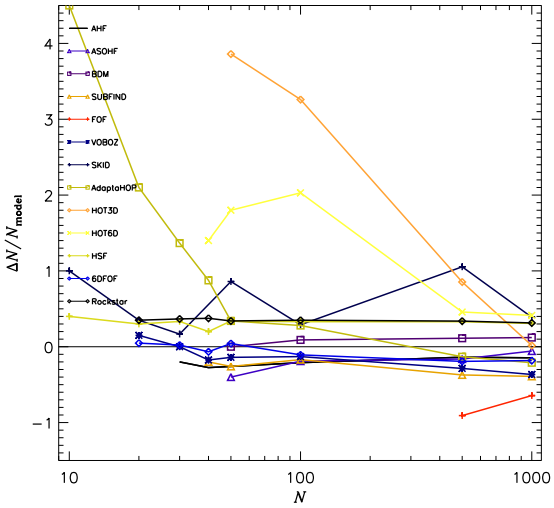

Figure A.13: Fractional difference between number of particles within the recovered R_{200} and number of particles belonging to the halo as returned by the respective halo finder vs. the number of particles inside the subhalo.

see that the vast majority of the halo finders did not assign any host particles to the subhalo. However, some halo finders appear to have picked up a fraction of host particles possibly leading to differences in the subhalo properties such as $v_{\rm max}$ investigated next. Note that the high contamination for `AdaptaHOP` is due to the lack of an unbinding procedure.

Maximum of Rotation Curve As the number of particles is merely a measure for the cross-performance of halo finders and not (directly) related to credible subhalo properties we also need to have a look at $v_{\rm max}$ again. The fractional error as a function of the (theoretical) number of subhalo particles is plotted in Fig. A.15. We note that aside from those halo finders who showed a contamination by host particles all codes recover the theoretical maximum of the rotation curve down to the limit of their subhalo's visibility (although possibly the last data point for the lowest number of particles should be discarded in that regard).

A.4.1.5 The "Blind Test"

Aside from the mock haloes analysed before we also designed a particular test where none of the participants had foreknowledge of what it contained; only Stuart Muldrew, who generated all the mock haloes, knew the setup that is summarised in Table A.4 where the type "host" refers to the host halo and "sub" to a subhalo. We dubbed this individual test the "blind test". Please note that some of the subhalo's density profiles in this test followed a Hernquist model (Hernquist 1990, marked "Hern" in the Table) instead of the NFW profile. Further, two haloes were deliberately placed at the same location yet with diametrically opposed velocities.

As this test more or less marked the end of the workshop and was primarily considered a fun exercise, we did not include it in the actual data set presented in Section A.3.1. Please note that not all halo finders participated and that we did not give the players in the game a chance to tune their code parameters to the data set. Nevertheless we decided to simply show visual impressions of those who returned results in Fig. A.16. There we merely show the projections of the (fiducial) R_{200} and $R_{\rm vmax}$ radii in the $x-y$ plane as the z coordinate of all haloes is identical.

It is interesting to note that the phase-space halo finders were again capable of locating the two overlapping subhaloes even though this is not clearly visible in the projection (as their circles are obviously overlapping). Of the 3D finders `SKID` noticed that there was some-

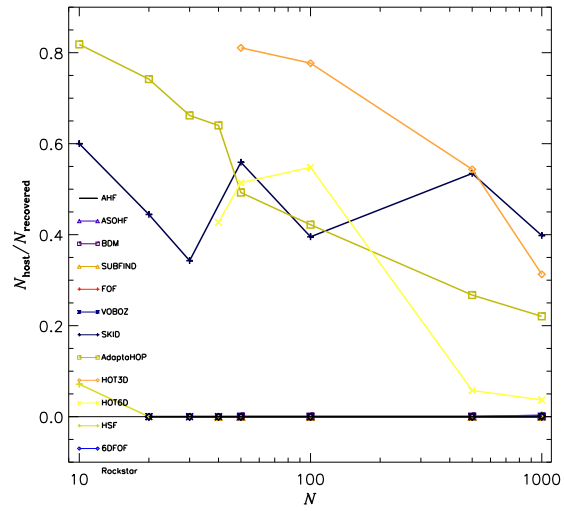

Figure A.14: Fraction of host's particles identified to be part of the subhalo as a function of particles inside the subhalo.

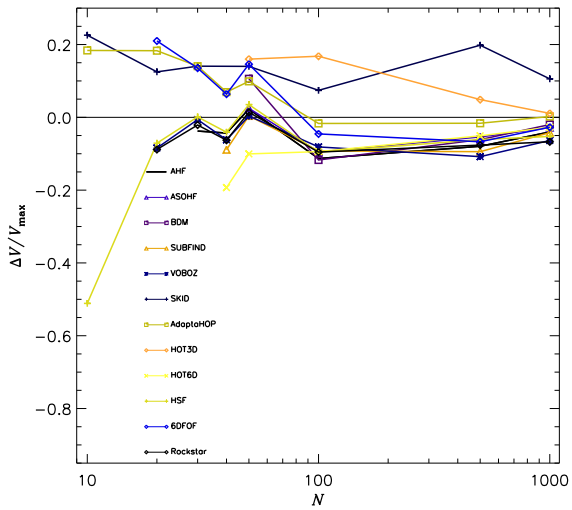

Figure A.15: Fractional difference between theoretical maximum of the rotation curve and the numerically derived maximum vs. the theoretical maximum for the subhalo.

Table A.4: Summary of the haloes in the blind test. Positions are given in h^{-1} Mpc and velocities in km/sec.

type	N_{100}	x	y	z	v_x	v_y	v_z	profile
host	10^6	50	50	50	0	0	0	NFW
sub	10^4	50.5	50	50	-10^3	0	0	NFW
sub	10^4	50.5	50	50	10^3	0	0	NFW
sub	10^4	49.5	50	50	10^3	0	0	Hern
sub	10^2	50	49.8	50	10^3	10^3	0	NFW
sub	10^2	50	50.2	50	0	-10^3	0	Hern

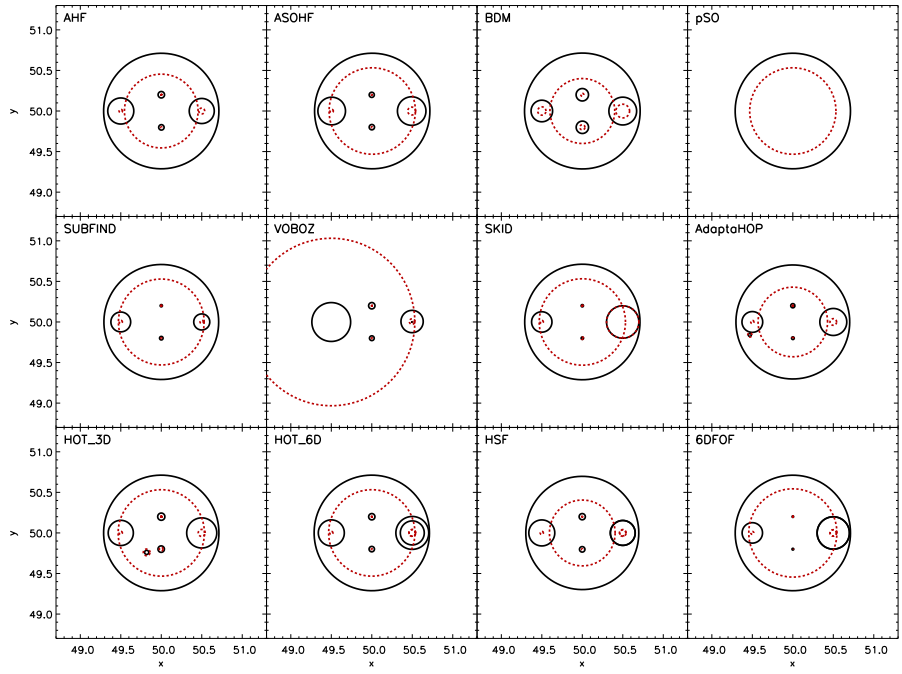

Figure A.16: Visual impression of the "blind test" (projection into $x-y$ plane). Each halo found is represented by a circle with a radius equal to the fiducial R_{200} value (solid black) and the $R_{\rm vmax}$ value (dashed red).

thing odd at that position, returning one object with double the mass (and $R_{\rm vmax}$ extending out to the outer radius). All other halo finders only found one of the two subhaloes. Also remember that `pSO` is not (yet) designed to find subhaloes and hence only the host has been returned. It is further remarkable that none of the halo finders had trouble finding the two small subhaloes while the host had not been found for some of the codes.

Again, we would like to stress that this test should not be taken too seriously. However, we nevertheless remark that analysing a cosmological simulation is also a sort of "blind" analysis as the answer is not previously known.

A.4.2 Cosmological Simulation

We now turn to the comparison of a real cosmological simulation including a substantial number of objects formed and embedded within the large-scale structure of the Universe.

However, even though the simulation contains a large number of particles (i.e. up to 1024^3 in the highest resolved data set) the given volume of side length $500h^{-1}$ Mpc does not allow for a study of subhaloes in detail: for the fiducial 512^3 particle run the largest object in the simulation box merely contains of order 10 subhaloes with the number of substructure objects dramatically decreasing when moving to (potentially) lower mass host haloes. We therefore stress that this particular comparison only focuses on field haloes and hence is well suited even for those codes that (presently) cannot cope with subhaloes.

Further, as mentioned already in Section A.3.2 we have the data available at various resolutions ranging from 256^3 to 1024^3 particles. We decided to use the highest resolution analysis performed by each finder as has already been summarised in Table A.3 in the subsequent comparison plots. The analysis in this particular Section primarily revolves around the (statistical) recovery of halo properties. In that regard we are nevertheless limiting our analysis to properties akin to the ones already studied in Section A.4.1, namely the mass M, the position $\vec{R}$, the peak of the rotation curve $v_{\rm max}$, and the (bulk) velocity $V_{\rm bulk}$. We are going to utilise masses as defined via $200 \times \rho_{\rm crit}$, i.e. M_{200}.

We like to re-iterate at this point again that for this particular comparison each halo finder returned halo properties as derived from applying the code to the actual data set; we aim at comparing the results of the codes for each and every single one being applied to the data individually. We consider this the most realistic comparison as this directly gauges the differences of the resulting halo catalogues.

We have already seen that all halo finders are capable of recovering the mass of mock haloes, irrespective of whether the density profile is cored or has a cusp (cf. Fig. A.5). We therefore do not expect to find surprising differences in the first and most obvious comparison, i.e. the (cumulative) mass function presented in Fig. A.17. Please note that `pFOF` discarded objects below 100 particles and hence did not return haloes below $\approx 8 \times 10^{12} h^{-1}{\rm M}_{\odot}$; similarly, `pSO` discarded objects with fewer than 50 particles, according to the criterion laid out in equation (30) of Lukić et al. (2007). And in each case the (cumulative) mass function starts to flatten at approximately the resolution limit of the simulation analysed by the respective code.

However, `ORIGAMI` seems to miss some low-mass structures caught by other halo-finders. One possible reason is that some smaller density enhancements seen by other finders have not undergone shell-crossing along three axes, and therefore do not meet `ORIGAMI`'s definition of a halo. Another is that `ORIGAMI` may be missing many subhaloes, which it does not attempt to separate from parent haloes.

Further, the `LANL` halo finder is designed to be an FOF finder and, if needed, SO objects are defined on top of such friends-of-friends haloes. Thus, for smaller haloes completeness is an issue as not every SO halo will have an FOF counterpart. Of course, it is possible to run the code in the limit $b \to 0$ and $N_{min} = 1$, having each particle serving as a potential centre of an SO halo, but the increase in computational cost would make this impractical, as direct SO halo finders which do precisely this in a more effective manner already exist. Nevertheless, we can see that computationally very fast method of growing SO spheres on top of FOF proxy haloes result in excellent match when compared to direct SO finders for well sampled haloes ($\sim$500 particles per halo).

In order to better view (possible) differences in the mass functions we further calculated the "mean mass function" in 10 logarithmically placed bins across the range 2×10^{11} – $1 \times 10^{15} h^{-1}{\rm M}_{\odot}$ alongside 1σ error bars for the means. Note that all codes only contributed to those bins where their data set is considered complete. We further deliberately stopped the binning at $1 \times 10^{15} h^{-1}{\rm M}_{\odot}$ to not be dominated by small number statistics for the few largest objects. The results can also be viewed in Fig. A.17 too, where we also show in the bottom panel the fractional difference between the mean and the code mass functions across

the respective mass range. And we additionally added as thin solid black line to the actual mass function plot in the upper panel of Fig. A.17 the numerically determined mass function of Warren et al. (2006) which is based upon a suite of sixteen 1024^3 simulations of the ΛCDM universe as well as the one derived by Tinker et al. (2008) derived from a substantial set of cosmological simulations actually including the ones used by Warren et al. (2006) (cf. their Fig.1). Note that the former is based upon FOF and the latter on SO masses.

As highlighted in the Introduction A.1.3 the peak value of the rotation curve may be a more suitable quantity to use when it comes to comparing the masses of (dark matter) haloes. We therefore show in the Fig. A.18 the cumulative distribution of $v_{\rm max}$. Apart from the expected flattening at low $v_{\rm max}$ due to resolution we now note that this is in fact the case: codes that did not estimate masses according to the standard definition $M(< R) = 4\pi/3\ R^3\ \Delta\rho$ nevertheless recovered the correct $v_{\rm max}$ values. Given the ability of comparing $v_{\rm max}$ to observational data (cf. Section A.1.3) we conclude that $v_{\rm max}$ is a more meaningful quantity which can serve as a proxy for mass. Please note again the flattening of some curves at the low-$v_{\rm max}$ end due to either the resolution of the simulation analysed or an imposed minimum number of particles cut and that not all FOF-based finders returned a $v_{\rm max}$ value.

We have seen in Section A.4.1 that there exists some scatter between halo finders in the recovery of the halo position. It therefore appears mandatory to check for differences in halo positions recovered from the cosmological simulation, too. To this extent we calculated the 2-point correlation function and present the results in Fig. A.19. In order to analyse a comparable data set (remember that some codes analysed the 1024^3, some the 512^3, and some the 256^3 particle simulation) we restricted the haloes to the 10000 most massive objects and found excellent agreement.[12] The smallest scale considered in this comparison is $2h^{-1}$ Mpc in order not to probe the interiors of galaxy clusters. The minute drop of the correlation function for `pFOF` at the smallest scale probed may be explained by the usage of the marginally larger linking length of $b = 0.2$ applied during their analysis and the fact that `pFOF` uses the centre of mass instead of the density peak as the centre of the halo.

Finally we cross-compare the bulk velocities of haloes in Fig. A.20 where we find excellent agreement. We further give in the legend the medians of the distribution for each halo finder: the mean (of the medians) is 489 km/sec with a $1-\sigma$ of 9 km/sec (i.e. 2% deviation).

[12] Please note that it makes little difference to use the 10000 objects with the largest $v_{\rm max}$ value as there is a strong correlation between M and $v_{\rm max}$ for each code. In the end we are interested in limiting the analyses to the N most massive objects and hence a "mis-calculation" of the mass is irrelevant as long as differences in mass are systematic as in our case.

A.5 Summary & Conclusions

We have performed an exhaustive comparison of 18 halo finders for cosmological simulations. These codes were subjected to various suites of test scenarios all aimed at addressing issues related to the subject of identifying gravitationally bound objects in such simulations.

The tests consisted of idealized mock haloes set up according to a specific matter density profile (i.e. NFW and Plummer) where we studied isolated haloes as well as (sub-)subhaloes. We further utilized a cosmological simulation of the large-scale structure of the universe primarily containing field haloes. The requirement for the mock haloes was to simply return the centres of the identified objects alongside a list of particles (possibly) belonging to that halo. We then applied a universal tool to calculate all other quantities (e.g. bulk velocity, rotation curve, (virial) mass, etc.). For the cosmological data the code representatives were simply asked to return their "best" values for a suite of canonical values.

Mock Haloes We found that the deviation of the recovered position to the actual centre of the object is largest for FOF-based methods which is naturally explained by the fact that they define centres as centre-of-mass whereas most other codes identify a peak in the density field. Further, dark matter haloes that have an intrinsic core (e.g. a Plummer sphere) yield larger differences between the input centre and the recovered centre for most codes. Such density profiles are not expected within the Universe we inhabit. However, the bulk velocities, (virial) masses, and $v_{\rm max}$ values satisfactorily agreed with the analytical input irrespective of the underlying density profile – at least for host and subhaloes; sub-subhaloes still showed at times departures as large as 50% in mass and 20% for $v_{\rm max}$. Please note that all results are based upon the same post-processing software and only the list of particles (and the centre) were determined by each halo finder individually. Hence, variations in the centre will automatically lead to differences as both mass and

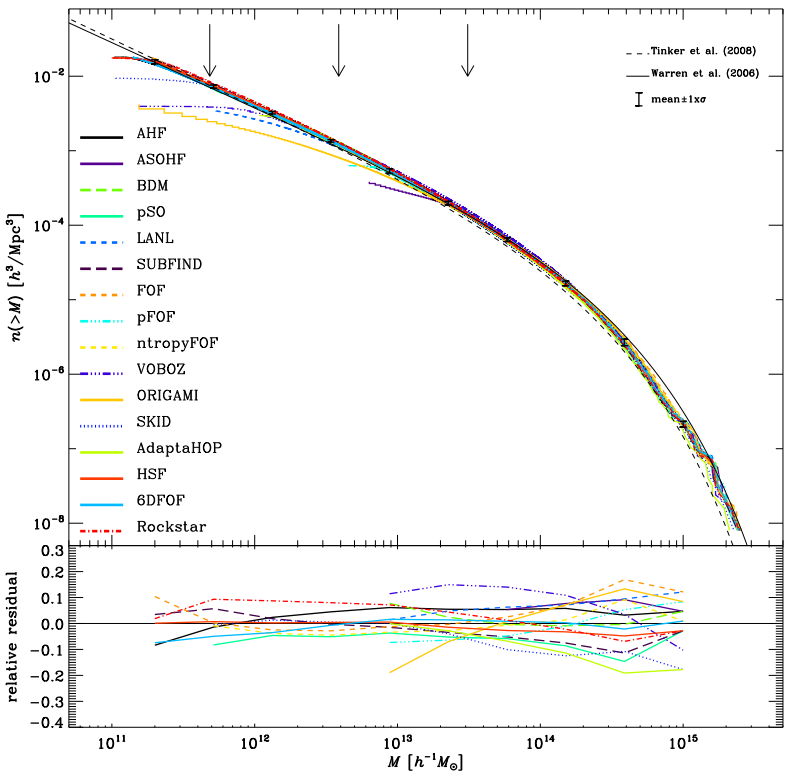

Figure A.17: Upper panel: the cumulative mass (M_{200}) function. The arrows indicate the 50 particle limit for the 1024^3 (left), 512^3 (middle), and 256^3 (right) simulation data. The thin black lines crossing the whole plot corresponds to the mass function as determined by Warren et al. (2006, (solid)) and Tinker et al. (2008, (dashed)). The error bars represent the mean mass function of the codes ($\pm 1\sigma$). Lower panel: the fractional difference of the mean and code halo mass functions. For more details please refer to the text.

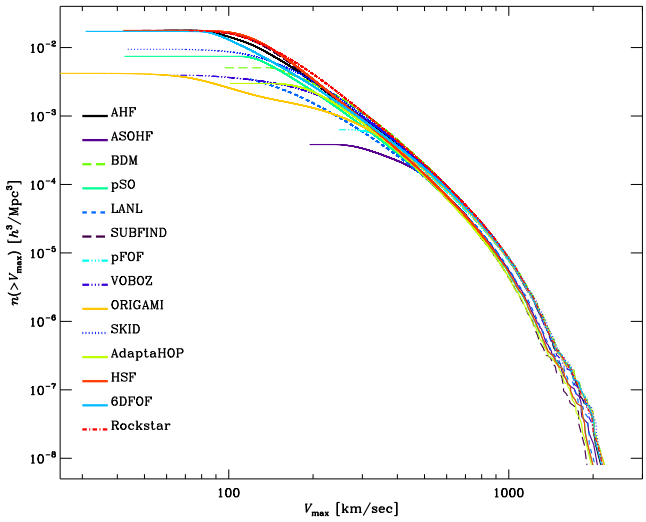

Figure A.18: The cumulative $v_{\max}$ function.

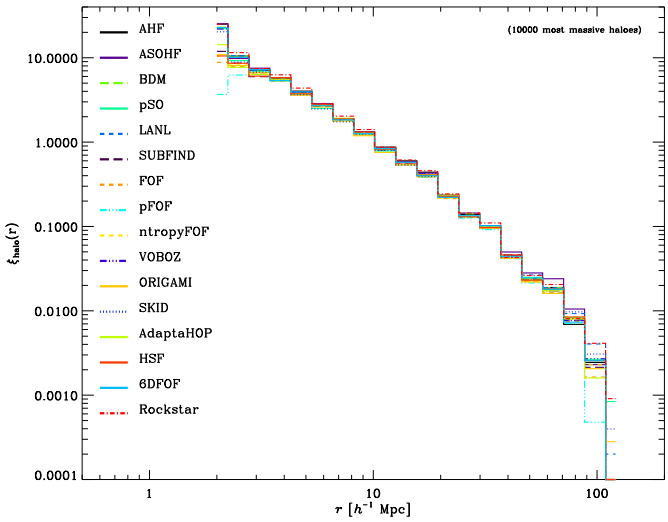

Figure A.19: The 2-point correlation function for the 10000 most massive objects.

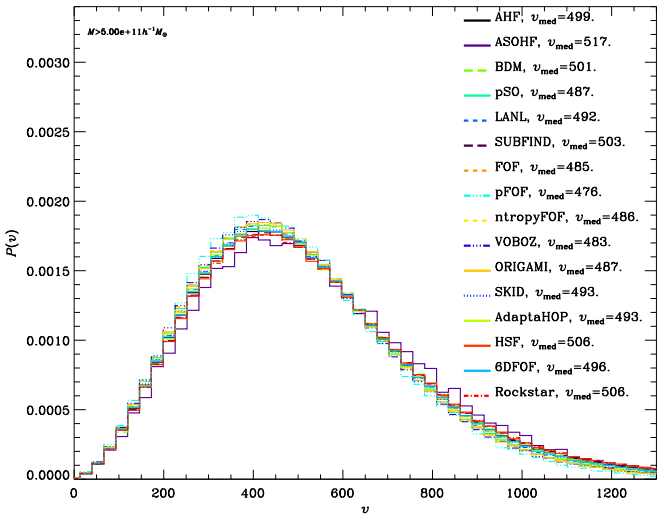

Figure A.20: The distribution of bulk velocities for objects more massive than $5 \times 10^{11} h^{-1} \mathrm{M}_{\odot}$.

rotation curve are spherically averaged quantities.

We further investigated the dependence of subhalo properties upon the position within the host, in particular its distance to the centre. There we found that – while all codes participating in this exercise recovered excellent $v_{\rm max}$ values for a NFW subhalo sampled with 10000 particles inside a NFW host two orders of magnitude more massive[13] – phase-space finders excelled by also locating the subhalo when it overlapped with the centre of the host. However, in this case they struggle to properly calculate its properties.

Putting a subhalo at varying positions inside a host is closely related to a subhalo actually falling into a host. However, the latter also introduces distortions in the shape of the subhalo due to tidal forces while it is plunging through the background potential of the host. We performed a simulation of the scenario where a subhalo initially containing 10000 particles shoots right through the centre of a host two orders of magnitude more massive. While we found that the number of particles significantly drops when the subhalo approaches the host's centre, it rises again to a plateau level after the central passage – and this is apparent in all codes. The peak of the rotation curve, which should be less susceptible to (tidally induced) variations in the outer subhalo regions, shows less variation. However, $v_{\rm max}$ actually rises shortly after the subhalo leaves the very central region indicative of two (related) effects: contamination with host particles and problems with the unbinding procedure. Nevertheless, these problems are (still) common to all halo finders used in this particular study and they all mutually agree upon the initial and final value.

Another question addressed during our tests with the mock haloes was the number of particles required in a subhalo in order to still be able to separate it from the host background. To this extent we successively lowered the number of particles used to sample a subhalo that had been placed at half the M_{100} radius of the host. We found that the majority of finders participating in this exercise are capable of identifying the subhalo down to 30-40 particles. Yet again, (most of) the phase-space finders even locate the object with as few as 10-20 particles. Some of the configuration space finders also tracked down the subhalo to such low numbers of particles, however, they did not obtain the correct particle lists leading to subhalo properties that differ from the analytical input values.

[13] Note that only halo finders capable of identifying substructure can participate in a comparison of (sub-)subhalo properties.

We would like to close this part of the summary with the notion that while there is a straight-forward relation between (virial) mass and the peak of the rotation curve for isolated field haloes (once the density profile is known), the mass of a subhalo is more ambiguously defined. As we have seen, it is (in most situations) more meaningful to utilize the peak of the rotation curve as a proxy for mass (cf. Fig. A.8 vs. Fig. A.9 as well as Fig. A.10 vs. Fig. A.11). However, as could also be witnessed in Fig. A.11, quite a number of halo finding techniques gave rise to an artificial increase of $v_{\rm max}$ right after the passage through the centre of its host obscuring its applicability as a mass representative.

Cosmological Simulation As a matter of fact there is little to say regarding the comparison of the cosmological data set; as can be seen in Figs. A.17 through A.20 the agreement is well within the (omitted) error bars for the basic properties investigated here (i.e. mass, velocity, position, and $v_{\rm max}$). And unless we can be certain which halo finding technique is the ultimate (if such exists at all), the observed scatter indicates the accuracy to which we can determine these properties in cosmological simulations. We would though like to caution that the haloes found within the cosmological simulation are primarily well defined and isolated objects and hence it is no surprise that we find such an agreement. Subhaloes, however, are not well defined and therefore lead to larger differences between halo finders as seen during the comparison of the mock haloes. For those codes that diverge from the general agreement the differences are readily explained and have been discussed in Section A.4.2.

Concluding Remarks The agreement amongst the different codes is rather remarkable and reassuring. While they are based upon different techniques and – even for those based upon same techniques – different technical parameters they appear to recover comparable properties for dark matter haloes as found in state-of-the-art simulations of cosmic structure formation. We nevertheless need to acknowledge that some codes require improvement. For instance, phase-space finders find halo centres even if the centre overlaps with another (distinct) object and recover subhaloes to smaller particle number, however they still have problems with the (separated) issue of assigning the correct particles in these cases and hence deriving halo properties afterwards.

We close with the remark that we deliberately did not dwell on the actual technical parameters of each and every halo finder as this is beyond the scope of this paper and we refer the reader to the respective code papers for this. However, it is important to note that with an appropriate choice of these parameters the results can be brought into agreement. This is an important message from this particular study. We are not claiming that all halo finders need to return identical results, but they can (possibly) be tuned that way. In that regards we also like to remind the reader again that this particular comparison is aimed at comparing codes as opposed to algorithms: we even tried to gauge the differences found when applying codes based upon the same algorithm to identical data sets.

REFERENCES

Agertz O., Moore B., Stadel J., Potter D., Miniati F. F., Read J., Mayer L., Gawryszczak A., Kravtsov A., Nordlund Å., Pearce F., Quilis V., Rudd D., Springel V., Stone J., Tasker E., Teyssier R.,Wadsley J., Walder R., 2007, MNRAS, 380, 963

Ascasibar Y., 2010, in prep.

Ascasibar Y., Binney J., 2005, MNRAS, 356, 872

Ascasibar Y., Gottlöber S., 2008, MNRAS, 386, 2022

Aubert D., Pichon C., Colombi S., 2004, MNRAS, 352, 376

Bagla J. S., Khandai N., 2009, MNRAS, 396, 2211

Behroozi P., 2010, in prep.

Bertschinger E., Gelb J. M., 1991, Computers in Physics, 5, 164

Binney J., Tremaine S., 1987, Galactic dynamics. Princeton, NJ, Princeton University Press, 1987, 747 p.

Bode P., Ostriker J. P., Xu G., 2000, ApJS, 128, 561

Bullock J. S., Kolatt T. S., Sigad Y., Somerville R. S., Kravtsov A. V., Klypin A. A., Primack J. R., Dekel A., 2001, MNRAS, 321, 559

Cohn J. D., White M., 2008, MNRAS, 385, 2025

Couchman H. M. P., Thomas P. A., Pearce F. R., 1995, ApJ, 452, 797

Courtin J., Rasera Y., Alimi J., Corasaniti P., Boucher V., Fuzfa A., 2010, MNRAS, pp 1745

Davis M., Efstathiou G., Frenk C. S., White S. D. M., 1985, ApJ, 292, 371

Dekel A., Devor J., Hetzroni G., 2003, MNRAS, 341, 326

Diemand J., Kuhlen M., Madau P., 2006, ApJ,

649, 1
Doumler T., Knebe A., 2010, MNRAS, 403, 453
Dubinski J., Kim J., Park C., Humble R., 2004, New Astronomy, 9, 111
Eisenstein D. J., Hut P., 1998, ApJ, 498, 137
Falck B., Neyrinck M. C., Aragon-Calvo M., Szalay A., 2010, in prep.
Frenk et al. C. S., 1999, ApJ, 525, 554
Fryxell B., Olson K., Ricker P., Timmes F. X., Zingale M., Lamb D. Q., MacNeice P., Rosner R., Truran J. W., Tufo H., 2000, ApJS, 131, 273
Gardner J. P., Connolly A., McBride C., 2007a, in Proceedings of TeraGrid 07:Broadening Participation in the TeraGrid Enabling knowledge discovery in a virtual universe. ACM Press
Gardner J. P., Connolly A., McBride C., 2007b, in Proceedings of the 2007 Symposium on Challenges of Large Applications in Distributed Environments (CLADE 2007) Enabling rapid development of parallel tree search applications. ACM Press
Gelb J. M., 1992, PhD thesis, MASSACHUSETTS INSTITUTE OF TECHNOLOGY.
Gelb J. M., Bertschinger E., 1994, ApJ, 436, 467
Gill S. P. D., Knebe A., Gibson B. K., 2004, MNRAS, 351, 399
Gnedin N. Y., 1995, ApJS, 97, 231
Gottlöber S., Klypin A. A., Kravtsov A. V., 1999, in G. Giuricin, M. Mezzetti, & P. Salucci ed., Observational Cosmology: The Development of Galaxy Systems Vol. 176 of Astronomical Society of the Pacific Conference Series, Halo evolution in a cosmological environment. pp 418+
Gottlöber S., Yepes G., 2007, ApJ, 664, 117
Governato F., Moore B., Cen R., Stadel J., Lake G., Quinn T., 1997, NewA, 2, 91
Habib S., Pope A., Lukić Z., Daniel D., Fasel P., Desai N., Heitmann K., Hsu C., Ankeny L., Mark G., Bhattacharya S., Ahrens J., 2009, Journal of Physics Conference Series, 180, 012019
Hayashi E., Navarro J. F., Taylor J. E., Stadel J., Quinn T., 2003, ApJ, 584, 541
Heitmann K., Lukić Z., Fasel P., Habib S., Warren M. S., White M., Ahrens J., Ankeny L., Armstrong R., O'Shea B., Ricker P. M., Springel V., Stadel J., Trac H., 2008, Computational Science and Discovery, 1, 015003
Hernquist L., 1990, ApJ, 356, 359
Hernquist L., 1993, ApJS, 86, 389
Jenkins A., Frenk C. S., White S. D. M., Colberg J. M., Cole S., Evrard A. E., Couchman H. M. P., Yoshida N., 2001, MNRAS, 321, 372
Kazantzidis S., Magorrian J., Moore B., 2004, ApJ, 601, 37
Kim J., Park C., 2006, ApJ, 639, 600
Klimentowski J., Łokas E. L., Kazantzidis S., Mayer L., Mamon G. A., 2009, MNRAS, 397, 2015
Klypin A., Gottlöber S., Kravtsov A. V., Khokhlov A. M., 1999, ApJ, 516, 530
Klypin A., Holtzman J., 1997, ArXiv Astrophysics e-prints
Klypin A., Trujillo-Gomez S., Primack J., 2010, ArXiv e-prints
Knebe A., Green A., Binney J., 2001, MNRAS, 325, 845
Knebe A., Kravtsov A. V., Gottlöber S., Klypin A. A., 2000, MNRAS, 317, 630
Knollmann S. R., Knebe A., 2009, ApJS, 182, 608
Kravtsov A. V., Klypin A. A., Khokhlov A. M., 1997, ApJS, 111, 73
Kruskal Joseph B. J., 1956, Proceedings of the American Mathematical Society, 7, 48
Lacey C., Cole S., 1994, MNRAS, 271, 676
Łokas E. L., Mamon G. A., 2001, MNRAS, 321, 155
Lukić Z., Heitmann K., Habib S., Bashinsky S., Ricker P. M., 2007, ApJ, 671, 1160
Lukić Z., Reed D., Habib S., Heitmann K., 2009, ApJ, 692, 217
Lux H., Read J. I., Lake G., 2010, MNRAS, 406, 2312
Maciejewski M., Colombi S., Alard C., Bouchet F., Pichon C., 2009, MNRAS, 393, 703
Maciejewski M., Colombi S., Springel V., Alard C., Bouchet F. R., 2009, MNRAS, 396, 1329
Merz H., Pen U., Trac H., 2005, NA, 10, 393
Muldrew S. I., Pearce F. R., Power C., 2011, MNRAS, 410, 2617
Navarro J. F., Frenk C. S., White S. D. M., 1995, MNRAS, 275, 720
Navarro J. F., Frenk C. S.,White S. D. M., 1996, ApJ, 462, 563
Navarro J. F., Frenk C. S.,White S. D. M., 1997, ApJ, 490, 493
Navarro J. F., Ludlow A., Springel V., Wang J., Vogelsberger M., White S. D. M., Jenkins A., Frenk C. S., Helmi A., 2010, MNRAS, 402, 21
Neyrinck M. C., Gnedin N. Y., Hamilton A. J. S., 2005, MNRAS, 356, 1222
O'Shea B. W., Bryan G., Bordner J., Norman M. L., Abel T., Harkness R., Kritsuk A., 2004, ArXiv Astrophysics e-prints
O'Shea B. W., Nagamine K., Springel V., Hernquist L., Norman M. L., 2005, ApJS, 160, 1
Pen U., 1995, ApJS, 100, 269
Pfitzner D. W., Salmon J. K., eds, 1996,

Parallel halo finding in N-body cosmology simulations.
Planelles S., Quilis V., 2010, A&A, 519, A94+
Plummer H. C., 1911, MNRAS, 71, 460
Press W. H., Schechter P., 1974, ApJ, 187, 425
Quilis V., 2004, MNRAS, 352, 1426
Rasera Y., Alimi J., Courtin J., Roy F., Corasaniti P., Fuzfa A., Boucher V., 2010, in J.-M. Alimi & A. Fuozfa ed., American Institute of Physics Conference Series Vol. 1241 of American Institute of Physics Conference Series, Introducing the Dark Energy Universe Simulation Series (DEUSS). pp 11341139
Read J. I., Lake G., Agertz O., Debattista V. P., 2008, MNRAS, 389, 1041
Read J. I.,WilkinsonM. I., Evans N.W., Gilmore G., Kleyna J. T., 2006, MNRAS, 367, 387
Robertson B. E., Kravtsov A. V., Tinker J., Zentner A. R., 2009, ApJ, 696, 636
Schaap W. E., van de Weygaert R., 2000, A&A, 363, L29
Sharma S., Steinmetz M., 2006, MNRAS, 373, 1293
Shaw L. D., Weller J., Ostriker J. P., Bode P., 2007, ApJ, 659, 1082
Sheth R. K., Tormen G., 1999, MNRAS, 308, 119
Shiloach Y., Vishkin U., 1982, Journal of Algorithms, 3, 57
Skory S., Turk M. J., Norman M. L., Coil A. L., 2010, ArXiv eprints
Springel V., 2005, MNRAS, 364, 1105
Springel V., 2010, MNRAS, 401, 791
Springel V., White S. D. M., Tormen G., Kauffmann G., 2001, MNRAS, 328, 726
Springel V., Yoshida N., White S. D. M., 2001, New Astronomy, 6, 79
Stadel J., Potter D., Moore B., Diemand J., Madau P., Zemp M., Kuhlen M., Quilis V., 2009, MNRAS, 398, L21
Stadel J. G., 2001, PhD thesis, UNIVERSITY OF WASHINGTON
Sutter P. M., Ricker P. M., 2010, ApJ, 723, 1308
Tasker E. J., Brunino R., Mitchell N. L., Michielsen D., Hopton S., Pearce F. R., Bryan G. L., Theuns T., 2008, MNRAS, 390, 1267
Teyssier R., 2002, A&A, 385, 337
Tinker J., Kravtsov A. V., Klypin A., Abazajian K., Warren M.,Yepes G., Gottlober S., Holz D. E., 2008, ApJ, 688, 709
Tweed D., Devriendt J., Blaizot J., Colombi S., Slyz A., 2009, A&A, 506, 647
van Kampen E., 1995, MNRAS, 273, 295
Warren M. S., Abazajian K., Holz D. E., Teodoro L., 2006, ApJ, 646, 881
Weller J., Ostriker J. P., Bode P., Shaw L., 2005, MNRAS, 364, 823
White M., 2001, A&A, 367, 27
White M., 2002, ApJSS, 143, 241
Zemp M., Moore B., Stadel J., Carollo C. M., Madau P., 2008, MNRAS, 386, 1543

Bibliography

Aarseth, S.J., 1963. MNRAS, 126

Aarseth, S.J., 2001. New Astronomy, 6:277

Abell, G.O., 1958. ApJS, 3:211

Abell, G.O., Corwin, H.G.J., & Olowin, R.P., 1989. ApJS, 70:1

Agertz, O., Moore, B., Stadel, J., Potter, D., Miniati, F., Read, J., Mayer, L., Gawryszczak, A., Kravtsov, A., Nordlund, A., Pearce, F., Quilis, V., Springel, D.R.V., Stone, J., Tasker, E., Teyssier, R., Wadsley, J., & Walder, R., 2007. MNRAS, 380:963

Allgood, B., Flores, R.A., Primack, J.R., Kravtsov, A.V., Wechsler, R.H., Faltenbacher, A., & Bullock, J.S., 2006. MNRAS, 367

Arnaud, M. & Evrard, A.E., 1999. MNRAS, 305:631

Bagla, J.S., 2002. Journal of Astrophysics and Astronomy, 23:185

Bahcall, N.A., McKay, T.A., Annis, J., Kim, R.S.J., Dong, F., Hansen, S., Goto, T., Gunn, J.E., Miller, C., Nichol, R.C., Postman, M., & Schneider, D., 2003. ApJS, 148:243

Bailin, J. & Steinmetz, M., 2005. ApJ, 627:647

Balogh, M.L., Pearce, F.R., Bower, R.G., & Kay, S.T., 2001. MNRAS, 326:1228

Barnes, J. & Hut, P., 1986. Nature, 324:446

Bartelmann, M. & Schneider, P., 2001. Physics Reports, 340:291

Bauer, F.E., Fabian, A.C., Sanders, J.S., Allen, S.W., & Johnstone, R.M., 2005. MNRAS, 359:1481

Berger, M.J. & Colella, P., 1989. J. Comp. Phys., 82:64

Berger, M.J. & Oliger, J., 1984. J. Comp. Phys., 53:484

Bertschinger, E., 1998. ARA&A, 36:599

Bertschinger, E. & Gelb, J.M., 1991. Computer in Physics, 5:164

Bialek, J.J., Evrard, A.E., & Mohr, J.J., 2001. ApJ, 555:597

Biviano, A., 2000. *Constructing the Universe with Clusters of Galaxies*. IAP 2000 meeting, Paris. Eds. F. Durret and D. Gerbal

Blandford, R. & Eichler, D., 1987. Physics Reports, 154:1

Blumenthal, G.R., Faber, S.M., Primack, J.R., & Rees, M.J., 1984. Nature, 311:517

Bode, P. & Ostriker, J.P., 2003. ApJS, 145:1

Borgani, S., Fabjan, D., Tornatore, L., Schindler, S., Dolag, K., & Diaferio, A., 2008. SSRv, 134:379

Borgani, S., Governato, F., Wadsley, J., Menci, N., Tozzi, P., Quinn, T., Stadel, J., & Lake, G., 2002. MNRAS, 336:409

Borgani, S. & Kravtsov, A., 2009. ArXiv0906.4370

Borgani, S., Murante, G., Springel, V., Diaferio, A., Dolag, K., Moscardini, L., Tormen, G., Tornatore, L., & Tozzi, P., 2004. MNRAS, 348:1078B

Borgani, S. & Viel, M., 2009. MNRAS, 392:L26

Bouchet, F.R. & Hernquist, L., 1988. ApJS, 68:521

Bradt, H., Mayer, W., Naranan, S., Rappaport, S., & Spada, G., 1967. ApJL, 150:L199+

Branchesi, M., Gioia, I.M., Fanti, C., & Fanti, R., 2007. A&A, 472:739

Bryan, G.L., 2000. ApJL, 544:L1

Bryan, G.L. & Norman, M.L., 1997. ASP Conf. Ser. 123: Computational Astrophysics; 12th Kingston Meeting on Theoretical Astrophysics, page 363

Bryan, G.L. & Norman, M.L., 1998. ApJ, 495:80

Bryan, G.L., Norman, M.L., Stone, J.M., Cen, R., & Ostriker, J.P., 1995. Computer Physics Communication, 89:149

Burns, J.O., 1990. AJ, 99:14

Burns, J.O., Hallman, E.J., Gantner, B., Motl, P.M., & Norman, M.L., 2008. ApJ, 675:1125

Byram, E.T., Chubb, T.A., & Friedman, H., 1966. Science, 152:66

Carlstrom, J.E., Holder, G.P., & Reese, E.D., 2002. ARA&A, 40:643

Cavaliere, A.G., Gursky, H., & Tucker, W.H., 1971. Nature, 231:437

Cen, R., 1992. ApJS, 78:341

Cen, R. & Ostriker, J., 1992. ApJ, 393:22

Cen, R. & Ostriker, J., 1999. ApJ, 514:1

Chen, Y., Reiprich, T.H., Böhringer, H., Ikebe, Y., & Zhang, Y.Y., 2007. A&A, 466:805

Churazov, E., Brüggen, M., Kaiser, C.R., Böhringer, H., & Forman, W., 2001. ApJ, 554:261

Cole, S. & Lacey, C., 1996. MNRAS, 281:716

Cole, S., Percival, W.J., Peacock, J.A., Norberg, P., Baugh, C.M., Frenk, C.S., Baldry, I., Bland-Hawthorn, J., Bridges, T., Cannon, R., Colless, M., Collins, C., Couch, W., Cross, N.J.G., Dalton, G., Eke, V.R., Propris, R.D., Driver, S.P., Efstathiou, G., Ellis, R.S., Glazebrook, K., Jackson, C., Jenkins, A., Lahav, O., Lewis, I., Lumsden, S., Maddox, S., Madgwick, D., Peterson, B.A., Sutherland, W., & Taylor, K., 2005. MNRAS, 362:505

Colella, P. & Woodward, P.R., 1984. J. Comp. Phys., 54:174

Colless, M., Dalton, G., Maddox, S., Sutherland, W., Norberg, P., Cole, S., Bland-Hawthorn, J., Bridges, T., Cannon, R., Collins, C., Couch, W., Cross, N., Deeley, K., Propris, E.D., Driver, S.P., Efstathiou, G., Ellis, R.S., Frenk, C.S., Glazebrook, K., Jackson, C., Lahav, O., Lewis, I., Lumsden, S., Madgwick, D., Peacock, J.A., Peterson, B.A., Price, I., Seaborne, M., & Taylor, K., 2001. MNRAS, 328:1039

Couchman, H.M.P., 1991. ApJL, 368:L23

Crain, R., Theuns, T., Vecchia, C.D., Eke, V.R., Frenk, C.S., Jenkins, A., Kay, S.T., Peacock, J.A., Pearce, F.R., Schaye, J., Springel, V., Thomas, P.A., White, S.D.M., & Wiersma, R.P.C., 2009. MNRAS, 399:1773

Crocce, M., Pueblas, S., & Scoccimarro, R., 2006. MNRAS, 373:369

Croston, J.H., Pratt, G.W., Böhringer, H., Arnaud, M., Pointecouteau, E., Ponman, T.J., Sanderson, A.J.R., Temple, R.F., Bower, G.R., & Donahue, M., 2008. A&A, 487:431

Dalton, G.B., Maddox, S.J., Sutherland, W.J., & Efstathiou, G., 1997. MNRAS, 289:263

Davé, R., Hernquist, L., Katz, N., & Weinberg, D.H., 1999. ApJ, 511:521

Davé, R., Katz, N., & Weinberg, D.H., 2002. ApJ, 579:23

Davis, M., Efstathiou, G., Frenk, C.S., & White, S.D.M., 1985. ApJ, 292:381

de Grandi, S., Ettori, S., Longhetti, M., & Molendi, S., 2004. A&A, 419:7

de Grandi, S. & Molendi, S., 2002. ApJ, 567:163

de Lapparent, V., Geller, M.J., & Huchra, J.P., 1986. ApJL, 302:L1

de Lucia, G., Kauffmann, G., Springel, V., White, S.D.M., Lanzoni, B., Stoehr, F., Tormen, G., & Yoshida, N., 2004. MNRAS, 348:333

Diemand, J., Kuhlen, M., & Madau, P., 2006. ApJ, 649:1

Diemand, J., Kuhlen, M., & Madau, P., 2007. ApJ, 657:262

Dolag, K., Bartelmann, M., & Lesch, H., 1999. A&A, 348:351

Dolag, K., Bykov, A.M., & Diaferio, A., 2008. SSRv, 134:311

Donahue, M., Horner, D.J., , Cavagnolo, K.W., & Voit, G.M., 2006. ApJ, 643:730

Drury, L.O. & Falle, S.A.E.G., 1986. MNRAS, 223:353

Dunkley, J., Komatsu, E., Nolta, M.R., Spergel, D.N., Larson, D., Page, G.H.L., Bennett, C.L., Gold, B., Jarosik, N., Weiland, J.L., Halpern, M., Hill, R., Kogut, A., Limon, M., Meyer, S.S., Tucker, G., Wollack, E., & Wright, E.L., 2009. ApJS, 180:306

Edge, A.C. & Freyer, D.T., 2003. ApJ, 594:13

Efstathiou, G., Davis, M., White, S.D.M., & Frenk, C.S., 1985. ApJS, 57:241

Eilek, J.A., 2003. Proceedings of "The Riddle of Cooling Flows in Galaxies and Clusters of Galaxies", astro-ph/0310011

Eisenstein, D.J. & Hu, W., 1998. ApJ, 511:5

Eke, V.R., Cole, S., & Frenk, C.S., 1996. MNRAS, 282:263

Elvis, M., 1976. MNRAS, 177:7P

Ensslin, T.A., Biermann, P.L., Klein, U., & Kohle, S., 1998. A&A, 332:395

Ettori, S., Borgani, S., Moscardini, L., Murante, G., Tozzi, P., Diaferio, A., Dolag, K., Springel, V., Tormen, G., & Tornatore, L., 2004a. MNRAS, 354:111

Ettori, S. & Brighenti, F., 2008. MNRAS, 387:631

Ettori, S., Tozzi, P., Borgani, S., & Rosati, P., 2004b. A&A, 417:13

Evrard, A.E., 1988. MNRAS, 235:911

Evrard, A.E., 1990. ApJ, 363:349

Evrard, A.E. & Henry, J.P., 1991. ApJ, 383:95

Fabian, A.C., Crawford, C.S., Edge, A.C., & Mushotzky, R.F., 1994. MNRAS, 267:779

Fabian, A.C., Nulsen, P.E.J., & Canizares, C.R., 1984. Nature, 310:733

Fabjan, D., Borgani, S., Tornatore, L., Saro, A., Murante, G., & Dolag, K., 2010. MNRAS, 401:1670

Franx, M., Illingworth, G., & de Zeeuw, T., 1991. ApJ, 383:112

Frenk, C.S., White, S.D.M., Bode, P., Bond, J.R., Bryan, G.L., Cen, R., Couchman, H.M.P., Evrard, A.E., Gnedin, N., Jenkins, A., Khokhlov, A.M., Klypin, A., Navarro, J.F., Norman, M.L., Ostriker, J.P., Owen, J.M., Pearce, F.R., Pen, U.L., Steinmetz, M., Thomas, P.A., Villumsen, J.V., Wadsley, J.W., Warren, M.S., Xu, G., & Yepes, G., 1999. ApJ, 525:554

Frenk, C.S., White, S.D.M., Davis, M., & Efstathiou, G., 1988. ApJ, 327:507

Fritz, G., Davidsen, A., Meekins, J.F., & Friedman, H., 1971. ApJL, 164:L81+

Fryxell, B., Olson, K., Ricker, P., Timmes, F.X., Zingale, M., Lamb, D.Q., MacNeice, P., Rosner, R., Truran, J.W., & Tufo, H., 2000. ApJS, 131:273

Fujita, Y. & Sarazin, C.L., 2001. ApJ, 563:660

Gabici, S. & Blasi, P., 2003. ApJ, 583:695

Gao, L., White, S.D.M., Jenkins, A., Stoehr, F., & Springel, V., 2004. MNRAS, 355:819

Gelb, J.M. & Bertschinger, E., 1994. ApJ, 436:467

Gheller, C., Pantano, O., & Moscardini, L., 1998. MNRAS, 295:519

Ghigna, S., Moore, B., Governato, F., G., L., Quinn, T., & Stadel, J., 2000. ApJ, 544:616

Giacintucci, S., Venturi, T., Macario, G., Dallacasa, D., Brunetti, G., Markevitch, M., Cassano, R., Bardelli, S., & Athreya, R., 2008. A&A, 486:347

Gill, S.P.D., Knebe, A., & Gibson, B.K., 2004. MNRAS, 351:399

Gingold, R.A. & Monaghan, J.J., 1977. MNRAS, 181:375

Giocoli, C., Tormen, G., Sheth, R.K., & van den Bosch, F.C., 2009. MNRAS, 404:502

Giocoli, C., Tormen, G., & van den Bosch, F.C., 2008. MNRAS, 386:2135

Gladders, M.D. & Yee, H.K.C., 2000. AJ, 120:2148

Gnedin, N.Y., 1995. ApJS, 97:231

Godunov, S.K., 1959. Matematicheskii Sbornik, 47:271

Gonzalez, A.H., Zaritsky, D., & Zabludoff, A., 2007. ApJ, 666:147

Götz, M., Huchra, J.P., & Branderberger, R.H., 1998. astroph9811393

Gunn, J.E., 1977. ApJ, 218:592

Gursky, H., Kellogg, E., Murray, S., Leong, C., Tananbaum, H., & Giacconi, R., 1971. ApJL, 167:L81

Haardt, F. & Madau, P., 1996. ApJ, 461:20

Hamilton, A.J.S., Kumar, P., Lu, E., & Mathews, A., 1991. ApJ, 374:L1

Hartley, W.G., Gazzola, L., Pearce, F.R., Kay, S.T., & Thomas, P.A., 2008. MNRAS, 386:2015

Heitmann, K., Higdon, D., White, M., Habib, S., Williams, B.J., Lawrence, E., & Wagne, C., 2009. ApJ, 705:156

Heitmann, K., White, M., Wagner, C., Habib, S., & Higdon, D., 2008. ApJ

Hernquist, L. & Katz, N., 1989. ApJS, 70:419

Herschel, F.W., 1785. Phil. Trans., 75:213

Hincks, A.D., Acquaviva, V., Ade, P., Aguirre, P., Amiri, M., Appel, J.W., Barrientos, L.F., Battistelli, E.S., Bond, J.R., Brown, B., Burger, B., Chervenak, J., Das, S., Devlin, M.J., Dicker, S.R., Doriese, W.B., Dunkley, J., Dnner, R., Essinger-Hileman, T., Fisher, R.P., Fowler, J.W., Hajian, A., Halpern, M., Hasselfield, M., Hernndez-Monteagudo, C., Hilton, G.C., Hilton, M., Hlozek, R., Huffenberger, K., Hughes, D.H., Hughes, J.P., Infante, L., Irwin, K.D., Jimenez, R., Juin, J., Kaul, M., Klein, J., Kosowsky, A., Lau, J.M., Limon, M., Lin, Y.T., Lupton, R.H., Marriage, T.A., Marsden, D., Martocci, K., Mauskopf, P., Menanteau, F., Moodley, K., Moseley, H., Netterfield, C.B., Niemack, M.D., Nolta, M.R., Page, L.A., Parker, L., Partridge, B., Quintana, H., Reid, B., Sehgal, N., Sievers, J., Spergel, D.N., Staggs, S.T., Stryzak, O., Swetz, D.S., Switzer, E.R., Thornton, R., Trac, H., Tucker, C., Verde, L., Warne, R., Wilson, G., Wollack, E., & Zhao, Y., 2010. ApJS, 191:423

Hockney, R.W. & Eastwood, J.W., 1988. *Computer Simulation Using Particles*. Bristol: Hilger

Hoffman, Y. & Ribak, E., 1991. ApJL, 380:L5

Holtzman, J.A., 1989. ApJS, 71:1

Horner, D.J., 2001. Ph.D. Thesis, Univ. Maryland

Jessop, C., Duncan, M., & Chau, W.Y., 1994. J. Comp. Phys., 115:339

Kaiser, N., 1986. MNRAS, 222:323

Kaiser, N., 1991. ApJ, 383:104

Kang, H. & Jones, T., 2005. ApJ, 620:44

Kang, H., Jones, T., & Gieseler, U.D.J., 2002. ApJ, 579:337

Kang, H., Ryu, D., R, C., & Ostriker, J.P., 2007. ApJ, 669:729

Katz, N., 1992. ApJ, 391:502

Katz, N., Weinberg, D., & Hernquist, L., 1996. ApJS, 105:19

Katz, N. & White, S.D.M., 1993. ApJ, 412:455

Kay, S.T., da Silva, A.C., Aghanim, N., Blanchard, A., Liddle, A.R., Puget, J.L., Sadat, R., & Thomas, P.A., 2007. MNRAS, 377:317

Kay, S.T., Thomas, P.A., Jenkins, A., & Pearce, F.R., 2004. MNRAS, 355:1091

Kay, S.T., Thomas, P.A., & Theuns, T., 2003. MNRAS, 343:608

Kennicutt, R.C., 1998. ApJ, 498:541

Klypin, A., Gottlöber, S., Kravtsov, A., & Khoklov, A., 1999a. ApJ, 516:530

Klypin, A., Kravtsov, A., Valenzuela, O., & Prada, F., 1999b. ApJ, 522:82

Klypin, A.A. & Shandarin, S.F., 1983. MNRAS, 204:891

Knebe, A., Green, A., & Binney, J., 2001. MNRAS, 325:845

Knebe, A., Knollmann, S.R., Muldrew, S.I., Pearce, F.R., Aragon-Calvo, M.A., Ascasibar, Y., Behroozi, P.S., Ceverino, D., Colombi, S., Diemand, J., Dolag, K., Falck, B.L., Fasel, P., Gardner, J., Gottlöber, S., Hsu, C., Iannuzzi, F., Klypin, A., Lukić, Z., Maciejewski, M., McBride, C., Neyrinck, M.C., Planelles, S., Potter, D., Quilis, V., Rasera, Y., Read, J.I., Ricker, P.M., Roy, F., Springel, V., Stadel, J., Stinson, G., Sutter, P.M., Turchaninov, V., D.Tweed, Yepes, G., & Zemp, M., 2010. Submitted to MNRAS.

Knollmann, S. & Knebe, A., 2009. ApJS, 182:624

Komatsu, E., Smith, K., Dunkley, J., Bennett, C., Gold, B., Hinshaw, G., Jarosik, N., Larson, D., Nolta, M., Page, L., D.N. Spergel, D., Halpern, M., Hill, R., Kogut, A., Limon, M., Meyer, S., Odegard, N., Tucker, G., Weiland, J., Wollack, E., & Wright., E., 2010. 2010arXiv1001.4538K

Kowalski, M., Rubin, D., Aldering, G., Agostinho, R., Amadon, A., Amanullah, R., Balland, C., Barbary, K., Blanc, G., Challis, P., Conley, A., Connolly, N., Covarrubias, R., Dawson, K., Deustua, S., Ellis, R., Fabbro, S., Fadeyev, V., Fan, X., Farris, B., Folatelli, G., Frye, B., Garavini, G., Gates, E., Germany, L., Goldhaber, G., Goldman, B., Goobar, A., Groom, D., Haissinski, J., Hardin, D., Hook, I., Kent, S., Kim, A., Knop, R., Lidman, C., Linder, E., Mendez, J., Meyers, J., Miller, G., Moniez, M., ao, A., Newberg, H., Nobili, S., Nugent, P., Pain, R., Perdereau, O., Perlmutter, S., Phillips, M., Prasad, V., Quimby, R., Regnault, N., Rich, J., Rubenstein, E., Ruiz-Lapuente, P., Santos, F., Schaefer, B., Schommer, R., Smith, R., Soderberg, A., Spadafora, A., Strolger, L., M.Strovink, Suntzeff, N., Suzuki, N., Thomas, R., Walton, N., Wang, L., Wood-Vasey, W., & Yun, J., 2008. ApJ, 686:749

Kravtsov, A.V., Klypin, A., & Hoffman, Y., 2002. ApJ, 571:563

Kravtsov, A.V., Klypin, A., & Khokhlov, A.M., 1997. ApJS, 111:73

Kravtsov, A.V., Nagai, D., & Vikhlinin, A.A., 2005. ApJ, 625:588

Kravtsov, A.V. & Yepes, G., 2000. MNRAS, 318:227

Lacey, C. & Cole, S., 1993. MNRAS, 262:627

Lacey, C. & Cole, S., 1994. MNRAS, 271:676

LeVeque, R.J., 1992. *Numerical methods for conservation laws*. Birkhäuser Verlag

Lin, Y.T., Mohr, J.J., & Stanford, S.A., 2003. ApJ, 591:749

Loken, C., Norman, M.L., Nelson, E., Burns, J., Bryan, G.L., & Motl, P., 2002. ApJ, 579:571

Lucy, L.B., 1977. AJ, 82:1013

Lumsden, S.L., Nichol, R.C., Collins, C.A., & Guzzo, L., 1992. MNRAS, 258:1

Lynden-Bell, D., 1969. Nature, 223:690

Mantz, A., Allen, S.W., Rapetti, D., & Ebeling, H., 2010. MNRAS, 406:1759

Markevitch, M., 1998. ApJ, 504:27

Markevitch, M., Gonzalez, A.H., David, L., Vikhlinin, A., Murray, S., Forman, W., Jones, C., & Tucker, W., 2002. ApJ, 567:L27

Markevitch, M., Sarazin, C.L., & Vikhlinin, A., 1999. ApJ, 521:526

Markevitch, M. & Vikhlinin, A., 2007. Physics Reports, 443:1

Martínez-Serrano, F.J., Serna, A., Domínguez-Tenreiro, R., & Mollá, M., 2008. MNRAS, 388:39

Mather, J.C., Cheng, E.S., Eplee, R.E., Isaacman, R.B., Meyer, S.S., Shafer, R.A., Weiss, R., Wright, E.L., Bennet, C.L., Boggess, N.W., Dwek, E., & Gulkis, S., 1990. ApJL, 354:L37

Maughan, B.J., Jones, L.R., Ebeling, H., & C.Scharf, 2006. MNRAS, 365:509

Mazzotta, P., Rasia, E., Moscardini, L., & Tormen, G., 2004. MNRAS, 354:10

McCarthy, I.G., 2007. MNRAS, 376:497

McCarthy, I.G., Schaye, J., Ponman, T.J., Bower, R.G., Booth, C.M., Vecchia, C.D., Crain, R.A., Springel, V., Theuns, T., & Wiersma, .P.C., 2010. MNRAS, 406:822

Meekins, J.F., Fritzand, G., Chubb, T.A., & Friedman, H., 1971. Nature, 231:107

Messier, C., 1784. *Connaissance des Temps*. Paris

Miniati, F., Ryu, D., Kang, H., & Jones, T.W., 2001. ApJ, 559:59

Miniati, F., Ryu, D., Kang, H., Jones, T.W., Cen, R., & Ostriker, J.P., 2000. ApJ, 542:608

Mitchell, N.L., McCarthy, I.G., Bower, R.G., Theuns, T., & Crain, R.A., 2009. MNRAS, 395:180

Mitchell, R., Culhane, J., Davison, P.J.N., & Ives, J., 1976. MNRAS, 175:29P

Moore, B., Ghigna, S., Governato, F., Lake, G., Quinn, T., Stadel, J., & Tozzi, P., 1999. ApJL, 524:19

Morandi, A. & Ettori, S., 2007. MNRAS, 380:1521

Motl, P.M., Burns, J.O., Loken, C., Norman, M.L., & Bryan, G., 2004. ApJ, 606:635

Muanwong, O., Thomas, P.A., Kay, S.T., & Pearce, F.R., 2002. MNRAS, 336:527

Muanwong, O., Thomas, P.A., Kay, S.T., Pearce, F.R., & Couchman, H.M.P., 2001. ApJL, 552:L27

Nagai, D., Kravtsov, A.V., & Vikhlinin, A., 2007. ApJ, 668:1

Navarro, J., Frenk, C.S., & White, S.D.M., 1995a. MNRAS, 275:720

Navarro, J., Frenk, C.S., & White, S.D.M., 1995b. MNRAS, 275:56

Navarro, J., Frenk, C.S., & White, S.D.M., 1997. ApJ, 490:493

Neyrinck, M.C., Knedin, N.Y., & Hamilton, A.J.S., 2005. MNRAS, 356:1222

Nichol, R.C., 2004. *Carnegie Astrophysics Series, Vol. 3: Clusters of Galaxies: Probes of Cosmological Structure and Galaxy Evolution*. Cambridge University Press. Eds.: J. S. Mulchaey and A. Dressler and A. Oemler

O'Hara, T.B., Mohr, J.J., Bialek, J.J., & Evrard, A.E., 2006. ApJ, 639:64

Okamoto, T., Jenkins, A., Eke, V.R., Quilis, V., & Frenk, C.S., 2003. MNRAS, 345:429

Osmond, J.P.F. & Ponman, T.J., 2004. MNRAS, 305:1511

Pavlidou, V. & Fields, B.D., 2006. ApJ, 642:734

Peacock, J.A. & Dodds, S.J., 1996. MNRAS, 280:L19

Pearce, F.R., Thomas, P.A., Couchman, H.M.P., & Edge, A.C., 2000. MNRAS, 317:1029

Peebles, P.J.E., 1970. AJ, 75:13

Peebles, P.J.E., 1980. *The large scale structure of the Universe*. Princeton University Press

Peebles, P.J.E., 1993. *Principles of physical cosmology.* Princeton Series in Physics, Princeton, NJ: Princeton University Press

Pen, U.L., 1995. ApJS, 100:269

Percival, W., Nichol, R., Eisenstein, D., Frieman, J., Fukugita, M., Loveday, J., Pope, A., Schneider, D., Szalay, A., Tegmark, M., Vogeley, M., Weinberg, D., Zehavi, I., Bahcall, N., N.A, Brinkmann, J., Connolly, A., & Meiksin, A., 2007a. ApJ, 657:645

Percival, W., Nichol, R., Eisenstein, D., Weinberg, D., Fukugita, M., Pope, A., Schneider, D., Szalay, A., Vogeley, M., Zehavi, I., I, Brinkmann, N.B.J., Connolly, A., Loveday, J., & Meiksin, A., 2007b. ApJ, 657:51

Perlmutter, S., Aldering, G., Goldhaber, G., Knop, R.A., Nugent, P., Castro, P.G., Deustua, S., Fabbro, S., A.Goobar, nd I. M. Hook, D.E.G., Kim, A.G., Kim, M.Y., Lee, J.C., Nunes, N.J., Pain, R., Pennypacker, C.R., Quimby, R., Lidman, C., Irwin, R.S.E.M., McMahon, R.G., Ruiz-Lapuente, P., Walton, N., Schaefer, B., Boyle, B.J., Filippenko, A.V., Matheson, T., Fruchter, A.S., Panagia, N., Newberg, H.J.M., Couch, W.J., & Project, T.S.C., 1999. ApJ, 517:565

Perucho, M., Quilis, V., & Martí, J.M., 2011. Proceedings of the IAU Symposium "Jets at all Scales", 275:125

Peterson, J.R., Kahn, S.M., Paerels, F.B.S., Kaastra, J.S., Tamura, T., Bleeker, J.A.M., Ferrigno, C., & Jernigan, J.G., 2003. ApJ, 590:207

Pfrommer, C., Enßlin, T.A., & Springel, V., 2008. MNRAS, 385:1211

Pfrommer, C., Springel, V., Enßlin, T.A., & Jubelgas, M., 2006. MNRAS, 367:113

Planelles, S. & Quilis, V., 2009. MNRAS, 399:410

Planelles, S. & Quilis, V., 2010. A&A, 519:A94

Ponman, T.J., Sanderson, A.J.R., & Finoguenov, A., 2003. MNRAS, 343:331

Poole, G.B., Babul, A., McCarthy, I.G., Fardal, M.A., Bildfell, C.J., Quinn, T., & Mahdavi, A., 2007. MNRAS, 380:437

Poole, G.B., Babul, A., McCarthy, I.G., Sanderson, A.J., & Fardal, M.A., 2008. MNRAS, 391:1163

Poole, G.B., Fardal, M.A., Babul, A., McCarthy, I.G., Quinn, T., & Wadsley, J., 2006. MNRAS, 373:881

Postman, M., Lubin, L.M., Gunn, J.E., Oke, J.B., Hoessel, J.G., Schneider, D.P., & Christensen, J.A., 1996. AJ, 111:615

Pratt, G.W., Böhringer, H., Croston, J.H., Arnaud, M., Borgani, S., Finoguenov, A., & Temple, R.F., 2007. A&A, 461:71

Press, W.H. & Schechter, P., 1974. ApJ, 425:187

Press, W.H., Teukolsky, S.A., Vetterling, W.T., & Flannery, B.P., 1996. *Numerical Recipes in FORTRAN 77: The Art of Scientific computing*. Cambridge University Press

Puchwein, E., Sijacki, D., & Springel, V., 2008. ApJL, 687:L53

Quilis, V., 2004. MNRAS, 352:1426

Quilis, V., Bower, R.G., & Balogh, M.L., 2001. MNRAS, 328:1091

Quilis, V., Ibáñez, J.M., & Sáez, D., 1993. RMxAA, 25:117

Quilis, V., Ibáñez, J.M., & Sáez, D., 1994. A&A, 286:1

Quilis, V., Ibáñez, J.M., & Sáez, D., 1996. ApJ, 469:11

Quilis, V., Ibáñez, J.M., & Sáez, D., 1998. ApJ, 502:518

Rasmussen, J. & Ponman, T.J., 2007. *Metallicity Structure in X-ray Bright Galaxy Groups*. Springer-Verlag. Eds.: I. Saviane, V. D. Ivanov, & J. Borissova

Raymond, J.C. & Smith, B.W., 1977. ApJS, 35:419

Reed, D., Bower, R., Frenk, C.S., Jenkins, A., & Theuns, T., 2007. MNRAS, 374:2

Reiprich, T. & Böhringer, H., 2002. ApJ, 567:716

Renzini, A., 1997. ApJ, 488:35

Ricker, P.M. & Sarazin, C.L., 2001. ApJ, 561:621

Riess, A., Filippenko, A.V., Challis, P., Clocchiatti, A., Diercks, A., Garnavich, P.M., Gilliland, R.L., Hogan, C.J., Jha, S., Kirshner, R.P., Leibundgut, B., Phillips, M.M., Reiss, D., Schommer, B.P.S.R.A., Smith, R.C., Spyromilio, J., Stubbs, C., Suntzeff, N.B., & Tonry, J., 1998. ApJ, 116:1009

Roe, P.L., 1981. J. Comp. Phys., 43:357

Rosati, P., Borgani, S., & Norman, C., 2002. ARA&A, 40:539

Rozo, E., Wechsler, R., Rykoff, E., Annis, J., Becker, M., Evrard, A., Frieman, J., Hansen, S., Hao, J., Johnston, D., Koester, B., Sheldon, T.M.E., & Weinberg, D., 2010. ApJ, 708:645

Ryu, D., Kang, H., Hallman, E., & Jones, T.W., 2003. ApJ, 593:599

Ryu, D., Ostriker, J.P., Kang, H., & Cen, R., 1993. ApJ, 414:1

Sanderson, A.J.R., Ponman, T.J., Finoguenov, A., Lloyd-Davies, E.J., & Markevitch, M., 2003. MNRAS, 340:989

Sanderson, A.J.R., Ponman, T.J., & O'Sullivan, E., 2006. MNRAS, 372:1496

Sarazin, C., 1988. *X-Ray Emission from Clusters of Galaxies*. Cambridge University Press

Sarazin, C.L., 2002. *Merging Processes in Galaxy Clusters*. Astrophysics and Space Science Library

Schindler, S. & Diaferio, A., 2008. SSRv, 134:363

Serlemitsos, P., Smith, B., Boldt, E., Holt, S., & Swank, J., 1977. ApJ, 211:L63

Serna, A., Domínguez-Tenreiro, R., & Sáiz, A., 2003. ApJ, 597:878

Shaw, L.D., Weller, J., Ostriker, J.P., & Bode, P., 2006. ApJ, 646:815

Sheth, R. & Tormen, G., 1999. MNRAS, 308:119

Short, C.J., Thomas, P.A., Young, O.E., Pearce, F.R., Jenkins, A., & Muanwong, O., 2010. MNRAS, 408:2213

Shu, C. & Osher, C., 1988. J. Comp. Phys., 77:439

Skillman, S.W., O'Shea, B.W., Hallman, E.J., Burns, J.O., & Norman, M.L., 2008. ApJ, 689:1063

Smith, R.E., Peacock, J.A., Jenkins, A., White, S.D.M., Frenk, C.S., Pearce, F.R., Thomas, P.A., Efstathiou, G., & Couchman, H.M.P., 2003. MNRAS, 341:1311

Snowden, S.L., Mushotzky, R.F., Kuntz, K.D., & Davis, D.S., 2008. A&A, 478:615

Spergel, D.N., Verde, L., Peiris, H.V., Komatsu, E., Nolta, M.R., Bennett, C.L., Halpern, M., Hinshaw, G., Jarosik, N., Kogut, A., Limon, M., & Meyer, S.S., 2003. ApJS, 148:175

Splinter, R.J., 1996. MNRAS, 281:281

Springel, V., 2005. MNRAS, 364:1105

Springel, V. & Hernquist, L., 2003. MNRAS, 339:289

Springel, V., White, S.D.M., Tormen, G., & Kauffmann, G., 2001a. MNRAS, 328:726

Springel, V., White, S., Jenkins, A., Frenk, C., Yoshida, N., Gao, L., Navarro, J., Thacker, R., Croton, D., Helly, J., Peacock, J., Cole, S., Thomas, P., Couchman, H., Evrard, A., Colberg, J., & Pearce, F., 2005. Nature, 435:629

Springel, V., Yoshida, N., & White, S.D.M., 2001b. New Astronomy, 6:79

Sun, M., Voit, G.M., Donahue, M., Jones, C., Forman, W., & Vikhlinin, A., 2009. ApJ, 693:1142

Sunyaev, R.A. & Zel'dovich, Y.B., 1970. Astrophysics and Space Science, 7:3

Sunyaev, R.A. & Zel'dovich, Y.B., 1972. Comments on Astrophysics and Space Physics, 4:173

Sutherland, R. & Dopita, M.S., 1993. ApJS, 88:253

Tasker, E.J., Brunino, R., Mitchell, N.L., Michielsen, D., Pearce, S.H.F.R., Bryan, G.L., & Theuns, T., 2008. MNRAS, 390:1267

Tegmark, M., Blanton, M.R., Strauss, M.A., Hoyle, F., Schlegel, D., Scoccimarro, R., Vogeley, M.S., Weinberg, D.H., Zehavi, I., Berlind, A., Budavari, T., Connolly, A., Eisenstein, D.J., Finkbeiner, D., Frieman, J.A., Gunn, J.E., Hamilton, A.J.S., Hui, L., Jain, B., Johnston, D., Kent, S., Lin, H., Nakajima, R., Nichol, R.C., Ostriker, J.P., Pope, A., Scranton, R., Seljak, U., Sheth, R.K., Stebbins, A., Szalay, A.S., Szapudi, I., Verde, L., Xu, Y., Annis, J., Bahcall, N.A., Brinkmann, J., Burles, S., Castander, F.J., Csabai, I., Loveday, J., Doi, M., Fukugita, M., Gott, J.R., Hennessy, G., Hogg, D.W., Ivezic, Z., Knapp, G.R., Lamb, D.Q., Lee, B.C., Lupton, R.H., McKay, T.A., Kunszt, P., Munn, J.A., O'Connell, L., Peoples, J., Pier, J.R., Richmond, M., Rockosi, C., Schneider, D.P., Stoughton, C., Tucker, D.L., Berk, D.E.V., Yanny, B., & York, D.G., 2004. ApJ, 606:702

Tegmark, M., Eisenstein, D.J., Strauss, M.A., Weinberg, D.H., Blanton, M.R., Frieman, J.A., Fukugita, M., Gunn, J.E., Hamilton, A.J.S., Knapp, G.R., Nichol, R.C., Ostriker, J.P., Padmanabhan, N., Percival, W.J., Schlegel, D.J., Schneider, D.P., Scoccimarro, R., Seljak, U., Seo, H.., Swanson, M., Szalay, A.S., Vogeley, M.S., Yoo, J., Zehavi, I., Abazajian, K., Anderson, S.F., Annis, J., Bahcall, N.A., Bassett, B., Berlind, A., Brinkmann, J., Budavari, T., Castander, F., Csabai, I., M.Doi, Finkbeiner, D., Gillespie, B., Glazebrook, K., G.S.Hennessy, Hogg, D., Ivezic, Z., Jain, B., Johnston, D., Kent, S., Lamb, D., Lee, B., Lin, H., Loveday, J., Lupton, R., Munn, J., Pan, K., Park, C., Peoples, J., Pier, J., Pope, A., Richmond, M., Rockosi, C., Scranton, R., Sheth, R., Stebbins, A., Stoughton, C., Szapudi, I., Tucker, D., Berk, D., Yanny, B., & York, D., 2006. Physical Review D, 74:123507

Teyssier, R., 2002. A&A, 385:337

Theuns, T., Leonard, A., Efstathiou, G., Pearce, F.R., & Thomas, P.A., 1998. MNRAS, 301:478

Thomas, P.A. & Couchman, H.M.P., 1992. MNRAS, 257:11

Tormen, G., 1998. MNRAS, 297:648

Tormen, G., Moscardini, L., & Yoshida, L., 2004. MNRAS, 350:1397

Tornatore, L., Borgani, S., Springel, V., Matteucci, F., Menci, N., & Murante, G., 2003. MNRAS, 342:1025

Toro, E., 1997. *Riemann solvers and numerical methods for fluid dynamics.* Springer-Verlag

Tozzi, P. & Norman, C., 2001. ApJ, 546:63

Valdarnini, R., 2002. ApJ, 567:741

Valdarnini, R., 2003. MNRAS, 339:1117

van Kampen, E., 1995. MNRAS, 273:295

Vanderlinde, K., Crawford, T.M., de Haan, T., Dudley, J.P., Shaw, L., Ade, P.A.R., Aird, K.A., Benson, B.A., Bleem, L.E., Brodwin, M., Carlstrom, J.E., Chang, C.L., Crites, A.T., Desai, S., Dobbs, M., Foley, R., George, E., Gladders, M.D., Hall, N.R., Halverson, N.W., High, F.W., Holder, G.P., Holzapfel, W.L., Hrubes, J.D., Joy, M., Keisler, R., Knox, L., Lee, A.T., M.Leitch, E., Loehr, A., Lueker, M., Marrone, D.P., McMahon, J.J., Mehl, J., Meyer, S.S., Mohr, J.J., Montroy, T.E., Ngeow, C., Padin, S., Plagge, T., Pryke, C., Reichardt, C.L., Rest, A., Ruel, J., Ruhl, J.E., Schaffer, K.K., Shirokoff, E., Song, J., Spieler, H.G., Stalder, B., Staniszewski, Z., Stark, A.A., Stubbs, C.W., van Engelen, A., Vieira, J.D., Williamson, R., Yang, Y., Zahn, O., & Zenteno, A., 2010. ApJ, 722:1180

Vazza, F., Brunetti, G., & Gheller, C., 2009. MNRAS, 395:1333

Vikhlinin, A., Burenin, R., Forman, W.R., Jones, C., Hornstrup, A., Murray, S.S., & Quintana, H., 2006a. astro-ph/0611438

Vikhlinin, A., Kravtsov, A., Forman, W., Jones, C., Markevitch, M., Murray, S.S., & Speybroeck, L.V., 2006b. ApJ, 640:691

Vikhlinin, A., Kravtsov, A.V., Burenin, R.A., Ebeling, H., Forman, W.R., Hornstrup, A., Jones, C., Murray, S.S., Nagai, D., Quintana, H., & Voevodkin, A., 2009. ApJ, 692:1060

Vikhlinin, A., Markevitch, M., Murray, S.S., Jones, C., Forman, W., & Speybroeck, L.V., 2005. ApJ, 628:655

Vikhlinin, A., VanSpeybroeck, L., Markevitch, M., Forman, W.R., & Grego, L., 2002. ApJL, 578:L107

Vikhlinin, A., Voevodkin, A., Mullis, C.R., VanSpeybroeck, L., Quintana, H., McNamara, B.R., Gioia, I., Hornstrup, A., Henry, J.P., Forman, W.R., & Jones, C., 2003. ApJ, 590:15

Villumsen, J.V., 1989. ApJS, 71:407

Voit, G.M., 2005. Reviews of Modern Physics, 77:207

Voit, G.M. & Bryan, G.L., 2001. Nature, 414:425

Voit, G.M., Kay, S.T., & Bryan, G.L., 2005. MNRAS, 364:909

von Neumann, J., 1951. *Various techniques used in connection with random digits. Monte Carlo methods.* Nat. Bureau Standards

Wadsley, J.W., Stadel, J., & Quinn, T., 2004. New Astronomy, 9:137

Warren, M.S., Quinn, P.J., Salmon, J.K., & Zurek, W.H., 1992. ApJ, 399:405

Weinberg, D., Hernquist, L., & Katz, N., 1997. ApJ, 477:8

Wetzstein, M., Nelson, A.F., Naab, T., & Burkert, A., 2009. ApJS, 184:298

White, S.D.M., 1976. MNRAS, 177:717

White, S.D.M., 2002. ApJ, 143:241

Wu, X.P., Xue, Y.J., & Fang, L.Z., 1999. ApJ, 524:22

Yaryura, C.Y., Baugh, C.M., & Angulo, R.E., 2010. Submitted to MNRAS, arXiv:1003.4259

Yepes, G., Kates, R., Khokhlov, A., & Klypin, A., 1997. MNRAS, 284:235

York, D.G., Adelman, J., Anderson, J.E., & Anderson, S.F., 2000. ApJ, 120:1579

Zel'dovich, Y.B., 1970. Astrophysics, 6:164

Zwicky, F., 1933. Helv. Phys. Acta, 6:110

Zwicky, F., 1937. ApJ, 86:217